Aeroacoustics of corrugated pipes

Document Version:
Publisher's PDF, also known as Version of Record (includes final page, issue and volume numbers)

Please check the document version of this publication:

• A submitted manuscript is the version of the article upon submission and before peer-review. There can be important differences between the submitted version and the official published version of record. People interested in the research are advised to contact the author for the final version of the publication, or visit the DOI to the publisher's website.
• The final author version and the galley proof are versions of the publication after peer review.
• The final published version features the final layout of the paper including the volume, issue and page numbers.

Link to publication

AEROACOUSTICS OF CORRUGATED PIPES

PROEFSCHRIFT

ter verkrijging van de graad van doctor aan de
Technische Universiteit Eindhoven, op gezag van de
rector magnificus, prof.dr.ir. C.J. van Duijn, voor een
commissie aangewezen door het College voor
Promoties in het openbaar te verdedigen
op maandag 26 maart 2012 om 16.00 uur

door

Güneş Nakiboğlu

geboren te Kahramanmaraş, Turkije

Dit proefschrift is goedgekeurd door de promotoren:

prof.dr.ir. A. Hirschberg
en
prof.dr.ir. H.W.M. Hoeijmakers

Cover design by Paul Verspaget

aileme,

à Judith.

Contents

Introduction

1.1 Corrugated pipes and the problem

In thin walled pipes, corrugations provide local stiffness while keeping global flexibility, see figure 1. The local rigidity prevents the collapse of the pipe during bending. This unique characteristic makes corrugated pipes suitable for a broad range of industrial applications. The main drawback of corrugated pipes is that the flow through these pipes can cause self sustained oscillations, which produce high amplitude whistling sounds. This problem has been reported in applications such as ventilation systems, domestic appliances and heat exchangers [Petrie and Huntley, 1980; Elliott, 2004]. Whistling is an environmental nuisance. For applications at elevated operating pressures such as offshore natural gas transportation systems, self-sustained oscillations can also induce severe structural vibrations leading in extreme circumstances to mechanical failure [Ziada and Bühlmann, 1991; Belfroid et al., 2007; Kristiansen and Wiik, 2007; Popescu and Johansen, 2008; Goyder, 2010]. Corrugated pipes are also used as musical toys. The musical instrument called *Hummer*, is a flexible plastic corrugated pipe of approximately 75 cm length and 3 cm diameter. Holding one end of the tube while swinging the tube above the head, various tones can be produced. This chorus like sound is musically interesting [Silverman and Cushman, 1989; Serafin and Kojs, 2005; Debut et al., 2007]. The underlying physical phenomenon investigated in the present study is closely related to a broader range of applications including, mufflers, wall perforations, side branches, orifices, complex pipe systems and even shallow water flows in rivers [Martínez-Lera et al., 2009; Aurégan and Leroux, 2008; Tonon et al., 2010; Meile et al., 2010; Lacombe et al., 2011].

Figure 1.1: A short segment of a typical corrugated pipe, showing a longitudinal cross section of the corrugated wall

1.2   Overview of the literature

A brief overview of the literature on whistling in corrugated pipes is given below. More detailed accounts of the literature specific to the particular problems of interest are provided in the introduction sections of the corresponding chapters.

The study of whistling corrugated pipes has been initiated by Burstyn [1922] and Cermak [1922]. Fundamental results were obtained by Binnie [1961] concerning the effect of pipe geometry on the frequency of whistling (f). He also noticed that the velocity of the acoustic waves inside a corrugated pipe (c_{eff}) is smaller than the velocity of sound (c_0). In the following decades the research has been focused on the prediction of the frequency of whistling for relatively short corrugated pipes with open terminations, such as the Hummer [Crawford, 1974; Nakamura and Fukamachi, 1984; Cadwell, 1994]. Whistling was associated to a specific value of the Helmholtz number $He = fL/c_0$ based on the pipe length (L); as well as a specific value of the Strouhal number ($Sr = fL_{\text{c}}/U$) based on a characteristic length (L_{c}) and the grazing flow velocity (U). The corrugation pitch i.e. the wavelength of the corrugation [Binnie, 1961; Crawford, 1974; Nakamura and Fukamachi, 1991; Serafin and Kojs, 2005; Popescu and Johansen, 2008] and the cavity length in streamwise direction (W) [Elliott, 2004; Belfroid et al., 2007; Kristiansen and Wiik, 2007] are two extensively used dimensions for L_{c}. A commonly observed phenomenon in the Hummer, is the absence of whistling at the fundamental mode, $He \approx 0.5$, [Cermak, 1922; Crawford, 1974; Silverman and Cushman, 1989; Nakamura and Fukamachi, 1991; Cadwell, 1994; Elliott, 2004]. This has been associated to the low Reynolds number (Re) of the flow through the pipe at the fundamental mode [Crawford, 1974; Cadwell, 1994]. The conclusion of Cadwell [1994] was that turbulence is an essential factor that promotes whistling. This conclusion, however, was not firmly established.

Nakamura and Fukamachi [1991] have shown that the flexibility of the tube is not necessary for the sound generation in corrugated tubes. However, a mechanical vibration induced by the unsteady forcing on the walls can have a significant influence on the whistling. For water flow, Ziada and Bühlmann [1991] observed a strong coupling of the whistling with the pipe wall vibration modes. Elliott [2004] showed that for short corrugated pipe segments the resonant frequencies could be

predicted as multiples of a half-wave length along the pipe using an effective speed of sound (c_{eff}) for plane wave propagation in the pipe. Tonon et al. [2010] and Golliard et al. [2010] reported for multiple side branch systems and corrugated pipes, respectively, that the acoustic sources are localized around the pressure nodes of the standing acoustic wave along the tube. This indicates a dipolar nature of the sound source. The sound is generated by the reaction force of the wall on the flow due to the unsteady vortex shedding [Gutin, 1948; Curle, 1955].

1.3 Aim and scope

While the literature has provided some crucial information, until now it has not been attempted to develop a method for the quantitative prediction of the whistling of corrugated tubes. The main objective of the thesis is to develop a physical understanding of aeroacoustic sound generation due to self sustained flow oscillations in ducted cavities and to provide a quantitative prediction method for the whistling of corrugated pipes.

The work presented here is kept limited to relatively low flow speeds such that the acoustic wave length is large compared to the pipe diameter (D) and the cavity width (W). Transverse acoustic resonances observed at very high velocities [Kriesels et al., 1995; Dequand et al., 2003a; Meile et al., 2010] are excluded. The focus of the project is gas transport pipes in which the coupling between flow instabilities and wall vibrations is expected to be weak [Nakamura and Fukamachi, 1991]. Therefore, wall vibrations are not considered in the current work.

1.4 Outline of this thesis

The thesis consists of five main chapters, which correspond to three published and two submitted journal papers. This unavoidably implies some repetitions in subsequent chapters. In chapter 2, experimental data obtained by TNO on corrugated pipes are used together with original experimental data on multiple side branch system. The aim of this chapter is to demonstrate the similarities between the whistling behavior of these two geometrically periodic systems and to address the effect of some geometrical parameters, e.g. the cavity edge radius and the side branch depth, on the whistling. The chapter also provides a brief introduction to the Vortex Sound Theory of Howe [1975, 1998]. In chapter 3, a numerical methodology that combines incompressible flow simulations and Vortex-Sound Theory is proposed to estimate the acoustic source power produced by a single corrugation. This approach is used to predict the ranges of Strouhal numbers with acoustic energy production and explain the nonlinear saturation mechanism responsible for the stabilization of the shear layer to a limit cycle oscillation. This saturation explains the finite whistling am-

plitude of corrugated pipes. The proposed numerical method is also used to explore the effect of the main flow velocity profile on the whistling. Chapter 4 discusses the aeroacoustics of the Hummer. The first part of this chapter is dedicated to sound generation, while the second part is devoted to sound radiation. This should provide understanding of the musical quality of this instrument. Chapters 5 and 6 focus on the whistling of axisymmetric cavities. Corrugated pipes can be considered, in first approximation, as a series of axisymmetric cavities placed along a duct coupled by the longitudinal standing wave along the tube. In fact, the corrugated pipe can be considered as a *Sound Amplification by Stimulated Emission of Radiation* (SASER), because the longitudinal acoustic wave triggers and coordinates the radiation of sound by individual cavities. Chapter 5 focuses on the whistling of a single axisymmetric cavity and addresses the effect of the depth of the cavity on the whistling. Chapter 6 is dedicated to the hydrodynamic interference between cavities. Each chapter provides detailed conclusion on its own; in chapter 7 emerging pervasive conclusions and future research directions are presented.

1.5   The framework of the project and the contribution of the author

This thesis has been carried out within the frame work of STW project on "Aeroacoustics of corrugated pipes" (Project No. 08126) supported by the industrial partners: TNO, ASML, Shell, Philips and KEMA.

During the project there has been a close collaboration with TNO, in particular with J. Golliard and S. P. C. Belfroid involving many discussions on the application of the proposed numerical prediction to practical problems in industry. In chapter 2 and 3 some data from the experimental database of TNO on corrugated pipes [Bastiaansen, 2005; Tummers, 2006] are used. This data base has been created in a framework of a Joint Industrial Project (JIP) involving BP, UK Health and Safety Executive, Bureau Veritas, Exxon Mobil, Statoil and TNO. The technical support for experiments at TU/e was provided by J. F. H. Willems, H. B. M. Manders, F. M. R. van Uittert, E. de Cocq and A. Holten. In chapter 4, O. Rudenko has collaborated in the study on the sound radiation of the Hummer. A. Hirschberg has mainly provided theoretical feedback. These supports are recognized by including some of the above mentioned individuals as co-authors of the published, submitted journal papers and conference papers, see List of Publications. In accordance with regulations governing the conferral of the doctor's degree at Eindhoven University of Technology (Chapter 6, Art.15.), the author hereby declares that except for the above mentioned contributions, all the experiments, numerical simulations and the analysis presented in this thesis have been performed by the author.

Whistling behavior of periodic systems: corrugated pipes and multiple side branch system

2.1 Abstract

Whistling behavior of two geometrically periodic systems are investigated: corrugated pipes and a multiple side branch system. In both systems frequency is a non-decreasing piecewise constant function of the Mach number, whose increase on average is approximately linear. The plateaus, lock-in frequencies, of this piecewise constant function correspond to the longitudinal acoustic pipe modes. In both systems fluctuation amplitude changes non-monotonically with Mach number with local maxima that correspond to the lock-in frequencies. A characteristic length, equal to cavity width plus upstream edge radius, yields the smallest scatter in the measured peak-whistling Strouhal number for both systems. For both systems the upstream edge radius of the cavity/side branch has a strong effect on pressure fluctuation amplitudes. Whistling amplitudes increase by a factor of 3 to 5 upon rounding off the upstream cavity/side branch edges. The radius of the downstream edge has a less pronounced effect on the sound amplitude and frequency. The geometric parameters of the multiple side branch system can easily be modified. This makes the multiple side branch system a convenient tool for making experiments on the effects of various geometric parameters. A number of aspects are addressed with the multiple side branch system such as the effect of pipe termination geometry, source localization, side branch depth to diameter ratio, a gradient in cavity depth along the pipe and hysteresis upon change in flow velocity.

2.2   Introduction

Pipes with transversally corrugated walls are used in many industrial applications because they are globally flexible and locally rigid. At critical conditions, the flow through corrugated pipes cause severe noise problems, called whistling. It is known that geometric parameters of these pipes can have significant effects on the whistling phenomenon. But there are a number of geometric parameters and each may vary within a fairly large range [Belfroid et al., 2007; Binnie, 1961]. Thus, a systematic investigation for all possible values of these geometric parameters seems rather time consuming and costly. For this reason, we consider another periodic system, which shows whistling behavior similar to that of corrugated pipes, namely: the multiple side branch system. The main advantage of doing fundamental research on the multiple side branch system over corrugated pipes is that geometric parameters can easily be modified. Furthermore, the multiple side branch system is an interesting system on its own right.

The cross section of a generic corrugated pipe and multiple side branch system is shown in figure 2.1. In both systems the cross sectional area of the pipe (S_{p}) is periodically oscillating along the pipe of length (L). The wave length of this variations in pipe diameter is called pitch (Pt). In corrugated pipes the variation in the cross section is due to axisymmetric slit shaped cavities with a width (W) and depth (H). Whereas in multiple side branch system, the side branches along the main pipe cause this spatial variation of the pipe cross section. The depth and diameter of the side branches are denoted as H and D_{sb}, respectively. Depending on the flow direction, the edge radius of cavities and side branches denoted as r_{up} or r_{dwn}. The constant diameter (D) part between two cavities or side branches is called plateau (L_{p}).

In this paper we first briefly discuss the acoustic analogy developed by Howe [1975, 1980] by particularly emphasizing the acoustic resonance (Sec. 2.3.1), the local spatial distribution of the acoustic field (Sec. 2.3.2) and non-linear saturation phenomenon (Sec. 2.3.3), all which are essential for the interpretation of the results. In the following section (Sec. 2.4), we describe the experimental setups (Sec. 2.4.1)together with the data analysis method (Sec. 2.4.2)that was employed. In Sec. 2.5, we present the experiments performed with corrugated pipes on the determination of the optimal characteristic length for the Strouhal number [Belfroid et al., 2007] and the effect of the shape of the cavity edge on whistling phenomenon, which is known to be important in pipe systems with deep resonant side branches [Bruggeman et al., 1991]. In Sec. 2.6, we first highlight the similarities in the whistling behavior of multiple side branch system and corrugated pipes, then we discuss the following aspects for the multiple side branch system:
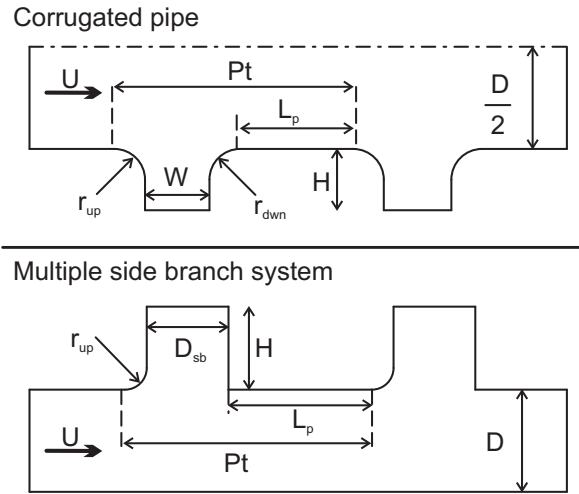
Figure 2.1: The geometric parameters of the corrugated pipes and multiple side branch system.

- We investigate the effects of pipe termination geometry on whistling amplitude, which is expected to be strong [Hirschberg et al., 1989], in Sec. 2.6.1.

- We discuss the effect of the position of sound sources relative to the acoustic standing wave pattern, which has been a subject of controversy [Kristiansen and Wiik, 2007; Tonon et al., 2010; Golliard et al., 2010], in Sec. 2.6.2

- In parallel to the experiments with corrugated pipes (Sec. 2.5), we address the effect of edge shape on the whistling phenomenon in Sec. 2.6.3.

- We present our results on the effect of cavity depth, which is a parameter that is relatively easy to investigate with a multiple side branch system, in Sec. 2.6.4.

- We investigate the impact of a gradient in depth of the side branches along the pipe in Sec. 2.6.5, as a model for a temperature gradient.

- We explore Hysteresis, which is a frequently mentioned phenomenon in the literature on corrugated pipes [Petrie and Huntley, 1980; Nakamura and Fuka-machi, 1991], in Sec. 2.6.6.

In the last section we state our conclusions on the whistling behavior of these two periodic systems.

2.3   Vortex Sound Theory and Whistling

The intrinsic instability of separated flows, such as wakes and free jets, acts as a source of unsteadiness for flows at high Reynolds numbers. An unsteady flow induces an unsteady force on the walls bounding the flow. The reaction force of the walls to this hydrodynamic force is a source of sound [Gutin, 1948; Curle, 1955]. A familiar example of this effect is the aeolian tone generated by a cylinder. Strouhal [1878] found that, when a uniform flow of velocity U passes along a cylinder of diameter D_c the frequency f of the sound radiated satisfies, $Sr = fD_c/U$ where Sr is a constant known as Strouhal number. Rayleigh [1896] recognized that the production of the sound is connected with the instability of the vortex sheets in the cylinder wake, which results into the formation of a von Kármán vortex street.

It is essential to realize that the cylinder walls do not need to vibrate in order to generate the sound. However, if a mechanical vibration of the cylinder is induced by the oscillating lift force, this can significantly enhance the spatial coherence and result into a stronger tone with a frequency which is a compromise between the "natural" Strouhal vortex shedding frequency and the mechanical resonance frequency. A similar lock-in can occur with an acoustic standing wave at resonant mode when the cylinder is confined to a duct [Blevins, 2001]. This enhances the sound radiation even more because the acoustic standing wave provides an improved radiation impedance. In such a case the system behaves as an unstable feedback-loop with the flow as the amplifier (source of energy) and the acoustic mode as the filter. Such a coupling with a structural mode has been observed by Ziada and Bühlmann [1991] for a corrugated pipe.

Powell [1964] established the first formal relationship between vortex shedding and the sound generation which is limited to free-space conditions and low Mach numbers. Howe [1975] generalized this relation to arbitrary homentropic flows. Later, Howe [1980] proposed to use a Helmholtz decomposition of the flow field $\mathbf{u}$ to define the acoustic field as:

$$\mathbf{u} = \boldsymbol{\nabla}(\phi_0 + \phi') + \boldsymbol{\nabla} \times \boldsymbol{\Psi}, \tag{2.1}$$

where ϕ_0 and ϕ' are the steady and unsteady component of the scalar potential, respectively and $\boldsymbol{\Psi}$ is the stream function. The acoustic velocity field ($\mathbf{u}'$) is defined as the unsteady component of the potential flow, $\mathbf{u}' = \boldsymbol{\nabla}\phi'$ For low Mach numbers ($Ma = U/c_0 \ll 1$ where c_0 is the speed of sound), Howe [1980] proposed to estimate the time average acoustic power $\langle P_{\text{source}} \rangle$ by using the following approximation:

$$\langle P_{\text{source}} \rangle = -\rho_0 \left\langle \int_V (\boldsymbol{\omega} \times \mathbf{u}) \cdot \mathbf{u}' dV \right\rangle \tag{2.2}$$

where ρ_0 is the fluid density, $\boldsymbol{\omega}$ is the vorticity

$$\boldsymbol{\omega} = \boldsymbol{\nabla} \times \mathbf{u}$$

V is the volume in which the $\boldsymbol{\omega}$ is non vanishing and $< \cdot >$ is the time average.

The amplitude of steady-periodic self-sustained oscillations, i.e. whistling, described above can be estimated using the following energy balance equation:

$$\langle P_{\text{source}} \rangle = \langle P_{\text{visc}} \rangle + \langle P_{\text{rad}} \rangle \tag{2.3}$$

in which $\langle P_{\text{visc}} \rangle$ is the term for thermal-viscous losses and $\langle P_{\text{rad}} \rangle$ is the term for the radiation losses at the boundaries of the system. The wall vibrations are neglected.

The remainder of this section is devoted to discussion of three subjects, which are important in understanding of the whistling behavior of periodic systems, namely, passive resonance frequencies of a corrugated pipe/multiple side branch system, local behavior of acoustic velocity ($\mathbf{u}'$) depending on the geometry and non-linear saturation.

2.3.1 Acoustic resonance

Consider a corrugated pipe or a multiple side branch system of length L with pitch length Pt and cavity/side branch volume V_{c}. As a first approximation, the pipe is described as a tube of uniform cross section S_{p} in which acoustic waves are propagating at a modified speed of sound c_{eff}. Assuming that the acoustic compliance is determined by the pitch volume, $PtS_{\text{p}} + V_{\text{c}}$, and the inertia is determined by the mass in the main pipe, $\rho_0 PtS_{\text{p}}$; the propagation of low frequency, $fPt/U \ll 1$, acoustic waves along the tube has an effective speed c_{eff} [Elliott, 2004]:

$$c_{\text{eff}} = \frac{c_0}{\sqrt{1 + V_{\text{c}}/(S_{\text{p}} Pt)}} \tag{2.4}$$

where $V_{\text{c}} = \pi DHW$ for corrugated pipes and $V_{\text{c}} = \pi D_{\text{sb}} H/4$ for multiple side branch systems. In the above formula the convection by the main flow is neglected. Then the resonance frequencies (f_{n}) for an open-open pipe termination are given by

$$f_{\text{n}} = n(c_{\text{eff}}/2L) \qquad n = 1, 2, 3, \ldots$$

Tonon et al. [2010] showed for a multiple side branch system with sharp edges and $H/D_{\text{sb}} = 1.15$ that the predicted resonance frequencies are in agreement with measured frequencies within 3% accuracy, which is confirmed for other geometries in Sec. 2.6.4. The discussion here is limited to low frequencies, $fH/c_0 \ll 1$ so that the acoustic flux into the cavities/side branches can be neglected. This simplified model describe the global behavior, however a local description of the acoustic field $\mathbf{u}'$ is needed in order to apply the analogy of Howe [1975].

2.3.2   Local spatial distribution of the acoustic field and sound sources

Following the definition of the acoustic field [Howe, 1980] given in Eq. 2.1, the acoustic flow grazing along a cavity of a corrugated pipe or a side branch, is a potential flow. At low frequencies it is locally an incompressible potential flow. This flow can be calculated analytically for a two dimensional cavity with sharp edges using conformal mapping [Milne-Thomson, 1968]. The acoustic streamlines are sketched qualitatively in figure 2.2-a. The flow bends as it passes along the edges and the
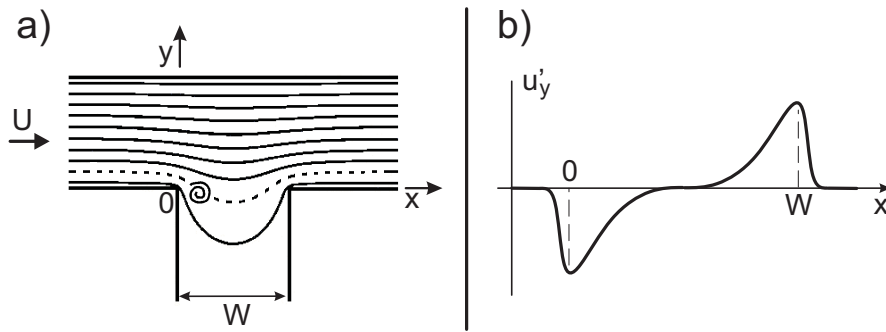
Figure 2.2: a) The acoustic streamlines (———) grazing over a cavity, b) y component of the acoustic velocity at the moment when the vortex detached along an acoustic streamline (- - - - -) passing close to the edges of the cavity.

flow velocity increases as we approach to edge. This acceleration corresponds to a pressure gradient which is responsible for the bending of the stream lines. A sharp edge implies a singularity in pressure and a locally infinitely large acoustic velocity. At the upstream edge of the cavity, the actual flow separates due to viscous effects so that vorticity is shed and a shear layer is formed. This shear layer separates the main flow from the almost stagnant fluid in the cavity.

The earlier studies [Bruggeman, 1987a; Hourigan et al., 1990; Nelson et al., 1983; Peters, 1993; Welsh et al., 1984] showed that a vortex is shed from the upstream edge at the moment when the acoustic velocity near the upstream edge turns from -x direction to +x direction (main flow direction), see figure 2.2-a. From Eq. 2.2 it is seen that $-\rho_0(\boldsymbol{\omega} \times \mathbf{u}) \cdot \mathbf{u}'$ is negative and large near the upstream edge because $\mathbf{u}'$ is locally normal to the convective velocity $\mathbf{u}$ and $\mathbf{u}'$ is locally singular. As the vorticity is convected away from the upstream edge in the main flow direction, the acoustic field $\mathbf{u}'$ bends in the direction of the convective velocity $\mathbf{u}$, see figure 2.2-b, so that absolute value of $-\rho_0(\boldsymbol{\omega} \times \mathbf{u}) \cdot \mathbf{u}'$ is reduced and vanishes halfway in the cavity opening. As the vorticity perturbation approaches to the downstream edge, the acoustic flow velocity becomes again normal to the convective velocity $\mathbf{u}$. Sound can now produced if the sign of the acoustic field is such that $-\rho_0(\boldsymbol{\omega} \times \mathbf{u}) \cdot \mathbf{u}'$ is positive. This occurs if the travel time of the vorticity across the cavity is less than the half of an oscilla-

tion period plus an integer number of oscillation period. For critical flow conditions the balance between the initial absorption and the later production results into a net sound production, so that whistling is possible. Bruggeman et al. [1991] showed that, if the vorticity is assumed to be concentrated in a point vortex and convected along a straight line parallel to the main pipe axis with a velocity $U_{\rm c} = 0.4U$. Then for consecutive hydrodynamic modes the peak-whistling Strouhal numbers, where the maximum amplitude in pressure fluctuations are registered, is given by:

$$Sr_{\rm p-w} = \frac{f_{\rm n}W}{U} = 0.13 + n\,0.40 \qquad\qquad n = 0, 1, 2... \qquad (2.5)$$

Later, more realistic calculations by Hofmans [1998] and Martínez-Lera et al. [2009] showed that the first hydrodynamic mode ($n = 0$) is rather weak. They have also indicated that for the second hydrodynamic mode ($n = 1$) the peak-whistling Strouhal number ($Sr_{\rm p-w}$) is around 0.6. This Strouhal number is larger than the prediction of Bruggeman et al. [1991].

The singularity at the edges can be reduced by rounding. This implies that rounding off the upstream edge decreases the initial absorption which leads to an increase in the net sound production $\langle P_{\rm source}\rangle$. This has been observed in the case of deep side branches by Bruggeman et al. [1991]. They also concluded that the characteristic length used in the Strouhal number definition should be the sum of the cavity width and the upstream edge radius, $W + r_{\rm up}$, because the travel distance of the vorticity perturbation is increased by rounding the upstream edge off. The downstream edge is less critical [Bruggeman et al., 1991; Nakiboğlu et al., 2009] because the vorticity (the shear layer) is less localized as it approaches the downstream edge than when it is shed from the upstream edge. The vortex core near the downstream edge is typically large compared to the edge radius. This effect will be demonstrated in Sec. 2.5, Sec. 2.6.1 and Sec. 2.6.3.

2.3.3 Non-linear saturation

The aeroacoustic behavior of corrugated pipes and the multiple side branch system depends strongly on the ratio of acoustic velocity to main flow velocity, $|u'|/U = |p'|/(\rho_0 c_0 U)$, where $|u'|$ is the acoustic velocity at a pressure node and $|p'|$ is the pressure amplitude at a pressure anti-node, of the standing wave. This was explained by Bruggeman et al. [1991] for the case of deep side branches. The instability of the shear layer at low amplitudes can be described by linear theory. At resonance, for low frequencies linear theory predicts an amplification of the perturbation by a factor $e^{2\pi} \approx 500$ over one hydrodynamic wave length [Bruggeman et al., 1986]. For a grazing flow along shallow cavities the peak-whistling Strouhal numbers described

by Eq. 2.5 correspond to an integer number n of hydrodynamic wave length plus a quarter hydrodynamic wave length matching the cavity width (W). Hence the first mode, $n = 0$ has only an amplification $(e^{2\pi})^{1/4} \approx 5$ while the second mode, $n = 1$, has an amplification of $(e^{2\pi})^{5/4} \approx 2500$. The exponential growth of the amplitude clearly imposes a limit condition for the use of linear theory because the perturbations should remain small. A non-linear saturation has to occur [Fletcher, 1979] which is the formation of the discrete vortices, where most of the vorticity of an hydrodynamic wave length is concentrated into a vortical structure [Bruggeman et al., 1991]. The recent numerical calculation of Martínez-Lera et al. [2009] on a single side branch at moderate Reynolds numbers, $Re = O(10^3)$, which globally agrees with the earlier studies [Bruggeman et al., 1991; Hofmans, 1998], showed that for the second hydrodynamic mode in the case of grazing acoustic velocity (Fig. 2.2-a), the non linear saturation of perturbations already appears around $|u'|/U \approx 10^{-2}$.

It is important to note that whistling at low amplitudes, in the range $|u'|/U \approx 10^{-3}$, is an extremely unstable phenomenon which correspond to an almost neutrally stable oscillation cycle where the net acoustic source power ($\langle P_{\mathrm{source}} \rangle$) and losses ($\langle P_{\mathrm{visc}} \rangle + \langle P_{\mathrm{rad}} \rangle$), which are both proportional to $|u'|^2$, are in equilibrium. A very small increase in losses will make the system stable and suppress the oscillations. Indeed, in Sec. 2.6.1 it is demonstrated that the low amplitude oscillations are very sensitive to small modifications in the system. Moderate amplitude oscillations with $|u'|/U \approx 10^{-1}$ are much more stable.

2.4 Experimental Setup & Data Analysis

In the first part of this section the experimental setups for corrugated pipes and the multiple side branch system are introduced. In the second part, the processing of the experimental data is briefly explained.

2.4.1 Experimental setups

The schema of the experimental setup that was employed in corrugated pipe experiments is shown in figure 2.3-a. From upstream to downstream the setup is composed of: a pressure vessel, a turbine flow meter, a flow control valve, a constant diameter ($D = 50.8$ mm) measurement section of 1.6 m long, a corrugated pipe segment, which is 3 m long, a second measurement section identical to the first one and a pressure vessel. Upstream and downstream measurement sections are equipped each with five flush mounted microphones (PCB 116A), which allow the reconstruction of traveling acoustic plane waves using the multi microphone method [Åbom and Bodén, 1988; Banks-Lee and Peng, 1989]. The amplitude of the pressure fluctuations at a pressure anti-node ($|p'|$) is calculated from the plane wave's amplitude and

phase. By means of a back pressure control valve, the system can be pressurized to operational pressures up to 12 bar which allows us also to study the Reynolds number dependency of the system [Belfroid et al., 2007].

The multiple side branch system is made of 19 equal T-joints that are connected

a) Corrugated Pipe Setup

b) Multiple Side Branch Setup
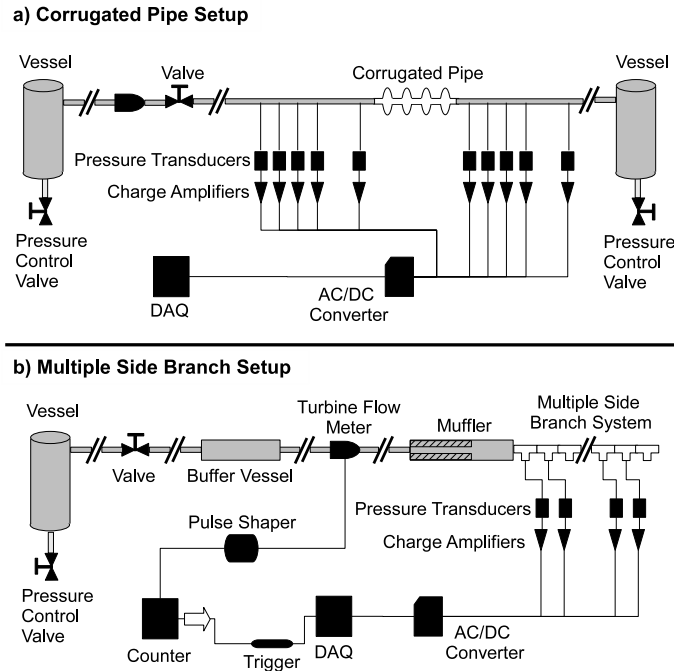
Figure 2.3: Experimental setups for corrugated pipes (a) and multiple side branch system (b).

to one another forming a row of equally spaced side branches along a main pipe, as demonstrated in figure 2.1-b. The T-joints (vacuum system ISO-KF) are cast in aluminum. The main pipe of the T-joint has an internal diameter (D) of 33 mm which is equal to the the inner diameter of the side branch (D_{sb}). The length of the main pipe of each T-joint is 100mm and the side branch is located half way of this segment. Using plugs at each side branch and changing their penetration depth the side branch depth was varied. One of the edges (r_{up} or r_{dwn}, depending on the flow direction) that connect the side branch to the main pipe is rounded and the other edge is sharp. The edge radius of curvature is 3 mm, which is approximately one tenth of the side branch diameter ($r/D_{\mathrm{sb}} \approx 0.1$). T-joints are connected to each other using standard ISO-KF clamps which incorporate O-rings for sealing. The end walls of four side branches are supplied with flush mounted microphones (PCB 116A). By using these microphones the standing wave pattern, which corresponds to a longi-

tudinal pipe mode, is reconstructed and the amplitudes of pressure fluctuations at a pressure anti-node ($|p'|$) is calculated. Typical reproducibility of data are 1% for the whistling frequency and 5% for the pressure fluctuation amplitude.

The downstream end of the multiple side branch system is open to the laboratory (a large room of 15×4×4 m). The upstream end is connected to the high pressure air supply system which is composed of, from upstream to downstream, a compressor, a vessel, a control valve, a buffer vessel, a turbine flow meter and an expansion chamber muffler as shown in figure 2.3-b.

The microphones (PCB 116A) are connected to charge amplifiers (Kistler 5011). These amplifiers are connected to a PC through a AC/DC converter acquisition board (National Instruments NI SCXI-1000). A turbine flow meter (Instromet SM-RI-X-KG250) is used to measure the mean flow velocity. The turbine flow meter is connected to a pulse shaper and a counter. The acquisition system of the setup has been improved after a first series of experiments described in [Nakiboğlu et al., 2009] using a trigger system which allows simultaneous measurement of volume flow from turbine flow meter and pressure from the piezo-electric pressure transducers. The temperature of the air is measured inside the expansion chamber muffler, with an accuracy of 0.1°C, by a digital thermometer (Eurotherm 91e).

It should be noted that due to the presence of different elements upstream of the test sections, the inflow velocity profiles for corrugated pipes and multiple side branch system are not the same. In corrugated pipe setup the upstream measurement section is long enough to have a fully developed turbulent flow before the corrugated pipe segment. Whereas, for multiple side branch system, the contraction from the expansion chamber to the inlet of the multiple side branch section imposes a uniform flow at the inlet of the pipe section. However, at these Reynolds numbers, O(10^4), the momentum thicknesses of the boundary layers in both configurations are very small compared to the cavity width and side branch diameter, respectively. Thus, an essential alteration in the whistling behavior of the systems is not expected due to this difference in the inlet velocity profiles [Bruggeman, 1987a].

2.4.2   Data analysis

In this subsection we present the way we have used experimental data to detect the frequency and amplitude of the whistling. The frequencies of whistling that of interest are in the range of 100-300 Hz and the sampling rate ($f_{samp} = 1/T_{samp}$) of the experiments was 5000 Hz. Thus the sampling rate is large enough to satisfy Nyquist criteria, so as to avoid any aliasing.

Evidently the sampling duration is finite, so the Fourier Transform of the continuous signal actually can not be calculated. However by sampling for long enough time, a discrete time signal can be obtained whose Discrete Fourier Transform (DFT) roughly represents the Fourier Transform of the continuous time signal [Bracewell, 1986]. For that purpose a sampling duration, T_s, of 6 seconds has been used.

The sampled values of the continuous signal, forms a discrete time signal:

$$\mathbf{x}[k] = x(kT_{\text{samp}}) \quad \text{for } k = 0, 1, 2, \ldots (n-1)$$

where $n = T_{\text{s}}/T_{\text{samp}}$. Total energy of this discrete time signal[1] is given by

$$E_{\text{t}} = \sum_{i=0}^{n-1} \mathbf{x}[k]^2. \tag{2.6}$$

As a result of the Parseval's theorem [Bracewell, 1986] E_{t} is equal to the total energy E_{f} of the DFT of $\mathbf{x}[k]$, $\mathbf{X}[j]$.

$$E_{\text{f}} = \sum_{k=0}^{n-1} ||\mathbf{x}[k]||^2 = \sum_{j=0}^{n-1} ||\mathbf{X}[j]||^2 \tag{2.7}$$

where,

$$\mathbf{X}[j] = \sum_{k=0}^{n-1} \mathbf{x}[k] \frac{e^{-i2\pi j \frac{k}{n}}}{\sqrt{n}} \tag{2.8}$$

To calculate the amplitude of the whistling mode, the frequency ($f_{\text{p−w}}$) with the largest energy in the frequency domain is chosen. Then the total energy in an interval ($E_{f_{\text{p−w}}}$) of $f_{\text{p−w}} \pm 1Hz$ is calculated and converted to an equivalent amplitude for a harmonic signal ($x(t) = A \sin(2\pi f_{\text{p−w}} t + \theta)$) through:

$$A = \sqrt{\frac{2E_{f_{\text{p−w}}}}{T_{\text{s}}}} \tag{2.9}$$

This method is checked with several test signals which are similar to actual experimental signals. The frequency and the amplitude of this artificial signals are retrieved with in an accuracy better than 1%. The energy content of the whistling mode ($E_{f_{\text{p−w}}}$) is compared with the total energy of the signal (E_{f}). This ratio is used as an identification for whistling which is an alternative to the method based on the quality factor proposed by Rockwell et al. [2003].

The simultaneous measurement of flow velocity and pressure allows a waterfall representation of the data, in which the frequency spectrum of the whistling at different
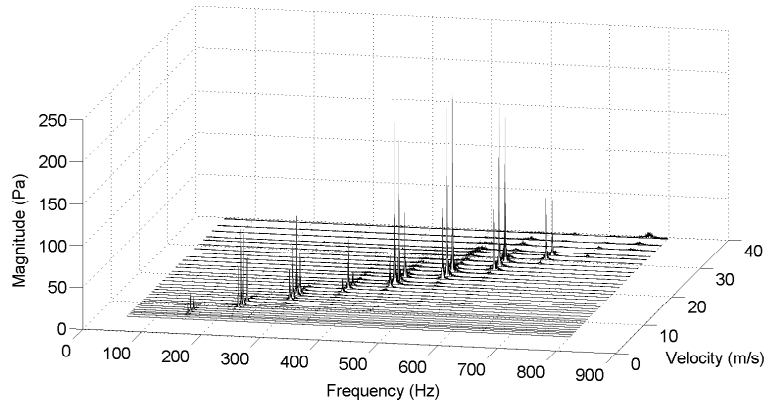
Figure 2.4: Waterfall representation of a typical result that is obtained with multiple side branch system (time resolution is nine times higher in the actual data, intermediate values are skipped for ease of representation).

flow velocities are presented in a single graph, figure 2.4. This interpretation can capture consecutive modes that appear simultaneously with the dominant mode, as observed in the literature for single axisymmetric cavities [Rockwell et al., 2003; Oshkai et al., 2005]. During the experimental campaign secondary modes were not observed. Hence for quantitative interpretation throughout the paper the data is presented separately as dimensionless fluctuation amplitude and Helmholtz number as a function of the Mach number.

2.5   Corrugated Pipes

Corrugated pipes manufactured from Polyvinyl chloride (PVC) were used in the experiments which allowed controlled variation in edge radii, depth and width of the corrugations. Geometric parameters of 11 different corrugated tubes that were tested at 14 different configurations are given in table 2.1. The pipes with asymmetric cavity geometries are tested in both flow directions and corresponding samples named configuration A and configuration B of the same pipe. For all geometries, the length of the pipe (L) is 3 m and the inner diameter of the pipe (D) is 49 mm, except for the Geo 11 which is a commercially available corrugated pipe with D of 53 mm.

  In figure 2.5, a typical result of a corrugated pipe (Geo 1) is presented. The other geometries showed also similar characteristics. It is seen that in average there is a linear increase of frequency with increasing velocity which corresponds to a peak-

---

[1]Because of our high sampling rate and long sampling duration, total energy of the continuous time signal $\int_0^{T_s} x(t)^2 dt$, in the interval $T = [0, T_s]$, is roughly equal to the $E_t T_{\text{samp}}$.

Table 2.1: Geometric parameters of tested corrugated pipes and peak-whistling Strouhal numbers.

Sample	W	H	r_{up}	r_{dwn}	L_p	Sr_{p-w}	Sample	W	H	r_{up}	r_{dwn}	L_p	Sr_{p-w}
Geo 1	8.0	4.0	2.0	2.0	0	0.42	Geo 6B	4.0	4.0	0.0	4.0	4.0	N/A
Geo 2	4.0	4.0	2.0	2.0	4.0	0.36	Geo 7	4.0	4.0	0.0	0.0	8.0	0.41
Geo 3A	4.0	4.0	3.0	1.0	4.0	0.35	Geo 8A	2.0	2.0	2.0	0.5	5.5	0.33
Geo 3B	4.0	4.0	1.0	3.0	4.0	N/A	Geo 8B	2.0	2.0	0.5	2.0	5.5	N/A
Geo 4	4.0	4.0	2.0	2.0	0	0.38	Geo 9	2.0	4.0	2.0	2.0	4.0	0.32
Geo 5	4.0	4.0	2.0	2.0	8.0	0.40	Geo 10	2.0	2.0	2.0	2.0	4.0	0.32
Geo 6A	4.0	4.0	4.0	0.0	4.0	0.36	Geo 11	7.0	5.0	1.5	1.5	0	0.49
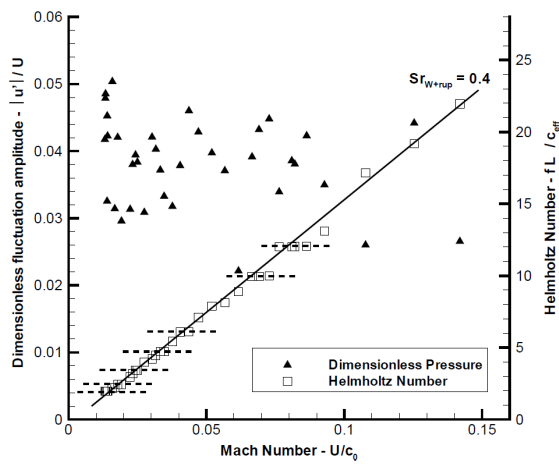
Figure 2.5: Dimensionless fluctuation amplitude and corresponding Helmholtz number as a function of Mach number for Geo 1.

whistling Strouhal number, which can be determined through a linear least square fit of consecutive excited modes with an uncertainty of ± 0.03. A closer look at the Helmholtz number reveals that the frequencies are not increasing continuously with increasing velocity. There are some plateaus (as stressed by the dashed lines) corresponding to lock-in of whistling to the longitudinal pipe modes. It is also observed that the whistling amplitude is not a monotonous function of the velocity. It displays local maxima at each lock-in with a pipe mode, when the oscillation frequency coincides with a passive acoustic resonance of the system.

Determination of the optimal characteristic length (L_c) for the Strouhal number ($Sr = f L_c / U$) is an essential point. Three different characteristic lengths are investigated. Figure 2.6, shows the Strouhal numbers for Geo 1, Geo 2 and Geo 3A based on pitch length, $Pt = r_{up} + W + r_{dwn} + L_p$, which is 12 mm for all three geometries. These geometries have different gap widths, $r_{up} + W + r_{dwn}$, and different width plus upstream edge radii, $W + r_{up}$, which we call the modified gap widths. Holding the pitch constant and varying other geometrical parameters results in a considerable range of Strouhal numbers $0.45 \leq Sr_L \leq 0.8$. This indicates that the pitch is not the

Figure 2.6: Comparison of pitch length and modified gap width ($W + r_{\mathrm{up}}$) based Strouhal numbers for two sets of corrugated pipes.
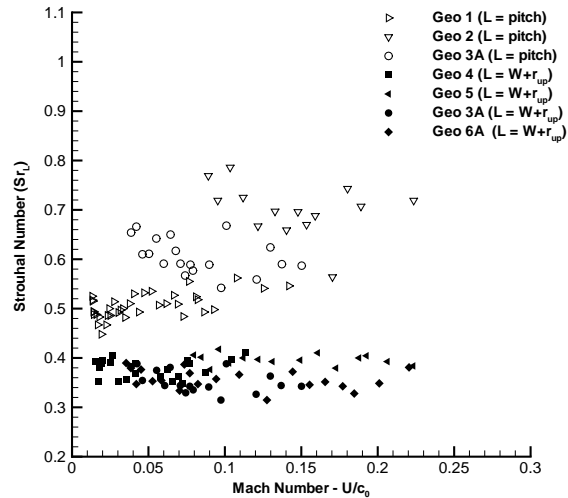
suitable length scale for the Strouhal number.

Comparison of Geo 4, Geo 5, Geo 3A and Geo 6A, suggests another way of defining Strouhal number, which is based on gap width. These four geometries have the same gap width of 8 mm with pitch lengths of 8 mm, 16 mm, 12 mm and 12 mm, respectively. They also have different modified gap width, which are 6 mm, 6 mm, 7 mm and 8 mm. Using the gap width as characteristic length, limits the variation of Strouhal numbers to $0.30 \leq Sr_{\mathrm{L}} \leq 0.55$. However, a much smaller scatter in the Strouhal numbers is observed, for the same four geometries when modified gap width is used as characteristic length in the expression for Strouhal number. It is seen (Fig. 2.6) that the variation is limited to the range $0.32 \leq Sr_{\mathrm{L}} \leq 0.42$. This optimal choice of characteristic length agrees with the results of Bruggeman et al. [1991] for deep side branches.

Experiments were performed in order to investigate the effect of edge radius of corrugations on the whistling amplitude. Configurations Geo 5 and Geo 7 have the same value for all the geometric parameters except the edge radius. Geo 5 has rounded edges with a radius of 2 mm which leads to a relative edge radius with respect to cavity width (r/W) of 0.5, whereas Geo 7 has sharp edges. Experiments performed at atmospheric pressure showed that for the sharp edge geometry (Geo 7) the whistling is hardly noticeable. Then, the same experiment was performed at a static pressure of 4 bar, to decrease the viscous losses through an increase in density. Dimensionless fluctuation amplitudes as a function of Strouhal number is presented in figure 2.7. As expected, an increase in $|u'|/U$ is observed due to decrease in viscous losses. The maximum dimensionless fluctuation amplitudes are around 10^{-1}
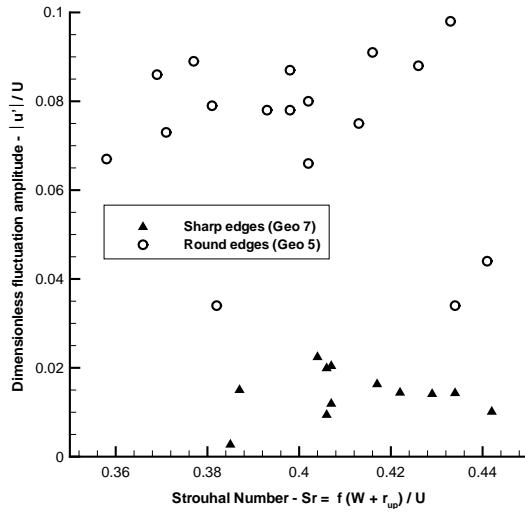
Figure 2.7:
Dimensionless fluctuation amplitude as a function of Strouhal number at a static pressure of 4 bar for sharp and rounded edge configurations.

for round edges (Geo 5) and 2×10^{-2} for sharp edges (Geo 7). It is concluded that rounding the edges does increase the pressure fluctuations by a factor 5. This is in agreement with the experimental results obtained for deep side branches [Bruggeman et al., 1991]. Qualitatively this can be predicted by Vortex Sound Theory, as explained in Sec. 2.3.2.

2.6 Multiple Side Branch System

In this section experiments performed on the multiple side branch system are presented. First, the similarities that are observed between the corrugated pipes and multiple side branch system are highlighted. In the following subsections; the effect of downstream pipe termination geometry, source localization, the effect of edge geometry, the effect of side branch depth, the effect of a gradient in side branch depth and finally the effect of flow acceleration or deceleration are discussed.

It should be noted that a main geometric difference between corrugated pipes and multiple side branch system is that the cross section of corrugation cavity is a slit whereas the side branches have circular cross sections (Fig. 2.1). Thus, the side branch diameters are converted to effective cavity width ($W_{\text{eff}} = \pi D_{\text{sb}}/4$) as proposed by Bruggeman et al. [1991], which is the average width of the side branch cross section.

As mentioned in the introduction and demonstrated in figure 2.5, in corrugated pipes the whistling frequency does not vary continuously with a monotonically in-

Figure 2.8:
Dimensionless fluctuation amplitude and corresponding Helmholtz number as a function of Mach number for (H/D_{sb}) ratio of 1.15 (19 side branches, round upstream edge-sharp downstream edge configuration).
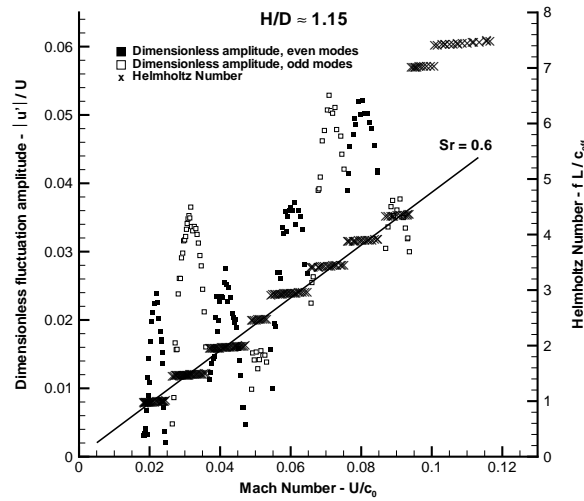
creasing flow rate, but rather in distinct steps. This characteristic is also observed in the multiple side branch system. In figures 2.8 and 2.9 measured whistling frequencies, in terms of Helmholtz number, are given as a function of Mach number for two values of cavity depth to side branch diameter ratio (H/D_{sb}). Here it can be noticed that Helmholtz numbers of $1, 1.5, 2...$ corresponds to $2^{nd}, 3^{rd}, 4^{th}...$ acoustic modes of the multiple side branch system, respectively. These observations agree with the observations on corrugated pipes.

A closer look to the Helmholtz numbers reveals an additional feature which is the slight, but discernible, increase in whistling frequency within the same mode which is in agreement with the observation in literature [Sarohia, 1977; Ziada et al., 2003]. For both deep and shallow side branches there exist a global constant slope between Helmholtz number and Mach number. This indicates a peak-whistling Strouhal number (Sr_{p-w}) for the system where the peak-whistling Strouhal numbers of consecutive modes coincide, within a discrepancy band of approximately 5%. This is another typical corrugated pipe attribute. For the deep and the shallow cases the peak-whistling Strouhal numbers (Sr_{p-w}) are 0.6 and 0.5, respectively which corresponds to 2nd hydrodynamic mode for a grazing acoustic flow [Bruggeman et al., 1991; Hofmans, 1998; Martínez-Lera et al., 2009]. The whistling amplitude displays local maxima at each lock-in with a longitudinal pipe mode. For the deep cavity case (Fig. 2.8) a global increase in whistling amplitude with an increasing Mach number can also be mentioned, with an exception of a dip at the 4th and the 5th acoustic mode. This dip is due to an acoustic resonance of the upstream muffler (Fig. 2.3-b) around 360Hz [Tonon et al., 2010].
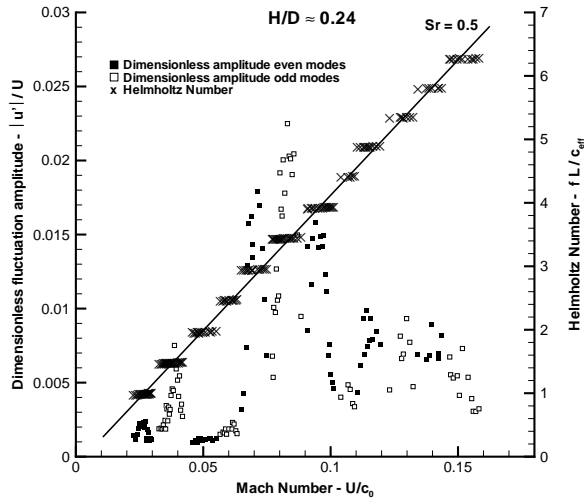
Figure 2.9: Dimensionless fluctuation amplitude and corresponding Helmholtz number as a function of Mach number for (H/D_{sb}) ratio of 0.24 (19 side branches, round upstream edge-sharp downstream edge configuration).

For the deep cavities ($H/D_{\text{sb}} = 1.15$, figure 2.8) above a critical Mach number ($Ma \approx 0.1$), a mode with a different Strouhal number is excited. This study is kept limited to the regime where the whistling behavior is similar to that of corrugated pipes. Thus, we are only interested in Mach numbers below this limit. Whereas for the shallow cavities ($H/D_{\text{sb}} = 0.24$, figure 2.9) it is seen that even for Mach numbers higher than $Ma \geq 0.15$ the whistling frequencies corresponds to a constant Strouhal number.

The corrugated pipes that are used in this study have typically 2×10^2 corrugations, whereas the multiple side branch system composed of only 19 T-joints. However, whistling frequencies that are observed with corrugated pipes are rather high (Fig 2.5) compared to the ones in the multiple side branch system. Thus, the typical number of corrugations per wave length in corrugated pipes at high frequencies ($fL/c_{\text{eff}} = O(10)$) is close to that of multiple side branch system at low frequencies ($fL/c_{\text{eff}} = O(1)$). Consequently, in the multiple side branch system the attention is given to the lowest modes.

Whistling has not been observed for the 1st acoustic mode in any of the experiments. This is, probably, due to the fact that viscous and radiation losses are higher than the sources of sound. In literature it has also been reported that for corrugated pipes the first acoustic mode does not whistle [Binnie, 1961; Nakamura and Fukamachi, 1991; Petrie and Huntley, 1980]. Maximum dimensionless fluctuation amplitude at the first whistling mode, which is the 2nd acoustic mode, is $|u'|/U = 2.5 \times 10^{-2}$ for the deep cavity and $|u'|/U = 2.5 \times 10^{-3}$ for the shallow cavity. These fluctuation am-

plitudes correspond to rather low amplitude levels. As explained in Sec. 2.3.3, the
system is extremely sensitive to small perturbations at this low amplitude regime.
For the 3rd acoustic mode, dimensionless fluctuation amplitude for deep and shal-
low cavities are $|u'|/U = 3.7 \times 10^{-2}$ and $|u'|/U = 7.5 \times 10^{-3}$, respectively. Since these
amplitudes are higher, whistling is more stable than the 2nd acoustic mode. For this
reason, in the rest of the paper the discussion is based on the 3rd acoustic mode. As
a consequence throughout the Sec. 2.6.1 to Sec. 2.6.6, where the multiple side branch
system is investigated, instead of making a linear least square fit to all the acoustic
modes, the peak-whistling Strouhal number is determined based on the 3rd acoustic
mode. The peak-whistling Strouhal number is calculated by taking average of two
Strouhal numbers, which are corresponding to 80% of the maximum amplitude.

2.6.1   Effect of pipe termination

It is expected that the edge geometry of the pipe termination has a strong effect on
the sound absorption there. To investigate this phenomena, we performed experi-
ments with sharp and "whistler nozzle" type [Hirschberg et al., 1989] pipe termina-
tions, see figure 2.10. The sharp terminations has $D = 33$ mm and $D_t = 34$ mm.
Whistler nozzle type termination has a step wise increase in the pipe diameter from
$D = 33$ mm to $D_n = 34$ mm over a nozzle length (L_n) of 3 mm upstream of the pipe
termination with a termination diameter (D_t) of 54 mm.

When there is a sharp pipe termination, there exists a strong absorption of sound
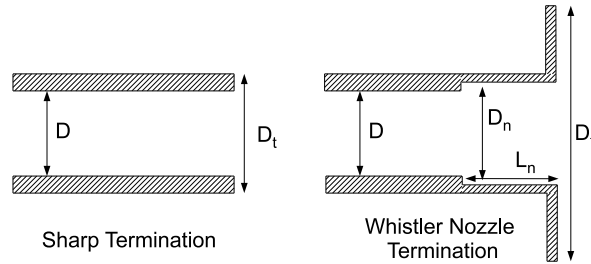
Figure 2.10: Sharp and "whistler nozzle" type pipe terminations.

due to vortex shedding at the outlet of the multiple side branch system. This could
be explained again on the basis of Vortex Sound Theory [Howe, 1975]. Replacing the
sharp edges with "whistler nozzle", we decrease the singularity of the acoustic flow
at the separation point. Furthermore the acoustic velocity shortly downstream of
the separation point is almost directed along the pipe axis, which will also strongly
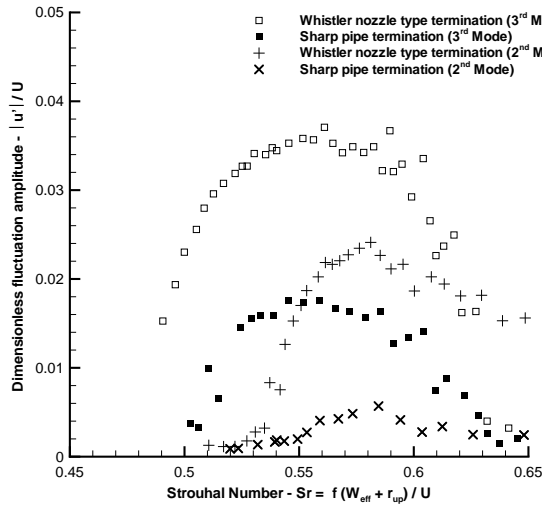
Figure 2.11: Dimensionless fluctuation amplitude for the 2nd and 3rd acoustic mode as a function of Strouhal number for sharp and "whistler nozzle" type pipe terminations. ($H/D_{sb} = 0.79$, 19 side branches, round upstream edge-sharp downstream edge configuration).

decrease the scalar triple product $\langle P_{source} \rangle$. Therefore initial sound absorption becomes quite low. In this respect, the whistler nozzle is shifting the balance of initial absorption and later production, in favor of the production [Hirschberg, 2001]. In the current study for the Strouhal numbers considered, based on the nozzle length ($L_n = 3$ mm) which are in the order of 0.06, the whistler nozzles creates a reduction of absorption but no net sound production. This nozzle is expected to whistle only for a Strouhal number in the order of 0.2 or higher [Hirschberg et al., 1989].

Measured dimensionless fluctuation amplitude for the 2nd and the 3rd acoustic modes as a function of Strouhal number is shown in figure 2.11. Due to a decrease in the initial sound absorption with the whistler nozzle, maximum amplitudes for the 3rd mode are 3.7×10^{-2} for the whistler nozzle and 1.4×10^{-2} for the sharp pipe termination. For the 2nd mode the effect is even more pronounced due to the fact that dimensionless fluctuation amplitude levels correspond to a lower amplitude regime. At lower amplitudes the whistling is less stable, as explained in Sec. 2.3.3. The amplitude decreases almost by a factor 5. To avoid this strong absorption the experiments presented in this paper are performed with a whistler nozzle termination.

2.6.2 Source localization

In the literature [Kristiansen and Wiik, 2007], it has been suggested that the regions of sound production in corrugated pipes are at velocity nodes. The study of Tonon et al. [2010] with multiple side branches demonstrated that the sound is produced mainly in pressure nodes where the grazing acoustic velocity is maximum. That study was done for a system of 15 side branches with sharp edges and $H/D_{sb} = 1.15$. Here an

Figure 2.12:
Dimensionless fluctuation amplitude for the 3rd acoustic mode as a function of Strouhal number for the cases where none of the side branches are plugged, side branches near the pressure nodes are plugged and side branches near the velocity nodes are plugged.(H/D_{sb} = 1.15, 19 side branches, round upstream edge-sharp downstream edge configuration).
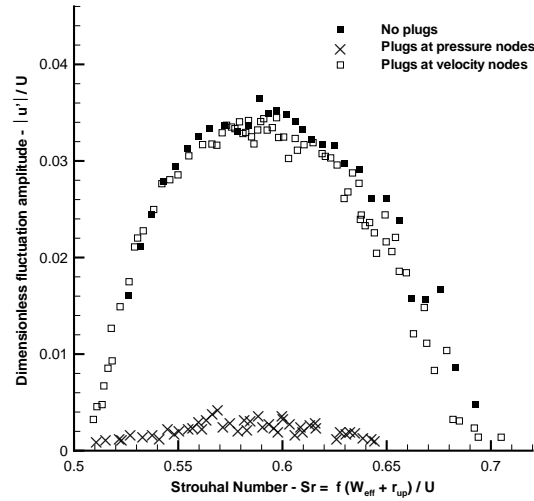
experiment with rounded upstream edges and 19 side branches with $H/D_{sb} = 1.15$ is considered.

Three experiments were performed, as shown in figure 2.12. In the first test none of the side branches were plugged for reference. In the second one, four side branches (6, 7, 13, 19) close to the pressure nodes were plugged thus the contribution to the sound production from those side branches were suppressed. In the third test, three side branches (3, 10, 16) close to the velocity nodes were plugged.

It is seen from figure 2.12 that the contribution of the side branches to the sound production which are close to the velocity nodes is negligible. Whereas when the side branches close to the pressure nodes are suppressed, almost an order of magnitude drop, from 3.6×10^{-2} to 4.0×10^{-3} is observed in the dimensionless fluctuation amplitude. Experiments performed for the 2nd acoustic mode lead to the same conclusion that sound is mainly produced by the grazing acoustic flow at the cavities close to the pressure nodes of the longitudinal standing waves along the pipe. This can be justified through Vortex Sound Theory [Howe, 1975],

2.6.3 Effect of edge shape

Following the experiments with corrugated pipes, the effect of edge geometry is also investigated with the multiple side branch system. In figure 2.13, measured dimensionless fluctuation amplitude for the 3rd acoustic mode as a function of Strouhal number for round upstream-sharp downstream case and sharp upstream-round downstream case are given. The radius of the rounded edge is 3 mm which is approxi-
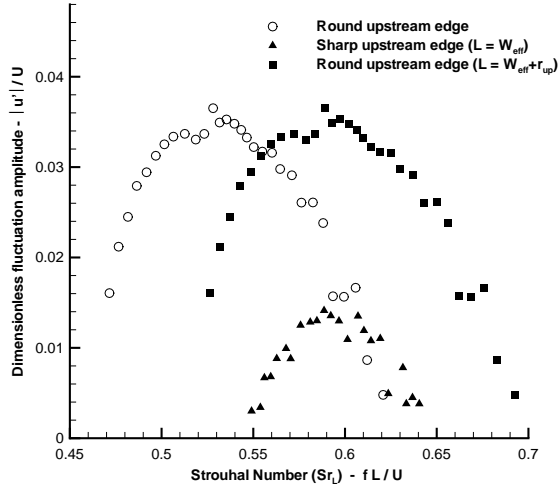
Figure 2.13: Dimensionless fluctuation amplitude for the 3rd acoustic mode as a function of Strouhal number for round upstream-sharp downstream case and sharp upstream-round downstream case ($H/D_{\text{sb}} = 1.15$, 19 side branches).

mately 10% of the cavity width ($W_{\text{eff}} = \pi D_{\text{sb}}/4$). As explained in Sec. 2.3 through Vortex Sound Theory [Howe, 1975], higher pressure fluctuation amplitudes were expected from round upstream-sharp downstream case than sharp upstream-round downstream case. Indeed, maximum dimensionless fluctuation amplitudes are $|u'|/U = 3.7 \times 10^{-2}$ for rounded upstream edge and $|u'|/U = 1.4 \times 10^{-2}$ for sharp upstream edge. As for corrugated pipe results, using the modified gap ($W_{\text{eff}} + r_{\text{up}}$) as the characteristic length for the Strouhal number decreases the discrepancy in the Strouhal numbers observed, see figure 2.13.

2.6.4 Effect of cavity depth

Using plugs at each side branch and changing their penetration depth the effect of side branch depth to side branch diameter ratio (H/D_{sb}) was investigated. Increasing the side branch depth (H) decreases the effective speed of sound (c_{eff}), this decrease can be predicted by using the model of Elliott [2004], as explained in Sec. 2.3.1. For the 3rd acoustic mode, if c_{eff} was known exactly then the whistling frequency would provide a Helmholtz number of 1.5. In figure 2.14 Helmholtz numbers are presented as a function of Mach number for 10 different H/D_{sb} ratios, for the 3rd acoustic mode. The variation around $He = 1.5$ is 3% which confirms the proposed acoustical model of Tonon et al. [2010]. A closer look to the collapse of data, indicates that for very shallow cavities the effective speed of sound definition is less succesful. This is due to a difficulty in estimating the effective acoustical volume V_{c} for very shallow cavities [Nederveen, 1998].

In figure 2.15 and 2.16 the dimensionless fluctuation amplitudes as a function of

Figure 2.14: Helmholtz number as a function of Mach Number for various cavity depth to side branch diameter ratios: $0.18 \leq H/D_{sb} \leq 1.15$ (3rd acoustic mode, 19 side branches, round upstream edge-sharp downstream edge configuration).
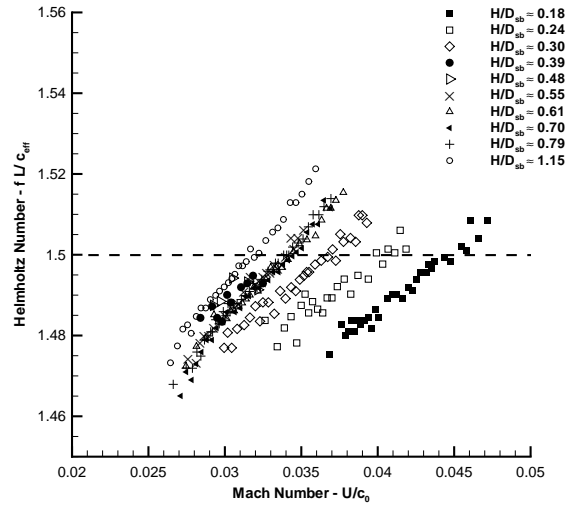
the Strouhal number are presented. Two distinct ranges of H/D_{sb} are distinguished. In the first range (Fig. 2.15), $0.61 \leq H/D_{sb} \leq 1.15$, a saturation behavior is observed in the amplitude of pressure fluctuations with an almost constant peak-whistling Strouhal number. The difference in the pressure fluctuation amplitude in this range is less then 10% and the shift in peak-whistling Strouhal number is less than 5%. In this range (relatively "deep cavity"), the whistling is very stable. For all the H/D_{sb} ratios a ± 1 Hz window around the whistling frequency contains more than 90% of the total energy of the whole frequency spectrum.

A closer look to figure 2.16 reveals different sub-regimes for the shallow side branch range. For the side branches with a H/D_{sb} ratio less then 0.25, an increase in the side branch depth leads to an increase in peak-whistling Strouhal number which is parallel to the observations of Heller and Bliss [1975]; Ethembabaoglu [1973] and Ziada et al. [2003] for shallow cavities ($H/W \leq 0.5$). Increase in cavity depth in this range does also increase the amplitude of oscillations. More than 80% of the energy content of the whole frequency spectrum is concentrated in a ± 1 Hz window around the whistling frequency which is an indication of coherent oscillations [Charwat, 1961]. In the range $0.25 \leq H/D_{sb} \leq 0.5$ dimensionless fluctuation amplitudes are relatively low, usually less than 3×10^{-3}. In this range a frequency window of ± 1 Hz around the whistling frequency contains at most 50% of the total energy of the spectrum, which indicates less coherent oscillations. Finally a transitional regime can be distiguised between $0.50 \leq H/D_{sb} \leq 0.60$. Here it is observed that the amplitude of oscillations increases an order of magnitude from 3×10^{-3} to 3×10^{-2} as the H/D_{sb} ratio increases from 0.48 to 0.61. Also a shift in the peak-whistling Strouhal number

Figure 2.15: Dimensionless fluctuation amplitude for the 3rd acoustic mode as a function of Strouhal number for different H/D_{sb} ratios ranging between 0.61-1.15 (19 side branches, round upstream edge-sharp downstream edge configuration).

Figure 2.16: Dimensionless fluctuation amplitude for the 3rd acoustic mode as a function of Strouhal number for different H/D_{sb} ratios ranging between 0.18-0.61 (19 side branches, round upstream edge-sharp downstream edge configuration).

from 0.67 to 0.60 is recorded in the same interval. This transition regime could be related to the change in the flow patterns observed in rectangular cavities, refered as open and closed flow [Gloerfelt, 2009].

In figure 2.17 an overview of the peak-whistling Strouhal numbers is given and compared with the data obtained for corrugated pipes (Table 2.1). For the multiple side branch experiments two groups,namely, the moderate amplitude and the low amplitude, can be distinguished. For the moderate amplitude range ($\approx 2.5 \times 10^{-2}$) there is hardly any dependence of the peak-whistling Strouhal number on the H/D_{sb} ratio. For the low amplitude regime ($\approx 5 \times 10^{-3}$) there is a pronounced shift in peak-whistling Strouhal number with varying H/D_{sb} ratio. It should be mentioned that among the corrugated pipes that are tested, there are only two configurations (Geo 9 and Geo 10) for which all the parameters are kept constant except the depth. As pointed out in figure 2.17 a shift in peak-whistling Strouhal number is not observed between these two corrugated pipes. Also it can be highlighted that experiment performed with a commercially available corrugated pipe (Geo 11) give a peak-whistling Strouhal number ($Sr_{p-w} \approx 0.49$) between the multiple side branch system and the other corrugated pipes that are tested in this study.

It is interesting to note that the range of the peak-whistling Strouhal numbers found for corrugated pipes ($0.32 \leq Sr_{p-w} \leq 0.49$) are much larger than the one predicted

Figure 2.17: Peak-whistling Strouhal number as a function of $H/(W_{\text{eff}} + r_{\text{up}})$ for multiple side branch and $H/(W + r_{\text{up}})$ for corrugated pipes.
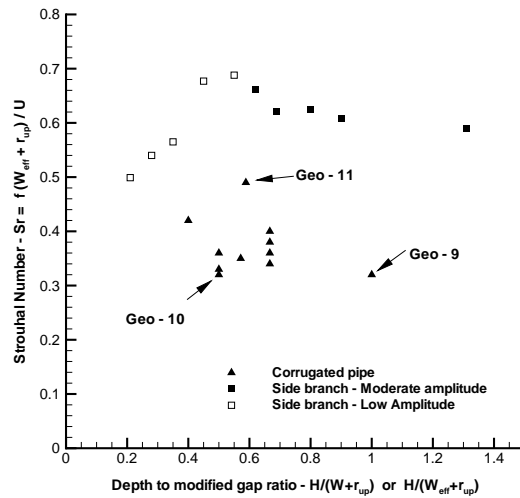
for the first hydrodynamic mode ($Sr \leq 0.13$) but lower than the one predicted for the second hydrodynamic mode ($Sr \approx 0.60$) [Bruggeman et al., 1991; Hofmans, 1998; Martínez-Lera et al., 2009]. This is an essential difference between the multiple side branch system and corrugated pipes. A possible explanation is that we observe here an effect of the relative size of corrugations compared to the momentum thickness of the main pipe flow. Another explanation, as observed by Binnie [1961], could be the influence of pipe diameter (D) to cavity width (W) ratio, where a shift in Strouhal number from 0.4 up to 0.7 was observed with a decrease in D/W ratio. Unfortunately, Binnie [1961] did not specify the length scale used to define the Strouhal number.

2.6.5 Effect of a gradient in side branch depth

In this subsection the effect of a gradient in the side branch depth is considered. This is a linearly changing cavity depth where the side branches at the upstream end of the system have deeper cavities than the ones at the downstream end. This can be a model for a temperature gradient along the pipe which causes a change in speed of sound.

To investigate this approach an experiment was performed with 19 side branches. The depth of the side branches decreased in three steps where the first five have a H/D_{sb} ratio of 0.79. The next two sets of five side branches have H/D_{sb} ratio of 0.66 and 0.55, respectively. The last four side branches have a H/D_{sb} ratio of 0.42. In figure 2.18, the whistling frequency in terms of Helmholtz number is given as a function of Mach number for the linearly decreasing cavity depth and for the correspond-
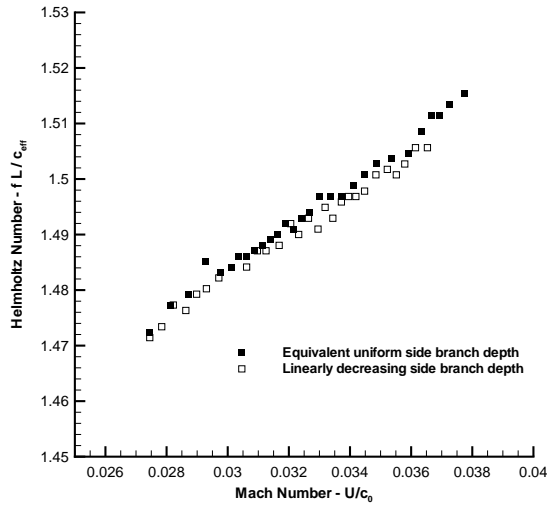
Figure 2.18: Helmholtz number as a function of Mach number for linearly decreasing side branch depth and equivalent uniform side branch depth configurations (3rd acoustic mode, 19 side branches, round upstream edge-sharp downstream edge configuration).

ing equivalent uniform side branch depth (H/D_{sb} = 0.61) configurations. It is seen that the two configurations have almost the same whistling frequencies. However the dimensionless fluctuation amplitude of linearly decreasing side branch depth is 2.5×10^{-2} whereas it is 3.4×10^{-2} for equivalent uniform side branch depth, see figure 2.19. In Sec. 2.6.2 it is showed that sound is produced mainly at the side branches which are close to the pressure nodes. For the 3rd acoustic mode there are four pressure nodes along the pipe. One node, closest to the downstream pipe termination, is in a region where the H/D_{sb} ratio corresponds to a depth in which low amplitude pressure fluctuations was observed (Fig. 2.16). The other nodes correspond to H/D_{sb} ratios producing moderate amplitude pressure fluctuations (Fig. 2.15). Assuming that individual contributions (to the sound production) of pressure nodes at the ends of the pipe are half as much as the other pressure nodes, a 15% drop in amplitude is expected from the linearly decrasing side branch configuration compared to the equivalent uniform depth configuration. This estimation is reasonably close to the actual drop which is 25%.

2.6.6 Hysteresis

Hysteresis is reported in corrugated pipe whistling [Petrie and Huntley, 1980; Nakamura and Fukamachi, 1991] state that a jump to the next acoustic mode occurs for an increasing airspeed at a slightly lower air velocity than for a decreasing one. A similar effect is also observed with the multiple side branch system. In figure 2.20, an experiment that is performed with first an increasing flow velocity and then with a decreasing flow velocity is presented. The trends are similar for the 2nd and the 3rd acoustic modes. From figure 2.20-a it is seen that, with an increasing velocity the

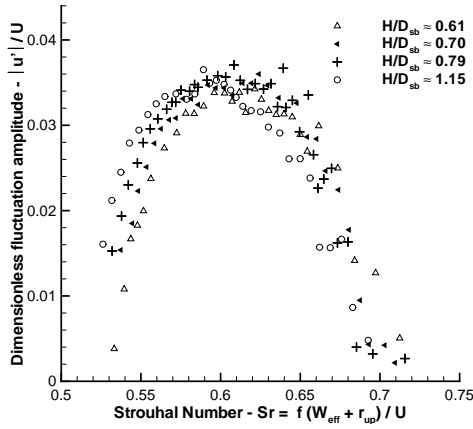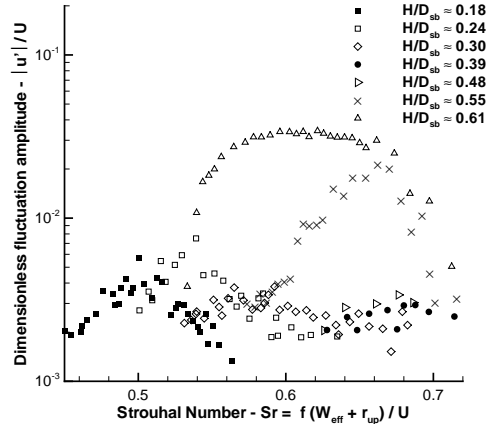**Figure 2.19:**
Dimensionless fluctuation amplitude for the 3rd acoustic mode as a function of Strouhal number for linearly decreasing side branch depth and equivalent uniform side branch depth configurations (19 side branches, round upstream edge- sharp downstream edge configuration).
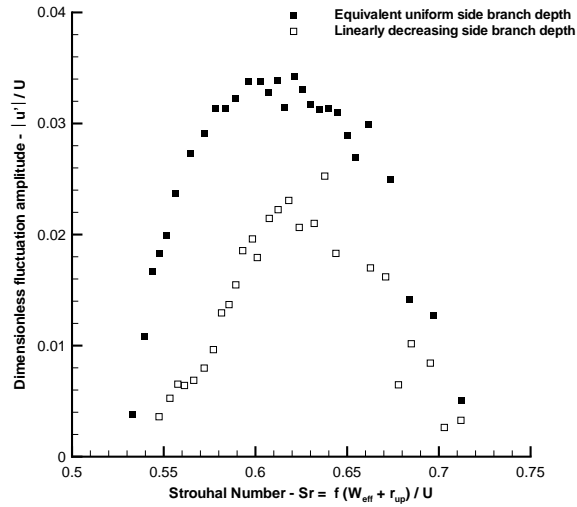
jump from 2nd mode to 3rd mode occurs around $Ma = 0.025$ whereas with decreasing velocity it is around $Ma = 0.028$. On the other hand, from figure 2.20-b displaying the amplitude of the 3rd acoustic mode, it is seen that the hysteresis does not have a pronounced effect on the maximum amplitude.

The above experiment on the hysteresis was already performed very slowly (Fig. 2.20-a). The time interval for each acoustic mode before jumping to the next one is in the order of 10^4 oscillation periods. But as shown in figure 2.20-b, a hysteresis could still be observed. The hysteresis effect vanished only when the acceleration & deceleration rates are lowered down to 10^5 periods for each mode. Corresponding data points are indicated as "neutral" in figure 2.20-b.

2.7   Conclusion

In this study whistling behavior of corrugated pipes and a multiple side branch system are compared. In both systems, it is observed that frequency (Helmholtz number) is a non-decreasing piecewise constant function of the Mach number, whose increase on average is approximately linear. The plateaus, lock-in frequencies, of this piecewise constant function correspond to the longitudinal acoustic pipe modes. In both system non-monotonic behavior in whistling amplitude as a function of flow velocity is observed with local maxima that correspond to lock-in frequencies.

Various characteristic lengths were considered in the definition of the Strouhal number. It appears that the cavity width plus the upstream edge radius, $W + r_{up}$, yields
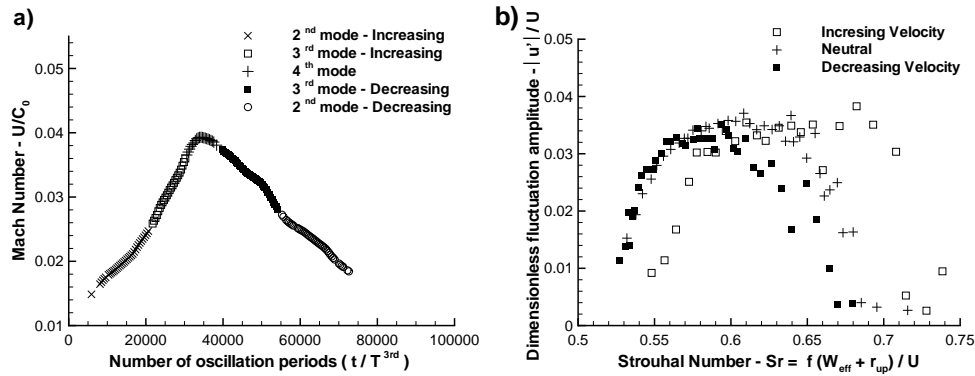
Figure 2.20: a) Acceleration and deceleration rates during the experiment for the 2nd and 3rd mode. b) Dimensionless fluctuation amplitude and corresponding Strouhal number for increasing velocity, decreasing velocity and neutral cases (19 side branches, round upstream edge-sharp downstream edge configuration).

the smallest scatter of the Strouhal number data for corrugated pipes as well as for the multiple side branch system.

The upstream edge of the cavity has a significant effect on pressure fluctuation amplitudes for both corrugated pipes and the multiple side branch system. Rounding the upstream edges of the cavities increases the amplitude of the pressure fluctuation up to 5 times compared to the sharp edges. The radius of the downstream edge does not have such a pronounced effect on the sound production.

While corrugated pipes and multiple side branch systems have very similar whistling behaviors, the peak-whistling Strouhal numbers, where the maximum amplitude in the dimensionless fluctuation amplitudes are registered, are different for these two periodic systems. It is found that $0.32 \leq Sr \leq 0.5$ for corrugated pipes whereas with multiple side branches, in agreement with the theory, it is observed that $0.5 \leq Sr \leq 0.6$. The difference in the peak-whistling Strouhal numbers of these two systems is not yet understood.

A number of geometric parameters and their respective effects are addressed in multiple side branch system. Exact geometry of the downstream pipe termination appears to be very important for pressure fluctuation amplitudes. With a "whistler type" pipe termination pressure fluctuation amplitudes increase more than a factor two compared to the sharp pipe termination.

Experiments confirm the source localization close to the pressure nodes as proposed by Tonon et al. [2010]. This demonstrate that the whistling is due to vortex shedding

induced by the grazing acoustic flow at cavities around pressure nodes.

The effect of side branch depth to side branch diameter ratio (H/D_{sb}) was investigated. Using the effective speed of sound (c_{eff}) as defined by Elliott [2004], whistling frequencies can be estimated with in an error of $\pm 3\%$. Considering the change of Strouhal number and amplitude with H/D_{sb} ratio, two intervals with qualitatively different behaviours are determined. Between $0.61 \leq H/D_{sb} \leq 1.15$ a saturation behavior is observed in the amplitude of pressure fluctuations with an almost constant peak-whistling Strouhal number. In the range of $0.18 \leq H/D_{sb} \leq 0.55$, which can be considered as relatively shallow compared to cavities in common corrugated pipes, a strong dependence of pressure fluctuation amplitude and peak-whistling Strouhal number on H/D_{sb} ratio is observed. In the range $0.25 \leq H/D_{sb} \leq 0.5$ rather weak and incoherent oscillations is observed. Also a transition regime is distinguised between $0.50 \leq H/D_{sb} \leq 0.60$, where the amplitude of oscillations increased an order of magnitude with a shift in peak-whistling Strouhal number from 0.67 to 0.60.

The effect of a gradient in cavity depth along the multiple side branch system is considered. A decrease of H/D_{sb} from 0.79 upstream to 0.42 downstream result into a whistling behavior which is an average of the whistling behaviors of individual side branches. The gradient does not induce a pronounced new behavior.

In the literature hysteresis during the transition from one to the next acoustic mode has been reported for corrugated pipes. For the multiple side branch system a similar effect observed, but it depends on the rate of change in flow velocity. At very low rate of change no hysteresis has been observed.

Note :

This chapter is based on the publication:

Nakiboğlu, G., Belfroid, S. P. C., Willems, J. F. H. and Hirschberg, A. Whistling behavior of periodic systems: Corrugated pipes and multiple side branch system, International Journal of Mechanical Sciences, Vol 52: 1458-1470, 2010

In the conclusion it is stated that "The difference in the peak-whistling Strouhal numbers of these two systems (corrugated pipes and close side branch systems) is not yet understood." This difference has later been understood and explained in chapters 3 and 4.

On the whistling of corrugated pipes: effect of pipe length and flow profile

3.1 Abstract

Whistling behavior of two geometrically periodic systems, namely corrugated pipes and multiple side branch systems, are investigated both experimentally and numerically. Tests are performed on corrugated pipes with various lengths and cavity geometries. Experiments show that the peak-whistling Strouhal number, where the maximum amplitude in pressure fluctuations is registered, is independent of the pipe length. Experimentally a decrease of the peak-whistling Strouhal number by a factor of two is observed with increasing confinement ratio, i.e the ratio of pipe diameter to cavity width. A numerical methodology that combines incompressible flow simulations with Vortex Sound Theory is proposed to estimate the acoustic source power in periodic systems. The methodology successfully predicts the Strouhal number ranges of acoustic energy production/absorption and the non-linear saturation mechanism responsible for the stabilization of the limit cycle oscillation. The methodology predicts peak-whistling Strouhal numbers in agreement with experiments and explains the dependency of the peak-whistling Strouhal number on the confinement ratio. Combined with an energy balance the proposed methodology is used to estimate the acoustic fluctuation amplitudes.
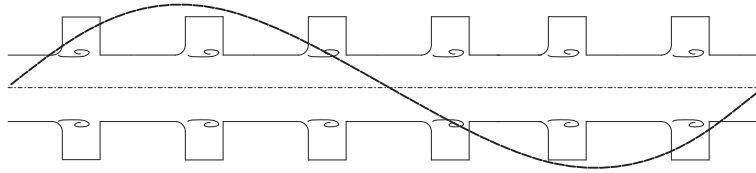
Figure 3.1: Schematic representation of a corrugated pipe, shear layers at the cavity openings and acoustic field for the 2nd longitudinal standing wave.

3.2   Introduction

In thin walled pipes corrugations make the structure locally stronger while keeping its global flexibility. This unique characteristic makes corrugated pipes convenient for various industrial utilizations. However, at critical conditions, the flow through these pipes causes self-sustained oscillations that lead to high amplitude sound generation, called whistling. These noise problems are encountered in applications e.g. domestic appliances, ventilation systems and heat exchangers [Petrie and Huntley, 1980; Elliott, 2004]. For applications at elevated operating pressures e.g. offshore natural gas transportation systems, self-sustained oscillations also lead to dangerous structural vibrations [Belfroid et al., 2007; Goyder, 2009].

In corrugated pipes sound generation is due to an oscillation driven by a flow-acoustic interaction as pointed out by Burstyn [1922] and Cermak [1922]. Flow separation occurring at the upstream edge of each cavity generates a shear layer, see figure 3.1, which is a source of unsteadiness. This unsteady flow induces an unsteady force on the walls bounding the flow. The reaction force of the walls to this hydrodynamic force is the source of sound [Gutin, 1948; Curle, 1955].

It is important to note that the flexibility of the tube is not a necessary facet for the sound generation in corrugated tubes as shown by Nakamura and Fukamachi [1991]. However a mechanical vibration induced by the unsteady forcing on the walls can have a significant effect. For water flow, Ziada and Bühlmann [1991] observed a strong coupling of whistling with pipe wall vibrations.

A more frequently observed coupling of shear layers occurs with longitudinal acoustic standing waves in the pipe, see figure 3.1 [Petrie and Huntley, 1980; Nakamura and Fukamachi, 1991; Kristiansen and Wiik, 2007; Kop'ev et al., 2008; Nakiboğlu et al., 2010]. The resulting high amplitude oscillations control the vortex shedding [Rockwell, 1983; Bruggeman et al., 1991]. These kinds of flow pulsations are called self-sustained oscillations, which can be explained through a feedback loop composed of a hydrodynamic and an acoustic subsystem [Nakamura and Fukamachi, 1991; Tonon et al., 2010]. The shear layer instability, which is the hydrodynamic subsystem, acts as an amplifier and supplies acoustic energy to the system. Longitudinal standing wave, which is the acoustic subsystem, acts as a band pass filter and maintains the synchronization in this feedback mechanism. This band pass
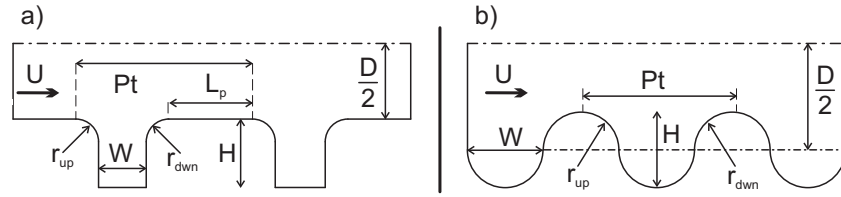
Figure 3.2: Typical cross-sections of corrugated pipes with geometric parameters [Tonon et al., 2010; Nakiboğlu et al., 2010] (a), [Binnie, 1961; Elliott, 2004](b).

filter is the reason of stepwise increase of the whistling frequency at certain flow velocities, which has been pointed out in numerous experimental studies [Binnie, 1961; Crawford, 1974; Silverman and Cushman, 1989; Cadwell, 1994; Elliott, 2004; Kristiansen and Wiik, 2007; Kop'ev et al., 2008]. Each step corresponds to the resonance frequency of an acoustic mode. Another widely observed characteristic is that for each corrugated pipe the whistling frequencies are close to a single non-dimensional frequency, called Strouhal number, which is discussed in detail in section 3.3.3.

Depending on the application, geometric parameters of corrugated pipes may vary in a fairly large range and it is known that these parameters have a significant effect on the whistling phenomena [Petrie and Huntley, 1980; Nakiboğlu et al., 2010]. Thus, in the course of designing silent corrugated pipes, it is an asset for industry to be able to estimate quantitatively the effect of modifications in geometric parameters on the whistling. In figure 3.2, relevant geometric parameters are shown for two generic corrugated pipe cross-sections. Corrugations form a periodic variation of the inner diameter of the pipe. The wave length of a corrugation is called pitch (Pt). Depending on structural requirements and manufacturing technique the cavity geometries of corrugated pipes can also vary in complexity. In the simplest case, see figure 3.2-a, each corrugation is a slit shaped cavity with a width (W) and a depth (H). The radius of the edges are denoted r_{up} and r_{dwn} for upstream and downstream edges, respectively. The plateau (L_p) is defined as the length of the constant inner diameter (D) part between two cavities. Another commonly used corrugated pipe with a simple cavity geometry, is shown in figure 3.2-b [Binnie, 1961]. There is no plateau between cavities and since the cavity width is changing continuously with the cavity depth, width (W) is defined at the mid-depth of the cavity [Elliott, 2004].

It should be noted that axisymmetry of the cavities is not a necessary feature for the whistling phenomenon observed in corrugated pipes. Experiments performed with multiple side branch system, which is a non-axisymmetric system with a periodically changing cross-section area along the pipe length, exhibit a whistling behavior similar to that of corrugated pipes [Nakiboğlu et al., 2009; Tonon et al., 2010; Nakiboğlu et al., 2010]. Another important result obtained by Nakiboğlu et al. [2010] is that the whistling amplitude is independent of the depth (H) for $1.2 \geq H/W \geq 0.5$. For shallow cavities ($H/W \leq 0.5$), on the other hand, the whistling amplitude de-

pends on the depth. In this study only the $H/W \geq 0.5$ range is addressed.

Experiments on the localization of the region of sound production in periodic systems have shown that the contribution of each cavity or side branch on the sound production is not the same [Tonon et al., 2010; Nakiboğlu et al., 2010; Golliard et al., 2010]. Their individual contributions depend on their positions with respect to the shape of the coupling acoustic standing wave. It was demonstrated that the sound production is dominant within the regions of high grazing acoustic velocities, which are located around the acoustic pressure nodes of the coupling standing wave along the main pipe.

Another outcome of earlier studies [Elliott, 2004; Tonon et al., 2010; Nakiboğlu et al., 2010] is that acoustic waves in periodic systems propagate at an effective speed of sound (c_{eff}), which is lower than the speed of sound (c_0). Assuming that the acoustic compliance is determined by the pitch volume, $\pi D \left[(Pt\, D/4) + HW \right]$, and the inertia is determined by the mass in the main pipe, $\rho_0\, Pt\, \pi D^2/4$, the effective speed of sound for low frequency, $fPt/c_0 \ll 1$, acoustic waves along the pipe can be estimated as follows:

$$c_{\text{eff}} = c_0 / \sqrt{1 + V_{\text{c}}/(S_{\text{p}} Pt)} \tag{3.1}$$

where $S_{\text{p}} = \pi D^2/4$ is the cross-sectional area of the tube and $V_{\text{c}} = \pi DHW$ is the cavity volume.

In this paper both experimental and numerical investigations of whistling in periodic systems are reported. The first part of the paper is dedicated to the experimental results. In Sec. 3.3.1, experimental setups are presented, followed by Sec. 3.3.2 where the periodic systems that have been tested are introduced with the respective geometric details. Before presenting the experimental results, a section is devoted to a detailed discussion of Strouhal numbers in periodic systems (Sec. 3.3.3). In subsequent three sections the effects of system length (Sec. 3.3.4), helical configuration (Sec. 3.3.5) and confinement ratio (Sec. 3.3.6) on whistling are addressed, respectively. In the second part of the paper a numerical methodology is proposed and appraised for the investigation of the aeroacoustic response of whistling periodic systems (Sec. 3.4.1 - Sec. 3.4.3). Later in Sec. 3.4.4, using the proposed methodology, the reason of the broad range of Strouhal numbers observed in periodic systems is clarified. In Sec. 3.4.5 and Sec. 3.4.6 the capability of the method in predicting dimensionless fluctuation amplitudes in whistling periodic systems is explored. In Sec. 3.4.7, the limitations of the proposed approach and the possible improvements are reviewed. In the last section, the conclusions are stated.

3.3 Experiments

3.3.1 Experimental setups

Different experimental setups were employed to test corrugated pipes and multiple side branch systems. Pressure fluctuations could easily be measured in the multiple side branch system by means of flush mounted microphones placed at the end of side branches. For corrugated pipes, however, positioning microphones directly on the walls is very difficult. Consequently, for a reliable installation of flush mounted microphones, straight pipe segments were used both upstream and downstream of the corrugated pipes under investigation. These two experimental setups are shortly described below [Tonon et al., 2010; Nakiboğlu et al., 2010].

The schema of the experimental setup that was employed in corrugated pipe experiments is shown in figure 3.3-a. From upstream to downstream the setup is composed of: a pressure vessel, a turbine flow meter, a flow control valve, a measurement section, a corrugated pipe segment, a second measurement section and a pressure vessel. Using the downstream pressure control valve the system can be pressurized up to 12 bar, which allows for the testing of the Reynolds number dependency of the system [Belfroid et al., 2007]. The constant diameter, $D = 50.8$ mm (2 Inches), upstream and downstream measurement sections are each 1.6 m long and equipped with five flush mounted microphones. By means of a multi-microphone method [Åbom and Bodén, 1988; Peters et al., 1993] traveling acoustic plane waves were reconstructed. Corrugated pipe segments with various cavity geometries and lengths were tested between the two measurement sections. To calculate the flow velocity in the test section from the volume flow measurement, pressure (p) and temperature (T) measurements were recorded at three different locations, the first one close to the turbine flow meter (p_{meter}, T_{meter}), the second one upstream (p_{up}, T_{up}) and the third one downstream (p_{down}, T_{down}) of the text section. By doing so the pressure drop and the change in temperature through the pipe are taken into account. This becomes essential for corrugated pipes longer than 10m. The flow velocities at the upstream and downstream terminations of the test section are determined as follows:

$$U_{\mathrm{up}} = \frac{Q_{\mathrm{meter}}}{S_{\mathrm{p}}} \frac{T_{\mathrm{up}}}{T_{\mathrm{meter}}} \frac{p_{\mathrm{meter}}}{p_{\mathrm{up}}} \qquad U_{\mathrm{down}} = \frac{Q_{\mathrm{meter}}}{S_{\mathrm{p}}} \frac{T_{\mathrm{down}}}{T_{\mathrm{meter}}} \frac{p_{\mathrm{meter}}}{p_{\mathrm{down}}} \tag{3.2}$$

where Q_{meter} is the volumetric flow rate measured by the turbine flow meter and S_{p} is the minimum cross sectional area of the corrugated pipe. The flow velocity in the test section is taken as the arithmetic average of the upstream and downstream flow velocities, $U = (U_{\mathrm{up}} + U_{\mathrm{down}})/2$.

The setup used for the multiple side branch system experiments is shown in figure 3.3-b. The upstream termination of the multiple side branch system is connected to the high pressure air supply system which is composed of, from upstream
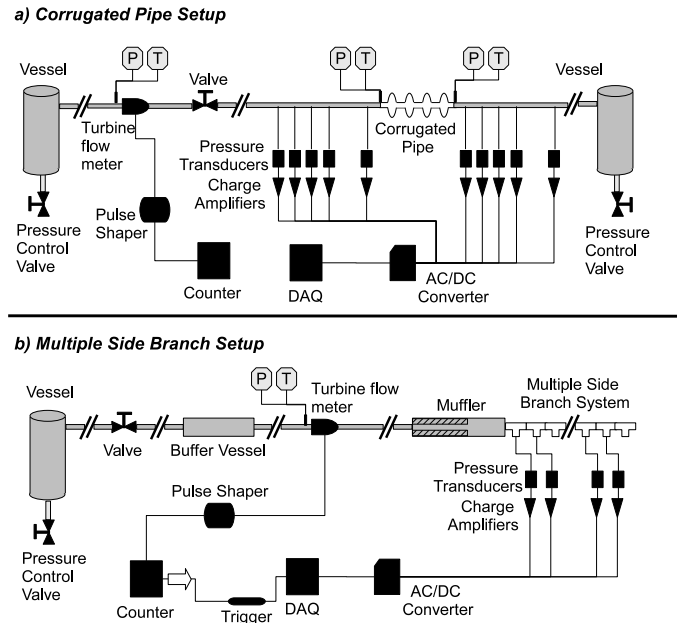
Figure 3.3: Experimental setups for corrugated pipe (a) and for multiple side branch system (b).

to downstream, a compressor, a vessel, a control valve, a buffer vessel, a turbine flow meter and an expansion chamber muffler. The downstream termination is open to the laboratory, a large room of $15 \times 4 \times 4$ m. Even the longest multiple side branch system, that was employed in the experiments (≈ 2 m), is short enough to neglect changes in flow velocity through the system due to pressure drop. Thus, it was not necessary to make pressure and temperature measurements at multiple locations as in corrugated pipe experiments.

In both setups, the microphones (PCB 116A) are connected to charge amplifiers (Kistler 5011). These amplifiers are connected to a PC through a AC/DC converter acquisition board (National Instruments NI SCXI-1000). A turbine flow meter (Instromet SM-RI-X-KG250) is used to measure the volumetric flow rate. The turbine flow meter is connected to a pulse shaper and a counter. In the setup for multiple side branch system the turbine flow meter and the piezo-electric pressure transducers are synchronized by means of a trigger. The simultaneous measurement of flow velocity and pressure allows a waterfall representation of the data, in which the frequency spectra of the whistling at different flow velocities are presented in a single graph. This interpretation can capture consecutive modes that appear simultaneously with the dominant hydrodynamic mode, as observed in the literature for single axisymmetric cavities [Rockwell et al., 2003; Oshkai et al., 2005]. However,
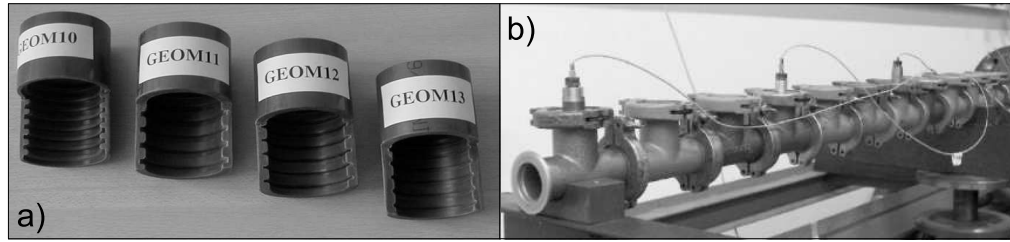
Figure 3.4: Samples of corrugated pipes manufactured from PVC (a), multiple side branch system (b).

Sample	W (mm)	H (mm)	r_up (mm)	r_dwn (mm)	L_p (mm)	Sample	W (mm)	H (mm)	r_up (mm)	r_dwn (mm)	L_p (mm)
Geo 1	8.0	4.0	2.0	2.0	0	Geo 7	4.0	4.0	0.0	0.0	8.0
Geo 2	4.0	4.0	2.0	2.0	4.0	Geo 8A	2.0	2.0	2.0	0.5	5.5
Geo 3A	4.0	4.0	3.0	1.0	4.0	Geo 8B	2.0	2.0	0.5	2.0	5.5
Geo 3B	4.0	4.0	1.0	3.0	4.0	Geo 9	2.0	4.0	2.0	2.0	4.0
Geo 4	4.0	4.0	2.0	2.0	0	Geo 10	2.0	2.0	2.0	2.0	4.0
Geo 5	4.0	4.0	2.0	2.0	8.0	Com 1	0.6	1.7	1.1	1.4	5.2
Geo 6A	4.0	4.0	4.0	0.0	4.0	Com 2	0.6	1.8	1.6	1.3	4.7
Geo 6B	4.0	4.0	0.0	4.0	4.0	Com 3	7.0	5.0	1.5	1.5	0

Table 3.1: Geometric parameters of tested corrugated pipes (Geo: PVC corrugated pipes and Com: commercial corrugated pipes).

during the experimental campaign secondary modes were not observed.

3.3.2 Corrugated pipes and multiple side branch system

Throughout the experimental campaign both commercially available corrugated pipes and corrugated pipes manufactured from Polyvinyl chloride (PVC) tubes were used, see figure 3.4-a. The geometric parameters of the tested pipes are specified in table 3.1. The pipes with asymmetric cavity geometries are tested in both flow directions and corresponding samples denoted configuration A and B of the same pipe. The cavity geometries of the commercial corrugated pipes (Com 1 and Com 2) are quite different from those of PVC pipes (Geo), see figure 3.5-a. The technical specifications of those pipes obtained from the manufacturers are also presented in the table 3.1. Com 3 is another commercially available corrugated pipe. It has a relatively simple cavity shape, see figure 3.5-b, similar to that of the PVC corrugated pipes. For all geometries, the inner diameter of the pipe (D) is 50±1 mm.

The multiple side branch system is made of a series of identical T-joints connected to each other, forming a row of equally spaced side branches along a main pipe, see figure 3.4-b. The T-joint elements are standard vacuum appliances (ISO-KF) cast in aluminum. The main pipe of the T-joint has a diameter (D) of 33 mm which is equal to the diameter of the side branch (D_sb). The length of the main pipe of each T-joint is 100 mm and the side branch, located half way of this segment, has a length (L_sb)
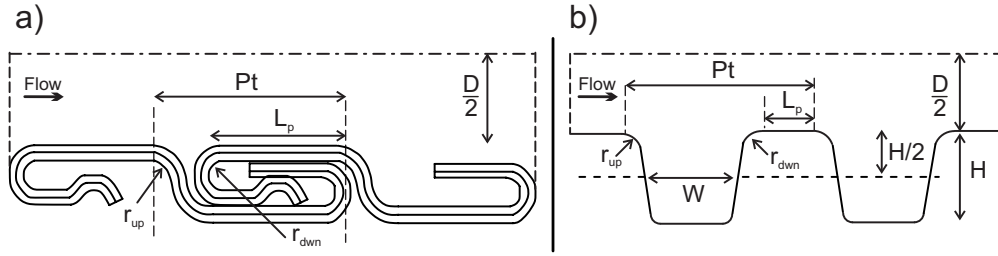
Figure 3.5: Schematic drawing of commercially available corrugated pipes: Com1 & Com2 (a) and Com3 (b) in table 1.

of 33 mm. The upstream edge of the side branch, which is connected to the main pipe, has a radius of curvature of $r_{up} = 3$ mm, which is approximately one tenth of the side branch diameter ($r_{up}/D_{sb} \approx 0.1$). T-joints are connected to each other using standard ISO-KF clamps which incorporate O-rings for sealing.

3.3.3   Definition of Strouhal number for whistling periodic systems

The Strouhal number is a commonly used dimensionless parameter for oscillating flows, as in the case of whistling. The Strouhal number is defined as:

$$Sr = \frac{f L_c}{U} \tag{3.3}$$

where f is the frequency of the oscillation, L_c is the characteristic length and U is the average flow speed inside the corrugated pipe. Average flow speed U is defined in terms of the volumetric flow rate (Q) and inner diameter of the pipe as:

$$U = 4Q/(\pi D^2) \tag{3.4}$$

The wavelength of the corrugations, the pitch, has been a commonly used characteristic length [Binnie, 1961; Crawford, 1974; Nakamura and Fukamachi, 1991; Serafin and Kojs, 2005; Popescu and Johansen, 2008]. However, testing pipes with more marked differences between cavity width and pitch showed that the peak-whistling Strouhal number depends on the cavity width rather than on the pitch [Elliott, 2004; Belfroid et al., 2007; Kristiansen and Wiik, 2007; Tonon et al., 2010; Nakıboğlu et al., 2010]. It was also concluded that the characteristic length used in the Strouhal number definition should include the upstream edge radius (r_{up}) because of the increase in the distance traveled by the vorticity perturbation due to rounding off the upstream edge. The downstream edge radius is less critical because vortical perturbations at the upstream edge of the cavity diffuse as they are swept along the cavity mouth. When they reach the downstream edge, they are less localized than when they are close to the upstream edge. As a consequence, the radius of the downstream edge (r_{dwn}) does not effect the travel time of the perturbations [Bruggeman

et al., 1991; Belfroid et al., 2007; Nakiboğlu et al., 2009] as significantly as the one of the upstream edge. Following this, the sum of the cavity width and the upstream edge radius, $W + r_{\mathrm{up}}$ appears to be the most suitable characteristic length, which is used in the remainder of this paper.

It is important to realize that since the peak-whistling Strouhal number is independent of pitch length, the distance between the cavities, plateau length (L_{p}), is not important for the sound production [Nakiboğlu et al., 2010]. This implies that sound production is a local effect which can be, in a first order approximation, studied for a single cavity. In the present analysis the possible hydrodynamic interaction between successive cavities is neglected.

Another point that should be highlighted is that within a specific resonant mode with increasing flow velocity, the whistling frequency shows a slight increase [Sarohia, 1977; Bruggeman et al., 1991; Ziada et al., 2003]. Thus, within the same resonant mode, as the flow velocity in the main pipe increases, the Strouhal number decreases. As a result, for each resonant mode there is a range of Strouhal numbers where the whistling phenomenon is observed. The highest Strouhal number for a resonant mode is called critical Strouhal number (Sr_{cr}), because it indicates the onset of oscillations for that particular acoustic mode. After the onset of resonance, within the same resonant mode, increasing the flow velocity increases the amplitude of pressure oscillations till it reaches a peak value. Further increase of the flow velocity decreases the amplitude of acoutic fluctuations. The Strouhal number which corresponds to the maximum pressure fluctuation amplitude for a given acoustical mode is called the peak-whistling Strouhal number ($Sr_{\mathrm{p-w}}$). The former is crucial to develop design charts to avoid acoustic resonances by predicting the critical flow velocities [Ziada and Shine, 1999]. The latter is also important in the estimation of the maximum amplitudes that the system will experience [Tonon et al., 2010]. The peak-whistling Strouhal number of a corrugated pipe is determined through a linear least square fit of consecutive excited acoustic modes [Nakiboğlu et al., 2010].

The definition of the Strouhal number in multiple side branch systems is similar to that of corrugated pipes. Instead of using the sum of cavity width and upstream edge radius ($W + r_{\mathrm{up}}$) as characteristic length, the sum of the effective cavity width and upstream edge radius ($W_{\mathrm{eff}} + r_{\mathrm{up}}$) is used. This distinction in the characteristic length is due to a geometric difference between corrugated pipes and multiple side branch systems. The cross section of a corrugation cavity is a slit whereas the side branches have circular cross sections, see figure 3.4-b. Thus, the side branch diameters are converted to an effective cavity width ($W_{\mathrm{eff}} = \pi D_{\mathrm{sb}}/4$) as proposed by Bruggeman et al. [1991], which is the average width of the side branch cross section.

There is also a difference in the determination of the peak-whistling Strouhal number between corrugated pipes and multiple side branch systems. The corrugated pipes (Geo, Table 3.1) used in this study have typically 2×10^2 corrugations, whereas the multiple side branch systems used in the experiments are composed of

14 to 19 T-joints. Whistling frequencies that are observed with corrugated pipes are rather high compared to the ones in the multiple side branch system. Thus, the typical number of corrugations per wave length in corrugated pipes at high frequencies ($fL/c_{\text{eff}} = O(10)$) is close to that of the multiple side branch systems at low frequencies ($fL/c_{\text{eff}} = O(1)$) [Tonon et al., 2010; Nakiboğlu et al., 2010]. Correspondingly, in the multiple side branch systems the attention is only given to the lowest acoustical modes.

3.3.4   Effect of pipe length on the whistling behavior of periodic systems

Though there is an extensive study on corrugated pipes, in many instances it is limited to short pipe segments [Binnie, 1960, 1961; Cadwell, 1994; Crawford, 1974; Elliott, 2004; Popescu and Johansen, 2008]. Ziada and Bühlmann [1991] investigate the long corrugated pipes with water flow. They observed a strong coupling between whistling and pipe wall vibrations. For gas flows such an effect of wall vibration has not been observed. Here the effect of pipe length (L) on the whistling phenomenon is addressed, which has been a subject of limited consideration. Experiments have been performed with commercially available corrugated pipes (Com 3 - Table 3.1) with lengths of 20, 40, 60, 100 and 200 pipe diameters. The whistling frequencies are plotted as a function of Mach number (*Ma*) in figure 3.6-a. Linear least square fits used for the determination of peak-whistling Strouhal numbers for $L/D = 20$ and $L/D = 200$ are also shown. It is seen that the peak-whistling Strouhal number is independent of the length of the pipe segment with the value $Sr_{\text{p-w}} = 0.49 \pm 0.04$. In figure 3.6-b the dimensionless fluctuation amplitude as a function of Mach number is given for the same five corrugated pipe segments. The dimensionless amplitude, $|p'|/(\rho_0 c_0 U) = |u'|/U$, is defined as the amplitude of the standing pressure wave at a pressure anti-node inside the main pipe $|p'|$, divided by the air density ρ_0, the speed of sound c_0 and the main flow velocity U; it is equal to the amplitude of the acoustic velocity at a pressure node inside the main pipe $|u'|$ divided by main flow velocity U. An increase in dimensionless fluctuation amplitude is observed with increasing corrugated pipe length until L/D of 100. Further increase of the pipe length to $L/D = 200$ does not change the amplitude. A saturation of dimensionless fluctuation amplitude is observed at $|u'|/U \approx 0.1$.

   Experiments were performed also with corrugated pipe segments (L/D) of 400, 600 and 800, as shown in figure 3.7. It is clear that also for these long corrugated pipe segments (up to 4000 pitch lengths) the peak-whistling Strouhal number does not depend significantly on the length of the pipe segment. It is evident that the saturation level of fluctuation amplitude $|u'|/U \approx 0.1$ is also independent of the pipe length.

   The saturation in dimensionless fluctuation amplitude is observed also with cor-
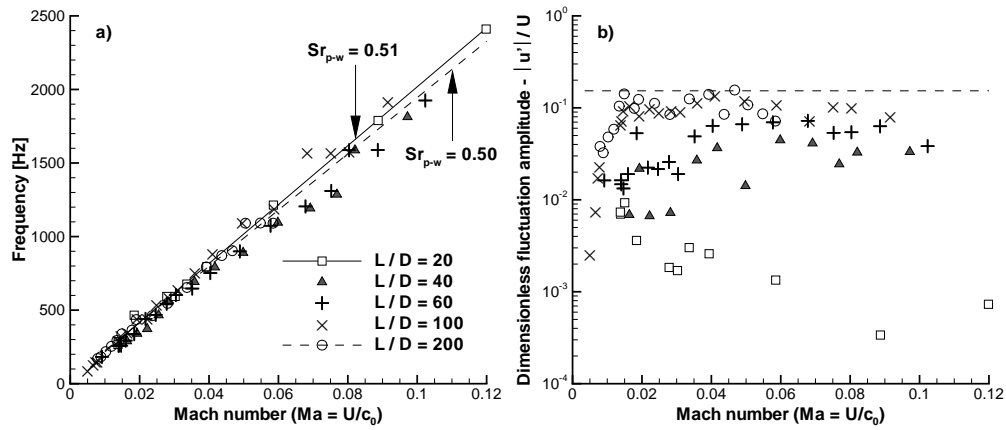
Figure 3.**6:** Experiments performed with a commercial corrugated pipe (Com 3 - Table 3.1) with 5 different pipe lengths between $L/D = 20$ & $L/D = 200$. Whistling frequency plotted against Mach number (a), dimensionless fluctuation amplitude $|u'|/U$ plotted against Mach number (b).
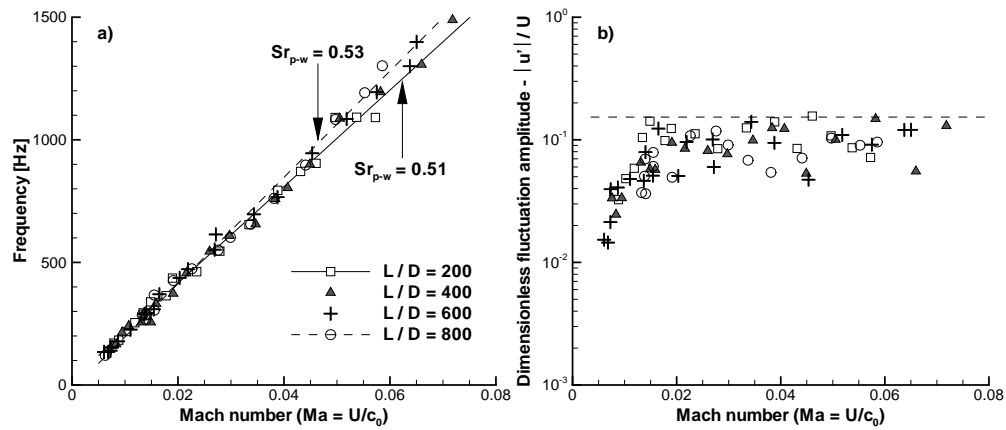
Figure 3.**7:** Experiments performed with a commercial corrugated pipe (Com 3 - Table 3.1) with 4 different pipe lengths between $L/D = 200$ & $L/D = 800$. Whistling frequency plotted against Mach number (a), dimensionless fluctuation amplitude $|u'|/U$ plotted against Mach number (b).

Figure 3.8:
Dimensionless fluctuation amplitude $|u'|/U$ plotted against Mach number for a PVC corrugated pipe (Geo 4 - Table 3.1) with 4 different pipe lengths between $L/D = 40$ & $L/D = 100$.
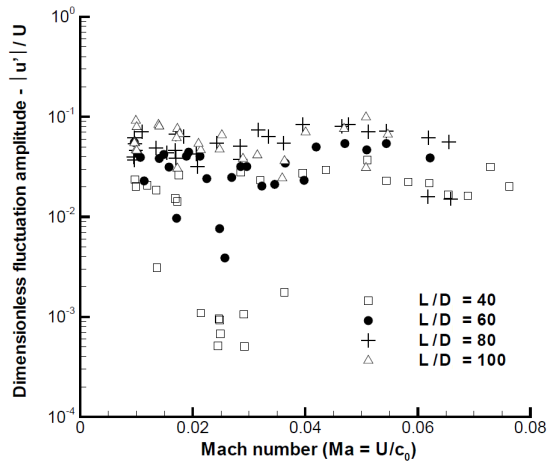
rugated pipes manufactured from PVC, with simple cavity geometries. As demonstrated in figure 3.8 for Geo 4 (Table 3.1), acoustic velocity fluctuations reach a saturation amplitude of $|u'|/U \approx 0.1$ already with a L/D of 60. Testing longer pipes $L/D = 80$ and $L/D = 100$ does not further increase the fluctuation amplitude. This saturation amplitude in corrugated pipes is considerably lower than the ones that are observed for deep closed side branches in cross flow direction $|u'|/U \approx O(1)$ [Kriesels et al., 1995; Ziada and Shine, 1999; Dequand et al., 2003a] and along the main flow direction $|u'|/U \approx 0.6$ [Bruggeman et al., 1991] as well as Helmholtz resonators $|u'|/U \approx 0.6$ [Dequand et al., 2003b].

Multiple side branch systems with different numbers of T-joints were constructed for the study, from 14 for the shortest system to 19 for the longest. In figure 3.9, measured dimensionless fluctuation amplitudes for the 3rd acoustic mode are plotted as a function of Strouhal number. Similarly to corrugated pipes the peak-whistling Strouhal number remains unaltered with changing system length, and is 0.62 ± 0.01. Also a saturation in dimensionless fluctuation amplitude at $|u'|/U \approx 0.035$ is reached for 19 side branches. This is close to the level found for corrugated pipes of equal length ($L/D = 40$).

3.3.5 Effect of helical corrugations

Experiments have been performed to investigate the whistling behavior of helical (spiral wound) corrugated pipes. A corrugated pipe is manufactured with the same cavity geometry as Geo 4 (Table 3.1) but with a helical configuration, instead of a periodic arrangement of cavities as shown in figure 3.2. The pitch, which is the width of one complete helix, is also the same as the pitch length of Geo 4.

Introducing helical corrugations has no significant effect on the whistling behav-
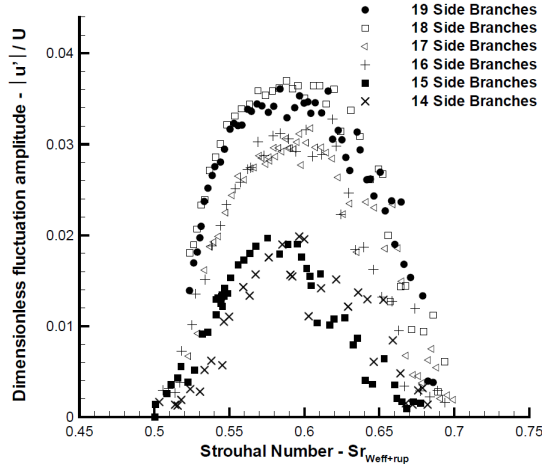
Figure 3.9: Dimensionless fluctuation amplitude $|u'|/U$ plotted against Strouhal number Sr for the 3rd acoustic mode for multiple side branch systems that are composed of different numbers of T-joints.

ior. Observed fluctuation amplitudes and respective saturation level remains the same. A slightly lower peak-whistling Strouhal number $Sr_{p-w} = 0.34$ is recorded with the helical configuration compared to the periodic configuration $Sr_{p-w} = 0.38$. Experiments on helical corrugated pipes reported by Kop'ev et al. [2008] indicate also a behavior analogous to that of non-helical (periodic) corrugated pipes.

3.3.6 Effect of confinement ratio on Strouhal number in periodic system

In periodic systems a broad range of peak-whistling Strouhal numbers has been observed. For corrugated pipes a range between $0.3 \leq Sr_{p-w} \leq 0.5$ has been found [Binnie, 1961; Petrie and Huntley, 1980; Nakamura and Fukamachi, 1991; Nakiboğlu et al., 2010]. For multiple side branch systems, however, a relatively high peak-whistling Strouhal number $Sr_{p-w} = 0.6$ has been recorded [Tonon et al., 2010]. Binnie [1961] explained this wide range of Strouhal numbers as an outcome of confinement ratio which is defined as the ratio of pipe diameter to cavity width (D/W). He used a single corrugated pipe but by using rods of different diameters (D_r) placed coaxially inside the pipe, he was able to vary the confinement ratio. In the presence of a rod, the confinement ratio is defined as $((D - D_r)/W)$. As mentioned in section 3.3.3 in the case of rounded cavity edges, it is essential to include the value of r_{up} in the characteristic length. Thus, here the confinement ratio is modified as $(D - D_r)/(W + r_{up})$. Unfortunately, Binnie [1961] did not provide any explicit information on the edge geometry of the cavities. However, by comparing similar commercial corrugated pipes (see, figure 3.2-b) to the ones mentioned in his paper, the edge radius is estimated as 25% of the cavity width. Then it is concluded that Binnie observed a shift in the peak-whistling Strouhal number from 0.53 to 0.34 with

Figure 3.10: Peak-whistling Strouhal number plotted against confinement ratio, $(D - D_{\mathrm{r}})/(W + r_{\mathrm{up}})$, for various periodic systems (Binnie [1961]; Elliott [2004]).
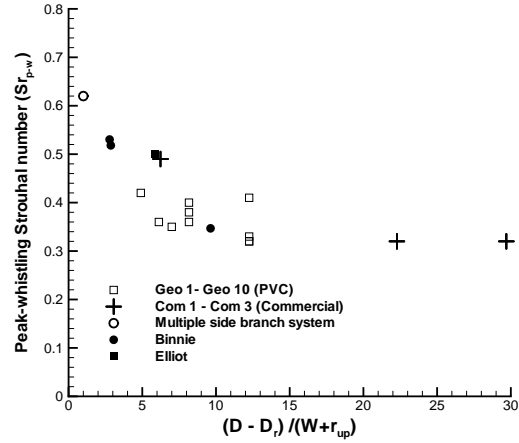
an increasing confinement ratio $(D - D_{\mathrm{r}})/(W + r_{\mathrm{up}})$ from 2.8 to 9.6. In figure 3.10 peak-whistling Strouhal number data is presented as a function of confinement ratio for the corrugated pipes (Table 3.1) and the multiple side branch system, together with the measurements of Binnie [1961] and Elliott [2004]. A decrease in the peak-whistling Strouhal number with increasing confinement ratio is found. Though these experiments clearly demonstrate the shift of the peak-whistling Strouhal number due to the confinement ratio, the reason of the shift remains evasive. In experiments with a tandem side branch configuration, Ziada and Shine [1999] observed a similar shift in the peak-whistling Strouhal number with increasing ratio of main pipe diameter to side branch diameter (D/D_{sb}). Ziada and Shine [1999] suggested the shift in peak-whistling Strouhal number was due to a decrease in the ratio of cavity width to gradient length of the velocity profile of the approach flow. This will be addressed in detail in section 3.4.4.

3.4 Numerical Methodology

In this section a new numerical technique is introduced to investigate the whistling in periodic systems. As mentioned in section 3.2, the self-oscillations observed in periodic systems are due to a feedback loop, in which the shear layer instability and the longitudinal standing wave act as an amplifier and a filter, respectively. The proposed technique is developed to study only the amplifier of this feedback loop and the velocity fluctuations controlling the shear layer oscillations are imposed as inlet boundary conditions. As explained in section 3.3.3, by neglecting a possible hydrodynamic interaction between successive cavities sound generation in periodic systems can be studied, in a first order approximation, on a single cavity. The method combines incompressible flow simulations with Vortex Sound Theory to estimate the
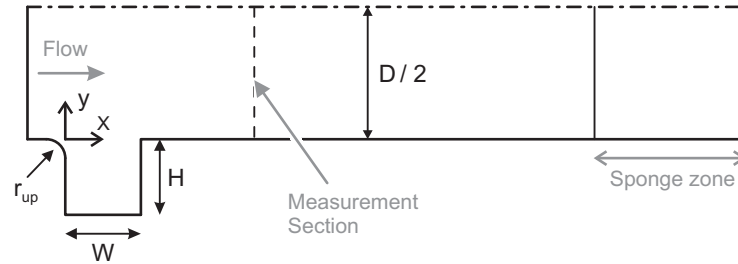
Figure 3.11: The domain and the relevant geometric parameters, axis of symmetry (cylindrically symmetric flow) or upper wall (plane flow) (— - —).

strength of an acoustic source due to the interaction of a single cavity in a pipe flow at high Reynolds number with a low frequency acoustic field. In the following two sections, these two parts of the approach are explained. Then, the proposed numerical methodology is used to explain some of the phenomena observed in whistling periodic systems such as the non-linear saturation of the amplitude, and the effect of the confinement ratio on the peak-whistling Strouhal number.

3.4.1   Incompressible simulations

In corrugated pipes the cavity width of the corrugations and respectively in multiple side branch systems the diameter of the side branches are usually small compared to the wave length (λ) of the standing waves ($Pt/\lambda < 10^{-1}$). The flow in such a cavity/side branch can be assumed to be locally incompressible. Accordingly, unsteady incompressible flow simulations are performed [Martínez-Lera et al., 2009] for a single cavity in a confined flow. All the simulations are performed in 2D domains. The domain and the relevant geometric parameters are shown in figure 3.11. In some simulations, cylindrical symmetric domains are used to mimic a circumferential cavity as found in corrugated pipes. In those simulations, the upper wall of the confining pipe is replaced by an axis of symmetry. The inner diameter of the pipe is denoted by D, the depth of the cavity by H, the width of the cavity by W and the radius of curvature of the upstream cavity edge by r_{up}. The inlet is located at $0.5W$ upstream of the cavity, such a short inlet pipe section is chosen to make sure that the imposed inlet velocity profiles do not evolve significantly before reaching the cavity. The outlet is placed at a reasonably far location, 9W downstream, from the cavity. In all the simulations, the cavity depth is taken equal to the cavity width. A previous experimental study [Nakiboğlu et al., 2010] showed that $H/W = 1$ is in the range ($0.5 \leq H/W \leq 1.2$) where a saturation behavior is observed in the dimensionless fluctuation amplitude. In this range, variations in H/W ratio neither influence the amplitude nor the peak-whistling Strouhal number. Unless mentioned otherwise in all the simulations the upstream cavity edge radius is taken as $r_{\mathrm{up}} = 0.25W$, which

is a typical value for corrugated pipes, see figure 3.2-b.

A finite volume commercial code, Fluent 6.3, is used. A pressure-based segre-
gated solution algorithm, SIMPLE [Patankar and Spalding, 1972] is employed. The
second-order implicit time discretization scheme together with the second-order up-
wind space discretization for convective terms is chosen. No turbulence modeling
is applied. For each simulation, initially a steady flow solution is performed with
an unexcited fully developed turbulent velocity profile $u(y,t) = u(y)$ which has an
average velocity of U. These inlet velocity profiles are determined through RANS
simulations at a Reynolds number of 5×10^4 for each different pipe diameter (D).
The iterations are continued until all the residuals drop below 10^{-12}. Then a velocity
perturbation $u'(t)$ with a frequency (f) and an amplitude ($|u'_{\text{cav}}|$):

$$u'(t) = |u'_{\text{cav}}| \sin(2\pi f t). \tag{3.5}$$

is superposed on the inlet velocity profile ($u(y,t) = u(y) + u'(t)$), where $|u'_{\text{cav}}|$ is
the amplitude of the acoustic velocity induced by the longitudinal standing wave
at the position of the cavity considered. This amplitude can be much lower than
$|u'|$, if the cavity considered is close to a velocity node of the standing wave. The
outlet boundary condition $\partial u_x / \partial x = 0$ is used. After checking different computation
times, a typical time of 5 periods of the excitation frequency appeared to be sufficient,
simulations with longer computation times provide the same results. The time step
size is chosen as $\Delta t = 0.01 W / U$.

The computational domain contains approximately 70000 quadrilateral cells which
are clustered close to the opening of the cavity and to the walls, where there are
high gradients of velocity due to shear layer and boundary layer, respectively. In
the domain between $6W$ and $9W$ downstream of the cavity, shown as sponge zone
in figure 3.11, cells with high aspect ratio ($\Delta x / \Delta y \gg 1$) are employed. By doing so
problems that can arise due to reverse flow at the outlet boundary condition are min-
imized. A study on mesh dependency has been carried out. The same computation
was performed with 2 times and 4 times more densely meshed domains, producing
differences in the calculated acoustic source power of less than 5%.

3.4.2   Calculation of acoustic source power

Using the Theory of Vortex Sound, the strength of the acoustic source for high Reynolds
number flows is calculated from enthalpy differences, which are acquired from rela-
tively low Reynolds number simulations ($Re = O(10^3)$). This is achieved by means
of an extrapolation method. The effect of friction on the enthalpy losses is estimated
considering a reference flow through a straight smooth pipe (without cavity). In this
subsection this approach is explained in detail.

The acoustic field can be defined by using a Helmholtz decomposition of the flow

field $\mathbf{u}$, as proposed by Howe [1980]:

$$\mathbf{u} = \boldsymbol{\nabla}(\phi_0 + \phi') + \boldsymbol{\nabla} \times \boldsymbol{\Psi} \tag{3.6}$$

where $\boldsymbol{\Psi}$ is the stream function, ϕ_0 and ϕ' are the steady and unsteady components of the scalar potential, respectively. Recognizing that the solenoidal vector field is incompressible $\boldsymbol{\nabla} \cdot (\boldsymbol{\nabla} \times \boldsymbol{\Psi}) = 0$, the acoustic field corresponds to the unsteady potential component of the flow $\boldsymbol{\nabla} \phi'$, which is compressible. The acoustical flow velocity ($\mathbf{u}'$) is defined by Howe [1980] as:

$$\mathbf{u}' = \boldsymbol{\nabla}\phi'. \tag{3.7}$$

For a subsonic flow with sufficiently high Reynolds number the effect of friction can be neglected in the bulk of the flow. Assuming a homentropic flow, the momentum equation (Crocco's equation) can be written as follows:

$$\boldsymbol{\nabla}B = -\frac{\partial \mathbf{u}}{\partial t} - \boldsymbol{\omega} \times \mathbf{u} \tag{3.8}$$

where $\boldsymbol{\omega} = \boldsymbol{\nabla} \times \mathbf{u}$ is the vorticity and B is the total enthalpy:

$$B = \frac{1}{2}|\mathbf{u}|^2 + i, \tag{3.9}$$

where i is the specific enthalpy. Here it can be noted that the first term in the right hand side of the momentum equation Eq. 3.8, is related to the potential flow solution and the second term corresponds to the Coriolis force density, $\boldsymbol{f}_c = -\rho_0(\boldsymbol{\omega} \times \mathbf{u})$, experienced by an observer moving with the flow velocity ($\mathbf{u}$). The latter is interpreted as the source of the sound.

Using the energy corollary of Howe [1998], the time average acoustic source power $\langle P_{\text{source}} \rangle$ due to the Coriolis force can be estimated for low Mach number flows as follows:

$$\langle P_{\text{source}} \rangle = -\rho_0 \left\langle \int_V (\boldsymbol{\omega} \times \mathbf{u}) \cdot \mathbf{u}' \, dV \right\rangle \tag{3.10}$$

where V is the volume in which $\boldsymbol{\omega}$ is non vanishing and $< \cdot >$ is the time averaging. Combining Eq. 3.10 with Eq. 3.8, $\langle P_{\text{source}} \rangle$ can be determined as follows:

$$\langle P_{\text{source}} \rangle = -\rho_0 \left\langle \int_V \boldsymbol{\nabla}B' \cdot \mathbf{u}' \, dV \right\rangle + \rho_0 \left\langle \int_V \frac{\partial \mathbf{u}}{\partial t} \cdot \mathbf{u}' \, dV \right\rangle \tag{3.11}$$

where B' is the fluctuating total enthalpy. Knowing that in a compact source region $\boldsymbol{\nabla} \cdot \mathbf{u}'$ is negligibly small, the source term, $\boldsymbol{\nabla}B' \cdot \mathbf{u}'$, can be replaced by $\boldsymbol{\nabla} \cdot (\mathbf{u}'B')$. Neglecting the contribution of the second integral in Eq. 3.11 and using the divergence theorem $\langle P_{\text{source}} \rangle$ reads:

$$\langle P_{\text{source}} \rangle = \rho_0 \left\langle \int_S (B' \, \mathbf{u}') \cdot \mathbf{n} \, dS \right\rangle \tag{3.12}$$

It is seen from Eq. 3.12 that the acoustic source power generated in a control volume can be calculated through the surface integral of fluctuating total enthalpy over the boundary of the control volume.

In this derivation attention should be drawn to two points. Firstly, it is assumed in the momentum equation Eq. 3.8 that the effect of friction in the bulk of the fluid is small enough to be neglected. Secondly, it is assumed that the second integral in Eq. 3.11 has no contribution to the sound generation. The same conclusion can be deduced using as starting point the exact energy corollary of Myers [1986, 1991]:

$$\langle P_{source} \rangle = \left\langle \int_S (B' \, \mathbf{m}') \cdot \mathbf{n} \, dS \right\rangle \tag{3.13}$$

where

$$B' = \frac{p'}{\rho_0} + \mathbf{u}_0 \cdot (\mathbf{u}' + \mathbf{u}'_\mathrm{h}), \quad \mathbf{m}' = \rho_0(\mathbf{u}' + \mathbf{u}'_\mathrm{h}) + \rho_0'\mathbf{u}_0$$

where $\mathbf{u}_0$ is the time averaged velocity and the fluctuations are split into the acoustical (potential) part $\mathbf{u}'$ and the hydrodynamical (rotational) part $\mathbf{u}'_\mathrm{h}$. When ρ_0' is neglected (in agreement with the use of incompressible flow model) and the contribution of the hydrodynamic velocity fluctuations ($\mathbf{u}'_\mathrm{h}$) to the integral is also neglected, Eq. 3.12 is recovered. The contribution of the hydrodynamic velocity fluctuations is expected to depend on the spatial location of the control surface. It has been verified that by choosing a large enough control volume such a dependency can be avoided.

The recent study of Martínez-Lera et al. [2009] showed that after the time averaging, what they called the potential term, the second integral in Eq. 3.11 could still have a non-zero contribution to $\langle P_\mathrm{source} \rangle$. These authors concluded that it is essential to remove the term $(-\partial \mathbf{u}/\partial t)$ from the enthalpy difference ($\Delta B'$) before taking the time averaging. Their technique is based on successive linear least-square fits of the total pressure jumps considering many measuring planes both upstream and downstream of the cavity. This procedure provides promising results. However, the drawback is that the bounds of the source region cannot be determined. Due to the uncertainty in the spatial linear fit, $\langle P_\mathrm{source} \rangle$ appears to depend significantly on the arbitrary choice of the position of the measuring planes. This is an indication that this approach is not able to completely remove the contribution of the hydrodynamic velocity fluctuations to the source power.

Here an alternative method is proposed where the contribution of hydrodynamic velocity fluctuations effectively removed from the source power. This is done by means of a reference flow simulation in a straight pipe with identical boundary conditions with the respective cavity simulation and using the same measurement sections in the duct, e.g. x_1 and x_2, see figure 3.12. Then $\langle P_\mathrm{source} \rangle$ can be estimated as follows:

$$\langle P_\mathrm{source} \rangle = \rho_0 \left\langle \frac{1}{4} \left[(B'_{x_2} - B'_{x_1})_\mathrm{cav} - (B'_{x_2} - B'_{x_1})_\mathrm{ref} \right] . u' \pi D^2 \right\rangle \tag{3.14}$$
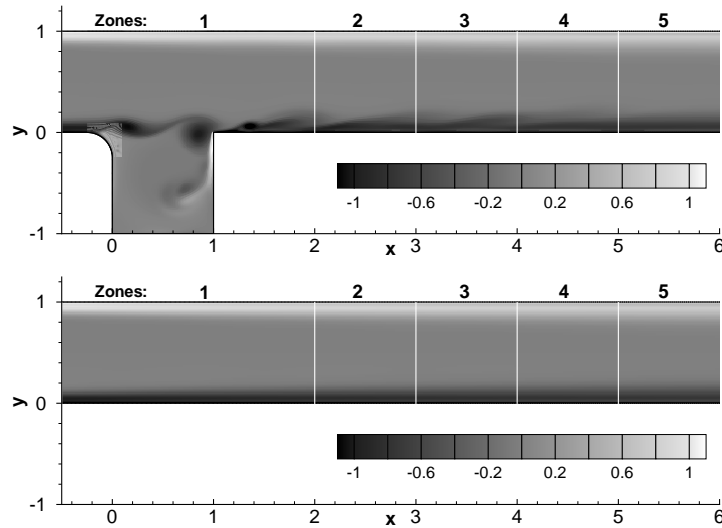
Figure 3.12: Normalized vorticity contours for a confined cavity flow and a reference flow in a straight pipe ($Re = 4000$, $Sr = 0.6$ and $|u'|/U = 0.2$). White lines represent the measurement sections where area averaged total enthalpy is recorded.

The proposed approach is an extrapolation method for high Reynolds number flows, where the solution is expected to be Reynolds number independent. For a simulation with a perturbation amplitude of $|u'|/U = 0.1$, from figure 3.13 it is seen that calculated average acoustic source powers are converging to a Reynolds number independent limit. Other simulations that are considered here have also similar characteristics in which above a certain Reynolds number $\langle P_{\mathrm{source}} \rangle$ can be assumed weakly depend on Reynolds number. Within the accuracy of the proposed approach (5%) this limit is determined as $Re = 4000$, which is used in all the simulations. By increasing the number of cells in the computational domain, simulations with higher Reynolds numbers can be achieved, which will increase the Reynolds number independency of the results.

Using this approach the extent of the source region in the duct can be determined. All the numerical simulations independent of the Strouhal number and perturbation amplitude have a similar bound for the source region, which is between $0.5W$ upstream of the cavity and W downstream of the cavity, shown as *Zone 1* in figure 3.12. $\langle P_{\mathrm{source}} \rangle$ remains constant within 5% when the bounds of the control volume are extended to include the zones 2, 3 and 4. In some calculations the reference flow solution for smooth pipes are carried out with slip boundary condition for the section of the wall, which corresponds to the cavity location. The results are almost identical to the results presented here.

Simulations have been performed to check the capability of the proposed ap-

Figure 3.13: Convergence to high Reynolds number limit: 1/Re is plotted against dimensionless average acoustic source power $\langle P_{\text{source}} \rangle / (\rho_0 U S_{\text{p}} |u'|^2)$ for $D/W = 2$ and $|u'|/U = 0.1$.
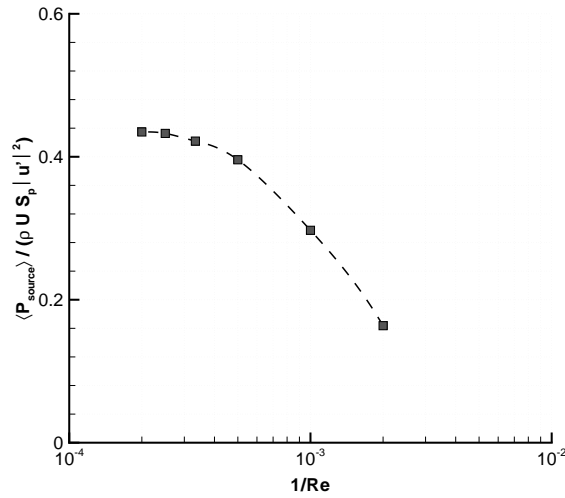
proach in predicting the Strouhal number range where there is sound production. In figure 3.14, the dimensionless average acoustic source power $\langle P_{\text{source}} \rangle / (\rho_0 U S_{\text{p}} |u'|^2)$ is displayed as a function of Strouhal number for a cavity with sharp edges and for a perturbation amplitude of $|u'|/U = 0.2$. The results are presented together with the data obtained by Hofmans [1998], using an inviscid two-dimensional vortex blob method for a T-joint with the same geometry and perturbation amplitude for a configuration similar to corrugated pipes, where there is a grazing flow in the main pipe. Two ranges of Strouhal number with positive dimensionless average acoustic source power are distinguished where there is sound production. The lower ($Sr < 0.1$) and the higher ($0.52 < Sr < 0.74$) Strouhal number ranges correspond to the first and the second hydrodynamic modes, respectively. In the first hydrodynamic mode there exist a single vortex in the cavity mouth and the traveling time of the vortex across the opening is 0.25 oscillation period. Whereas for the second hydrodynamic mode two vortices are present at the same moment in the cavity mouth. A vortex takes 1.25 oscillation period to travel across the cavity [Bruggeman et al., 1991]. It is clear that the second hydrodynamic mode is stronger than the first one, explaining why the experimentally observed peak-whistling Strouhal numbers belong to the second hydrodynamic mode. Acoustic source powers predicted by the present methodology are in agreement with the data of Hofmans [1998]. A peak whistling Strouhal number $Sr_{\text{p-w}}$ of 0.6 is estimated. This is close to the experimental observation with multiple side branch systems which is $Sr_{\text{p-w}} = 0.62 \pm 0.02$, figure 3.9. The peak-whistling Strouhal number will be further discussed in Section 3.4.4.

Figure 3.14: Strouhal number plotted against dimensionless average acoustic source power $\langle P_{\text{source}} \rangle / (\rho_0 U S_{\text{p}} |u'|^2)$ for a cavity (present study) and a T-joint [Hofmans, 1998] with $r_{\text{up}}/W = 0$ and $|u'|/U = 0.2$.

3.4.3 Nonlinear saturation of the shear layer

The aeroacoustic behavior of corrugated pipes and the multiple side branch system depends strongly on the perturbation amplitude, $|u'|/U$. At low perturbation amplitudes the instability of the shear layer can be described by linear stability theory [Rayleigh, 1896], where the acoustic source power $\langle P_{\text{source}} \rangle$ grows quadratically with perturbation amplitude [Bruggeman et al., 1991]. In this regime, the vorticity disturbances are amplified by a factor $e^{2\pi}$ over one hydrodynamic wave length in the shear layer [Bruggeman et al., 1986]. For the 2nd hydrodynamic mode this corresponds to an amplification of $e^{5\pi/2} \approx 2.6 \times 10^3$. Evidently, this imposes a perturbation amplitude limit around 10^{-3} to the validity of the linear theory above which nonlinearities become essential [Tam and Block, 1978]. In this range the amplitude of the oscillations is determined by nonlinearities, such as roll-up of the shear layer into discrete vortices [Fletcher, 1979; Keller, 1984; Bruggeman et al., 1991; Rowley et al., 2006].

The proposed approach predicts the linear range and the nonlinear saturation of the shear layer, as demonstrated in figure 3.15 for a simulation with $D/(W + r_{\text{up}}) = 3.2$. For small perturbation amplitudes $|u'|/U \leq 10^{-3}$, the shear layer behaves linearly. Therefore, the acoustic source power grows quadratically with $|u'|/U$, making the dimensionless average acoustic source power $\langle P_{\text{source}} \rangle / (\rho_0 U S_{\text{p}} |u'|^2)$ constant. Eventually, around $|u'|/U \approx 10^{-2}$ nonlinearities become dominant and dimensionless acoustic source power $\langle P_{\text{source}} \rangle / (\rho_0 U S_{\text{p}} |u'|^2)$ starts to decrease with $|u'|/U$.

This amplitude dependency test of $\langle P_{\text{source}} \rangle$ is performed for Strouhal numbers of 0.5, 0.56 and 0.63. Similarly to the simulations discussed in the previous section, initially simulations have been performed at a constant perturbation amplitude $(|u'|/U)$ with various Strouhal numbers to determine the peak-whistling Strouhal number for a confinement ratio of $D/(W + r_{\text{up}}) = 3.2$. The peak-whistling Strouhal

Figure 3.15: Perturbation amplitude $|u'|/U$ plotted against dimensionless average acoustic source power $\langle P_{\text{source}} \rangle / (\rho_0 U S_{\text{p}} |u'|^2)$ for $D/(W + r_{\text{up}}) = 3.2$ and for Strouhal numbers of 0.5, 0.56 and 0.63.
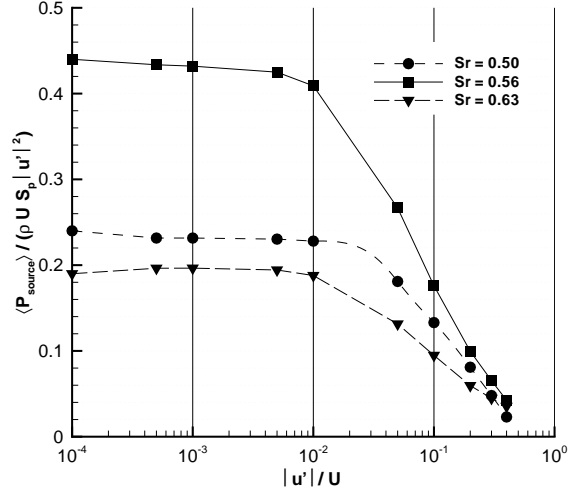
number $Sr_{\text{p−w}}$ is estimated as 0.56. Then two other Strouhal numbers close to the peak-whistling Strouhal number, are also studied to investigate whether there is a dependency of the peak-whistling Strouhal number on perturbation amplitude. From figure 3.15, it is seen that the peak-whistling Strouhal number does not alter significantly with the perturbation amplitude.

3.4.4 Peak-whistling Strouhal number difference in periodic systems

Previous studies on whistling periodic systems showed that there is a difference in the peak-whistling Strouhal numbers between multiple side branch systems and corrugated pipes [Tonon et al., 2010; Nakiboğlu et al., 2010]. As demonstrated in figure 3.10, the peak-whistling Strouhal number observed in multiple side branch systems $Sr_{\text{p−w}} = 0.62$, is higher than the ones observed in most corrugated pipes $0.3 < Sr_{\text{p−w}} < 0.6$. To investigate the reason of this variation in $Sr_{\text{p−w}}$, two sets of simulations have been performed. In multiple side branch system simulations, a 2D domain is used with a confinement ratio of $D/(W + r_{\text{up}}) = 0.8$, close to the experimental value. For corrugated pipe simulations, a cylindrical symmetric 2D domain is used to mimic a circumferential cavity. Also a larger confinement ratio is chosen for corrugated pipe simulations $D/(W + r_{\text{up}}) = 3.2$. Taking the confinement ratio of actual corrugated pipes $2 \le D/(W + r_{\text{up}}) \le 30$ (Table 3.1) into account, the pipe that is simulated has a rather small confinement ratio. In both set of simulations, a perturbation amplitude $|u'|/U$ of 0.05 is used. This particular perturbation amplitude is a typical dimensionless fluctuation amplitude observed in experiments as shown in figures 3.6-3.8 and 3.9 [Nakiboğlu et al., 2010; Belfroid et al., 2007]. The results for

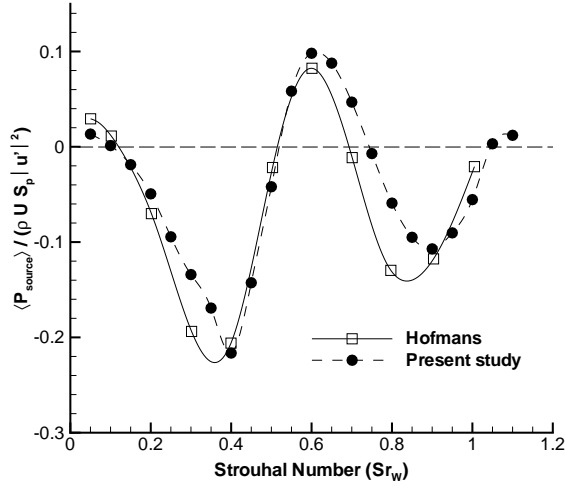**Figure 3.16:** Strouhal number plotted against dimensionless average acoustic source power $\langle P_{\text{source}}\rangle/(\rho_0 U S_{\text{p}}|u'|^2)$ for a multiple side branch system (MSBS) with a confinement ratio of $D/(W + r_{\text{up}}) = 0.8$ and for a corrugated pipe with a confinement ratio $D/(W + r_{\text{up}}) = 3.2$. ($|u'|/U = 0.05$)

these two set of simulations are presented in figure 3.16. In parallel to the experimental data, for the multiple side branch system a higher peak-whistling Strouhal number $Sr_{\text{p-w}} = 0.65$ is observed than for the corrugated pipe $Sr_{\text{p-w}} = 0.55$. Although these simulations show that the proposed numerical approach can predict the difference in peak-whistling Strouhal numbers between these two periodic systems, the reason of this difference remains unexplained.

As discussed in section 3.3.6, experiments indicate that there is a dependence of the peak-whistling Strouhal number on the confinement ratio $D/(W + r_{\text{up}})$. To address this effect of confinement, three sets of numerical simulations have been performed, which correspond to the experiments of Binnie [1961]. The result of the first set of simulations is already presented in figure 3.16, where a cavity in a cylindrical symmetric configuration is solved for a $D/(W + r_{\text{up}})$ ratio of 3.2. In the other two sets of simulations, the same cylindrical symmetric domain is used together with rods of diameter $D_{\text{r}} = 2W$ or $D_{\text{r}} = 3W$ respectively, which are placed coaxially inside the pipe to vary the confinement ratio. As explained in section 3.3.6, in the presence of a rod, the confinement ratio is defined as $(D - D_{\text{r}})/(W + r_{\text{up}})$. Dimensionless average acoustic source power $\langle P_{\text{source}}\rangle/(\rho_0 U S_{\text{p}}|u'|^2)$ for these configurations are presented as a function of Strouhal number in figure 3.17. It is seen that in accordance with the experimental observations as the confinement ratio decreases, the peak-whistling Strouhal number increases. For confinement ratios $(D - D_{\text{r}})/(W + r_{\text{up}})$ of 3.2, 1.6 and 0.8, peak-whistling Strouhal numbers $Sr_{\text{p-w}}$ of 0.55, 0.67 and 0.73 are estimated, respectively.

Ziada and Shine [1999] explained the shift in the peak-whistling Strouhal number by a change in the velocity profile. To investigate this argument, the same sets of simulations that are presented in figure 3.17 are repeated. But instead of using a

Figure 3.17: Strouhal number plotted against dimensionless average acoustic source power $\langle P_{\text{source}} \rangle / (\rho_0 U S_{\text{p}} |u'|^2)$ for a corrugated pipe with $D/(W + r_{\text{up}}) = 3.2$ and for rod diameters of $D_{\text{r}}/W = 0$, $D_{\text{r}}/W = 2$ and $D_{\text{r}}/W = 3$. ($|u'|/U = 0.05$, $\theta/D = 3 \times 10^{-2}$)
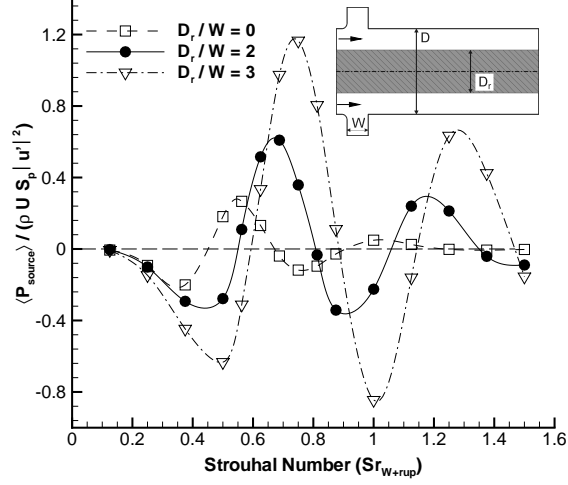
fully developed turbulent velocity profile, in all the simulations the same boundary layer profile which was also used by Martínez-Lera et al. [2009] is considered: a uniform velocity profile in the core of the flow with a boundary layer of momentum thickness $\delta_2 = 0.0065D$. The momentum thickness [Eggels et al., 1994] is defined here as:

$$\delta_2(D - \delta_2) = 2 \int_0^{D/2} r \frac{u(r)}{U_{\text{axs}}} \left(1 - \frac{u(r)}{U_{\text{axs}}}\right) dr \qquad (3.15)$$

where $u(r)$ is the radial profile of the axial velocity, U_{axs} is the velocity at the centerline of the duct and for coordinates see figure 3.11. The dimensionless average acoustic source powers $\langle P_{\text{source}} \rangle / (\rho_0 U S_{\text{p}} |u'|^2)$ for these three configurations are presented as a function of Strouhal number in figure 3.18. It is seen that the peak-whistling Strouhal number $Sr_{\text{p-w}} = 0.68$ remains constant with changing confinement ratio $(D - D_{\text{r}})/(W + r_{\text{up}})$, if the same velocity profile is used at the inlet. Thus, in agreement with the interpretation of Ziada and Shine [1999] the observed shift in the peak-whistling Strouhal number can be attributed to a change in the velocity profile due to an alteration in confinement ratio, rather than a pure confinement effect.

To evaluate the capability of the proposed numerical approach in predicting the peak-whistling Strouhal number, simulations with larger confinement ratios are also carried out. In figure 3.19, the available experimental data (figure 3.10) is compared with the numerical estimations. Although estimated peak-whistling Strouhal numbers are somewhat larger than the measured values, using the proposed numerical approach the dependency of the peak-whistling Strouhal number on confinement ratio is successfully captured.

For grazing flows along wall-mounted cavities in presence of turbulent boundary layers, a dependency of the convection velocity of shear layer perturbations (U_{c}) on
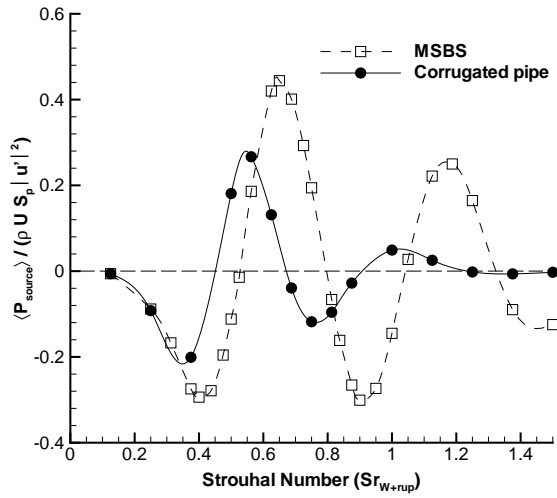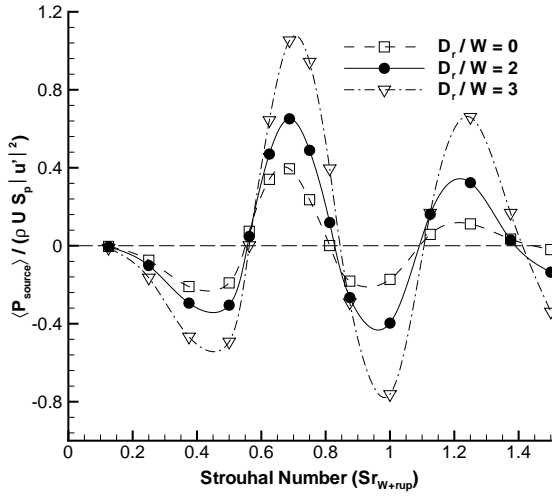
Figure 3.18: Strouhal number plotted against dimensionless average acoustic source power $\langle P_{\text{source}}\rangle/(\rho_0 U S_{\text{p}}|u'|^2)$ for a corrugated pipe with $D/(W + r_{\text{up}}) = 3.2$ and for rod diameters of $D_{\text{r}}/W = 0$, $D_{\text{r}}/W = 2$ and $D_{\text{r}}/W = 3$. Same approach velocity profile Eq. 3.15 is used in all simulations. ($r_{\text{up}}/W = 0.25$, $|u'|/U = 0.05$, $\theta/D = 6.5 \times 10^{-3}$)

the non-dimensional boundary layer thickness ($\Gamma = \delta_2/W$) has been reported by Elder et al. [1982]. Later for orifices subjected to a grazing turbulent boundary layer flow, Golliard [2002] proposed an empirical formula for the convection velocity as a function of non-dimensional boundary layer thickness as follows:

$$\frac{U_{\text{c}}}{U_\infty} = 0.4\Gamma^{-0.2} \tag{3.16}$$

where U_∞ is the free stream velocity. Associating the convection velocity [Kooijman et al., 2008], the peak-whistling Strouhal number can be stated as follows:

$$Sr_{\text{p-w}} = \left(\frac{f(W_{\text{eff}} + r_{\text{up}})}{U_{\text{c}}}\right)\left(\frac{U_{\text{axs}}}{U}\right)\left(\frac{U_{\text{c}}}{U_{\text{axs}}}\right) \tag{3.17}$$

Here $(W_{\text{eff}} + r_{\text{up}})/U_{\text{c}}$ is the time that it takes a vortex to cross the cavity mouth, which is 1.25 oscillation periods for the 2$^{\text{nd}}$ hydrodynamic mode [Bruggeman et al., 1991]. The second term is the ratio of maximum velocity (U_{axs}) to the average velocity (U) in the duct, which is taken as 1.23 considering the fully developed turbulent profiles ($Re = 5 \times 10^4$) used in the simulations [Schlichting, 1979]. For the last term an empirical formula similar to Eq. 3.16 is employed. The free stream velocity (U_∞) and dimensionless boundary layer thickness (Γ) are replaced by the maximum velocity in the duct ($U_\infty = U_{\text{axs}}$) and the confinement ratio ($\Gamma = (D - D_{\text{r}})/(W + r_{\text{up}})$), respectively. Finally, an empirical formula for the peak-whistling Strouhal number as a function of confinement ratio is obtained for fully turbulent flows as:

$$Sr_{\text{p-w}} = 0.63\left(\frac{D - D_{\text{r}}}{W + r_{\text{up}}}\right)^{-0.2}, \tag{3.18}$$

A power-law fit of the experimental data yields 0.58 instead of 0.63, which is shown in figure 3.19. It is seen that this rather simple empirical formula explains the broad

Figure 3.19: Measured and estimated peak-whistling Strouhal numbers plotted against confinement ratio together with the proposed formula, $Sr_{\mathrm{p-w}} = 0.58\left[(D-D_{\mathrm{r}})/(W_{\mathrm{eff}}+r_{\mathrm{up}})\right]^{-0.2}$
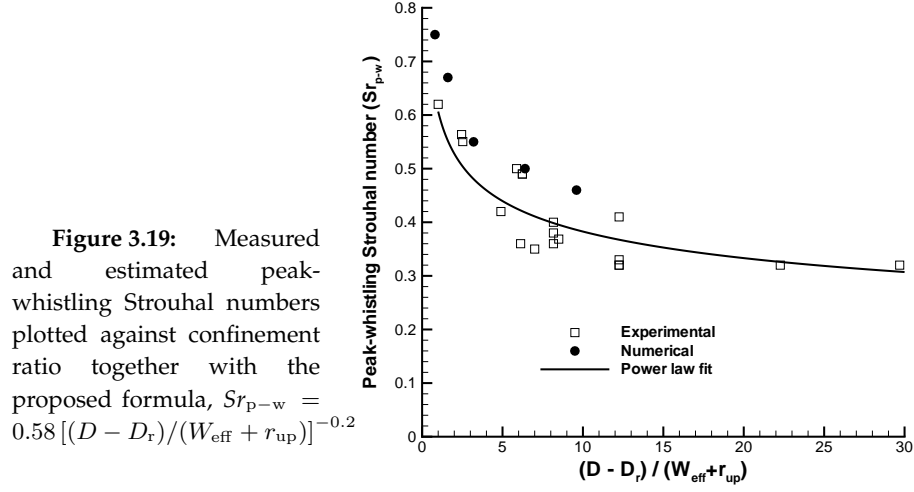
range of peak-whistling Strouhal numbers observed in periodic systems as an effect of changing velocity profile due to changing confinement ratio.

3.4.5 Time averaged acoustic source power in periodic systems

Up to now the attention was given to the peak-whistling Strouhal number. In this section, the time averaged acoustic source power produced in periodic systems is addressed. From figure 3.17, it is seen that the non-dimensional time averaged acoustic source power $\langle P_{\mathrm{source}}\rangle/(\rho_0 U S_{\mathrm{p}}|u'|^2)$ is decreasing almost linearly with increasing confinement ratio $((D-D_{\mathrm{r}})/(W+r_{\mathrm{up}}))$ for the 2nd hydrodynamic mode. Thus, if the non-dimensional averaged acoustic source power is normalized with the confinement ratio as $(D-D_{\mathrm{r}})/(W+r_{\mathrm{up}})\langle P_{\mathrm{source}}\rangle/(\rho_0 U S_{\mathrm{p}}|u'|^2)$, then a universal graph of source power for periodic systems with various confinement ratios can be obtained. In figure 3.20 normalized non-dimensional average acoustic source power is shown as a function of Strouhal number based on the convection velocity ($Sr_{\mathrm{c}} = f(W+r_{\mathrm{up}})/U_{\mathrm{c}}$). Considering the convection velocity U_{c}, instead of the mean flow velocity U in the Strouhal number definition, collapses the peak-whistling Strouhal numbers into a single peak ($Sr_{\mathrm{c}} = 1.4$). From figure 3.20, it is seen that for the 3rd hydrodynamic mode ($Sr_{\mathrm{c}} = 2.5$) as the confinement ratio increases the normalized dimensionless averaged acoustic source power decreases. This decrease could be explained on the basis of the linear theory of Michalke [1965] on the effect of finite momentum thickness (δ_2) on spatial amplification of the shear layer instability. Following the theory above a critical value of $f\delta_2/U = 0.04$ the amplification vanishes [Bruggeman et al., 1991]. It should be noted that the 3rd hydrodynamic mode has not been reported in any experimental study on corrugated pipes. It is therefore
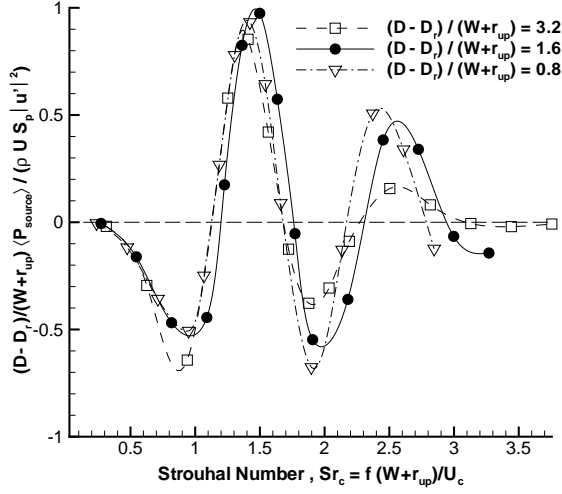
Figure 3.20: Strouhal number based on convective velocity $Sr_c = f(W+r_{up})/U_c$ plotted against normalized dimensionless average acoustic source power $(D - D_r)/(W + r_{up})\langle P_{source}\rangle/(\rho_0 U S_p|u'|^2)$ for confinement ratios, $(D - D_r)/(W + r_{up})$ of 3.2, 1.6 and 0.8.

difficult to verify this result. Another consequence of the theory is that Eq. 3.18 has a limited range of validity. Above a critical ratio of D/W whistling will not occur also for the 2nd hydrodynamic mode.

3.4.6 Estimation of the dimensionless fluctuation amplitude in a periodic system

To estimate the amplitude of a self sustained oscillations, i.e. whistling, in a periodic system an energy balance model is required, where the acoustic sources and the acoustic losses are equalized:

$$\langle P_{source}\rangle = \langle P_{visc}\rangle + \langle P_{conv}\rangle + \langle P_{rad}\rangle \tag{3.19}$$

where $\langle P_{source}\rangle$ is the time averaged acoustic source power. $\langle P_{visc}\rangle$, $\langle P_{conv}\rangle$ and $\langle P_{rad}\rangle$ are the time averaged power losses due to visco-thermal, convective and radiation effects, respectively. In contrary to the acoustic sources which are calculated spatially local as explained in section 3.4, acoustic losses are estimated for the whole system. Here, first the estimation of acoustic losses are considered [Tonon et al., 2010], and then the prediction of dimensionless fluctuation amplitudes are discussed for two periodic systems: namely, a corrugated segment in a smooth pipe and a unit length of a long corrugated pipe.

In order to calculate the acoustic power dissipated by the visco-thermal damping of acoustic waves in a periodic system, a standing wave built up of right p^+ and left p^- traveling waves of equal amplitude is assumed. Then the visco-thermal losses are given by

$$\frac{\langle P_{visc}\rangle}{\rho_0 U S_p|u'|^2} = \frac{1}{2}\frac{c_0{}^2\alpha L}{c_{eff}U} \tag{3.20}$$
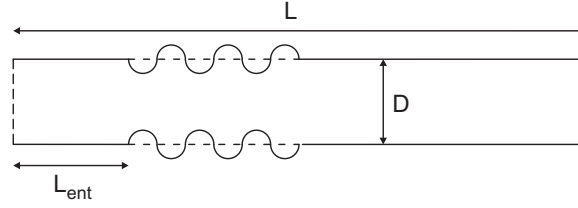
Figure 3.21: A corrugated segment in a smooth pipe as described in Elliott [2004].

where c_0 is the speed of sound, c_{eff} is the effective speed of sound in the pipe, L is the pipe length and α is the acoustic damping coefficient.

To determine the acoustic losses due to convective effects, vortex shedding at the downstream pipe termination is considered. Instead of describing the flow in detail, a quasi-steady free jet formed at the outlet of the pipe is assumed. Using the acoustic energy reflection coefficient of Ingard and Singhal [1975] and assuming the incompressible limit, the acoustic power loss due to vortex shedding at the outlet of the system is determined as follows:

$$\frac{\langle P_{\text{conv}}\rangle}{\rho_0 U S_{\text{p}}|u'|^2} = \frac{1}{2}\frac{c_0}{c_{\text{eff}}} \tag{3.21}$$

It should be noted that this approximation is limited to low frequencies. At high frequencies the approximation proposed by Munt [1977, 1990] should be used [Peters et al., 1993].

Furthermore, compared to the acoustic losses due to visco-thermal dissipation and convective effects, the radiation losses at the pipe terminations are rather small. Thus, they are neglected in the calculations.

A corrugated segment in a smooth pipe

A corrugated segment in a smooth pipe is technologically useful as it allows bending the pipe. When appropriately designed it should not whistle. Elliott [2004] performed tests with a corrugated segment composed of 10 corrugations in a smooth pipe as shown in figure 3.21. The pipe has a length (L) of 1031 mm and an inner diameter (D) of 10.65 mm. The pitch length of corrugations is $Pt = 2.13$ mm. Unfortunately, r_{up} is not explicitly mentioned by Elliott [2004]. Thus, r_{up} is taken as $0.25W$, which is a typical value for this type of corrugated pipes, see figure 3.2-b, which leads to a confinement ratio of $D/(W + r_{\text{up}}) = 5.8$. It is reported that when the corrugated segment is placed at the beginning of the pipe, $L_{\text{ent}} = 0$, the system just whistles at $U = 8.6$ m/s with a frequency of 1488Hz, which corresponds to the 9th axial mode.

Since the corrugated segment is 21.3 mm, which is only 2% of the total pipe length, while calculating $\langle P_{\text{visc}}\rangle$ and $\langle P_{\text{conv}}\rangle$, effective speed of sound c_{eff} is taken

equal to the speed of sound c_0. For the same reason, the theory of Kirchhoff [Pierce, 1989; Peters et al., 1993] for smooth pipes is used to estimate the damping coefficient α, as follows:

$$\alpha = \frac{L_{\text{per}}}{2S_{\text{p}}c_0}\sqrt{\frac{\pi f \mu}{\rho_0}}\left(1 + \frac{c_p/c_v - 1}{\sqrt{Pr}}\right) \tag{3.22}$$

where L_{per} is the perimeter of the pipe, f is the sound wave frequency, μ is the dynamic viscosity, c_p/c_v is the ratio of specific heat capacities and Pr is the Prandtl number. Then, using Eq. 3.20 and Eq. 3.21 the total acoustic loss is determined as $(D/(W + r_{\text{up}}))\langle P_{\text{loss}}\rangle/(\rho_0 U S_{\text{p}}|u'|^2) = 28.4$. Here the interaction between the acoustic boundary layer and the turbulent main flow is neglected. This is justified by the relatively low Reynolds numbers prevailing in the experiments [Peters et al., 1993; Howe, 1998].

To estimate the source power of the system, first the location of the corrugated segment with respect to the standing wave should be appraised. The average acoustic source power of a corrugation presented in figure 3.15 is valid only for cavities that are located in the vicinity of pressure nodes of the standing wave, where the sound production is maximum. Considering the fact that the system whistles at 9th acoustic mode, the wave length of the standing wave pattern is approximately $\lambda = 230$ mm. Thus, compared to the wave length, a segment of 21.3 mm at the beginning of the pipe is small enough to assume that all the corrugations are close to the pressure node.

In figure 3.22, the normalized dimensionless average acoustic source power is presented as a function of perturbation amplitude for a fully developed turbulent velocity profile and a thin boundary layer velocity profile Eq. 3.15. The proposed model predicts whistling with 15 corrugations instead of 10 corrugations as found in the experiments. The acoustic loss per corrugation, $(D/(W + r_{\text{up}}))\langle P_{\text{source}}\rangle/(\rho_0 U S_{\text{p}}|u'|^2) = 1.89$, is indicated with a horizontal line in figure 3.22 (Acoustic Losses - corrugated segment) and the respective predicted amplitude $|u'|/U = 1.1 \times 10^{-2}$ with a vertical line. It should be noted that since the corrugated segment is located at the beginning of the pipe, the velocity profile is not yet developed. Consequently, the source calculated for a thin boundary layer is used to predict the whistling and its amplitude.

Elliott [2004] reported that when the corrugated segment is shifted such that $L_{\text{ent}} > 100$ mm, no oscillations could be produced. This can be explained by the change of the velocity profile upstream from the corrugated segment. When the corrugated segment is shifted such that $L_{\text{ent}} > 10D_p$, instead of a thin boundary layer profile, a developed turbulent velocity profile will enter the corrugated segment. As shown in figure 3.22, the normalized dimensionless average acoustic source power is much smaller for the fully developed turbulent velocity profile than for the thin boundary layer velocity profile. Consequently, the system which is just whistling for $L_{\text{ent}} = 0$, stops whistling when it is shifted to the next pressure node of the standing wave.

Figure 3.22: Maximum perturbation amplitude $|u'|/U$ is plotted against normalized dimensionless average acoustic source power $(D/(W + r_{\mathrm{up}}))\langle P_{\mathrm{source}}\rangle/(\rho_0 U S_{\mathrm{p}}|u'|^2)$ for a fully developed turbulent velocity profile (Turbulent B. L.) and a thin boundary layer velocity profile (Thin B. L.).
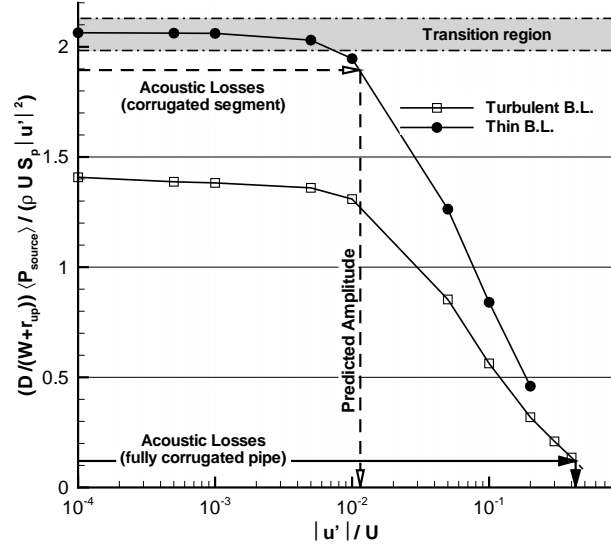
Figure 3.22 also indicates that in the transition region ($10^{-3} < |u'|/U < 10^{-2}$) a small increase in the acoustic losses can suppress the whistling. As a result, it is difficult to predict whistling in this amplitude zone.

A fully corrugated pipe

In this section the whistling amplitude for a long corrugated pipe is estimated for a unit length. A typical corrugated pipe geometry (Com 3 - Table 3.1) with a confinement ratio of $D/(W + r_{\mathrm{up}}) = 5.9$ is used for the calculations. The pitch length of the corrugations is $Pt = 10$ mm meaning that there is 100 corrugations in a unit length segment. For systems with such a high number of cavities, it can be assumed that the cavities are uniformly distributed along the standing wave. Thus, to estimate the average acoustic sound production per a cavity, the maximum acoustic sound production per cavity (see, figure 3.22) should be multiplied by $(2/\pi)$, which is the average of the absolute value of a cosine function. This factor corresponds to the assumption of a moderate amplitude behavior [Bruggeman et al., 1991; Tonon et al., 2010]. This assumption is only reasonable for high oscillation amplitudes $|u'|/U > 0.05$. Since the pipe is long, it can also be assumed that the convective losses are small compared to the viscous losses $\langle P_{\mathrm{conv}}\rangle \ll \langle P_{\mathrm{visc}}\rangle$ so that they can be neglected in Eq. 3.19.

As a first approximation, similar to the calculations in the previous section, the theory of Kirchhoff Eq. 3.22 is used to estimate the damping coefficient, $\alpha = 5.3 \times 10^{-2}$. Following Eq. 3.19 and Eq. 3.20 the normalized dimensionless acoustic loss per corrugation $(D/(W + r_{\mathrm{up}}))\langle P_{\mathrm{source}}\rangle/(\rho_0 U S_{\mathrm{p}}|u'|^2) = 2.8 \times 10^{-2}$ is determined. This leads to a maximum perturbation amplitudes, which are a factor 5 higher than the experimentally observed $|u'|/U = 0.1$.

As a second approach, assuming a quasi-steady flow [Ingard and Singhal, 1975] and linearizing the pressure gradient, the fluctuating pressure drop is stated as follows:

$$\frac{dp'}{dx} = \rho_0 U u' \frac{4c_f}{D} \tag{3.23}$$

where c_f is the experimentally determined resistance coefficient. For the corrugated pipe investigated (Com 3 - Table 3.1) $c_f \approx 0.025$. The damping coefficient for acoustic waves is given by:

$$\alpha = \frac{U_{axs}}{c_{eff}} \frac{4c_f}{D} \tag{3.24}$$

Similarly following Eq. 3.19 and Eq. 3.20, this approach leads to a maximum perturbation amplitude ($|u'|/U$) of 0.4, which is a factor 4 larger than the measured values (see figure 3.22, Acoustic Losses - fully corrugated pipe). However, it should be noticed that although the predicted fluctuation amplitude is rather close to the experimental observations, this approach has a fundamental drawback. While calculating the source power $\langle P_{source} \rangle$, the losses due to flow separation at each cavity are implicitly included in the simulations. By introducing the experimentally measured resistance coefficient (c_f) to calculate the damping coefficient, this non-linear effect is again taken into account in the quasi-steady approximation. Also the model neglects heat transfer losses. Thus, some of the loss terms are over estimated and some are excluded in this prediction. Finally, it should be noted that a quasi-steady approach is only valid at very low frequencies.

3.4.7 Discussion

In this study, a methodology which combines incompressible numerical simulations and the Theory of Vortex Sound is introduced to estimate the acoustic source power in periodic systems. Comparison with the experimental measurements and the earlier studies indicates that the proposed method is promising in many aspects for the physical understanding of the whistling behavior of periodic systems. However, the methodology has certain limitations.

First of all, it is assumed that the cavities are only acoustically coupled. Thus, any hydrodynamic interaction between cavities is neglected. Derks and Hirschberg [2004] showed that hydrodynamic interaction can be important for Helmholtz resonators if the plateau length between successive openings is smaller than the opening width ($L_p \leq W$). Similarly, for corrugated pipes with short plateau lengths, hydrodynamic interaction is expected to play a role.

Secondly, the approach does not include any turbulence modeling. This brings a limit to the cavity depth to cavity width ratio (H/W) that can be studied with this method. For shallow cavities ($H/W \leq 0.5$), where turbulence plays a significant role [Gloerfelt, 2009; Nakiboğlu et al., 2010], the approach is not applicable. How-

ever, most of the corrugated pipes used in industrial applications have deep cavities ($H/W \geq 0.5$).

Another point that can be improved is the inlet boundary condition for incompressible simulations. As demonstrated in sections 3.4.4 and 3.4.6, the velocity profile is essential for both the peak-whistling Strouhal number and the fluctuation amplitude. Instead of using a fully developed turbulent velocity profile for smooth pipes at the inlet boundary, for each corrugated pipe geometry respective fully developed velocity profiles can be estimated using RANS calculations. Preliminary calculations using this approach indicate a shift in predicted peak-whistling Strouhal numbers towards the proposed empirical power-law formula Eq. 3.18. Such an approach, however, will also be limited because whistling at large amplitudes is expected to affect the main flow profile, which cannot be predicted by RANS simulations.

It should be noted that using the theory of Kirchhoff for the estimation of the damping coefficient leads to over predicted fluctuation amplitudes in long corrugated pipes. The quasi-steady approximation is not a satisfactory alternative either. Further research is needed on the estimation of visco-thermal losses of acoustic waves propagating in corrugated pipes.

Our standing wave model is only reasonable when the resonator has a large quality factor. For the investigation of very long corrugated pipes, a traveling wave model could be employed rather than a standing wave model.

3.5   Conclusions

Experiments performed on corrugated pipe segments of various lengths and cavity geometries show that the peak-whistling Strouhal number, based on cavity width plus upstream edge radius as characteristic length, is independent of the pipe length.

The experiments on corrugated pipes revealed a saturation behavior in the amplitude of fluctuation $|u'|/U \approx 0.1$. Although the segment length, where this saturation level is reached, varies depending on the type of corrugated pipe, the saturation amplitude remains about the same.

The broad range of peak-whistling Strouhal numbers in corrugated pipes, $0.3 \leq Sr_{\mathrm{p-w}} \leq 0.6$, that has been reported in the literature, is observed experimentally. There exist a decrease in the peak-whistling Strouhal number with increasing confinement ratio, which is defined as the ratio of pipe diameter to cavity width plus upstream edge radius $D/(W + r_{\mathrm{up}})$.

The proposed numerical methodology predicts Strouhal number ranges of acoustic energy production and absorption, which are in agreement with earlier studies about periodic systems. The non-linear saturation of the shear layer, responsible for the stabilization of the limit cycle oscillation, is also successfully captured with the current approach.

It is explained that the variation observed in the peak-whistling Strouhal number is due to a change in the confinement ratio, results from a different main flow velocity profile. Assuming a fully developed turbulent velocity profile for a smooth channel flow at the inlet, the proposed methodology predicts the decrease of the peak-whistling Strouhal number with increasing confinement ratio. The estimated peak-whistling Strouhal numbers are in a reasonable agreement with the experimentally measured values. An empirical formula for the peak-whistling Strouhal number as a function of confinement ratio is proposed, which relates this effect to earlier observations from literature on cavities [Elder et al., 1982; Golliard, 2002; Kooijman et al., 2008] and deep resonant side branches [Ziada and Shine, 1999].

Combined with an energy balance, the proposed model is used to explain qualitatively the difference observed in acoustic fluctuation amplitudes in periodic systems due to variations of cavity geometry and flow parameters. However, it should be improved before being a quantitative tool for the prediction of the pulsation amplitude.

Aeroacoustics of the swinging corrugated tube: Voice of the Dragon

4.1 Abstract

When one swings a short corrugated pipe segment around his head, it produces a musically interesting whistling sound. As a musical toy it is called *Hummer* and as a musical instrument the *Voice of the Dragon*. The fluid dynamics aspects of the instrument are addressed, corresponding to the sound generation mechanism. Velocity profile measurements reveal that the turbulent velocity profile developed in a corrugated pipe differs notably from the one of a smooth pipe. This velocity profile appears to have a crucial effect both on the non-dimensional whistling frequency (Strouhal number) and on the amplitude of the pressure fluctuations. Using a numerical model based on incompressible flow simulations and Vortex Sound Theory, excellent predictions of the whistling Strouhal numbers are achieved. The model does not provide an accurate prediction of the amplitude. In the second part of the paper the sound radiation from a Hummer is discussed. The acoustic measurements obtained in a semi-anechoic chamber, are compared with a theoretical radiation model. Globally the instrument behaves as a rotating (Leslie) horn. The effects of Doppler shift, wall reflections, bending of the tube, non-constant rotational speed on the observed frequency and amplitude are discussed.
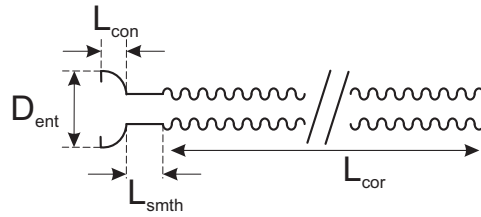
Figure 4.1: A schematic drawing of a Hummer

4.2   Introduction

In thin walled pipes corrugations provide local stiffness while allowing for a global flexibility. This makes corrugated pipes convenient for various industrial applications ranging from vacuum cleaners to offshore natural gas transportation [Belfroid et al., 2007]. Flow through this type of pipes can sustain high amplitude whistling tones, which do not occur in smooth pipes. This whistling is an environmental annoyance and associated vibration can lead to mechanical failure [Ziada and Bühlmann, 1991].

Short corrugated pipe segments are also used as musical toys and instruments. The *Hummer* [Crawford, 1974] is a flexible plastic corrugated pipe of approximately 75 cm length and 3 cm diameter, as shown in figure 4.1. While holding one end by swinging the tube around the head, various tones can be produced. This chorus like sound is musically interesting. The instrument has received the names *Voice of the Dragon* [Silverman and Cushman, 1989; Serafin and Kojs, 2005] and *Lasso d'Amore* [Schickele, 1976].

A more extensive review of the literature on corrugated pipes is given in the earlier papers of the authors [Nakiboğlu et al., 2010, 2011a]. Physical modelling of corrugated pipes by means of simple source models placed along a tube has been proposed by Debut et al. [2008] and Goyder [2010]. A Large eddy simulation has been attempted by Popescu and Johansen [2009], but results seem to be in contradiction with the experimental studies [Nakiboğlu et al., 2010; Tonon et al., 2010; Golliard et al., 2010].

In the present paper the physical modeling of this instrument is discussed. In the next section (Sec. 4.3), an overview of the basic principles is given. The following two sections (Sec. 4.4 and Sec. 4.5) focus on the flow and the associated sound production within the tube. In Sec. 4.6 the radiation of the sound from the open pipe terminations is explained. Sec. 4.7 covers some of the the mystery that is removed and remaining open questions. The last section concludes the study (Sec. 4.8).

4.3 Basic Principles

The whistling of the Hummer is induced by the flow through the pipe driven by its rotation. This can be demonstrated by closing the stationary pipe termination, which is held with the hand. Placing the thumb in the tube or covering the entrance with the palm are convenient ways to do so. This suppresses the whistling. Another way to demonstrate that it is the flow through the corrugated pipe that sustains the whistling, is to blow through the pipe. Our lung capacity is not sufficient to make a typical Hummer whistle. However, one can take a narrower corrugated pipe and make it whistle. A corrugated pipe with a diameter of $D = 1$ cm and a length of $L = 1$ m used as a protection jacket for electrical cables in buildings, whistles nicely at a rather high pitch.

In flows producing sound the fluid velocities are so high that the pressure forces are mainly balanced by the inertia of the fluid. The viscous forces are negligible in the bulk of the flow. They only become important within thin boundary layers close to the wall. The pressure in these boundary layers is imposed by the main flow [Schlichting, 1979]. In the boundary layer due to viscous losses a fluid particle does not have enough kinetic energy to travel against an adverse pressure gradient, as it would do in the bulk of the flow. This results in a back flow along the wall opposite to the main flow direction and ultimately a separation of the boundary layer from the wall at an abrupt pipe widening . This forms a so called shear layer, separating the high speed bulk flow region from the low speed flow region close to the walls. This separation occurs at each corrugation, leaving almost a stagnant fluid in the cavities. These shear layers are quite unstable and the resulting unsteadiness of the flow is a source of sound [Curle, 1955]. Furthermore the flow separation is also very sensitive to acoustical perturbations. These perturbations trigger the roll-up of the shear layer into vortices. This receptivity of the shear layer to acoustic perturbations is essential in the whistling process. It couples the vortex shedding developing at each corrugation with the global standing acoustical wave in the tube. As a consequence, the unsteadiness of the flow within each cavity (corrugation) along the pipe is synchronized with a global acoustic oscillation of the pipe. Actually, it is a feedback system in which the flow instability at each cavity is a power supply and the pipe is a filter, selecting a specific tone corresponding to a standing longitudinal wave (resonance mode). This is a SASER device: *Sound Amplification by Stimulated Emission of Radiation* analogous to a LASER. Such a feedback system can produce a periodic oscillation only if there is a non-linear saturation mechanism, which limits the amplitude [Fletcher and Rossing, 1991].

4.4 Fluid Dynamics

4.4.1 Frictionless model

The average flow velocity U through the swinging pipe can be estimated by assuming a steady frictionless flow. As the velocities are low compared to the speed of sound, the pressure difference across the pipe is very small compared to the atmospheric pressure. One can therefore neglect the density variation in the steady component of the flow. The fact that the air is almost incompressible implies that, in a steady flow, the volume flux Q along the tube must be independent of the position x along the tube, measured from the fixed open end. If we neglect changes in the shape of the velocity profile $U(r)$, with r is the distance from the pipe axis, the flow velocity remains constant along the pipe. This velocity is defined by $U = 4Q/\left(\pi D^2\right)$. Because of the swinging motion, the tube is rotating with an angular velocity Ω. A fluid particle, corresponding to a slice of the tube of length dx, will undergo a centrifugal force $\rho_0 \left(\pi\, dx\, D^2/4\right)\Omega^2 x$, where $\rho_0 = 1.2$ kg/m^3 is the air density. As the fluid velocity is constant, this force should be balanced by the pressure forces $-\left[p\left(x+dx\right) - p\left(x\right)\right]\pi D^2/4 = -dp\left(\pi D^2/4\right)$. This yields the differential equation for the pressure p:

$$dp = \rho_0 \Omega^2 x dx. \tag{4.1}$$

Integration between the stationary tube inlet $x = 0$ and the moving tube outlet $x = L$ yields:

$$p\left(L\right) - p\left(0\right) = \frac{1}{2}\rho_0\Omega^2 L^2. \tag{4.2}$$

Note that this equation has the opposite sign from the equation used by Silverman and Cushman [1989] and Serafin and Kojs [2005]. This is due to the fact that Silverman and Cushman [1989] ignored the impact of the centrifugal force on their measurement of the pressure difference and made the erroneous assumption that the inlet pressure $p\left(0\right)$ should be equal to atmospheric pressure p_{atm}. In fact, as a result of flow separation, a free jet is formed at the swinging outlet of the pipe. Like in the plume flowing out of a chimney, the pressure $p\left(L\right)$ in this free jet is equal to the surrounding atmospheric pressure p_{atm} [Shapiro, 1953]. The low pressure at the inlet,

$$p\left(0\right) = p_{\mathrm{atm}} - \frac{1}{2}\rho_0\Omega^2 L^2, \tag{4.3}$$

is actually sucking the surrounding air into the pipe. This explains the observation of Silverman and Cushman [1989] that small bits of tissue paper placed in the palm will be sucked up into the tube and discharged from the rotating end. Assuming a steady incompressible frictionless flow around the inlet, one finds from the conservation of mechanical energy (Bernoulli):

$$p_{\mathrm{atm}} = p\left(0\right) + \frac{1}{2}\rho_0 U^2, \tag{4.4}$$

which combined with Eq. 4.3 yields the very simple result:

$$U = \Omega L. \tag{4.5}$$

In this simple model the friction is neglected (except for flow separation at the outlet), which leads to a uniform velocity profile in the pipe. In reality, however, as a result of friction the velocity in the pipe will be lower near the walls than in the middle, so that a non-uniform velocity profile will develop. The shape of the velocity profile is expected to be important in corrugated pipes both for the frequency and the amplitude of the whistling [Nakiboğlu et al., 2011a]. In the Sec. 4.4.3, the velocity profile in a Hummer is addressed.

4.4.2 Experimental setup

The velocity profile in a Hummer was determined by means of hotwire measurements. Figure 4.2 shows the experimental setup. An aluminum pipe with a diameter of 33 mm and a length of 60 mm was inserted to the conical section at the inlet of the Hummer (Fig. 4.1). Using a clamp for standard vacuum appliances (ISO-KF), the aluminum pipe was attached to the settling chamber of the wind tunnel in an airtight manner. The settling chamber is a wooden box of 0.5 m×0.5 m×1.8 m. The flow is driven by a centrifugal ventilator. A 8 cm thick layer of acoustic foam on the inner walls of the settling chamber prevents acoustical resonances of the box. The Hummer lays on a horizontal table and passed through two rigid metal pipe segments with a diameter of 33 mm and length of 100 mm. Using these rigid pipe segments the Hummer was fixed on the table without pressing on the elastic plastic walls. Also by changing the position of the second rigid pipe, the Hummer could be bend in the horizontal plane. The effect of the bending is addressed in Sec. 4.7.2, all the other results that are presented were obtained with a straight Hummer. The average velocity (U) was calculated from the pressure difference across the inlet contraction using the equation of Bernoulli (Eq. 4.4). The pressure difference is measured by means of a Betz micromanometer. The velocity profile at the end of the Hummer was measured with a hotwire probe (Dantec probe type 55P11). The hotwire anemometer used in this study was a Dantec 90C10 CTA module installed within a Dantec 90N10 frame. The signal was amplified and low-pass filtered through a low-noise pre-amplifier (Stanford Research Systems, Model SR560) and sent to the computer via a National Instrument BNC-2090 data acquisition board with a 12-bit resolution at a sampling rate of 10 kHz. A sampling duration of 10 second was used for each position. All the data were obtained using the Dantec StreamWare software. The hotwire signals were compensated for variations in the flow temperature.

Experiments were performed on a Hummer manufactured by Jono Toys b.v. Holland. The Hummer has a corrugated length of $L_{\text{cor}} = 700$ mm, a smooth length of $L_{\text{con}} = 30$ mm, a conical section length of $L_{\text{cor}} = 10$ mm and an entrance diameter $D_{\text{ent}} = 33$ mm, as shown in figure 4.1. The remaining geometric parameters are
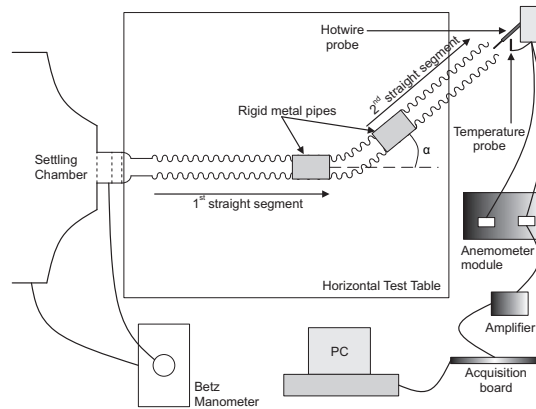
Figure 4.2: Experimental setup
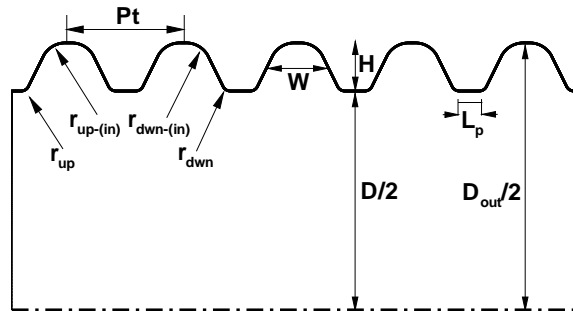
Figure 4.3: Cross-section of a segment of Hummer with geometric parameters.

shown in figure 4.3, where only a few corrugations are sketched. The wave length of a corrugation is (pitch) $Pt = 7$ mm. The depth of the cavity is $H = 2.7$ mm. Since the cavity width is changing continuously with the cavity depth, width is determined at the mid-depth of the cavity [Elliott, 2004] as $W = 5$ mm. The radius of the curvature for the edges inside the cavity is $r_{\mathrm{up-(in)}} = r_{\mathrm{dwn-(in)}} = 1$ mm. The radius of the curvature for the edges at the cavity mouth is $r_{\mathrm{up}} = r_{\mathrm{dwn}} = 0.5$ mm. The inner diameter is $D = 26.5$ mm. The plateau, which is the length of the constant inner diameter part between two cavities, is $L_{\mathrm{p}} = 1$ mm.

4.4.3　Results

Average velocity profile and turbulence intensity

All the velocity profiles that are presented were measured along an axis normal to the axis of hummer at a distance of 1 mm downstream from the pipe termination. Some
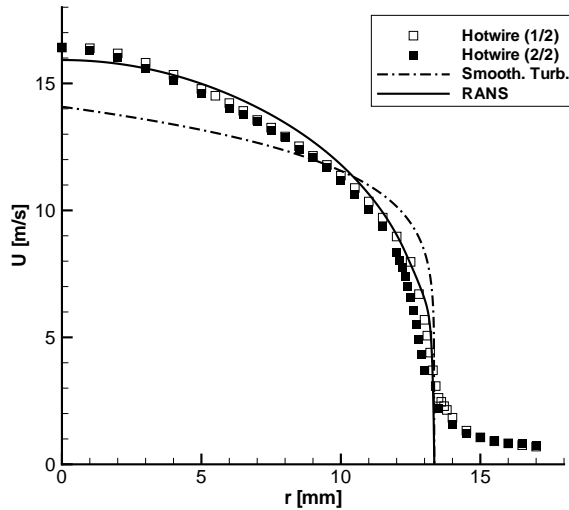
Figure 4.4: Measured velocity profiles $U(r)$ for a Hummer: Hotwire(1/2), Hotwire(2/2) are the 1st & 2nd half of the profile, respectively. Smooth. Turb. indicates a fully turbulent pipe profile for a smooth pipe. RANS indicates a profile that is obtained by RANS simulation of a Hummer.

measurements were also taken inside the corrugated pipe, the results are identical with the presented data. It is convenient to measure the profile outside the pipe, because when the probe is in the pipe it is difficult to make measurements close to the wall.

In figure 4.4 a measured velocity profile for a straight Hummer is presented together with a turbulent velocity profile for a smooth pipe and a profile that is obtained by Reynolds-averaged Navier Stokes (RANS) simulation of the Hummer. The velocity profile that is developed in the Hummer is rather different than the one of a smooth pipe. It is also seen that the RANS simulations can provide a reasonable estimation of the velocity profile. The RANS simulations were performed with the commercial finite volume code Fluent 6.3. The computational domain had the same geometry as the Hummer but composed of only 5 cavities, as shown in figure 4.3. A cylindrical symmetric 2D domain was used to mimic a circumferential cavity. The computational domain contained approximately 180000 cells, which were clustered close to the cavity mouth where there are high gradients of velocity due to the shear layer. The pressure-based segregated solution algorithm SIMPLE [Patankar and Spalding, 1972] was employed. A second-order upwind space discretization was used for convective terms. A $k - \epsilon$ turbulence model was used together with standard wall functions as near wall-treatment. The iterations were terminated when all residuals had dropped at least 8 orders of magnitude. In the first simulation a fully developed turbulent velocity profile for a smooth pipe was used as an inlet boundary condition. Then the converged velocity profile at the outlet was extracted and used as the inlet velocity profile for the next simulation. This procedure was repeated until a fully developed velocity profile was obtained, namely 11 times, such

that the imposed inlet velocity profile remained unaltered till the outlet. Thus, it took 50 corrugations for the flow to fully develop.

In figure 4.5, the measured turbulence intensity ($TI = u'_\text{h}/U \times 100$) profile for a straight Hummer is presented. This rather high turbulence level hides the acoustic perturbations u' under the broadband hydrodynamic perturbations (u'_h) in a signal in the time domain.

The dimensionless fluctuation/perturbation amplitude, $|p'|/(\rho_0 c_0 U) = |u'|/U$, is defined as the amplitude of the standing pressure wave at a pressure anti-node inside the main pipe $|p'|$, divided by the air density ρ_0, the speed of sound c_0 and the average flow velocity U; which is equal to the amplitude of acoustic velocity at a pressure node inside the main pipe $|u'|$ divided by the average flow velocity U. In figure 4.6 a power spectrum obtained from a typical hotwire measurement is presented. In the Fourier domain the whistling frequency can easily be identified among the broadband hydrodynamic perturbations by the distinct peak in the spectrum. The corresponding perturbation amplitude ($|u'|/U$) is determined as follows:

$$\frac{|u'|}{U} = \frac{\sqrt{\int P(f)\,df}}{U},\tag{4.6}$$

where $P(f)$ is the power density.
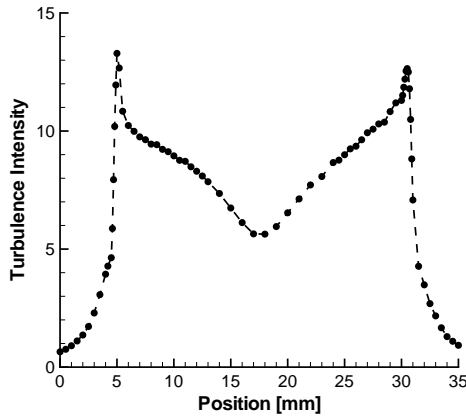
Figure 4.5: Measured turbulence intensity profiles ($TI = u'_\text{h}/U \times 100$) for a Hummer.
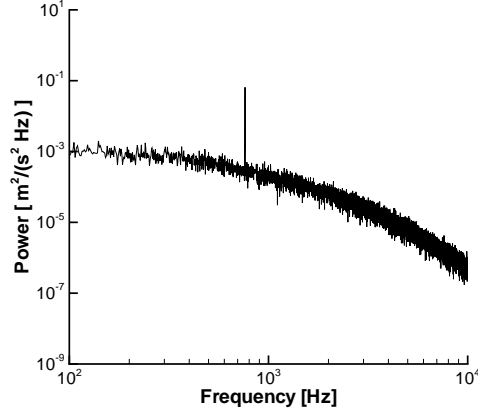
Figure 4.6: A typical power spectrum $P(f)$ of a hotwire measurement for a whistling Hummer.

Friction factor

The frictional pressure loss along a pipe of length (L) is defined by:

$$p(0) - p(L) = 4c_\text{f}\frac{1}{2}\rho_0 U^2 \frac{L}{D},\tag{4.7}$$

where c_f is the friction factor [Blevins, 1984]. Measuring the settling chamber pressure (p_0) as a function of average flow velocity U, the friction factor is determined as $c_f = 1.78 \times 10^{-2}$ independent of the Reynolds number for $8 \times 10^8 \leq Re \leq 4 \times 10^4$ ($Re = UD/\nu$ with $\nu = 1.5 \times 10^{-5}$). The pressure at the pipe inlet, $p(0)$, is calculated from the settling chamber pressure p_0 as follows $p(0) = p_0 + 1/2\rho_0 U^2$.

Knowing the friction factor c_f, a better estimation of the average flow velocity (U) can be proposed than the frictionless model as:

$$U = \frac{\Omega R}{\sqrt{1 + 4c_f \frac{L}{D}}},\tag{4.8}$$

where R is the rotation radius. As it is explained in Sec. 4.6.1, $R \leq L$.

Effective speed of sound

The acoustic field in a Hummer, in a first order approximation, can be described in terms of plane waves propagating along the pipe axis. Sound propagates along the Hummer at an effective speed of sound (c_{eff}) [Elliott, 2004], which is lower than the speed of sound in the air c_0. As a first order approximation, the Hummer can be described as a tube of uniform cross section with a diameter of D. The inertia is determined considering the mass in this tube. The air in the cavities has a limited contribution to the inertia [Nederveen, 1998], however, they behave like an extra volume of air, which has the effect of lowering the frequency of each resonance. Thus, the acoustic compliance is determined by the total volume of the Hummer. Then, for the propagation of low frequency acoustic waves along the tube, $f Pt/c_0 \ll 1$, the effective speed of sound is estimated as follows:

$$c_{\text{eff}} = c_0 \sqrt{\frac{V_{\text{in}}}{V_{\text{tot}}}},\tag{4.9}$$

where $V_{\text{in}} = \pi D^2/4L$ is the inner volume of the Hummer and V_{tot} is the total volume of the Hummer. To determine the total volume of the Hummer, a section composed of 20 pitches (140 mm) was cut and one of the termination was closed by gluing it to a plastic plate. Using a syringe, starting from the bottom the tube was slowly filled to avoid air bubble formation. Then the difference in the weight of the empty corrugated segment and the corrugated segment filled with water was measured by means of a balance with an accuracy of 0.01g. The ratio of inner volume to total volume is found as $V_{\text{in}}/V_{\text{tot}} = 0.83$, which leads to an effective speed of sound $c_{\text{eff}} = 310$ m/s at room temperature ($c_0 = 340$ m/s).

Whistling frequencies and Strouhal number

In corrugated pipes the whistling frequency does not vary continuously with a monotonically increasing flow rate, but rather in distinct steps, corresponding to open-

open resonant acoustic longitudinal modes of the pipe:

$$f_\text{n} = \frac{n\, c_\text{eff}}{2\, L_\text{eff}}, \quad n = 1, 2, 3... \;, \tag{4.10}$$

where L_eff is the effective length of the pipe. Considering the experimental setup presented in figure 4.2, L_eff corresponds to the combined length of the following elements: corrugated segment of the Hummer, the smooth segment of the Hummer, the connection piece to the wind tunnel and the end corrections [Bruggeman, 1987b; Nederveen, 1998]. Knowing the effective speed of sound and the whistling frequency of a given mode from an experiment, using Eq. 4.10 L_eff is determined as 822 mm.

In figure 4.7 whistling frequencies, obtained from spectra as demonstrated in figure 4.6, in terms of Helmholtz number ($He = f L_\text{eff}/c_\text{eff}$), are given as a function of Mach number ($Ma = U/c_0$) for the Hummer. Integer and half integer values of Helmholtz number correspond to the even and odd longitudinal resonant modes, respectively. There is a global linear relationship between Helmholtz number and Mach number, which indicates a constant Strouhal number:

$$Sr = f\, L_\text{c}/U, \tag{4.11}$$

where L_c is the characteristic length. Experiments have shown that the sum of the cavity width and the upstream edge radius ($L_\text{c} = W + r_\text{up}$) is the most suitable characteristic length for Strouhal number [Belfroid et al., 2007; Nakiboğlu et al., 2010]. The Strouhal number is determined as $Sr = 0.44$ for the Hummer. Furthermore, it is seen that above a critical Mach number, $Ma = 0.085$, a mode with a different Strouhal number is excited. The first mode above the critical Mach number corresponds to the first transversal pipe mode, $He = f L_\text{eff}/c_\text{eff} = 7$, based on the outer diameter D_out. This study is limited to the velocities below this critical Mach number.

The coupling of the flow instability at each cavity to the longitudinal standing wave can be described as a feedback loop which leads to a self-sustained oscillation. In self-sustained oscillations the flow perturbations should undergo a total phase shift, when traveling along the feedback loop, matching an integer number of 2π. The total phase shift is mainly composed of a phase shift due to the convection of vortices from the upstream edge toward the downstream edge and due to the acoustical response of the pipe. The convection time of the vortices over the cavity mouth is $(W + r_\text{up})/U_\text{c}$, where the convection velocity is about half the main flow velocity $U_\text{c} = U/2$. Around a pipe resonance there is a rapid change in the phase of the acoustical response with a maximum of π (change of sign). When the flow velocity in the pipe is increased the convection time of the vortices decreases so that the system increases the oscillation frequency f to match the phase oscillation condition [Fletcher and Rossing, 1991]. The slope df/dU is inversely proportional to the quality factor of the resonator. If the quality factor of the resonator is large a small change in frequency is sufficient to provide a large acoustical contribution to the compensation of
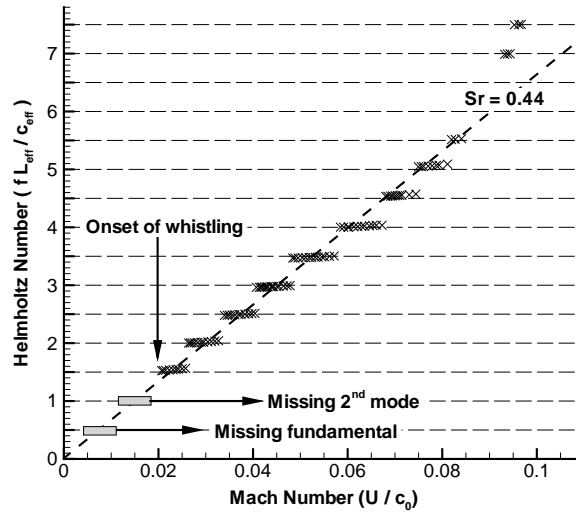
Figure 4.7: Helmholtz number ($He = fL_{\text{eff}}/c_{\text{eff}}$) plotted against Mach number ($Ma = U/c_0$).

the convective phase shift. A closer look at the figure 4.7 reveals this feature. There is a slight, but discernible, increase in the whistling frequency within each resonant pipe mode (f_{n}). Since the increase in the velocity is large compared to the corresponding increase in the frequency within the same acoustic resonant mode there is a range of Strouhal numbers, where the whistling is observed rather than a fixed Strouhal number [Sarohia, 1977; Ziada et al., 2003; Nakiboğlu et al., 2010]. However, the response of the resonator has a maximum at the passive resonance frequency f_{p} and therefore a maximum of the whistling amplitude at $f = f_{\text{p}}$. At this point the convection time of the vortices is close to a multiple of an oscillation period T_{p} plus a quarter $(m + 1/4)T_{\text{p}} = (m + 1/4)/f$ ($m = 1, 2, 3...$) [Bruggeman et al., 1991]. This is further discussed in Section 4.4.3.

In figure 4.8 normalized Helmholtz number ($He = 2fL_{\text{eff}}/(nc_{\text{eff}})$) is plotted against Strouhal number (Sr) for acoustic modes of 3rd-11th. It is seen that using the effective speed of sound (c_{eff}) definition of Elliott [2004], the whistling frequencies (f_{n}) in a corrugated pipe can be predicted within 4%.

Onset of the Whistling

The onset of the whistling in corrugated pipes has been observed at different longitudinal modes in the literature. In most of the studies the onset of whistling has been detected at the 2nd acoustic longitudinal mode [Crawford, 1974; Silverman and Cushman, 1989; Nakamura and Fukamachi, 1991]. Kristiansen and Wiik [2007] have
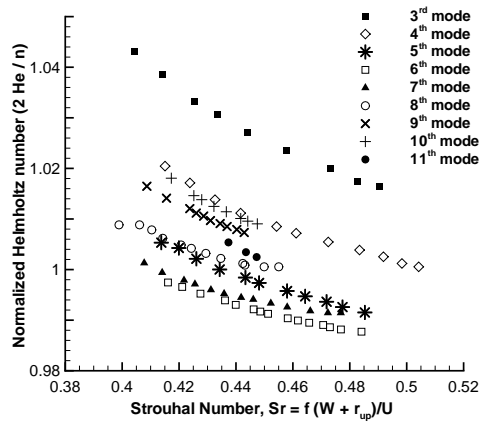
Figure 4.8: Normalized Helmholtz number ($He = 2fL_{\mathrm{eff}}/(nc_{\mathrm{eff}})$) plotted against Strouhal number (Sr) for acoustic modes of 3rd-11th.
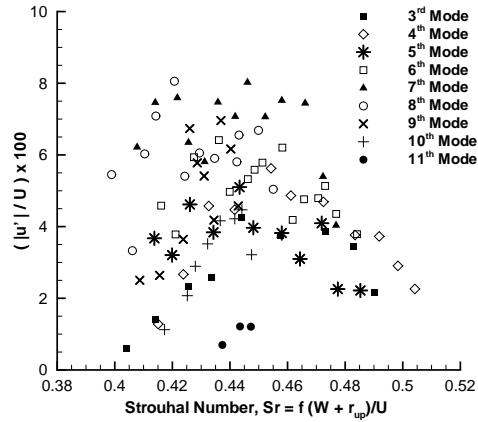
Figure 4.9: Perturbation amplitude ($|u'|/U$) plotted against Strouhal number (Sr) for acoustic modes of 3rd-11th.

recorded an excited fundamental mode. Elliott [2004] obtained the whistling first for the 9th mode. In the current study, the 3rd mode ($He = 1.5$) is recorded as the first whistling mode. It is suggested in the literature that turbulence triggers the whistling [Crawford, 1974; Cadwell, 1994; Angus and Lyon, 2008]. The absence of whistling at the fundamental mode is explained by the lack of turbulence.

At high flow rates the velocity field inside the pipe can display a complex unsteady chaotic motion called turbulence. The transition from a laminar (smooth-stationary) velocity field toward a turbulent (chaotic) flow is determined by the ratio of inertial to viscous forces. A measure for this is the Reynolds number. For a smooth pipe below $Re = 2300$ turbulence cannot be maintained. Depending on the inflow conditions, a laminar flow can, however, be maintained in a smooth pipe up to very high values of Re [Blevins, 1984]. In the case of rough walls (such as for a corrugated pipe) turbulence is commonly observed for $Re \geq 4000$ [Blevins, 1984]. Transition can occur for $Re \geq 2300$.

In figure 4.7 the expected Mach number ranges are indicated for the fundamental and the 2nd mode, if they had been observed. The fundamental and 2nd mode, would start whistling at $Ma = 0.004$ ($Re \approx 2400$) and $Ma = 0.012$ ($Re \approx 7200$), respectively. The 2nd mode corresponds to a fully turbulent flow, however it still does not sound. This experiment indicates that the absence of turbulence is not likely to be the essential factor determining whether a mode does not whistle. As it is explained later in Sec. 4.5.2 - Sec. 4.5.4, turbulence has an effect on the whistling through its effect on the average velocity profile.

Peak-whistling Strouhal number and whistling amplitude

In figure 4.9 the perturbation amplitude $|u'|/U$ is plotted against the Strouhal number for all the whistling modes ($3^{rd} - 11^{th}$). It is seen that all the modes appear in a narrow Strouhal number range between $0.4 \leq Sr \leq 0.5$. The highest Strouhal number for a resonant mode indicates the onset of oscillations for that particular acoustic mode. It is called the critical Strouhal number [Ziada and Shine, 1999] (Sr_{cr}). It is also seen from figure 4.9 that within the same resonant mode after the onset of resonance, increasing the flow velocity increases the amplitude of pressure oscillations until reaches a peak value. Further increase of the flow velocity decreases the amplitude of pressure fluctuations. The Strouhal number, which corresponds to the maximum pressure fluctuation amplitude for a given acoustical mode, is called the peak-whistling Strouhal number (Sr_{p-w}) [Tonon et al., 2010; Nakiboğlu et al., 2011a]. The peak-whistling Strouhal number of a corrugated pipe is determined through a linear least square fit of consecutive excited acoustic modes [Nakiboğlu et al., 2010]. The peak-whistling Strouhal number of the Hummer is determined to be $Sr_{p-w} = 0.44$, which is actually presented as the Strouhal number $Sr = 0.44$ in figure 4.7.

Experiments performed on commercial corrugated pipes of various lengths have shown that there exist a saturation in dimensionless fluctuation amplitude around $|u'|/U \approx 0.1$ when the pipe length (L) reaches L/D of 100. Further increase of the pipe length does not change the amplitude of fluctuations [Nakiboğlu et al., 2011a]. The Hummer produces a perturbation amplitude of $|u'|/U \leq 0.08$, which is lower than the observed saturation value. However, considering the length of a Hummer $L/D = 28$, it is reasonable that the observed perturbation amplitude is weaker.

4.5   Numerical Methodology

In the previous study [Nakiboğlu et al., 2011a] of the authors, a numerical methodology was proposed to investigate the aeroacoustic response of low Mach number confined flows to acoustic excitations. That study applied to corrugated pipes revealed the crucial importance of the velocity profile in the estimation of both the peak-whistling Strouhal number and the fluctuation amplitude. Experiments and RANS simulations carried out in the current study (Fig. 4.4), to provide a better prediction of the flow profile in corrugated pipes. Thus, the proposed numerical methodology is revisited with more realistic flow profiles. In the first part of this section the methodology is briefly summarized and in the second part the improvements in the estimations are presented.

4.5.1   An Overview of the methodology

The hydrodynamic instability, which is the driving force of the acoustic oscillations, is assumed to be a local phenomenon at each cavity [Nakiboğlu et al., 2010; Tonon

et al., 2010]. This implies that sound production is a local effect, which can be studied for a single cavity. Thus, one can try to describe the phenomenon by carrying out a numerical simulation of the flow within a single cavity instead of modeling the whole corrugated pipe. In this approach the possible hydrodynamic interactions between cavities are neglected and the oscillations are coupled through the longitudinal acoustical standing wave. Furthermore, knowing that pitch *Pt* is much smaller than the acoustic wavelength $c_{\text{eff}}/f_{\text{n}}$ of the produced sound wave, one can assume that wave propagation time is locally negligible. This corresponds to the assumption that the flow is locally incompressible [Martínez-Lera et al., 2009].

Following these ideas, incompressible 2D axisymmetric simulations were performed for a single cavity. The inlet of the computational domain is located at $0.5W$ upstream of the cavity; such a short inlet pipe section is chosen to make sure that the imposed inlet velocity profiles do not evolve significantly before reaching the cavity. The outlet is placed at a reasonably far location, $9W$ downstream, from the cavity. The computational domain contains approximately 70 000 quadrilateral cells which are clustered close to the opening of the cavity and to the walls, where there are high gradients of velocity due to shear layer and boundary layer, respectively. A study on mesh dependence has been carried out. The same computation was performed with 2 times and 4 times more densely meshed domains, producing differences in the calculated acoustic source power of less than 5%.

The simulations were carried out at low Reynolds numbers ($Re \approx 4000$) without turbulence modeling. The oscillating pressure differences $\Delta p'$ induced along the pipe by the cavity oscillation are extracted from these simulations. At the inlet a uniform acoustic oscillating velocity in the axial direction u' is imposed in addition to the time averaged inlet velocity profile $U(r)$. As the viscous effects are not accurately described, the simulations are corrected by subtracting the pressure differences $\Delta p'_{\text{visc}}$ obtained from simulations of the flow in a uniform pipe segment with the same boundary conditions as the cavity simulation. This correction can be interpreted as an extrapolation method for high Reynolds number flows, where the solution becomes Reynolds number independent [Nakiboğlu et al., 2011a]. The acoustic power produced by the source is calculated as follows:

$$\langle P_{\text{source}} \rangle = S_{\text{p}}\, u'\,\left(\Delta p' - \Delta p'_{\text{visc}}\right), \tag{4.12}$$

where S_{p} is the cross-sectional area. Finally, by taking the time average $\langle . \rangle$ of the calculated acoustic energy $\langle P_{\text{source}} \rangle$ over a sufficient number of oscillation periods, the spurious contribution due to the inertia is eliminated [Nakiboğlu et al., 2011a].

4.5.2   Effect of flow profile

In the study of Martínez-Lera et al. [2009] on T-joints in pipe systems, a top hat velocity profile with a thin boundary layer was used as an inlet boundary condition. Later Nakiboğlu et al. [2011a] showed that a fully turbulent velocity profile
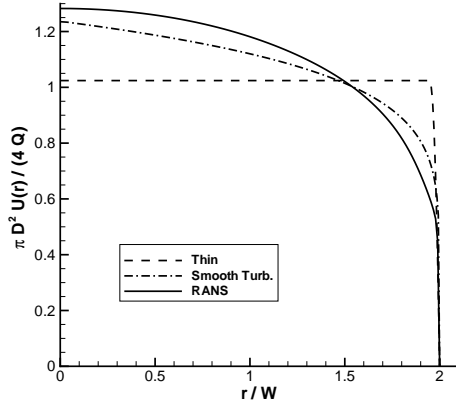
Figure 4.10: Velocity profiles that are used as inlet boundary conditions. Thin indicates the thin turbulent pipe profile used by Martínez-Lera et al. [2009] Smooth Turb. indicates a fully turbulent pipe profile for a smooth pipe. RANS indicates a profile that is obtained by RANS simulation of a generic corrugated pipe.
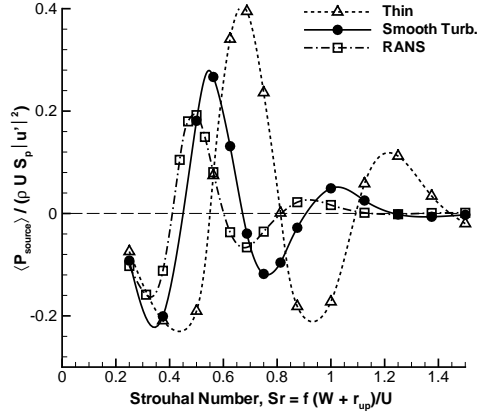
Figure 4.11: Strouhal number plotted against dimensionless average acoustic source power $\langle P_{\text{source}}\rangle/(\rho_0 U S_{\text{p}}|u'|^2)$ for a corrugated pipe with $D/(W + r_{\text{up}}) = 3.2$ and for a perturbation amplitude of $|u'|/U = 0.05$ for the 3 velocity profiles given in figure 4.10.

of a smooth pipe is a better approximation for corrugated pipes. Experiments discussed in Sec. 4.4.3 demonstrate that the turbulent velocity profile developed in a Hummer is noticeably different than that of smooth pipe (Fig. 4.4). Therefore, a series of RANS simulations was performed with a generic corrugated pipe geometry [Nakiboğlu et al., 2011a] to obtain a more realistic velocity profile to employ as an inlet boundary condition. The parameters for the RANS simulations are same as the ones used for the Hummer simulation. The geometric parameters of the generic corrugated pipe is as follows: $Pt = 2.25W$, $H = W$, $D = 4W$, $r_{\text{up}} = 0.25W$, $r_{\text{dwn}} = r_{\text{up-(in)}} = r_{\text{dwn-(in)}} = 0$. These three velocity profiles, namely top hat pipe profile used by Martínez-Lera et al. [2009], fully turbulent pipe profile for a smooth pipe and profile that is obtained by RANS simulation of a generic corrugated pipe are compared in figure 4.10.

For a confinement ratio of $D/(W + r_{\text{up}}) = 3.2$, in figure 4.11 estimated dimensionless average acoustic source power $\langle P_{\text{source}}\rangle/(\rho_0 U S_{\text{p}}|u'|^2)$ is presented as a function of Strouhal number for these velocity profiles. A negative $\langle P_{\text{source}}\rangle$ indicates that in that range of Strouhal numbers (Sr) the cavities act as acoustic sinks, which suppress the whistling. A positive $\langle P_{\text{source}}\rangle$ indicates that the cavities act as acoustic sources, which is a necessary condition for whistling. Here two ranges of Strouhal numbers (Sr) are observed for which $\langle P_{\text{source}}\rangle$ is positive. The lower ($0.4 < Sr < 0.8$) and the

higher ($0.8 < Sr < 1.4$) Strouhal number ranges with positive average acoustic source power correspond to the second and the third hydrodynamic modes, respectively. In the second hydrodynamic mode there exist two vortices in the cavity mouth and the traveling time of the vortex across the opening is 1.25 oscillation period. Whereas for the third hydrodynamic mode three vortices are present at the same moment in the cavity mouth and a vortex takes 2.25 oscillation period to travel across the cavity [Bruggeman et al., 1991]. Experimentally observed Strouhal numbers (Fig. 4.9) correspond to the second hydrodynamic mode. It is clear that the peak-whistling Strouhal number, where the highest acoustic source power is registered, depends strongly on the velocity profile. With increasing boundary layer thickness, the peak-whistling Strouhal number shifts to lower Strouhal numbers.

4.5.3   Estimation of peak-whistling Strouhal number

Considering the experimental data on corrugated pipes [Binnie, 1961; Elliott, 2004; Nakiboğlu et al., 2010], a correlation between confinement ratio $D/(W + r_{\mathrm{up}})$ and the measured peak-whistling Strouhal number $Sr_{\mathrm{p-w}}$ has been proposed [Nakiboğlu et al., 2011a]:

$$Sr_{\mathrm{p-w}} = 0.58 \left(\frac{D}{W + r_{\mathrm{up}}} \right)^{-0.2}. \tag{4.13}$$

In figure 4.12 the proposed empiric formula (Eq. 4.13) is presented. The peak-whistling Strouhal number obtained with the Hummer (Fig. 4.9) also follows this trend.

In the earlier study by the authors [Nakiboğlu et al., 2011a], using the numerical methodology summarized in Sec. 4.5.1 with a fully turbulent velocity profile of a smooth pipe (Fig. 4.10 - Smooth Turb.), the peak-whistling Strouhal numbers were over-estimated by 10% as shown in figure 4.12. As demonstrated in Sec. 4.4.3, by performing RANS simulation of a corrugated geometry, a better estimation of the measured velocity profile can be obtained compared to a profile of a fully turbulent smooth pipe. Using the average velocity profile obtained from the RANS simulation of a generic corrugated pipe (Fig. 4.10- RANS), the same simulations have been repeated in this study. The predicted peak-whistling Strouhal number as a function of confinement ratio $D/(W + r_{\mathrm{up}})$ is also shown in figure. 4.12. The numerical model predicts the peak-whistling Strouhal number within an accuracy of 2%. It is evident that by using a more realistic flow profile, the numerical methodology produce much better estimations of the peak-whistling Strouhal number. This excellent agreement between the experiments and the numerical model confirms the significance of the effect of mean flow profile on the whistling behavior.
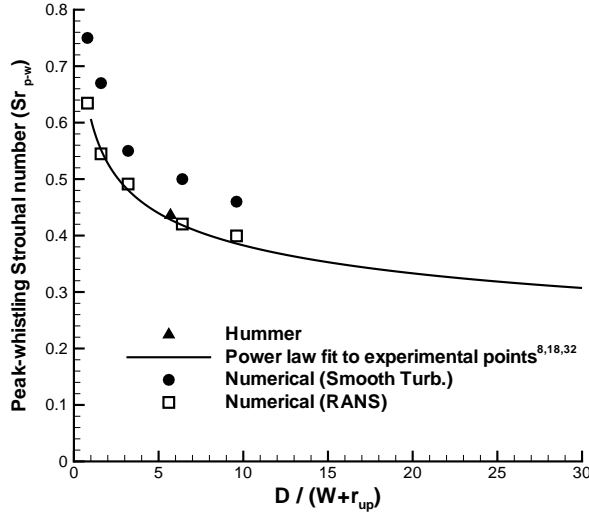
Figure 4.12: Measured and estimated peak-whistling Strouhal numbers plotted against confinement ratio, $D/(W + r_{up})$. Power law fit (Eq. 4.13) [Nakiboğlu et al., 2011a] to the 18 experimental points obtained from three earlier studies [Binnie, 1961; Elliott, 2004; Nakiboğlu et al., 2010]. Data point of the Hummer. Numerical estimation by using two different velocity profiles given in figure 4.10: Numerical (Smooth Turb.) [Nakiboğlu et al., 2011a] and Numerical (RANS).

4.5.4 Estimation of whistling amplitude in a long corrugated pipe

In figure 4.13 estimated normalized dimensionless average acoustic source power $(D/(W+r_{up}))\langle P_{source}\rangle/(\rho_0 U S_p |u'|^2))$ for a single corrugation is given as a function of perturbation amplitude $|u'|/U$ for the three different average velocity profiles given in figure 4.10 for a single cavity. The simulations were performed at respective peak-whistling Strouhal number of each profile, namely: $Sr_{p-w} = 0.65$ for Thin, $Sr_{p-w} = 0.55$ for Smooth Turb. and $Sr_{p-w} = 0.50$ for RANS.

It is seen that for all the profiles $|u'|/U \approx 5 \times 10^{-3}$ is the saturation point of the shear layer. For perturbations smaller than this the shear layer behaves linearly. Therefore, acoustic source power grows quadratically with $|u'|/U$, making the dimensionless average acoustic source power $\langle P_{source}\rangle/(\rho_0 U S_p |u'|^2)$ constant. Above the saturation point, nonlinearities become dominant and $\langle P_{source}\rangle/(\rho_0 U S_p |u'|^2)$ starts to decrease with $|u'|/U$. To estimate the amplitude of the whistling in a long corrugated pipe an energy balance model is required. In a first order approximation radiation losses at the pipe terminations and convective losses due to vortex shedding are small compared to the visco-thermal losses and can be neglected in a long corrugated pipe. Then the energy balance is simplified to:

$$\frac{2}{\pi}\langle P_{source}\rangle = \langle P_{visc}\rangle, \tag{4.14}$$

where $\langle P_{source}\rangle$ is the time averaged acoustic source power and $\langle P_{visc}\rangle$ is the time averaged power loss due to visco-thermal losses, which is estimated for a single
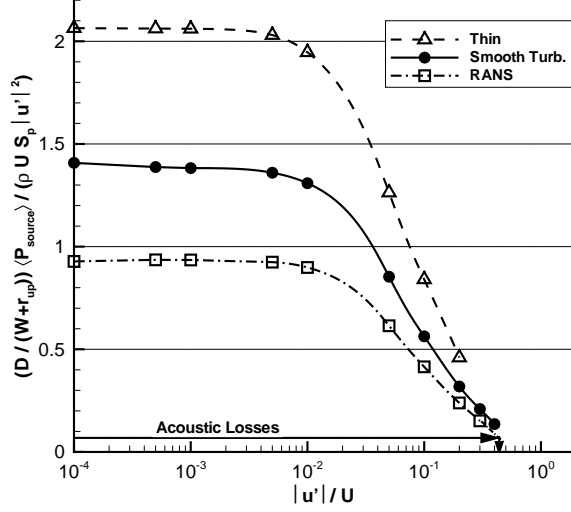
Figure 4.**13:** Perturbation amplitude $|u'|/U$ is plotted against normalized dimensionless average acoustic source power $(D/(W + r_{\mathrm{up}}))\langle P_{\mathrm{source}}\rangle/(\rho_0 U S_{\mathrm{p}}|u'|^2)$ for the 3 velocity profiles given in figure 4.10. The confinement ratio is the same for all simulations $D/(W + r_{\mathrm{up}}) = 3.2$.

cavity as follows:

$$\frac{\langle P_{\mathrm{visc}}\rangle}{\rho_0 U S_{\mathrm{p}}|u'|^2} = \frac{1}{2}\frac{c_{\mathrm{eff}}\alpha Pt}{U}. \tag{4.15}$$

The factor $(2/\pi)$ in Eq. 4.14 takes into account the spatial dependency of the acoustical velocity (u') along a standing wave [Nakiboğlu et al., 2011a]. Assuming a quasi-steady flow [Ingard and Singhal, 1975], the fluctuating pressure drop is stated as follows:

$$\frac{dp'}{dx} = \rho_0 U u'\frac{4c_{\mathrm{f}}}{D}, \tag{4.16}$$

where $c_{\mathrm{f}} = 1.78 \times 10^{-2}$ is the experimentally determined resistance coefficient and related to the damping coefficient for acoustic waves by:

$$\alpha = \frac{U}{c_{\mathrm{eff}}}\frac{4c_{\mathrm{f}}}{D}. \tag{4.17}$$

Combining Eq. 4.15 - Eq. 4.17, the normalized dimensionless visco-thermal losses is estimated as $(\pi/2)(D/(W + r_{\mathrm{up}}))\langle P_{\mathrm{visc}}\rangle/(\rho_0 U S_{\mathrm{p}}|u'|^2) = \pi c_{\mathrm{f}} Pt/(W + r_{\mathrm{up}}) = 0.065$. Which leads to a maximum perturbation amplitude of $|u'|/U \approx 0.45$ (Fig. 4.13). Considering the experimental data of $|u'|/U = 0.1$, all the profiles lead to an over estimated value.

It should be noticed that this approach has a fundamental drawback [Nakiboğlu et al., 2011a]. The losses due to flow separation at each cavity are implicitly included

in the simulations. By introducing the experimentally measured resistance coefficient (c_f) to calculate the damping coefficient, this non-linear effect is again taken into account in this approach. Also the model neglects heat transfer losses.

4.6   Radiation

Up to now the the flow inside the Hummer has been described. In this section the wave propagating from the open ends of the tube towards a listener is considered. First the theory is discussed, secondly the acoustic measurements are presented and in the last part the measured sound pressure levels are compared with the predictions from the theory.

4.6.1   Theory

The radiation from a Hummer can be modeled as a two pulsating spheres (monopoles) at the two open extremities of the tube. Depending on the acoustic mode (standing wave, $n = 1, 2, 3...$) they pulsate in phase or in opposite phase. The strength of these monopoles is estimated for a given acoustic mode as:

$$Q_n = u'_\text{n} S_\text{p} = \frac{u'_\text{n}}{U} U S_\text{p} = \frac{u'_\text{n}}{U} \frac{\Omega_\text{n} R}{\sqrt{1 + 4 c_\text{f} \frac{L}{D}}} S_\text{p}, \tag{4.18}$$

where $u'_\text{n}/U \approx 0.05$ is determined from the measurements (Fig. 4.9) and the average velocity is estimated from Eq. 4.8. Here S_p and R are cross-sectional area and the radius of the rotation of the Hummer, respectively. As shown schematically in figure 4.14, because of the swinging motion the Hummer bends. Thus, the radius of the rotation of the Hummer is smaller than the length of the Hummer ($R \leq L$). Knowing the Strouhal number from figure 4.9, the rotation speed Ω_n can be estimated as follows:

$$\Omega_\text{n} = \frac{f_\text{n}(W + r_\text{up})}{Sr\, R} \sqrt{1 + 4 c_\text{f} \frac{L}{D}}. \tag{4.19}$$

As indicated in figure 4.14 the location of the fixed monopole (S_1), the hand hold side of the Hummer, is taken as the origin of the space $\vec{x}_\text{s1} = (0, 0, 0)$. Then the location of the rotating source (S_2) is defined as $\vec{x}_\text{s2} = (R \cos(\Omega_\text{n} t_\text{e}), R \sin(\Omega_\text{n} t_\text{e}), h_\text{s})$. Here t_e is the emission time of the rotating source, S_2, and it is related to the time t at which the wave reaches the listener by:

$$t = t_\text{e} + \frac{|\vec{x} - \vec{x}_\text{s2}(t_\text{e})|}{c_0}, \tag{4.20}$$

and h_s is the vertical distance between the rotating and fixed sources.

Experiments have been performed in a semi-anechoic chamber, where the floor is reflecting. Reflections from the ground can be modeled by method of images [Pierce,
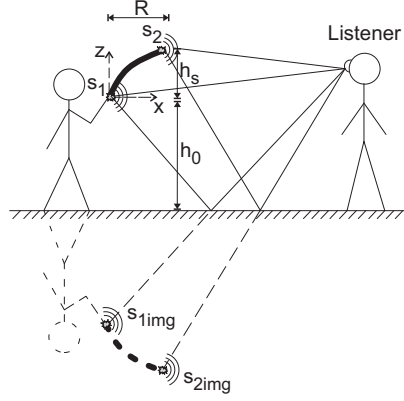
Figure 4.14: The schematic drawing of a Hummer in action with a listener.

1989]. The location of the fixed image source is $(S_{1\text{img}})$ is $\vec{x}_{s1\text{img}} = (0, 0, -2h_0)$. The position of the rotating image source $(S_{2\text{img}})$ as a function of emission time of the rotating image source (t_e^*) is given as $\vec{x}_{s2\text{img}} = (R\cos(\Omega_n t_e^*), R\sin(\Omega_n t_e^*), -(2h_0 + h_s))$. Please note that the emission time of the rotating image source is different than the emission time of the real source $t_e \neq t_e^*$. Emission time of the rotating image source is related to the time t at which the wave reaches the listener by:

$$t = t_e^* + \frac{|\vec{x} - \vec{x}_{s2\text{img}}(t_e^*)|}{c_0}, \tag{4.21}$$

The listener will hear a superposition of the direct waves from sources S_1, S_2 and the reflected waves, coming from the image sources $S_{1\text{img}}$, $S_{2\text{img}}$. Using a quasi-steady approach, in which the position of the moving sources $(S_2$ and $S_{2\text{img}})$ are parametrized as a function of retarded times $(t_e$ and $t_e^*)$, the pressure field at the listener position can be calculated, using the complex notation with $e^{i\omega t}$ convention as [Pierce, 1989]

$$\begin{aligned}
\hat{p}(\vec{x}, \omega_n) = {} & \rho_0 \frac{i\omega_n Q_n}{4\pi} \left(\left(\frac{e^{-ik_n|\vec{x} - \vec{x}_{s1}|}}{|\vec{x} - \vec{x}_{s1}|} + \frac{e^{-ik_n|\vec{x} - \vec{x}_{s1\text{img}}|}}{|\vec{x} - \vec{x}_{s1\text{img}}|} \right) \right. \\
& \left. + (-1)^{n+1} \left(\frac{e^{-ik_n|\vec{x} - \vec{x}_{s2}(t_e)|}}{|\vec{x} - \vec{x}_{s2}(t_e)|} + \frac{e^{-ik_n|\vec{x} - \vec{x}_{s2\text{img}}(t_e^*)|}}{|\vec{x} - \vec{x}_{s2\text{img}}(t_e^*)|} \right) \right)
\end{aligned} \tag{4.22}$$

Here the wave number is estimated as

$$k_n = \frac{\omega_n}{c_0} = \frac{2\pi f_n}{c_0} = \frac{\pi c_{\text{eff}}}{c_0\, n\, L}, \tag{4.23}$$

where n is the mode number, c_0 is the speed of sound, c_{eff} is the effective speed of sound (Eq. 4.9) and L is the length of the Hummer.

In the previous statement (Eq. 4.22) for the pressure field at the listener position, the effect of the Doppler shift due to the rotating source is not incorporated. As explained by Dowling and Williams [1983]; Rienstra and Hirschberg [2004], the sound field including the Doppler shift that is generated by a moving monopole source is given by:

$$p'(\vec{x}, t) = \rho_0 \frac{\partial}{\partial t} \left(\frac{Q(t_{\rm e})}{4\pi \, |\vec{x} - \vec{x}_{\rm s}(t_{\rm e})| \, |1 - Ma_{\rm s}(t_{\rm e})|} \right), \tag{4.24}$$

where $\vec{x}$ is the listener position, t_e is the retarded time, $Q(t_e)$ is the source strength and $c_0 M_s(t_e)$ is the component of the source velocity in the direction of the observer. In the case of the Hummer, by a superposition of the four sources of sound, the following expression is obtained in the time domain:

$$p'(\vec{x}, t) = \frac{-\omega_{\rm n} \rho_0 Q_n}{4\pi} \left(\frac{sin\left(\omega_n \left(t - \frac{|\vec{x} - \vec{x}_{\rm s1}|}{c_0}\right)\right)}{|\vec{x} - \vec{x}_{\rm s1}|} + \frac{(-1)^{n+1} \, \sin(\omega_n t_{\rm e})}{(1 - Ma_{\rm s2}(t_{\rm e}))^2 \, |\vec{x} - \vec{x}_{\rm s2}(t_{\rm e})|} \right)$$

$$+ \left(\frac{\rho_0 Q_{\rm n}}{4\pi} \frac{(\vec{x} - \vec{x}_{\rm s2}(t_{\rm e})) \frac{\vec{a}_{\rm s2}(t_{\rm e})}{c_0} + c_0 Ma_{\rm s2}(t_{\rm e}) - \frac{|\vec{v}_{\rm s2}(t_{\rm e})|^2}{c_0}}{|\vec{x} - \vec{x}_{\rm s2}(t_{\rm e})|^2 \, (1 - Ma_{\rm s2}(t_{\rm e}))^3} \right)$$

$$+ \frac{-\omega_{\rm n} \rho_0 Q_n}{4\pi} \left(\frac{\sin\left(\omega_n (t - \frac{|\vec{x} - \vec{x}_{\rm s1img}|}{c_0})\right)}{|\vec{x} - \vec{x}_{\rm s1img}|} + \frac{(-1)^{n+1} \sin(\omega_n t_{\rm e}^*)}{(1 - Ma_{\rm s2img}(t_{\rm e}^*))^2 \, |\vec{x} - \vec{x}_{\rm s2img}(t_{\rm e}^*)|} \right)$$

$$+ \left(\frac{\rho_0 Q_{\rm n}}{4\pi} \frac{(\vec{x} - \vec{x}_{\rm s2img}(t_{\rm e}^*)) \frac{\vec{a}_{\rm s2img}(t_{\rm e}^*)}{c_0} + c_0 Ma_{\rm s2img}(t_{\rm e}^*) - \frac{|\vec{v}_{\rm s2img}(t_{\rm e}^*)|^2}{c_0}}{|\vec{x} - \vec{x}_{\rm s2img}(t_{\rm e}^*)|^2 \, (1 - Ma_{\rm s2img}(t_{\rm e}^*))^3} \right), \tag{4.25}$$

where the following definitions are used for the velocity of the moving source and its image:

$$\vec{v}_{\rm s2}(t_{\rm e}) = \frac{\partial \vec{x}_{\rm s2}(t_{\rm e})}{\partial t_{\rm e}}, \quad \vec{v}_{\rm s2img}(t_{\rm e}^*) = \frac{\partial \vec{x}_{\rm s2img}(t_{\rm e}^*)}{\partial t_{\rm e}^*}, \tag{4.26}$$

the acceleration of the moving source and its image:

$$\vec{a}_{\rm s2}(t_{\rm e}) = \frac{\partial^2 \vec{x}_{\rm s2}(t_{\rm e})}{\partial t_{\rm e}^2}, \quad \vec{a}_{\rm s2img}(t_{\rm e}^*) = \frac{\partial^2 \vec{x}_{\rm s2img}(t_{\rm e}^*)}{\partial t_{\rm e}^{*2}}, \tag{4.27}$$

and the Mach number of the moving source and its image:

$$Ma_{\rm s2}(t_{\rm e}) = \frac{\vec{x} - \vec{x}_{\rm s2}(t_{\rm e})}{|\vec{x} - \vec{x}_{\rm s2}(t_{\rm e})|} \frac{\vec{v}_{\rm s2}(t_{\rm e})}{c_0},$$

$$Ma_{\rm s2img}(t_{\rm e}^*) = \frac{\vec{x} - \vec{x}_{\rm s2img}(t_{\rm e}^*)}{|\vec{x} - \vec{x}_{\rm s2img}(t_{\rm e}^*)|} \frac{\vec{v}_{\rm s2img}(t_{\rm e}^*)}{c_0}. \tag{4.28}$$

The first model (Eq. 4.22), which does not incorporate the Doppler shift, is compared with the second model (Eq. 4.25) in figure 4.15. Estimated pressure amplitudes from these two models $\hat{p}_{\rm wout}$ and $\hat{p}_{\rm with}$ for a listener position of $\vec{x} = (0.8{\rm m}, 0, 0)$ are given

Figure 4.15: Estimated pressure amplitudes for a listener position of $\vec{x} = (0.8\text{m}, 0, 0)$ for the fifth mode $n = 5$ for a single period of rotation for two models: without Doppler shift ($\hat{p}_{\text{wout}}$, Eq. 4.22) and with Doppler shift ($\hat{p}_{\text{with}}$, Eq. 4.25). Relative Difference is $(\hat{p}_{\text{wout}} - \hat{p}_{\text{with}})/(\hat{p}_{\text{with}})_{\max} \times 100$. Radius of rotation is $R = 0.8L$.
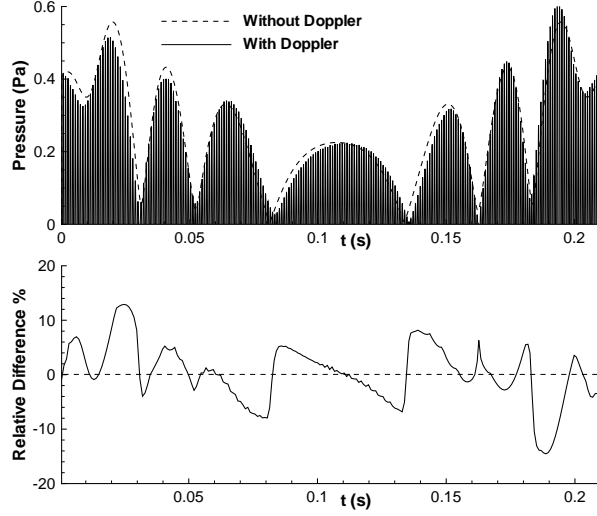
as a function of time for a single period of rotation for the fifth mode ($n = 5$). The first model can capture all the amplitude modulations. As shown in the combined deviation plot the relative difference, $(\hat{p}_{\text{wout}} - \hat{p}_{\text{with}})/(\hat{p}_{\text{with}})_{\max} \times 100$, between the predicted amplitudes is around 10% at maximum. $(\hat{p}_{\text{with}})_{\max}$ is the maximum of $\hat{p}_{\text{with}}$ over a rotation period.

In figure 4.16 estimated pressure amplitudes are presented for two different listener positions namely, $\vec{x} = (0.8\text{m}, 0, 0)$ and $\vec{x} = (3\text{m}, 0, 0)$, with and without floor reflections. The calculations are performed for the third mode ($n = 3$) using the simple model (Eq. 4.22). It is seen that for the listener position of $\vec{x} = (0.8\text{m}, 0, 0)$ the effect of the reflections on the amplitude is not pronounced. In particular, reflections have no effect on the maximum amplitude experienced by the listener at the moment when the Hummer reaches the closest position to the listener ($t = 0$, $t = 0.325$). This is simply because the rotating source (S_2) dominates all the other sources (S_1, $S_{1\text{img}}$ and $S_{2\text{img}}$) at such a close distance from the listener. At a listener position of $\vec{x} = (3\text{m}, 0, 0)$ the effect of the reflections is notable. Reflections increase the pressure amplitudes by 50% at the listener position. This is due to the fact that at such a listener position, the distance between the real sources (S_1, S_2) and the listener becomes comparable to the distance between the imaginary sources ($S_{1\text{img}}$, $S_{2\text{img}}$) and the listener.

From figure 4.15 and figure 4.16 it is concluded that the the Doppler shift does not have an essential role on the amplitude modulation. It is primarily controlled by the interference of the fixed (S_1) and moving (S_2) sources. Depending on the listener position the image sources ($S_{1\text{img}}$, $S_{2\text{img}}$) can also have a very strong affect on the amplitude modulation.

There is an essential difference in the amplitude modulation mechanism between
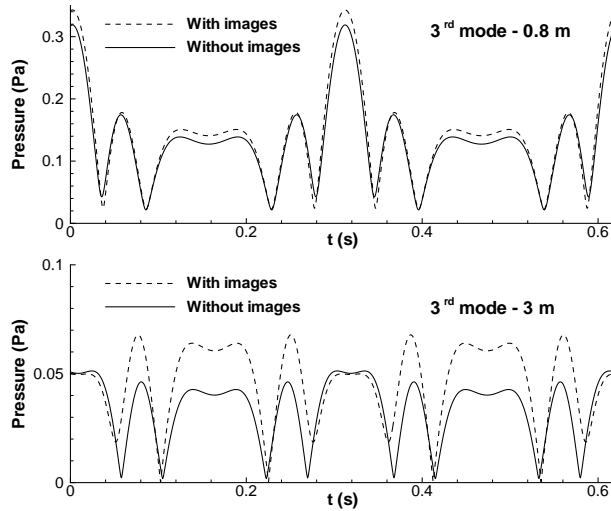
Figure 4.16: Estimated pressure amplitudes at listener positions of $\vec{x} = (0.8\text{m}, 0, 0)$ and $\vec{x} = (3\text{m}, 0, 0)$ for the third mode $n = 3$ for two periods of rotation: with (With images) and without (Without images) taking the reflections from the floor into account.

a Hummer and a Leslie horn. In a Leslie horn there exist only one monopole source [Smith et al., 2002]. Thus, the amplitude modulation depends on the presence of reflections [Kronland-Martinet and Voinier, 2008]. In the Hummer, however, as discussed the reflections are not a necessary condition for the interference pattern.

4.6.2 Experiments

Experiments were performed in a semi-anechoic room with a reflecting floor. The chamber has a volume of 100 m^3 and a cut-off frequency of 300 Hz. As schematically shown in figure 4.14, the Hummer was played by swirling it in a circular motion above the head of the performer roughly keeping the moving termination in a horizontal plane. The sound pressure level was recorded by means of two microphones (Brüel & Kjær type 4133 and 4165). One of the microphones was held by the Hummer player close to the pipe termination by holding the microphone and the Hummer together in the same hand. The microphone was placed against the tube 3 cm from the opening. This microphone will be referred as hand microphone. The second microphone was held by the listener at various distances from the performer, which will be referred as the distant microphone. The performer played approximately 15 seconds at each mode, while it was recorded simultaneously by the two microphones. The performer was also recorded by means of a video camera, which was used to estimate the rotation speed Ω_n, the radius of the rotation R and the vertical distance h_s between the rotating and the fixed sources.

In figure 4.17 the signals obtained from the hand and the distant microphone are shown when the performer was playing the 3rd acoustic mode for a duration of two periods of rotation. The distant microphone was 0.8 m from the performer. The sig-
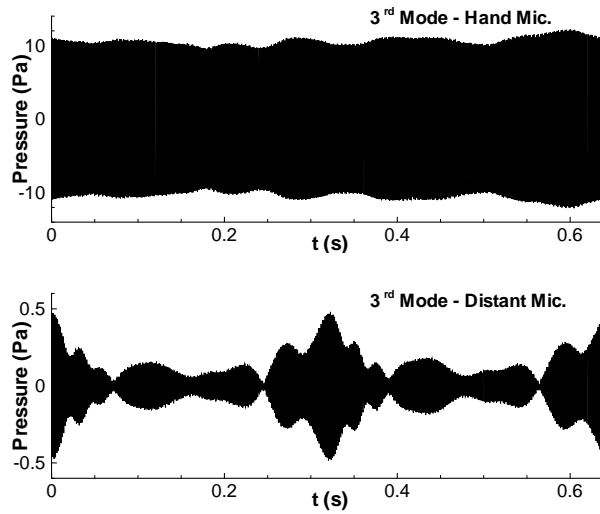
Figure 4.**17:** Signals from the distant microphone (0.8 m) and the hand microphone for the $3^{\rm rd}$ acoustic mode for two periods of rotation.

Figure 4.18:
Frequency spectrum plotted against the sound pressure level both for the distant microphone (0.8 m) and the hand microphone for the $3^{\rm rd}$ acoustic mode.
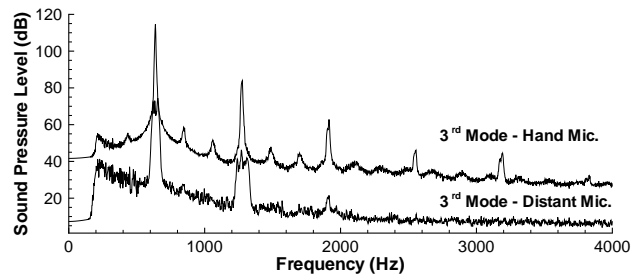
nal from the distant microphone shows a very strong amplitude modulation while the hand microphone displays a weak modulation. The amplitude modulations observed at the hand microphone is an indication of non-constant rotation velocity $\Omega_{\rm n}$ during the performance. The amplitude modulation of the distant microphone is discussed in the next section.

In figure 4.18 the same signals (Fig. 4.17) are presented in the Fourier domain. The sound pressure level (SPL) recorded in the vicinity of the fixed source was around 115 dB and 70 dB at a distance of 0.8 m from the performer. It is clear that the spectrum is dominated by the fundamental oscillation frequency $f_{\rm n} = 637$ Hz, corresponding to the third acoustic mode ($n = 3$) and its exact multiples at $m \ f_{\rm n}$ ($m = 1, 2, 3...$). These higher harmonics are due to the non-linear saturation mechanism, which limits the amplitude of the oscillations [Fletcher and Rossing, 1991] (Sec. 4.5.4).
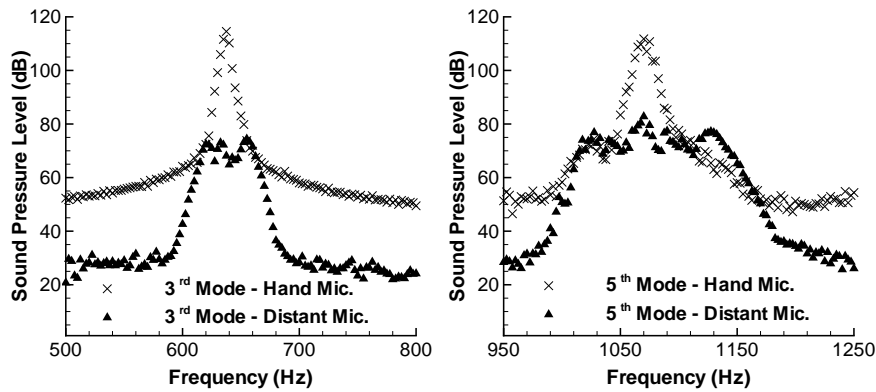
Figure 4.**19:** Frequency spectrum plotted against sound pressure level for the 3rd and 5th acoustic modes both for the hand and the distant (0.8m) microphones.

In figure 4.19 frequency spectra are plotted against sound pressure levels for the 3rd and 5th acoustic modes around their respective fundamental oscillation frequencies (whistling) both for the hand and the distant microphones (0.8 m). An obvious difference between the pressure recorded by the hand microphone and the distant microphone is the width of the peaks in the spectrum. The signal from the hand microphone has a sharp peak. The signal from the distant microphone, however, has a rather broad peak. This is due to the Doppler shift and is also observed for the Leslie horn [Kronland-Martinet and Voinier, 2008; Smith et al., 2002]. During a rotation when the Hummer is moving toward the microphone it creates a side peak at a higher frequency than recorded at the hand microphone, and vice versa when it is moving away from the microphone. It is also evident that these two side peaks are not exactly symmetric with respect to the center peak, particularly for the 3rd mode, which indicates that the rotation velocity towards and away from the microphone is not the same. The width of the broad peaks are 40 Hz and 120 Hz for the 3rd and 5th acoustic modes, respectively. The relative Doppler broadening reaches $\Delta f/f = 6\%$ which corresponds to half a tone. Therefore it is perceptually quite important.

4.6.3   Comparison

In this section the signals that are obtained from the experiments are compared with the estimated signals from the theory (Eq. 4.25). In figure 4.20 and figure 4.21 measured and estimated pressure amplitudes for the listener positions of $\vec{x} = (0.8\text{m}, 0, 0)$ and $\vec{x} = (3\text{m}, 0, 0)$ are given as a function of time during two periods of rotation for the modes of n = 3, 4 and 5, respectively. For ease of comparison the peaks in the pressure modulation are indexed.

Firstly, it should be mentioned that for the same mode (n) the period lengths
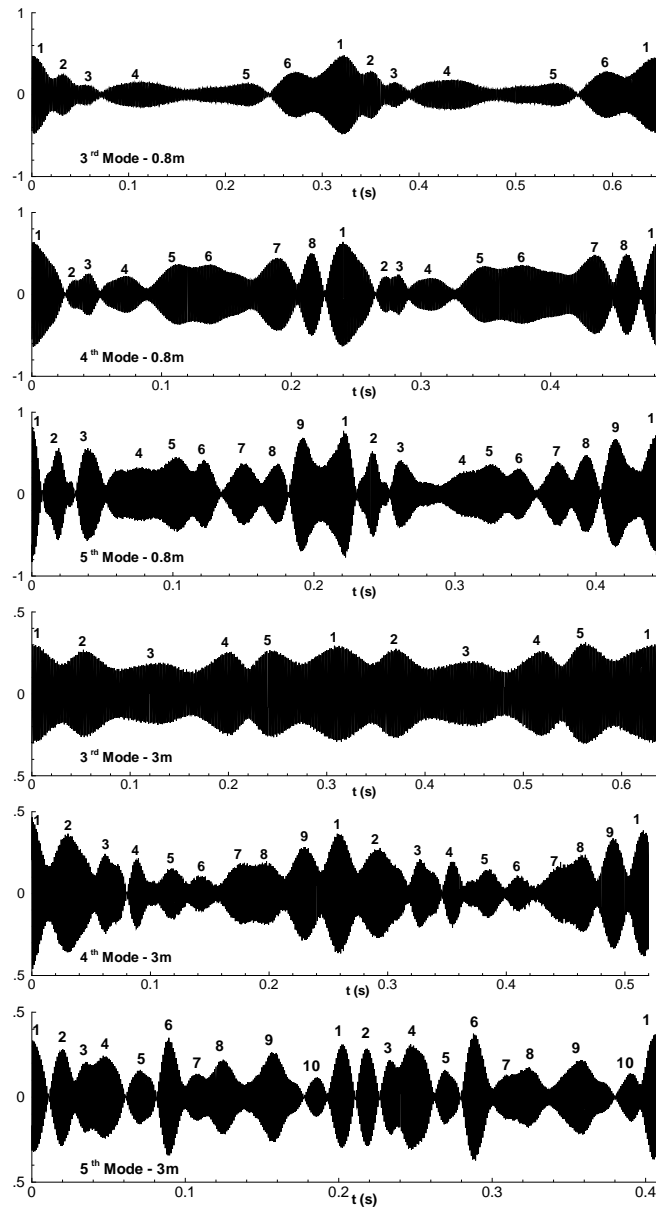
Figure 4.20: Measured pressure amplitudes for listener positions of $\vec{x} = (0.8\mathrm{m}, 0, 0)$ and $\vec{x} = (3\mathrm{m}, 0, 0)$ as a function of time during two periods of rotation for the modes of n = 3, 4 and 5.
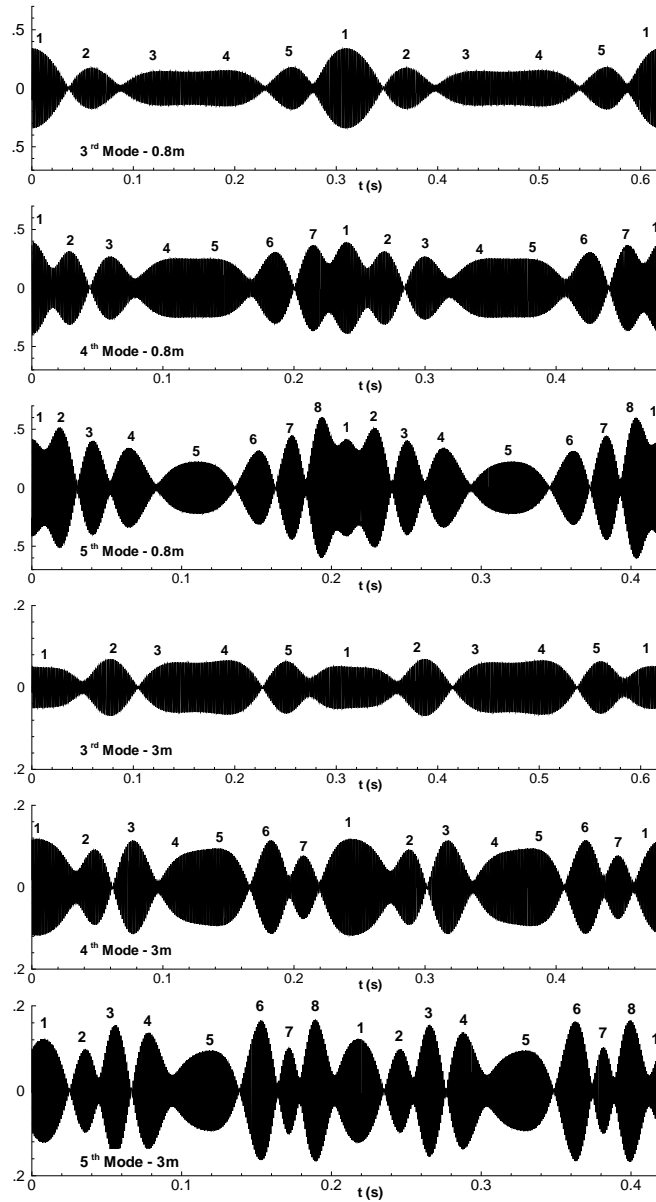
Figure 4.21: Estimated pressure amplitudes from the theory (Eq. 4.25) for listener positions of $\vec{x} = (0.8\mathrm{m}, 0, 0)$ and $\vec{x} = (3\mathrm{m}, 0, 0)$ as a function of time during two periods of rotation for the modes of n = 3, 4 and 5.

of the signals are not the same for the listener positions of 0.8 m and 3 m. This is due to the fact that the signals were obtained from two different experiments. As demonstrated in figure 4.7, the whistling occurs for a range of velocity within a specific mode. Thus during the experiments, although the Hummer was whistling at the same mode, the rotation speeds (Ω_n) were not the exactly the same. Secondly, it should be noted that for the calculation of the signals from the theory, the rotation speeds (Ω_n) obtained from the respective experiments are used instead of the ones obtained from the theory (Eq. 4.19). Theory overestimates Ω_n by $\approx 30\%$.

An apparent difference between the measured and the estimated signals is the lack of symmetry between the first and the second half of the rotation period. Due to the non-constant rotation velocity (Ω_n) during the performance, recorded as small fluctuations in the signal from the hand microphone (Fig. 4.17), there exist an asymmetry between the first and the second half of the rotation period for all the measured signals.

The Hummer produces radiation patterns similar to the ones observed in flue organ pipes as explained by Fletcher and Rossing [1991]. This is due to the fact that $c_{\text{eff}} \leq c_0$, so that the two radiating monopoles are at a distance from each other smaller than ($n\lambda/2$), where n is the acoustic longitudinal mode and λ is the wave length. In organ pipes the same effect (end correction) is due to the inertia of the flow through the pipe mouth [Fletcher and Rossing, 1991]. During the performance Hummer creates an amplitude modulation at a listener position due to the rotation of these radiation patterns. It is seen that the estimated signals from the theory globally resembles the measured signals. The model captures most of the modulations. It is noticeable that the estimations of the model for the listener position of $\vec{x} = (0.8\text{m}, 0, 0)$ is better than the $\vec{x} = (3\text{m}, 0, 0)$ considering both the shape of the signal and the levels of the pressure fluctuation amplitudes. This is probably due to the fact that at such a close distance from the source the radiation is dominated by the real sources (S_1, S_2). At a further distance, however, the reflections from the walls which are not included in the model can be substantial.

In figure 4.22 the frequency spectra are plotted against sound pressure levels for the 3rd and 5th acoustic modes around their respective fundamental oscillation frequencies for a microphone position of $\vec{x} = (0.8\text{m}, 0, 0)$ (presented in Fig. 4.19) together with the estimation of the theory. For the 3rd acoustic mode, the theory agrees very well with the experiment except that there exist a stronger central peak in the theory. Since the theory assumes constant rotation speed Ω_n, a central peak appears which is symmetric with respect to the side peaks appearing due to Doppler shift. The energy of the central peak comes from the fixed source (S_1) and from the rotating source (S_2) when its trajectory is not dominated by motion either toward nor away from the microphone. For the 5th acoustic mode the theory slightly underestimates the whistling frequency (≈ 10 Hz) and the width of the peak (≈ 115 Hz) compared to the experimental values.
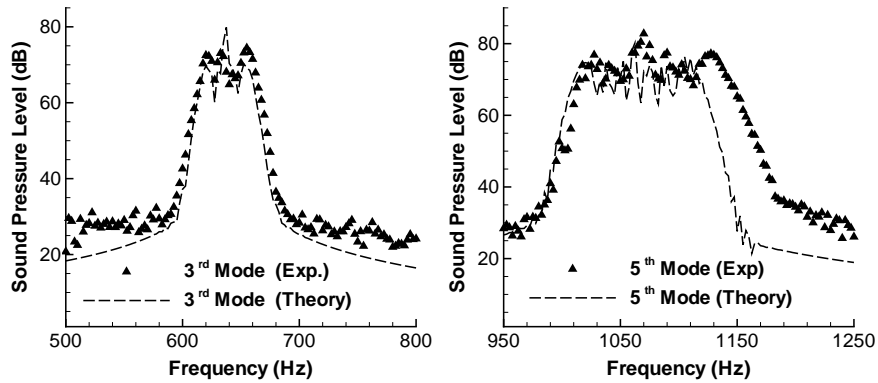
Figure 4.22: Frequency spectrum plotted against sound pressure levels for the $3^{\rm rd}$ and $5^{\rm th}$ acoustic modes for a microphone position of $\vec{x} = (0.8{\rm m}, 0, 0)$ both measured and estimated from the theory.

4.7 Discussion

4.7.1 Missing fundamental

A commonly observed phenomenon in short corrugated segments, e.g. Hummer, is the absence of whistling for the fundamental mode [Cermak, 1922; Crawford, 1974; Silverman and Cushman, 1989; Nakamura and Fukamachi, 1991; Cadwell, 1994; Elliott, 2004]. As addressed in Sec. 4.4.3, the flow is probably already turbulent for the velocities where the fundamental mode is expected. Thus, it is concluded that the absence of the missing fundamental is not related to the lack of turbulence as suggested in the literature [Crawford, 1974; Cadwell, 1994].

Experiments on the localization of the region of sound production in corrugated pipes have shown that the contribution of each cavity is not the same [Tonon et al., 2010; Nakiboğlu et al., 2010; Golliard et al., 2010]. It was demonstrated that the sound production is dominated by the cavities which are in the proximity of the acoustic pressure nodes of the standing wave along the main pipe. Considering the fundamental mode, there exist only two pressure nodes: one at the inlet and one at the outlet. Furthermore, a Hummer often has a smooth pipe segment of a few centimeters at its inlet, used to hold the pipe (Fig. 4.1), thus considerably decreasing the sound production capacity of the inlet section.

The developing velocity profile is another aspect that hinders the whistling for the fundamental mode. At the inlet of the Hummer a rather flat velocity profile (Fig. 4.10 - Thin) approaches to the corrugations, whereas at the outlet of the pipe a fully developed velocity (Fig. 4.10 - RANS) reaches the corrugations. As explained in Sec. 4.5.2, different velocity profiles promotes different peak-whistling Strouhal numbers ($Sr_{\rm p-w}$). For these two velocity profiles a difference of 50% in peak-whistling
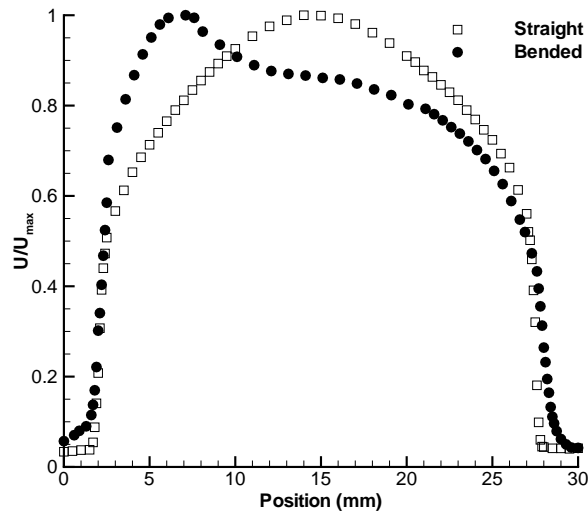
Figure 4.23: Measured velocity profiles for the bent and straight Hummer.

Strouhal number is predicted by the theory, as shown in figure 4.11. Thus, the source region at the inlet does not cooperate with the source region at the exit.

For these reasons the total sound source is rather weak for the fundamental mode compared to the higher modes. As a consequence the losses (Eq. 4.15) become large compared to the acoustic sources and the system remains silent. This corresponds to an overshoot in figure 4.13, where the acoustic losses (horizontal line) do not intersect with an acoustic source line.

4.7.2   Effect of bending

One of the marked advantage of corrugated pipe is its ability to bend while keeping its rigidity. Thus, in various industrial application corrugated pipes are used in a bent form. An experiment was performed with a Hummer to explore the effect of bending. The Hummer was strongly bent in a horizontal plane such that $\alpha = 35°$, as shown in figure 4.2. The length of the first and the second straight segments were 410 mm and 185 mm, respectively. In figure 4.23 measured velocity profiles for the bent and straight Hummer are presented.

It is clear that bending has a significant effect on the velocity profile even after a straight segment of 26 corrugations (185 mm). This is in agreement with the numerical simulations mentioned in Sec. 4.4.3, from which it is concluded that it takes 50 corrugations for the flow to reach a fully developed velocity profile.

A surprising result is that the Hummer, which was whistling (3$^{\text{rd}}$ acoustic mode) when it was straight, became silent in the bent configuration. A possible explanation

could be found in the effect of the velocity profile on the whistling. Different velocity profiles promotes different peak-whistling Strouhal numbers as explained in Sec. 4.5.2. Due to bending, the velocity profile approaching cavities of the Hummer is different on each side of the bend. Consequently they have different peak-whistling Strouhal numbers and might not cooperate. Thus, they can not produce the necessary acoustic source power for the whistling.

Although the Hummer bends during a performance due to the swinging motion, it keeps whistling. This suggest that there are more parameters involved, e.g. the angle of bending, the radius of bending, the source location with respect to the bend, etc. The importance of bending in corrugated pipe has, to the authors knowledge, not yet been addressed in the literature.

4.7.3   Uncertainties in the radiation model

In Sec. 4.6.1 an acoustic model is proposed to estimate the radiation from a Hummer at a given listener position. The model, Eq. 4.25, uses a number of parameters with a noticeable range of uncertainty. Here these parameters are listed with respective values and the way that are estimated or assumed. It should be noted at this point that these parameters were not modified intuitively from one case to another to force a better agreement with the experimental data. The aim of the radiation study is to see how much a simple model can explain the phenomena appearing in a real performance.

The radius of rotation (R), as shown in figure 4.14, is not the same as the length of the Hummer (L). By using camera recordings, the radius was estimated as 80% of the pipe length for all the modes. This is a rather crude approximation. It is evident from the movies that with increasing mode number the radius of rotation was increasing. It was, however, not included in the model.

The vertical distance between the fixed source (S_1) and the moving source (S_2) was taken as $h_s = 20$ cm for all the modes, again based on the camera recordings. Similar to the determination of radius of rotation (R), this is a first order approximation and the change with the mode number is not included.

The hand holding the tube forms a flange for one of the pipe termination. This can affect the sound radiation of the fixed source, resulting in an asymmetry between the two sources. This is not included in the radiation model and is a subject for further research.

It was assumed in the model that the rotating source (S_2) remains in a horizontal plane during all the performance. Yet it was apparent from the video recordings that the plane of rotation was tilted from the horizontal plane and did not preserve the same angle throughout the performance. Besides the non-constant rotation velocity (Ω_n), this is another cause of the asymmetry observed between the first and the second half of the period for the measured signals.

The listener positions $\vec{x} = (0.8\mathrm{m}, 0, 0)$ and $\vec{x} = (3\mathrm{m}, 0, 0)$ are simply the position of the audience holding the microphone at the level of the fixed source (S_1) during the performance of the Hummer player. As a consequence the spatial position of the microphones are also prone to a uncertainty (± 10 cm).

It is interesting to note that Kristiansen et al. [2011] observed a hysteresis in sound production of a corrugated tube upon low frequency (10 Hz) modulation of the flow. In their experiment, at a single flow velocity, the corrugated pipe produced a higher pulsation amplitude upon decreasing flow velocity than upon increasing flow velocity. This memory effect is also not included in the radiation model.

4.8   Conclusion

In this study the sound generation in short corrugated segments used as a musical toy, e.g. Hummer, and the associate sound radiation is investigated experimentally, numerically and analytically.

Using the effective speed of sound (c_{eff}) definition [Elliott, 2004], the whistling frequencies (f_{n}) in a corrugated pipe can be predicted within 4% (Fig. 4.8).

Velocity profiles measurements reveal that the fully turbulent velocity profile developed in a Hummer has a noticeably different shape than the one of a smooth pipe (Fig. 4.4).

Applying a numerical methodology [Nakiboğlu et al., 2011a] based on incompressible flow simulations and Vortex Sound Theory together with a representative velocity profile in a corrugated pipe, excellent predictions of the whistling Strouhal numbers are achieved (Fig. 4.12). The numerical approach combined with an energy balance can be used to to estimate the acoustic fluctuation amplitudes in corrugated pipe segments, however, it should be improved before being used as a quantitative tool for the prediction of the pulsation amplitude. An accurate prediction of the whistling amplitude remains as a challenge.

Experiments indicate that the Hummer can remain silent even if the flow is turbulent. Thus, it is concluded that the absence of whistling is not related to the lack of turbulence as it has been suggested in the literature. The reason for the absence of the fundamental mode in short corrugated pipes is likely due to the lack of cooperation between the acoustic sources at the inlet and the outlet of the pipe resulting from the difference in the mean velocity profile.

An analytical radiation model is proposed in which the Hummer is modeled as two pulsating spheres: one is fixed and the other one is following a circular pattern in a horizontal plane. The model takes the reflections from the floor into account, which appears to be essential (Fig. 4.16). The acoustic model can predict the sound pressure level within 3dB and the observed frequency at the listener position. The model can also predict qualitatively the amplitude modulation observed in the experiments (Fig. 4.21). It is also concluded that the amplitude modulation is mainly due to the

interference between the sources.

The Doppler shift due to the rotation of the pipe outlet has a minor effect on the amplitude modulation. It has, however, a pronounced effect on the frequency, which is increasing with the increasing mode number (Fig. 4.22). This effect is comparable to that observed in a Leslie horn and is expected to be perceptually important.

A strong effect of bending on the whistling of a corrugated pipe has been observed, which calls for further research.

Note :

This chapter is based on the publication:

Nakiboğlu, G., G., Rudenko, O. and Hirschberg, A. Aeroacoustics of swinging corrugated tube: Voice of the Dragon, Journal of Acoustic Society of America, Vol 131, Issue 1, pp. 749-765, 2012.

In the original publications there has been an error in the emission time of the rotating image source (t_e^*), which has now been corrected. This correction slightly modifies Fig. 4.15 and Fig. 4.22. These changes however do not change any of the conclusions that has been drawn in the original publication.

Aeroacoustic power generated by a compact axisymmetric cavity: prediction of self-sustained oscillation and influence of the depth

5.1   Abstract

Aeroacoustic power generation due to a self-sustained oscillation by an axisymmetric cavity exposed to a grazing flow is studied both experimentally and numerically. The feedback effect is produced by the velocity fluctuations resulting from a coupling with acoustic standing waves in a coaxial pipe. A numerical methodology that combines incompressible flow simulations with Vortex Sound Theory is used to predict the time averaged acoustic source power generated by the cavity. The effect of cavity depth on the whistling is addressed. It is observed that the whistling occurs around a peak-whistling Strouhal number which depends on the cavity depth to width ratio. The proposed numerical method provides excellent predictions of the peak-whistling Strouhal number as a function of cavity depth. The numerical method predicts the average acoustic source power within a factor of two. For deep cavities the time averaged acoustic source power appears to be independent of the cavity depth.

5.2   Introduction

This paper studies the aeroacoustic power generation associated with a self-sustained oscillation by an axisymmetric cavity exposed to a grazing flow. Flow-excited acoustic oscillations in cavities have been of interest both for industrial and academic research starting around 1950 [Krishnamurty, 1955; Roshko, 1955]. There has been a number of reviews on the topic which present the state of knowledge for different flow regimes and cavity configurations including Rockwell and Naudascher [1978]; Rockwell [1983]; Blake [1986]; Howe [1997, 1998]; Rowley and Williams [2006] and Gloerfelt [2009]. Despite the geometric simplicity of axisymmetric cavity-pipe configurations, the self-sustained cavity oscillations in such systems involve several complex fluid mechanics phenomena. Rockwell and Naudascher [1978] classified these oscillations into three categories based on the nature of the feedback: fluid dynamic, fluid-resonant and fluid-elastic oscillations. The current work deals with a fluid-resonant mechanism in which the feedback is produced by the velocity fluctuations at the upstream edge of the cavity. This results from a coupling of vortex shedding with a longitudinal acoustic pipe mode. This is similar to the experimental conditions in the studies of Schachenmann and Rockwell [1980]; Davies [1981]; Huang and Weaver [1991]; Geveci et al. [2003]; Oshkai et al. [2005] and English and Holland [2010]. In such a feedback loop, the shear layer instability at the mouth of the cavity and the longitudinal acoustic pipe modes can be considered as the amplifier and the filter of the feedback system, respectively [Blevins, 2001]. This results into stable self-sustained oscillations at discreet frequencies, which is called whistling. The motivation of the current study is the prediction of whistling in corrugated pipes, which can be considered, in first approximation, as a series of axisymmetric cavities placed along a duct. In view of this application, cavities which are small compared to the acoustic wave length, so-called compact cavities, are studied.

Previous work on multiple side branch systems [Tonon et al., 2010; Nakiboğlu et al., 2010] and corrugated pipes [Golliard et al., 2010] has shown that the spatial position of the cavity with respect to the coupling longitudinal standing wave is important for the sound production. The sound production is maximized when the cavity is placed in the vicinity of a pressure node.

Another parameter which has a strong effect on the sound production is the geometry of the upstream edge of the cavity. Experiments with side branches have shown that using rounded upstream cavity edge instead of sharp edge can increase the whistling amplitude by almost an order of magnitude [Bruggeman et al., 1991; Nakiboğlu et al., 2010]. In the design of the current experimental setup appropriate attention has been given to these considerations, see Sec. 5.3.1.

The early work on corrugated pipes [Binnie, 1961] has shown that the ratio of pipe diameter (D) to cavity mouth width in the streamwise direction (W) is an essential parameter for the sound production. Later Ziada and Shine [1999] and Ziada

et al. [2003] recorded in their experiments with side branches and axisymmetric cavities a similar dependency of the whistling frequency as a function of pipe diameter to cavity width ratio (D/W), which they called the confinement ratio. They suggested that this dependency is an effect of the velocity profile. Recently, Nakiboğlu et al. [2011a, 2012] reported a similar dependency and showed numerically that this dependency can be explained in terms of a change in the grazing mean flow velocity profile with D/W.

The aim of the current work is to investigate the potential of a numerical method introduced in an earlier paper [Nakiboğlu et al., 2011a] further, in predicting:

- the maximum of the time averaged aeroacoustic source power, $\langle P_{\text{source}} \rangle$, attained during whistling,

- the Strouhal number at which the maximum aeroacoustic source power is obtained, i.e. the peak-whistling Strouhal number, $Sr_{\text{p-w}}$,

- the variation of these two parameters, $\langle P_{\text{source}} \rangle$ and $Sr_{\text{p-w}}$, as a function of cavity depth to width ratio (H/W), which is known to be important from literature.

During the experiments attention is given to the accurate determination of the hydrodynamic (i.e. mean flow velocity profile) and acoustic boundary conditions (i.e. reflection coefficients) which are essential for the quantitative comparison of experimental results and predictions obtained by means of the numerical method.

The following section, Sec. 5.3, is dedicated to the description of the experiments and the analysis methods used on the experimental data. In subsections 5.3.1 and 5.3.2 the experimental setup, different configurations that were tested and the respective boundary conditions are introduced. Later in Sec. 5.3.3 the method for the determination of the time averaged aeroacoustic source power of the cavity is presented. In Sec 5.4 the numerical methodology developed in [Nakiboğlu et al., 2011a] is summarized. The last section, Sec. 5.5, covers the experimental and numerical results in three subsection: effect of velocity profile and hydrodynamic modes in Sec. 5.5.1, limit cycle amplitude due to nonlinear saturation in Sec. 5.5.2 and effect of cavity depth in Sec. 5.5.3.

5.3   Experiments

5.3.1   Experimental setup

An experimental setup has been constructed to investigate self-sustained oscillations due to a coupling of vortex shedding in an axisymmetric cavity exposed to grazing flow with a longitudinal standing wave. The test section is composed of a single axisymmetric cavity and two identical straight pipe sections. The cavity can be placed

close to the downstream (Configuration A) or upstream (Configuration B) termination of one of the straight pipe sections, see figure 5.1-a and 5.1-b, respectively. It can also be placed in the middle (Configuration C) of two straight pipe sections, see figure 5.1-c. Configuration A is similar to the one used by Schachenmann and Rockwell [1980] and Rockwell and Schachenmann [1982].

For configurations A and B, all the experiments are carried out at the first longitudinal acoustic mode. This is a standing wave of half-wave length in the pipe ($L \approx \lambda/2$). The system whistles also for the higher acoustic modes (i.e. $L \approx \lambda, 3/2\lambda, \cdots$). Experiments are performed at the lowest possible whistling mode to keep the sound source as compact as possible ($W \ll \lambda$), allowing an incompressible model for the flow in the cavity. Rockwell and Schachenmann [1982] reported, for configuration A, that the first whistling mode is obtained at the third longitudinal acoustic mode $L \approx 3/2\lambda$. This is because in their experiments a cavity with sharp edges was used together with a relatively long pipe. In the current study, cavities have rounded edges which promotes the sound production considerably and a relatively short pipe segment is used to limit the viscous losses [Bruggeman et al., 1991; Nakiboğlu et al., 2010]. The experiments for configuration C are performed at the second coupling longitudinal acoustic mode, for which there is a complete standing wave in the pipe ($L \approx \lambda$). However, the system length L is approximately two times longer for configuration C than for configurations A and B. Thus, the system whistles around the same frequency in each of the three configurations.

The mean flow velocity profile that is approaching the cavity is essential for the whistling phenomenon [Nakiboğlu et al., 2011a, 2012]. The cavity in configurations A and C experiences the same turbulent approach velocity profile while for configuration B the cavity experiences a *top-hat* velocity profile with a thin boundary layer. A sand paper strip with a width of 5 mm and a ISO/FEPA grid designation of P40 is placed on the inner pipe wall at the inlet of the pipe to trip the boundary layer such that it transits from laminar to turbulent. This avoids uncertainties due to the transition from laminar to turbulent flow. The velocity profiles are discussed in Sec. 5.3.2. In all configurations the cavity has approximately the same spatial position with respect to the coupling standing wave, which is close to a pressure node in order to maximize the sound production [Tonon et al., 2010; Nakiboğlu et al., 2010; Golliard et al., 2010].

The notation for the relevant geometrical parameters are shown in figure 5.2 for configuration A. The same notation is used for all configurations. The inner diameter and the length of the main straight pipe section are $D = 44$ mm and $L_1 = 850$ mm, respectively. The pipe is made of steel with a roughness height of $\epsilon \leq 4.0 \times 10^{-5}$ m (European Standard EN 10305-1) and has a wall thickness of 6 mm. Such a thick-walled pipe is used to avoid wall vibrations. Measurements of the reflection coefficient for a closed pipe have confirmed that there is no significant effect of pipe wall vibrations on the results of the measurements. The width
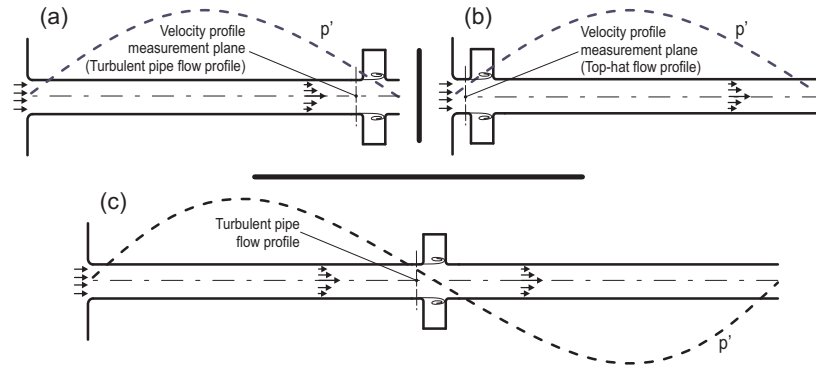
Figure 5.1: Schematic drawing of the three different configuration that have been investigated. The dotted line indicates the spatial distribution of the pressure amplitude (p') in the standing wave.
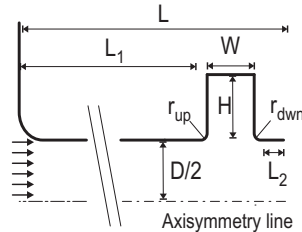
Figure 5.2: The relevant geometric parameters, shown for configuration A.

of the cavity is $W = 40$ mm. The depth of the cavity (H) is varied by inserting rings of different thickness in the cavity. Experiments have been performed for 8 different cavity depth to width ratios namely, $H/W = 0.2$, 0.25, 0.3, 0.4, 0.5, 0.675, 0.925, 1.175. The radii of the curvatures for the upstream and downstream edges are $r_{up} = r_{dwn} = 5$ mm. There is also a small straight pipe section of $L_2 = 15$ mm, which is placed downstream of the cavity for configuration A and upstream of the cavity for configuration B, see figure 5.1. For configurations A and B the total length of the system is $L = L_1 + W + r_{up} + r_{dwn} + L_2 = 915$ mm and for configuration C it is $L = L_1 + W + r_{up} + r_{dwn} + L_1 = 1750$ mm. All the components of the experimental setup have been built with an accuracy of 0.1 mm.

The set-up used for the experiments is shown in figure 5.3. The upstream termination of the test section is connected to a high-pressure air supply system, which is composed of, from upstream to downstream, a compressor, a constant pressure vessel, a control valve, a buffer vessel, a turbine flow meter and an expansion chamber muffler. The expansion chamber muffler has a length of 1.5 m and a diameter of 0.6 m. It is covered internally with sound absorbing foam with a thickness of 100 mm in order to avoid cavity resonances. The downstream termination is open to the laboratory, a large room of 15 m×4 m×4 m (not an anechoic chamber).

The acoustic pressure in each straight pipe segment (L_1) is measured by means
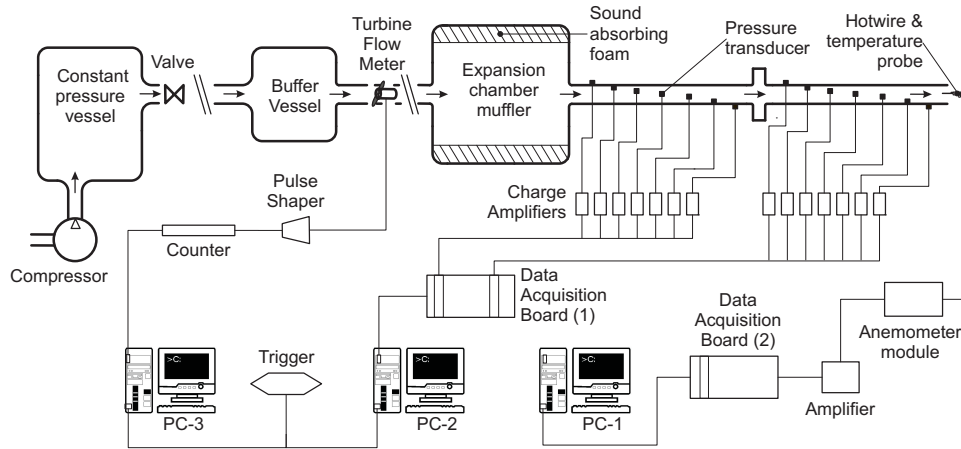
Figure 5.3: Schematic of the experimental setup and instrumentation.

of seven acceleration compensated piezo-electric pressure transducers (PCB 116A
- PCB Piezotronics Inc.). These gauges have a diameter of 10.3 mm and they are
flush mounted. These microphones have a separation distance of 108.33 mm in axial
direction and an angular position difference of $30°$ from each other in azimuthal
direction, see figure 5.3. The first and the last transducer are positioned 100 mm from
the pipe terminations. The signals from the microphones are amplified by means of
charge amplifiers (5007 - Kistler Instruments AG). These amplifiers are connected
to a combined data acquisition-PC system (NI PXIe-1062Q - National Instruments
Inc.) using two data acquisition boards (NI PXI-4472 - National Instruments Inc.)
each holds 8 port. The frequencies of whistling are in the range of $150-250$ Hz and
the sampling rate of the experiments was 5 kHz. Thus the sampling rate is large
enough to satisfy the Nyquist criteria. By sampling for long enough time, a discrete
time signal can be obtained whose discrete Fourier transform (DFT) approximately
represents the Fourier transform of the continuous time signal [Bracewell, 1986]. For
that purpose a sampling duration of 10 seconds has been used for each data point
for acoustic pressure measurements. For the multi-microphone method one of the
pressure signal was filtered around the peak frequency to obtain a reference signal.
This reference signal was used for a lock-in method from which the amplitude and
relative phases of all the pressure signals was obtained [Kooijman et al., 2008]. The
gauges are calibrated together with their adapter pieces in a closed pipe both for the
relative amplitude and relative phase difference.

A turbine flow meter (SM-RI-X-KG250 - Instromet) is used to measure the aver-
age velocity (U) through the volumetric flow rate. The turbine flow meter is con-
nected to a pulse shaper (FC 120 - Yokogawa Electric Corporation) and a counter
(NI SCB68 - National Instruments Inc.). The acquisition system of the turbine flow

meter and the piezo-electric pressure transducers are synchronized by means of a trigger pulse. The simultaneous measurement of flow velocity and pressure fluctuations allows a waterfall representation of the data, in which the frequency spectra of the whistling at different flow velocities are presented in a single graph. Using this waterfall diagram consecutive modes that appear simultaneously with the dominant hydrodynamic mode can easily be detected [Rockwell et al., 2003; Oshkai et al., 2005]. Such secondary modes were not observed for the flow range that has been studied in the current work. The temperature of the air is measured at the pipe termination with an accuracy of $0.1°C$ by means of a digital thermometer (HH309A - Omega Engineering Inc.).

Mean flow velocity profile measurements has been performed with a hotwire probe (55P11 - Dantec Dynamics). The probe is connected to a hotwire anemometer module (90C10 CTA - Dantec Dynamics) which is installed within a frame (90N10 - Dantec Dynamics.) The signal was amplified and low-pass filtered through a low-noise pre-amplifier (SR560 - Stanford Research Systems) and sent to the computer via a data acquisition board (BNC-2090 - National Instruments Inc.) with a 12-bit resolution at a sampling rate of 10 kHz. A sampling duration of 20 seconds was used for each location for the hotwire measurements. Using such a long sampling time decreases the error due to the fluctuations in the volumetric flow. The hotwire data is processed using the Dantec StreamWare$^©$ software. The hotwire signals were compensated for variations in the flow temperature.

5.3.2   Mean flow conditions

Mean velocity profile measurements were carried out to determine the approach flow profiles for different cavity positions. The profiles were measured along an axis normal to the axis of the straight pipe at 2 mm upstream of the cavity both for configurations A and B, see figure5.1 for the measurement planes. During the flow profile measurements the parts of the setups, which are downstream of the measurement planes, are removed to provide an easy access for the hotwire probe. The measured profiles are presented in figure 5.4. The legend *Turbulent Exp.* corresponds to configuration A and C and the legend *Top-Hat Exp.* corresponds to configuration B. Profile measurements were performed at a Reynolds number ($Re = UD/\nu$) of 3.5×10^4. This corresponds to a mean flow speed at which the system is whistling at the first acoustic mode. Piecewise third order polynomial curves are fitted to the experimental data for both configurations. These fits are also shown in figure 5.4.

It is clear that the cavity in configuration A experiences a much thicker boundary layer compared to the cavity in configuration B. The ratio of the average velocity (U) to the axis velocity, $u(0) = U_\mathrm{axs}$, is $U/U_\mathrm{axs} = 0.85$ for configuration A and $U/U_\mathrm{axs} = 0.96$ for configuration B. Displacement (δ_1) and momentum (δ_2) thick-

Figure 5.4: Measured approach velocity profiles $u(r)$ for configurations A and C (*Turbulent Exp.*) and for configuration B (*Top-Hat Exp.*). (1/2) and (2/2) are the 1st & 2nd half of the profile. *Turbulent Fit* and *Top-Hat Fit* are the fitted curves to the experiments. *Turbulent Num.* is the estimated turbulent velocity profile for configuration A obtained using RANS.
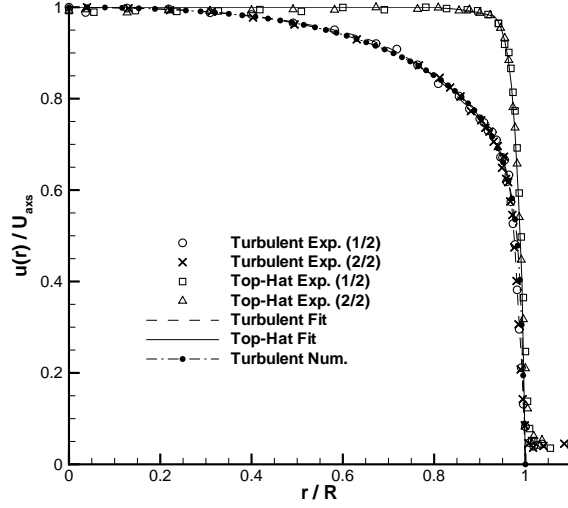
nesses are calculated from the following equations,

$$(R - \delta_1)^2 = \frac{2}{U_{\text{axs}}} \int_0^R ur\,dr \tag{5.1}$$

$$(R - \delta_1 - \delta_2)^2 = \frac{2}{U_{\text{axs}}^2} \int_0^R u^2 r\,dr \tag{5.2}$$

where R is the pipe radius and the integrals on the right hand sides of the equalities are carried out numerically using the experimental data. For configuration A, the displacement thickness (δ_1) and the momentum thickness (δ_2) are $\delta_1 = 1.7 \times 10^{-3}$ m and $\delta_2 = 1.2 \times 10^{-3}$ m, respectively. For configuration B, the displacement thickness is $\delta_1 = 3.9 \times 10^{-4}$ m and the momentum thickness is $\delta_2 = 2.0 \times 10^{-4}$ m.

The fitted velocity profile curves (*Turbulent Fit* and *Top-Hat Fit*) are used in the numerical simulations, see Sec. 5.4, as inlet boundary conditions. Note that the *Turbulent Exp.* is not a fully developed turbulent pipe flow profile. The last profile that is presented in figure 5.4 is the predicted turbulent velocity profile for configuration A using a numerical simulation based on Reynolds-averaged Navier Stokes (RANS) equations, which will be discussed in the next section.

5.3.3   Theory of plane wave propagation with a mean flow

In a cylindrical duct of radius R for a quiescent fluid, the first circumferential acoustic mode with wavenumber k that propagates corresponds to a Helmholtz number ($He = kR$) of 1.84. The first radial mode will propagate when He exceeds 3.8. With a mean flow at Mach number $Ma = U/c_0$, with U the mean flow velocity and c_0 the speed of sound, these critical Helmholtz numbers are approximately reduced by the
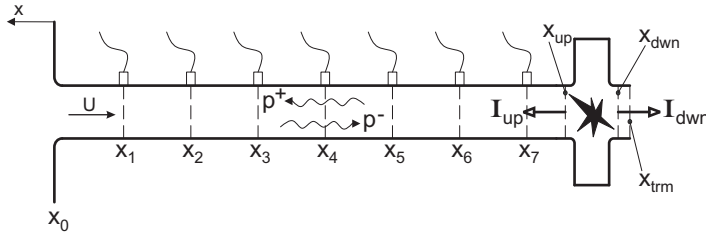
Figure 5.5: Schematic of plane wave propagation with a mean flow for configuration A.

factor $(1 - Ma^2)$ [Davies, 1988]. In the current study, recorded frequencies (f) for the first whistling mode ranges between 150-200 Hz and the corresponding mean flow velocity ranges between 4-15 m/s. Thus, the current work is limited to low Helmholtz numbers ($He \leq 0.08$) and low Mach numbers ($Ma \leq 0.05$). Hence there is only plane wave propagation. Since the acoustic pressure (p') in a plane wave is uniform over the cross-section, they can be measured at the duct surface, as described in Sec. 5.3.1.

In the current setup there is a standing wave along the duct, which results from the interference between the wave traveling away from the cavity (acoustic source) and the wave reflected back at the pipe termination, see figure 5.5. The acoustic conditions everywhere within the pipe can be described in terms of the incident pressure wave and the reflected pressure wave traveling inside the pipe in positive and negative directions.

Conditions within the duct are determined by the pressure, density and the flow velocity. The pressure at any point in the pipe is the sum of the ambient time averaged pressure p_0 and the fluctuating acoustic pressure p', i.e. $p = p_0 + p'$. Similarly the density $\rho = \rho_0 + \rho'$ and the velocity $u = U + u'$, where u' is the acoustic particle velocity. The main flow is assumed to be uniform outside the acoustic boundary layer, while the acoustic flow is assumed to be isentropic. Thus, the acoustic pressure and density are related following

$$\rho' = \frac{p'}{c_0{}^2}. \tag{5.3}$$

The fluid motion associated with the isentropic plane wave propagation in a pipe at a mean flow velocity U can be described using the linearized conservation laws for mass and momentum for frictionless flow, per unit volume, as:

$$\left(\frac{\partial}{\partial t} + U \frac{\partial}{\partial x} \right) \rho' = -\rho_0 \frac{\partial}{\partial x} u', \tag{5.4}$$

$$\rho_0 \left(\frac{\partial}{\partial t} + U \frac{\partial}{\partial x} \right) u' = -\frac{\partial}{\partial x} p', \tag{5.5}$$

Combining Eq. 5.3, Eq. 5.4 and Eq. 5.5; and eliminating velocity and density fluctuations, one obtains the one dimensional plane wave propagation equation for pres-

sure fluctuations in the presence of a steady mean flow U as:

$$\frac{1}{c_0{}^2}\left(\frac{\partial}{\partial t} + U\frac{\partial}{\partial x}\right)^2 p' - \frac{\partial^2 p'}{\partial x^2} = 0. \tag{5.6}$$

Note that similar one dimensional wave propagation equations can be obtained for velocity, u', and density fluctuations, ρ'. Here only the analysis for pressure fluctuation is presented. Wave equation (Eq. 5.6) has two solutions one corresponding to incident and one corresponding to reflected acoustic pressure waves. The upstream traveling wave, corresponding to the incident acoustic pressure wave, and the downstream traveling wave, corresponding to the reflected acoustic pressure wave, are given for a harmonic wave of frequency ($\omega = 2\pi f$) by

$$p^+(x,t) \;\; = \Re\left[P^+ e^{i(\omega t - k^+ x)}\right] \tag{5.7}$$

$$p^-(x,t) \;\; = \Re\left[P^- e^{i(\omega t + k^- x)}\right] \tag{5.8}$$

where k^+ and k^- are real-valued wave numbers given by $k^+ = \omega/(c_0 - U)$ and $k^- = \omega/(c_0 + U)$ and P^+ and P^- are the complex-valued constants.

Note that both incident and reflected waves described in Eq. 5.7 and Eq. 5.8, respectively, can be thought of as the real part of a complex-valued pressure wave. The time dependence of both incident and reflected waves are given by the same multiplicative factor $e^{i\omega t}$ hence the time dependence of the cumulative complex-valued pressure wave is also given by the same multiplicative factor $e^{i\omega t}$. Hence the pressure at any point in the tube at any time can be described using complex-valued pressure waves as follows,

$$
\begin{aligned}
p'(x,t) \;\; &= \Re\left[P^+ e^{i(\omega t - k^+ x)} + P^- e^{i(\omega t + k^- x)}\right] \\
&= \Re\left[\left(P^+ e^{-ik^+ x} + P^- e^{+ik^- x}\right) e^{i\omega t}\right] \\
&= \Re\left[P_x e^{i\omega t}\right]
\end{aligned}
$$

where

$$P_x = P^+ e^{-ik^+ x} + P^- e^{+ik^- x}. \tag{5.9}$$

When the propagating waves are subject to viscous forces, wave equation (Eq. 5.6) becomes nonhomogeneous. In order to take into account the visco-thermal attenuation in the thin acoustical boundary layer, real-valued wave numbers k^+ and k^- are replaced by complex-valued wave numbers

$$k^+ = \frac{\omega}{c_0 - U} + (1 - i)\alpha^+ \quad \text{and} \quad k^- = \frac{\omega}{c_0 + U} + (1 - i)\alpha^-. \tag{5.10}$$

where α^+ and α^- are the real-valued damping (attenuation) coefficients for upstream and downstream traveling waves.

The visco-thermal attenuation coefficient for plane wave propagation in a circular pipe has been studied extensively [Kirchhoff, 1868; Tijdeman, 1975; Ronneberger and Ahrens, 1977; Howe, 1984; Kergomard, 1985; Pierce, 1989; Peters et al., 1993]. For acoustic waves propagating in a quiescent medium for low Helmholtz numbers ($He \ll 1$) and for high shear numbers $Sh = R(\omega/\nu)^{1/2} \gg 1$, where ν is kinematic viscosity, viscothermal losses in the bulk of the flow can be neglected because dissipation is dominated by the viscothermal losses at the walls. The damping coefficient, α_0 then can be approximated by:

$$\alpha_0 = \frac{\omega}{c_0} \left(\frac{1}{\sqrt{2}Sh} \left(1 + \frac{\gamma - 1}{\sqrt{Pr}} \right) \right) \tag{5.11}$$

where γ is the ratio of the specific heats (Poissons's ratio) and Pr is the Prandtl number. For air at room temperature $\gamma = 1.4$, $Pr = 0.71$ and $\nu = 1.5 \times 10^{-5}$ m^2/s. For the experiments presented in this paper the upper bound for the Helmholtz number is $He \leq 0.08 \ll 1$ and the lower bound for the Shear number is $Sh \geq 174 \gg 1$.

In the presence of a mean flow the damping coefficient for the waves traveling upstream and downstream (α^+, α^-) deviate from the value (α_0) for a quiescent fluid. An important parameter in the determination of the damping coefficient in the presence of a mean flow is the ratio of acoustic boundary layer thickness (δ_{ac}) to viscous sublayer thickness (δ_l) [Ronneberger and Ahrens, 1977; Howe, 1984; Peters et al., 1993]:

$$\frac{\delta_{ac}}{\delta_l} = \frac{\sqrt{2\nu/\omega}}{10\nu/v^*} \tag{5.12}$$

where v^* is the friction velocity,

$$v^* = \sqrt{\frac{\tau_0}{\rho_0}}. \tag{5.13}$$

where τ_0 is the wall shear stress [Schlichting, 1979]. In the current experiment however, as shown in figure 5.4, the turbulent flow along the pipe is not fully developed and τ_0 is not known. Hence, a Reynolds-averaged Navier Stokes (RANS) simulation has been carried out to determine the wall shear stress τ_0 along the pipe.

The Reynolds-averaged Navier Stokes (RANS) simulations were performed with a commercial finite volume code FLUENT 6.3. The computational domain is the interior of the straight pipe segment between the exit of the expansion chamber muffler and the cavity, see figure 5.5. A 2D axisymmetric computational domain is used with 50×850 cells. The cells are clustered close to the wall such that the non-dimensional wall grid cell size is $y+ < 1$ throughout the pipe. The pressure-based segregated solution algorithm (SIMPLE) is employed. A second-order upwind space discretization was used for the convective terms. A standard $k - \omega$ turbulence model was utilized. As inlet boundary condition the curve fitted to the velocity profile measurements at the exit of the expansion chamber muffler is used (see figure 5.4, *Top-Hat Fit*). The numerical simulation was terminated when all residuals had dropped

at least eight orders of magnitude. In figure 5.4 the velocity profile that is obtained at the outlet of the computational domain (*Turbulent Num.*) is compared with the hotwire measurement at the same location (*Turbulent Exp.*). It is seen that the RANS simulation predicts accurately the velocity profile.

Using Eq. 5.12 and Eq. 5.13 with the numerically determined wall shear stress, the ratio of acoustic boundary layer thickness to viscous sublayer thickness is estimated to be in the range $0.49 < \delta_{\mathrm{ac}}/\delta_{\mathrm{l}} < 0.97$ for the current study. When the acoustic boundary layer is thinner than the viscous sublayer ($\delta_{\mathrm{ac}}/\delta_{\mathrm{l}} < 1$), the acoustic effect of the turbulent mixing can be neglected [Peters et al., 1993]. Thus, the quasi-laminar theory is expected to describe the damping of the acoustic waves quite accurately. Using a two dimensional flow model of Howe [1984] the damping coefficient is estimated as a function of the mean flow Mach number as:

$$
\frac{\alpha^+}{\alpha^-} = \frac{[1/(1 - Ma)^2] + (\gamma - 1)/\sqrt{Pr}}{[1/(1 + Ma)^2] + (\gamma - 1)/\sqrt{Pr}},
\tag{5.14}
$$

for the regime $\delta_{\mathrm{ac}}/\delta_{\mathrm{l}} < 1$. The upper bound of the Mach number that was reached in the experimental campaign is $Ma \leq 0.05$ and in average it is around $Ma = 0.03$. At such low Mach numbers the deviation in the damping coefficient of the upstream and downstream traveling waves ($\alpha^+ \; \alpha^-$) from the damping coefficient of the quiescent flow (α_0) is very small $0.02 < |\alpha^+ - \alpha_0|/\alpha_0 < 0.05$. Furthermore the deviations of the upstream and downstream traveling wave from α_0 have opposite signs, thus they largely compensate each other. Thus, in the current work the damping coefficient of the quiescent flow (α_0) given in Eq. 5.11 is used in both upstream and downstream traveling waves.

Determination of the maximum fluctuation amplitude

Knowing the pressure fluctuations at seven different spatial positions, $x_1, x_2, \ldots, x_7$, with a lock-in method [Kooijman et al., 2008] the equivalent complex-valued pressures at these positions $P^{\mathrm{m}}{}_{\mathrm{x}1}, P^{\mathrm{m}}{}_{\mathrm{x}2}, \ldots, P^{\mathrm{m}}{}_{\mathrm{x}7}$ can be obtained. Using the analysis given in Sec. 5.3.3, i.e. Eq. 5.9, an overdetermined system of equations can be written as

$$
\begin{pmatrix} P^{\mathrm{m}}{}_{\mathrm{x}1} \\ P^{\mathrm{m}}{}_{\mathrm{x}2} \\ \vdots \\ P^{\mathrm{m}}{}_{\mathrm{x}7} \end{pmatrix} = \begin{bmatrix} e^{-ik^+ x_1} & e^{ik^- x_1} \\ e^{-ik^+ x_2} & e^{ik^- x_2} \\ \vdots & \vdots \\ e^{-ik^+ x_7} & e^{ik^- x_7} \end{bmatrix} \cdot \begin{pmatrix} P^+ \\ P^- \end{pmatrix}.
\tag{5.15}
$$

Using linear regression based on a least squares approach P^+ and P^- are determined [Åbom and Bodén, 1988]. Using the calculated complex-valued wave amplitudes, the least squares fit of the pressure fluctuations at each transducer position can

be determined (P_{xi}). A maximum relative error bound for the least squares approach is given by:

$$E_{\mathrm{max}} = \frac{|P_{\mathrm{xi}} - P^{\mathrm{m}}{}_{\mathrm{xi}}|}{|P_{\mathrm{max}}|}, \quad i = 1, 2, ..., 7 \tag{5.16}$$

where $|P_{\mathrm{max}}|$ is the largest pressure fluctuation estimated in the standing wave. For all the data presented here $E_{\mathrm{max}} < 4\%$. Test of the setup by measurement of the reflection coefficient at a closed wall termination indicates an accuracy of the order of 1%.

In the rest of the paper the term *fluctuation amplitude* is used to specify the maximum dimensionless sound amplitude that is attained in the standing wave. The *fluctuation amplitude* is defined as

$$\frac{|p'_{\mathrm{max}}|}{\rho_0 c_0 U} = \frac{|u'_{\mathrm{max}}|}{U} \tag{5.17}$$

where $|p'_{\mathrm{max}}|$ is the amplitude of the standing pressure wave at a pressure anti-node inside the pipe and $|u'_{\mathrm{max}}|$ is the amplitude of acoustic velocity at a pressure node. Since the term *fluctuation amplitude* always refers to this maximum dimensionless sound amplitude; the subscript *max* will be dropped for convenience.

Determination of the acoustic energy flux

The time averaged acoustic source power ($\langle P_{\mathrm{source}} \rangle$) of the cavity can be estimated from the acoustic energy intensities going upstream, I_{up}, and downstream, I_{dwn} as:

$$\langle\langle P_{\mathrm{source}} \rangle\rangle = S_{\mathrm{p}} \left[\langle I_{\mathrm{up}} \rangle + \langle I_{\mathrm{dwn}} \rangle \right]. \tag{5.18}$$

The upstream energy flux can be determined just upstream of the cavity at x_{up}, see figure 5.5, for the plane wave propagation using the intensities of the incident and reflected waves as [Morfey, 1971]:

$$\langle I_{\mathrm{up}} \rangle = \frac{1}{2} \frac{(1 - Ma)^2 \left| P_{\mathrm{up}}^+ \right|^2 - (1 + Ma)^2 \left| P_{\mathrm{up}}^- \right|^2}{\rho_0 c_0}. \tag{5.19}$$

The distance between the downstream of the cavity, x_{dwn}, and the pipe termination, x_{trm}, is only 15 mm. The viscous losses in this segment of the pipe are neglected. Thus, the downstream acoustic energy flux of the cavity is assumed to be equal to the acoustic energy flux of the unflanged pipe termination, $\langle I_{\mathrm{dwn}} \rangle = \langle I_{\mathrm{trm}} \rangle$.

The acoustic energy flux of the downstream pipe termination is calculated using the theory of Munt [1977, 1990] for unflanged pipe opening at low Helmholtz numbers ($He \ll 1$) and low Mach numbers ($Ma \ll 1$), which has been derived by Cargill [1982] and Rienstra [1983]. The maximum values attained during the experiments $He \leq 0.08$ and $Ma \leq 0.05$ are inside the validity limits of this theory. Later there has been a number of experimental studies [Peters et al., 1993; Allam and Åbom,

2006] which support the theory. Following the theory of Munt [1977], the pressure reflection coefficient can be calculated as:

$$|R_{\text{trm}}| = (1 + Ma^*\mathcal{A})(1 - \frac{1}{2}He^2) \tag{5.20}$$

where $\mathcal{A}$ is the amplification factor, which is a function of Strouhal number $Sr_0 = He/Ma$ defined in Cargill [1971]. Ma^* could be the average Mach number ($Ma^* = Ma$) following Peters et al. [1993] or the axis Mach number ($Ma^* = Ma_{\text{axs}}$) of the duct as proposed by Allam and Åbom [2006] and da Silva et al. [2009], which is discussed later. Assuming that the source region is compact,

$$\left|u'_{\text{up}}\right| = \left|u'_{\text{dwn}}\right|. \tag{5.21}$$

Combining Eq. 5.20 and Eq. 5.21, the downstream acoustic energy flux of the cavity is estimated as:

$$\langle I_{\text{dwn}} \rangle = \frac{1}{2} \frac{(1 + Ma)^2 \left|P^+_{\text{dwn}}\right|^2 - (1 - Ma)^2 \left|P^-_{\text{dwn}}\right|^2}{\rho_0 c_0} \tag{5.22}$$

where,

$$\left|P^+_{\text{dwn}}\right| = \frac{\left|u'_{\text{up}}\right| \rho_0 c_0}{1 - |R_{\text{trm}}|} \qquad \left|P^-_{\text{dwn}}\right| = \left|P^+_{\text{dwn}}\right| |R_{\text{trm}}|. \tag{5.23}$$

Configuration C, see figure 5.1, is actually designed as a test case to assess the accuracy of the calculated acoustic intensity at the downstream termination $\langle I_{\text{trm}} \rangle$ in configuration A. In configuration C, $\langle I_{\text{trm}} \rangle$ can be directly measured using the microphone array downstream of the cavity, similar to the upstream acoustic intensity $\langle I_{\text{up}} \rangle$ for configuration A (Eq. 5.19). Comparison of this directly measured $\langle I_{\text{trm}} \rangle$ with the $\langle I_{\text{trm}} \rangle$ which is calculated using the acoustic velocity measured by upstream microphone array together with the theory of Munt and the compact source region assumption (Eq. 5.19-Eq. 5.22) provides a measure of accuracy, see table 5.1. As proposed by Allam and Åbom [2006] based on the work of Freymunt [1966] on the growth of disturbances at the outlet of a circular jet, using the axis Mach number $Ma^* = Ma_{\text{axs}}$ rather than the average Mach number $Ma^* = Ma$ of the duct in the theory Munt provides acoustic intensity predictions at the downstream termination, which are closer to the experiments. Later da Silva et al. [2009] also reported in their numerical work that better agreement with the theory is achieved with $Ma^* = Ma_{\text{axs}}$. Thus, in the current work the theory of Munt with $Ma^* = Ma_{\text{axs}}$ is used, see Eq. 5.20.

As explained for configuration A, the downstream acoustic intensity $\langle I_{\text{dwn}} \rangle$ is estimated from the theory of Munt. This approach systematically overestimates the $\langle I_{\text{total}} \rangle / (\rho_0 U |u'|^2)$ by approximately 15%. This provides an upper bound for our experimental error in the energy balance. By using configuration C, this systematic error in $\langle I_{\text{dwn}} \rangle$ can be avoided. Configuration C, however, has the second downstream pipe section which introduces extra viscous losses. As a consequence, the cavities

Methods	$\langle I_{\mathrm{trm}} \rangle / (\rho_0 U |u'|^2)$	$\langle I_{\mathrm{total}} \rangle / (\rho_0 U |u'|^2)$	Error in $\langle I_{\mathrm{total}} \rangle$
Direct Measurement	0.1587	0.8123	N/A
Munt's Theory ($Ma^* = Ma$)	0.3018	0.9721	+19.7%
Munt's Theory ($Ma^* = Ma_{\mathrm{axs}}$)	0.2666	0.9339	+14.9%

Table 5.1: Comparison of different methods for the calculation of the downstream termination acoustic energy flux $\langle I_{\mathrm{trm}} \rangle$ and its error on the total acoustic energy flux of the cavity $\langle I_{\mathrm{total}} \rangle$, for configuration C for $H/W = 0.675$.

whistles at lower amplitudes, which makes the source power prediction more difficult as explained in Sec. 5.5.2. Thus the effect of cavity depth on the whistling, understanding of which is the main objective of this paper, is investigated using configurations A and B.

5.4 Numerical Method

In a previous work of the authors Nakiboğlu et al. [2011a], a numerical methodology was proposed to investigate the aeroacoustic response of low Mach number confined flows to acoustic excitations. The method combines incompressible flow simulations with Vortex Sound Theory to estimate the strength of an acoustic source due to the interaction of a single cavity in a pipe flow at high Reynolds number with a low Helmholtz number acoustic field. This numerical approach is used in the present study for the investigation of two features. Firstly, to explore the capacity of the method in estimating the whistling amplitude for a system for which the acoustic losses can be accurately determined. Secondly, to explore whether the method can predict the influence of the cavity depth on the whistling behaviour i.e. peak-whistling Strouhal number and produced time averaged acoustic source power. In the first part of this section, the numerical simulations are briefly explained. In the second part, the calculation of the average acoustic source power is described.

5.4.1 Incompressible simulations

Knowing that the cavity width W (40 mm) is much smaller than the wavelength of the longitudinal standing wave λ (1750 mm), one can assume that the wave propagation time is locally negligible. Furthermore only low Mach numbers ($Ma \leq 0.05$) are considered. This corresponds to the assumption that the flow is locally incompressible [Martínez-Lera et al., 2009]. Therefore incompressible 2D-axisymmetric flow simulations were performed. The simulations were carried out at low Reynolds numbers ($Re = 4 \times 10^3$) without turbulence modeling. The diameter of the pipe (D) and the geometry of the cavity ($W, H, r_{\mathrm{up}}, r_{\mathrm{dwn}}$) are identical to the ones in the experiments. The inlet is located at $0.175W$ upstream of the cavity; such a short in-

let pipe section is chosen to make sure that the imposed inlet mean velocity profiles do not evolve significantly before reaching the cavity. The outlet of the numerical domain is placed at a reasonably far location, $9W$ downstream, from the cavity.

The finite volume commercial code FLUENT 6.3 is used. A pressure-based segregated solution algorithm is employed, the details of the simulation parameters are provided in Nakiboğlu et al. [2011a]. At the inlet a uniform acoustic oscillating velocity in the axial direction with a frequency, f, and an amplitude, $|u'|$:

$$u'(t) = |u'| \sin(2\pi\, f\, t). \tag{5.24}$$

is imposed in addition to the time averaged inlet velocity profile, u(r):

$$u(r,t) = u(r) + u'(t) \tag{5.25}$$

where $|u'|$ is the amplitude of the acoustic velocity induced by the longitudinal standing wave at the position of the cavity. In all the experiments performed, the cavity is placed close to a pressure node. Thus, through out the paper $|u'|$ stands for the maximum amplitude of the acoustic oscillation velocity in the standing wave, see Sec 5.3.3. The mean velocity profile $u(r)$ is determined experimentally. These profiles correspond to two different cavity positions: at the end of the straight pipe *Turbulent Fit* (configuration A) and at the inlet of the straight pipe *Top-Hat Fit* (configuration B), see figure 5.4. The outlet boundary condition $\partial u_x/\partial x = 0$ is used. After checking different simulation times, for the majority of the simulations, a typical time of 30 periods of the excitation frequency appeared to be sufficient to reach steady periodic results. For some simulations, however, steady periodic results are achieved only after 70 periods of the excitation frequency. After the solution has reached a steady periodic state, the simulation is continued for 10 more periods, which are used to calculate the time-averaged acoustic source power. The time step size is chosen as $\Delta t = 0.01W/U$.

The computational domains contain 8×10^4 to 1.2×10^5 quadrilateral cells depending on the cavity depth. The cells are clustered close to the opening of the cavity and to the walls, where there are high gradients of the velocity due to the shear layer and the boundary layer, respectively. In the domain between $6W$ and $9W$ downstream of the cavity, cells with high aspect ratio ($\Delta x/\Delta y \gg 1$) are employed. By doing so problems that can arise due to reverse flow at the outlet boundary condition are avoided. A study on mesh dependency has been carried out. The same computation was performed with 2 times and 4 times more densely meshed domains, producing differences in the calculated acoustic source power of less than 5%.

5.4.2   Time-averaged acoustic source power

Both the Vortex Sound Theory of Howe [1975, 1998] and the exact energy corollary of Myers [1986, 1991] asserts that for high Reynolds number flows, in which the effect

of friction in the bulk of the fluid is small enough to be neglected, the time averaged acoustic source power generated in a control volume, $\langle P_{\text{source}} \rangle$, is equal to the surface integral of the product of fluctuating total enthalpy, B', and mass flux, $\mathbf{m}'$, through the boundary of the control volume:

$$\langle P_{\text{source}} \rangle = \left\langle \int_S (B' \mathbf{m}') \cdot \mathbf{n} dS \right\rangle \tag{5.26}$$

where

$$B' = \frac{p'}{\rho_0} + \mathbf{u} \cdot (\mathbf{u}' + \mathbf{u}'_\mathbf{h}),$$
$$\mathbf{m}' = \rho_0 (\mathbf{u}' + \mathbf{u}'_\mathbf{h}) + \rho' \mathbf{u}$$

where $\mathbf{u} = (U, 0, 0)$ is the time averaged velocity and the fluctuations are split into the acoustical (potential) part $\mathbf{u}'$ and the hydrodynamical (rotational) part $\mathbf{u}'_\mathbf{h}$. In further calculations ρ' is neglected, in agreement with the use of incompressible flow simulations. The contribution of the hydrodynamic velocity fluctuations ($\mathbf{u}'_\mathbf{h}$) to Eq. 5.26 is also neglected. The contribution of the hydrodynamic velocity fluctuations is expected to depend on the spatial location of the control surface. It has been verified that by choosing a large enough control volume, such a dependence is avoided [Nakiboğlu et al., 2011a], so that there is no hydrodynamic contribution to the integral in Eq. 5.26.

Since the simulations are performed at low Reynolds numbers the viscous flow effects are not accurately described, the simulations are corrected by subtracting the total enthalpy differences $(\Delta B')_{\text{ref}}$ obtained from simulations of the flow in a uniform reference pipe segment with the same upstream and downstream boundary conditions as the numerical simulation of the duct with the cavity. This correction can be interpreted as an extrapolation method to high Reynolds numbers, in which the solution becomes Reynolds number independent. This has been demonstrated by Nakiboğlu et al. [2011a]. The acoustic power produced by the source is calculated in practice as follows:

$$\langle P_{source} \rangle = \rho_0 \left\langle \frac{1}{4} \left[(B'_{x_2} - B'_{x_1})_{\text{cav}} - (B'_{x_2} - B'_{x_1})_{\text{ref}} \right] u' \pi D^2 \right\rangle \tag{5.27}$$

in which x_1 and x_2 denote any two measurement sections in the computational domain, where the area-averaged total enthalpy, B', is recorded at every time step.

5.5 Results

5.5.1 Effect of velocity profile and hydrodynamic modes

The mean velocity profile is known to have a strong effect on the whistling of corrugated pipes, which can be considered as a series of axisymmetric cavities along a

Figure 5.6:
Measured dimensionless pressure fluctuation amplitude $|u'|/U$ plotted against Strouhal number $Sr = f(W + r_{\text{up}})/U$ for configurations A and B.
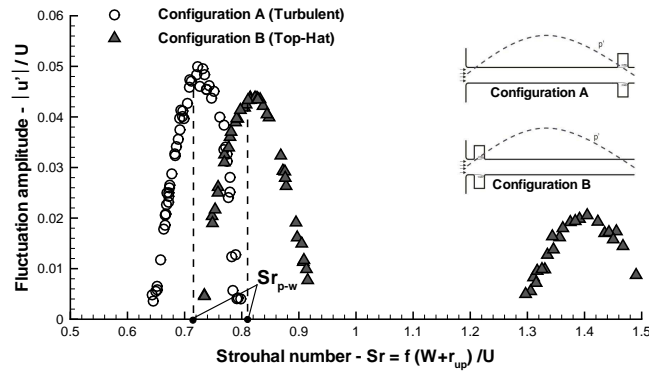
pipe [Nakiboğlu et al., 2011a, 2012]. In the current work, this aspect is briefly considered for a single axisymmetric cavity. In figure 5.6 measured fluctuation amplitude $|u'|/U$ is plotted against Strouhal number $Sr = f(W + r_{\text{up}})/U$ for the cases for which the cavity is placed close to the downstream pipe termination (configuration A) and upstream pipe termination (configuration B). It should be noted that the cavity position with respect to the standing wave remains invariant for configurations A and B. Although there is a minor difference between the two configurations due to the vortex shedding at the upstream edge of the cavity, considering the acoustics they are almost identical. Thus, the variation in the whistling behaviour of these two configurations is mainly due to the difference in the velocity profile that the cavities are experiencing, see figure 5.4.

There are four points that can be highlighted from figure 5.6. Firstly, in configuration A there exist only one range of Strouhal numbers, $0.65 \leq Sr \leq 0.80$, for which the whistling is observed, whereas for configuration B there exist two distinct ranges of whistling, $0.74 \leq Sr \leq 0.92$ and $1.30 \leq Sr \leq 1.50$. The fact that the whistling does not occur for the higher Strouhal number range ($1.30 \leq Sr \leq 1.50$) for configuration A can be explained through the difference in the mean flow velocity profiles for these two configurations. For low amplitudes the hydrodynamic growth of the perturbation along the shear layer at the cavity opening can be calculated by using the linearized theory of an inviscid quasi-parallel free shear layer [Michalke, 1965; Elder, 1980]. According to this theory the hydrodynamic growth of the perturbation along the shear layer will occur only at frequencies with sufficiently small Strouhal numbers, $Sr_{\delta2} < 4.0 \times 10^{-2}$ where $Sr_{\delta2} = f\delta_2/U$ and δ_2 is the initial shear layer momentum thickness. Above this critical Strouhal number the shear layer is linearly stable. Using the profile measurements, see Sec. 5.3.2, Strouhal numbers based on the boundary layer momentum thickness (δ_2) are calculated at $Sr = 1.4$ as $Sr_{\delta2} = 3.8 \times 10^{-2}$ and $Sr_{\delta2} = 6.2 \times 10^{-3}$ for configurations A and B, respectively. Although both of the calculated $Sr_{\delta2}$ are in the favorable range for the growth of unstable waves, for configuration A it is very close to limit value of
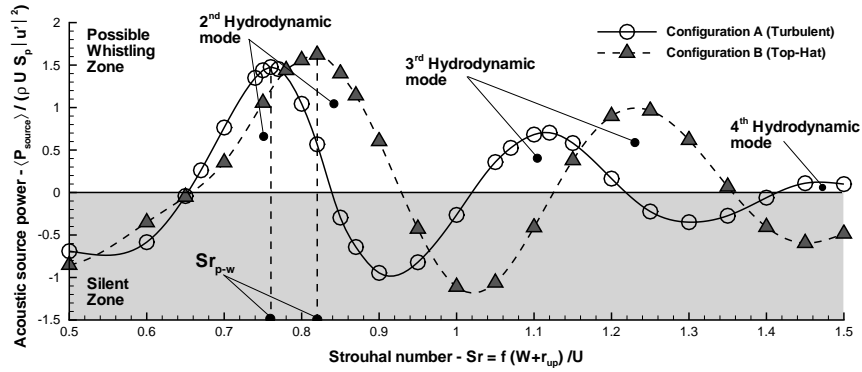
Figure 5.7: Predicted dimensionless average acoustic source power $\langle P_{\mathrm{source}}\rangle/(\rho_0 U S_{\mathrm{p}}|u'|^2)$ plotted against Strouhal number $Sr = f(W + r_{\mathrm{up}})/U$ for configurations A and B for a fluctuation amplitude of $|u'|/U = 0.05$.

$Sr_{\delta2} = 4.0 \times 10^{-2}$. Hence the hydrodynamic amplification for the higher Strouhal number range ($1.30 \leq Sr \leq 1.50$) will be considerably weaker for configuration A than for configuration B. Given that the acoustic losses are comparable for these two configurations, it is not surprising that whistling does not occur at the higher Strouhal number range for configuration A.

Secondly, it is clear that the whistling is stronger in the lower Strouhal number range compared to the whistling in higher Strouhal number range. These different range of Strouhal numbers correspond to different hydrodynamic modes, where different numbers of vortices appear simultaneously at the mouth of the cavity, see Peters [1993]. The present work is kept mostly limited to the lower Strouhal number range, in which the system whistles stronger. The Strouhal number in which the maximum amplitude in pressure fluctuations is attained, is called peak-whistling Strouhal number $Sr_{\mathrm{p-w}}$. Thirdly, within the lower range of Strouhal numbers in which the system whistles, configuration B whistles at higher Strouhal numbers than configuration A. This shift is expected to be linked to the difference in the momentum thickness of the boundary layer [Nakiboğlu et al., 2011a]. The last point is that there is not a large difference between the two configurations in the maximum fluctuation amplitudes for the lower range of Strouhal numbers.

Using the numerical method summarized in Sec. 5.4, the dimensionless average acoustic source power $\langle P_{\mathrm{source}}\rangle/(\rho_0 U S_{\mathrm{p}}|u'|^2)$ is calculated for configurations A and B. Experimentally determined profiles are used as inlet velocity profile, see figure 5.4. The simulations have been performed with a perturbation amplitude of $|u'|/U = 0.05$, which is the maximum amplitude attained during the experiments. In figure 5.7 the predicted dimensionless average acoustic source power is plotted as a function of Strouhal number for both configurations.

Similarly to the experimental observations, the numerical method predicts a pos-

itive acoustic source power $\langle P_{\text{source}}\rangle/(\rho_0 U S_{\text{p}}|u'|^2)$ at higher Strouhal numbers for configuration B (Top-Hat) compared to configuration A (Turbulent). The predicted peak-whistling Strouhal numbers ($Sr_{\text{p-w}}$), at which the maximum average acoustic source power $\langle P_{\text{source}}\rangle$ is registered, are $Sr_{\text{p-w}} = 0.76$ and $Sr_{\text{p-w}} = 0.82$ for configurations A and B, respectively. These values are very close to the measured peak-whistling Strouhal number in the experiments which are $Sr_{\text{p-w}} = 0.73$ and $Sr_{\text{p-w}} = 0.82$, respectively. It can also be noted that similar to the experiments, the maximum average acoustic source powers reached for the two configurations are close to each other.

In parallel to the experiments, in figure 5.7 there exist distinct ranges of Strouhal numbers, in which the average acoustic source power $\langle P_{\text{source}}\rangle$ is positive. In figure 5.8 normalized vorticity contours are given at the cavity mouth for configuration A for a perturbation amplitude of $|u'|/U = 0.05$ at three different Strouhal numbers which belong to three different ranges of positive acoustic source power, namely, $Sr = 0.76, 1.12$ and 1.5. It is seen that the number of vortices appearing simultaneously at the cavity mouth differs in these three cases. The first positive Strouhal number range, around $Sr = 0.76$, is identified by Bruggeman et al. [1991] as the second hydrodynamic mode, at which there exist two vortices at the same moment in the cavity mouth: one traveling and one forming. Similarly, the positive Strouhal number ranges around $Sr = 1.12$ and $Sr = 1.5$ are the third and the fourth hydrodynamic modes, respectively. It should be pointed out that a positive time averaged acoustic source power is a necessary condition for whistling but not a sufficient one. A negative time averaged acoustic source power, however, is a sufficient condition for silence. Thus, Strouhal number ranges with negative source power remain silent. To determine the occurrence of the whistling for the positive source power range, the produced acoustic source power should be compared with the acoustic losses by means of an energy balance. This also quantifies the amplitude comparison between experiments and simulations, which will be explained in the next section.

5.5.2 Limit cycle amplitude due to nonlinear saturation

The aeroacoustic behaviour of cavities and side branches depends strongly on the fluctuation amplitude $|p'|/(\rho_0 c_0 U) = |u'|/U$. For low amplitudes, $|u'|/U \leq O(10^{-3})$, the instability of shear layers corresponding to the second hydrodynamic mode can be explained by using the linear theory for frictionless parallel flows [Michalke, 1965]. In the linear range the acoustic source power $\langle P_{\text{source}}\rangle$ grows quadratically with the perturbation amplitude. Above $|u'|/U \geq O(10^{-3})$ the nonlinearities become essential [Tam and Block, 1978]. In this range, the amplitude of the oscillations is determined by nonlinearities, such as roll-up of the shear layer into discrete vortices [Fletcher, 1979; Keller, 1984; Bruggeman et al., 1991; Rowley et al., 2006].

In figure 5.9 estimated dimensionless average acoustic source power is plotted against fluctuation amplitude $|u'|/U$ for configuration A at Strouhal number $Sr =$
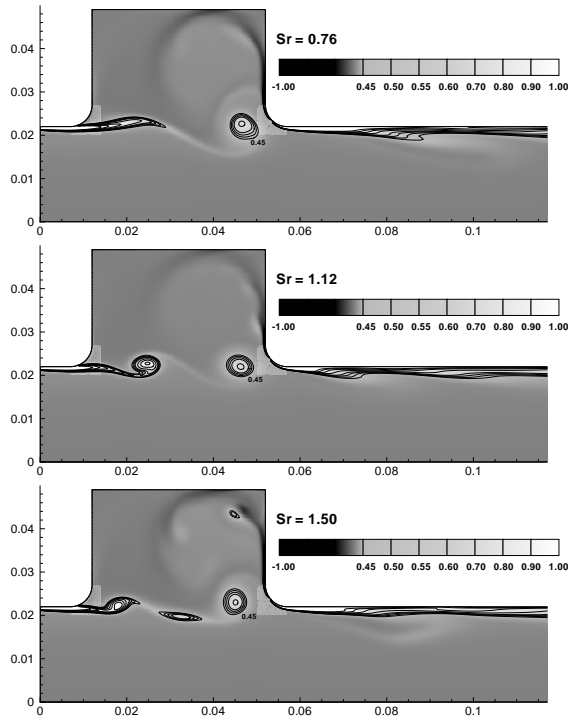
Figure 5.8: Predicted normalized vorticity contours are given in the proximity of the cavity for configuration A for three different Strouhal numbers: $Sr = 0.76$ (a); $Sr = 1.12$ (b); $Sr = 1.5$ (c) for a fluctuation amplitude of $|u'|/U = 0.05$.

0.76. As expected from the linear theory for low amplitudes $|u'|/U \leq O(10^{-3})$, the numerical method predicts a quadratic increase of $\langle P_{\text{source}} \rangle$ so that dimensionless average acoustic source power $\langle P_{\text{source}} \rangle/(\rho_0 U S_{\text{p}} |u'|^2)$ remains approximately constant. The fluctuation amplitudes that are recorded in the experiments are in the range $5 \times 10^{-3} \leq |u'|/U \leq 6 \times 10^{-2}$, which is in the nonlinear regime.

Using figure 5.9, experimental and numerical data can be quantitatively compared in two ways. In the first approach, all the possible acoustic losses, e.g., visco-thermal, convective and radiative, in the system are estimated. Equalizing the sum of time averaged acoustic power losses to the time averaged acoustic source power, a horizontal line can be drawn in figure 5.9 (shown in dashed line *measured acoustic losses*). The intersection point of this horizontal line and the predicted time averaged acoustic source power curve determines at which fluctuation amplitude this energy balance equilibrates (shown in dashed vertical line *predicted fluctuation amplitude*). It can happen that the calculated acoustic losses are so high that the corresponding horizontal line stays above the source curve, then the system will not whistle. It is seen from figure 5.9 that just below this non-whistling zone, in the linear range, a small change in the acoustic losses results in a large variation in the limit cycle fluctuation amplitude. This is demonstrated in Sec. 5.5.3. The second approach is in fact the inverse of the first approach. Thus, the measured fluctuation amplitude is taken from

Figure 5.9: Predicted dimensionless time averaged acoustic source power $\langle P_{\text{source}}\rangle/(\rho_0 U S_{\text{p}}|u'|^2)$ plotted against fluctuation amplitude $|u'|/U$ at Strouhal number $Sr = 0.76$ for configuration A for a depth to width ratio of $H/W = 0.675$.
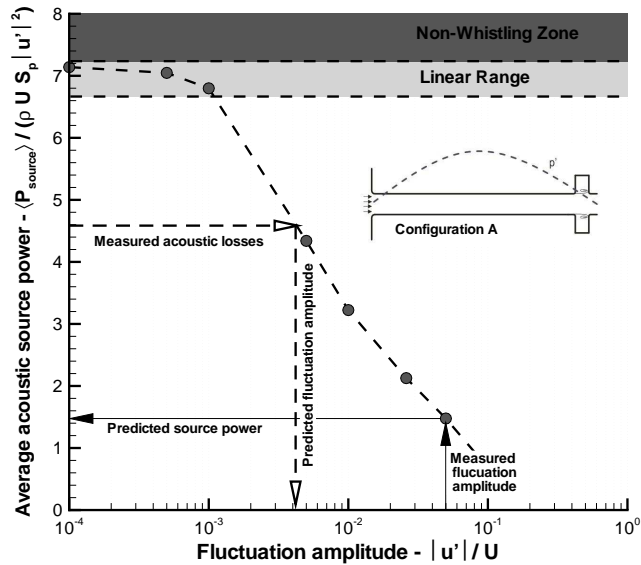
the experiment and a vertical line is drawn in figure 5.9 (shown in continuous line *measured fluctuation amplitude*) and the intersection with the source curve determines the time averaged acoustic source power necessary to produce this fluctuation amplitude (shown in continuous horizontal line *predicted source power*). The predicted time averaged source power can be compared with the measured one obtained by means of the multi-microphone method, see Sec. 5.3.3.

It should be noted that figure 5.9 is only valid for a single Strouhal number ($Sr = 0.76$) at which the simulations have been performed. Thus, to compare all of the experimental data with the numerical data a separate set of simulations with various perturbation amplitudes $|u'|/U$ should be carried out at each relevant Strouhal number. Such an approach is computationally heavy and does not provide further insight to the phenomenon than a comparison based on the peak amplitude. Therefore the current analysis is limited to the peak-Strouhal number of the second hydrodynamic mode. In the next section, the effect of the cavity depth on the whistling is discussed, including the quantitative comparison of the experimental data with theory is presented.

5.5.3   Effect of cavity depth

The effect of cavity depth on the whistling is investigated for acoustically compact cavities i.e. cavities in which the acoustics is dominated by the longitudinal standing wave in the pipe to which the cavity is attached. A broad range of cavity depth to cavity width ratios $0.2 \leq H/W \leq 1.175$ has been investigated both for config-

Figure 5.10: Measured dimensionless pressure fluctuation amplitude $|u'|/U$ plotted against Strouhal number $Sr = f(W + r_{\text{up}})/U$ for configuration A (exper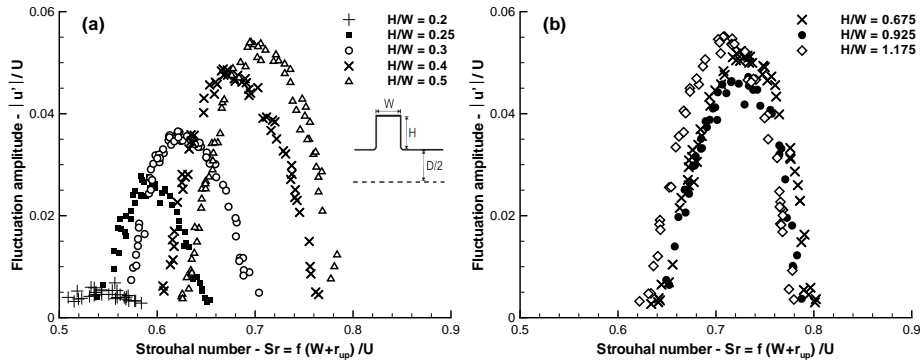iencing a turbulent approach velocity profile, see figure 5.4), with depth to width ratio of $H/W = 0.2, 0.25, 0.3, 0.4, 0.5$ (a) and $H/W = 0.675, 0.925, 1.175$ (b).

uration A (turbulent profile) and configuration B (top-hat profile). In this section first the salient features of the experimental data are listed. Physical phenomena behind those features will be explained later together with the predictions from the numerical method. In figure 5.10 and figure 5.11 measured dimensionless fluctuation amplitude $|u'|/U$ is plotted against Strouhal number $Sr = f(W + r_{\text{up}})/U$ for cavities with depth to width ratios of $H/W = 0.2, 0.25, 0.3, 0.4, 0.5$ (a) and $H/W = 0.675, 0.925, 1.175$ (b) for configuration A and for configuration B, respectively.

The first aspect, that is recognized from figure 5.10-a and figure 5.11-a is that, in the range $0.2 \leq H/W \leq 0.5$, as the cavity gets deeper the cavity whistles at higher Strouhal numbers and at higher amplitudes for both configurations. The second notable feature of figure 5.10-a is the sudden decrease of whistling amplitude from $|u'|/U = 3 \times 10^{-2}$ to $|u'|/U = 5 \times 10^{-3}$ with a relatively small decrease in the depth of the cavity from $H/W = 0.25$ to $H/W = 0.2$. A similar sudden drop is observed for configuration B when H/W decreases from 0.3 to 0.25, as shown in figure 5.11-a. Note that the peak amplitude does not vary much in the deep cavity range of $0.675 \leq H/W \leq 1.175$ for both configurations, see figures 5.10-b and 5.11-b. This is highlighted in figure 5.12 where the peak fluctuation amplitude $|u'|/U$ is plotted against cavity depth to width ratio (H/W) for both configurations. It is also seen that the recorded peak amplitudes are close to each other for the two configurations and their responses to a change in the cavity depth are similar.

In figure 5.13 predicted acoustic source power $\langle P_{\text{source}}\rangle/(\rho_0 U S_{\text{p}}|u'|^2)$ is plotted against Strouhal number $Sr = f(W + r_{\text{up}})/U$ for configuration A for a perturbation amplitude $|u'|/U = 0.05$ with depth to width ratio of $H/W = 0.2, 0.25, 0.3, 0.4, 0.5$ (a) and $H/W = 0.675, 0.925, 1.175$ (b). It is seen that similar to the experiments (see, figure 5.10) for the shallow cavity range ($H/W < 0.5$) as the cavity gets deeper
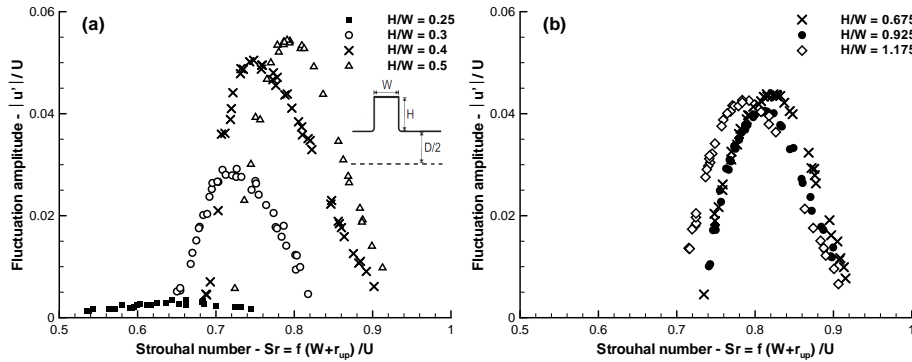
Figure 5.11: Measured dimensionless pressure fluctuation amplitude $|u'|/U$ plotted against Strouhal number $Sr = f(W + r_{\mathrm{up}})/U$ for configuration B (experiencing a top-hat approach velocity profile, see figure 5.4), with depth to width ratios of $H/W = 0.2, 0.25, 0.3, 0.4, 0.5$ (a) and $H/W = 0.675, 0.925, 1.175$ (b).

Figure 5.12:
Measured dimensionless pressure fluctuation amplitude $|u'|/U$ is plotted against cavity depth to width ratio (H/W) for the peak amplitudes for configurations A and B.
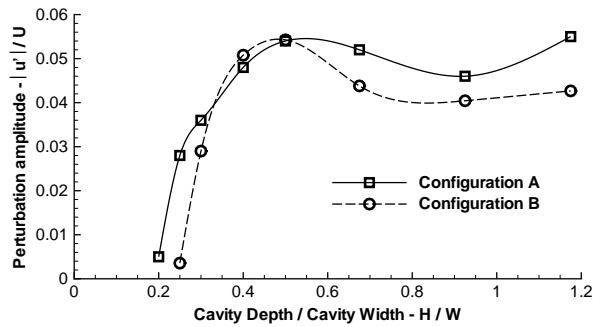
the positive acoustic source power range shifts to higher Strouhal numbers and the estimated acoustic source power increases. In the deep cavity range $0.675 \leq H/W \leq 1.175$ similar to the experimental observations the estimated peak-whistling Strouhal number and the acoustic source power do not vary considerably.

In figure 5.14 measured and estimated peak-whistling Strouhal numbers ($Sr_{\mathrm{p-w}}$), that are extracted from figures 5.10, 5.11 and 5.13, are plotted against the cavity width to depth ratio (W/H). It can be noted that there is almost a constant shift between configuration A and B for peak-whistling Strouhal number independently of the cavity depth. This suggests that the effect of velocity profile on the Strouhal number, which is discussed for a single cavity depth in Sec. 5.5.1, is independent of the cavity depth. The second point is that in the range $0.5 \leq W/H \leq 1.5$ (corresponding to $0.2 < H/W < 0.675$) there is a linear relationship between the peak-whistling Strouhal number and the cavity width to depth (W/H) ratio. This effect can be explained as a reduction of the convection speed of the vortex at the cavity mouth (U_c) due to the presence of the image vortex at the bottom of the shallow cavity (see
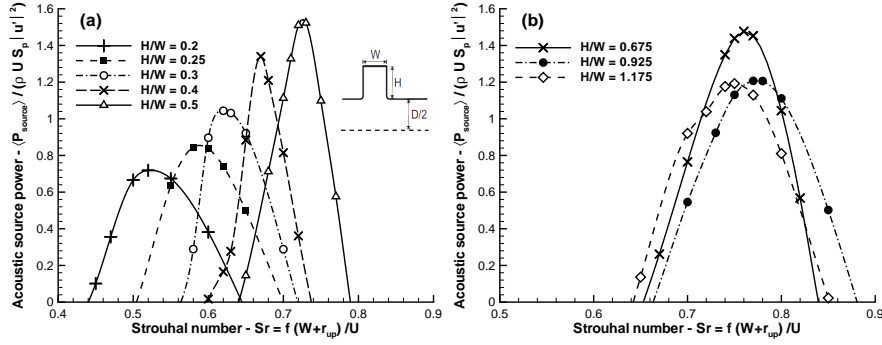
Figure 5.13: Predicted dimensionless average acoustic source power $\langle P_{\text{source}}\rangle/(\rho_0 U S_{\text{p}} |u'|^2)$ plotted against Strouhal number $Sr = f(W + r_{\text{up}})/U$ for configuration A at a perturbation amplitude of $|u'|/U = 0.05$, with depth to width ratio of $H/W = 0.2, 0.25, 0.3, 0.4, 0.5$ (a) and $H/W = 0.675, 0.925, 1.175$ (b).

figure 5.15) as

$$U_{\text{c}} = \frac{U}{2} - \frac{\Gamma}{4\pi H}. \tag{5.28}$$

The first term of the Eq. 5.28 is simply the average between the main flow velocity (U) and the low velocity of the fluid within the cavity. The second term is the velocity induced by the image vortex with a circulation of Γ at a distance of $2H$ from the cavity mouth. The image vortex has the same magnitude of the circulation as the real vortex. Following the model of Nelson et al. [1983], in which all the vorticity of the shear layer is concentrated into a point vortex, at moderate amplitudes $10^{-2} \leq |u'|/U \leq 10^{-1}$ the rate of vorticity shed ($d\Gamma/dt$) remains equal to its steady value $d\Gamma/dt = U U_{\text{c}}$ [Bruggeman et al., 1991; Dequand et al., 2003a]. Thus, the average circulation obtained in a period is

$$\Gamma = U (W + r_{\text{up}})/2. \tag{5.29}$$

Rewriting the Strouhal number as

$$Sr = \frac{f(W + r_{\text{up}})}{U} = \frac{f(W + r_{\text{up}})}{U_{\text{c}}} \frac{U_{\text{c}}}{U} \tag{5.30}$$

and combining with Eq. 5.28 and Eq. 5.29, gives

$$Sr = \frac{f(W + r_{\text{up}})}{2 U_{\text{c}}} \left(1 - \frac{W + r_{\text{up}}}{4\pi H}\right). \tag{5.31}$$

The first term of Eq. 5.31 is constant because the travel time of the vortex through the cavity mouth, $T_{\text{travel}} = (W + r_{\text{up}})/U_{\text{c}}$, should be a fixed fraction of the acoustic oscillation period, $T_{\text{period}} = 1/f$, [Bruggeman et al., 1991]. This constant can be
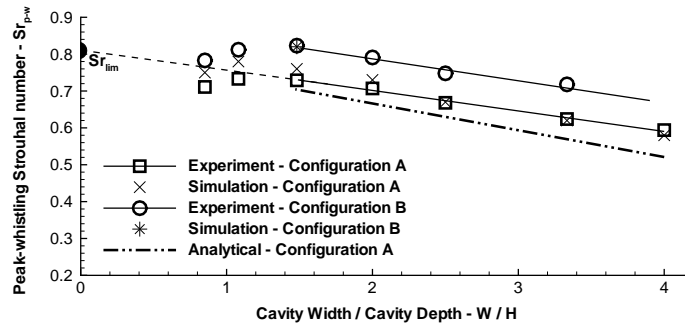
Figure 5.14: Measured and numerically and analytically predicted peak-whistling Strouhal numbers $Sr_{\mathrm{p-w}}$ plotted against the cavity width to depth ratio (W/H) for configurations A and B. Simulations were performed at a typical perturbation amplitude of $|u'|/U = 0.05$.

Figure 5.15: Schematic drawing of a concentrated vortex core at the cavity mouth and its image at the bottom of the cavity.
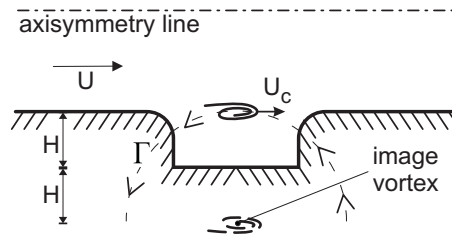
considered as a limiting Strouhal number (Sr_{lim}) for an infinitely deep cavity, i.e. the image vortex at the bottom of the cavity has no effect on the convection speed of the vortex at the cavity mouth. The limiting Strouhal number is determined through an extrapolation of the experimental data to $W/H = 0$, as $Sr_{\mathrm{lim}} = 0.81$, see figure 5.14. The second term of Eq. 5.31 is the cavity width to depth dependency (W/H) of the peak-whistling Strouhal number $(Sr_{\mathrm{p-w}})$. The predicted $Sr_{\mathrm{p-w}}$ from Eq. 5.31 is shown in figure 5.14 (with label *Analytical*). It is seen that for the shallow cavity range $0.5 \leq W/H \leq 1.5$ this analytical model, which takes only the image vortex at the bottom of the cavity into account, provides reasonable predictions. The measured slope of the $Sr_{\mathrm{p-w}}$ as a function of W/H is $d\,Sr/d\,(W/H) = -5.5 \times 10^{-3}$ while the analytically predicted slope is $d\,Sr/d\,(W/H) = -7.2 \times 10^{-3}$. For $W/H < 1.5$ this linear relation does not hold anymore. For such deep cavities the effect of the image vortex in the bottom becomes negligible compared to the effect of the side walls. This can be studied more systematically by means of a single vortex model using conformal mapping as proposed by Howe [1998].

As it is seen in figure 5.14, the proposed numerical method produces excellent predictions of the peak-whistling Strouhal number. It also captures the relationship for the deep cavities, although the predictions are not as good as the ones for the shallow cavities. Systematic simulations for configuration B (top-hat profile) were

not performed. A point obtained from figure 5.7 is shown in the figure 5.14.

Note that in figure 5.14 the depth to width ratio of $H/W = 0.2$ for configuration A and $H/W = 0.25$ for configuration B are not included. As it is seen from figure 5.10 and figure 5.11, respectively these two cases whistle at low amplitudes $|u'|/U \leq 5 \times 10^{-3}$. At such low amplitudes, the shear layer does not roll up into discrete vortices. Hence the image at the bottom of the cavity does not have a strong influence on the convection speed. This effect is illustrated in figure 5.16-a where the predicted peak-whistling Strouhal number $Sr_{\mathrm{p-w}}$ is plotted against the perturbation amplitude $|u'|/U$ for cavity depth to width ratios of $H/W = 0.2$, $H/W = 0.675$ and $H/W = 1.175$ for configuration A. Note that every point in this figure corresponds to a peak of a set of simulation at various Strouhal numbers with the same perturbation amplitude $|u'|/U$. It is seen that for a shallow cavity, $H/W = 0.2$, there are two distinct regions. For moderate amplitudes $10^{-2} \leq |u'|/U \leq 10^{-1}$ there is a strong dependency of perturbation amplitude on the peak-whistling Strouhal number. The peak-whistling Strouhal number shifts from $Sr_{\mathrm{p-w}} = 0.64$ to $Sr_{\mathrm{p-w}} = 0.48$ when increasing the perturbation amplitude from $|u'|/U = 10^{-2}$ to $|u'|/U = 10^{-1}$. In the low amplitude range $|u'|/U \leq 10^{-2}$ the peak-whistling Strouhal number remains independent of the amplitude as predicted by the linear theory. For deep cavities, i.e. $H/W \geq 0.675$, the peak-whistling Strouhal number remains almost constant independently of the depth and the perturbation amplitude. For deep cavities it is expected that the image vortex at the bottom of the cavity does not play a significant role.

In figure 5.16-b the predicted average acoustic source power that is obtained at the respective peak-whistling Strouhal number $Sr_{\mathrm{p-w}}$ is plotted against the perturbation amplitude $|u'|/U$ for the same depths ($H/W = 0.2$, $H/W = 0.675$ and $H/W = 1.175$) for configuration A. Deep cavities $H/W \geq 0.675$ produce almost equivalent amplitudes independent of the depth. The theory predicts that deep cavities produce higher average acoustic source power than shallow cavities at all perturbation amplitudes but at moderate amplitude range $|u'|/U \geq 10^{-2}$, as the perturbation amplitude increases, the difference in the average acoustic source power is becoming smaller. Furthermore for the deep cavities the nonlinearities appear already around $|u'|/U \geq 10^{-3}$, i.e. the nondimensional average acoustic source power starts to decrease with increasing amplitude, see Sec. 5.5.2. For shallow cavities this transition is predicted at higher perturbation amplitudes $|u'|/U \geq 10^{-2}$.

In figure 5.17 measured and predicted average acoustic source power are plotted against the cavity depth to cavity width ratio (H/W) for configuration A. It is noted that the measured average acoustic source power, see Eq. 5.18, remains almost the same in the whole range $0.2 \leq H/W \leq 1.175$ tested. The measured fluctuation amplitude, however, decreases considerably for cavities in the range $H/W \leq 0.5$ as the cavity gets shallower, see figure 5.10-a. As explained the acoustic source power should be balanced with the losses through an energy balance, see Sec. 5.5.2, to de-
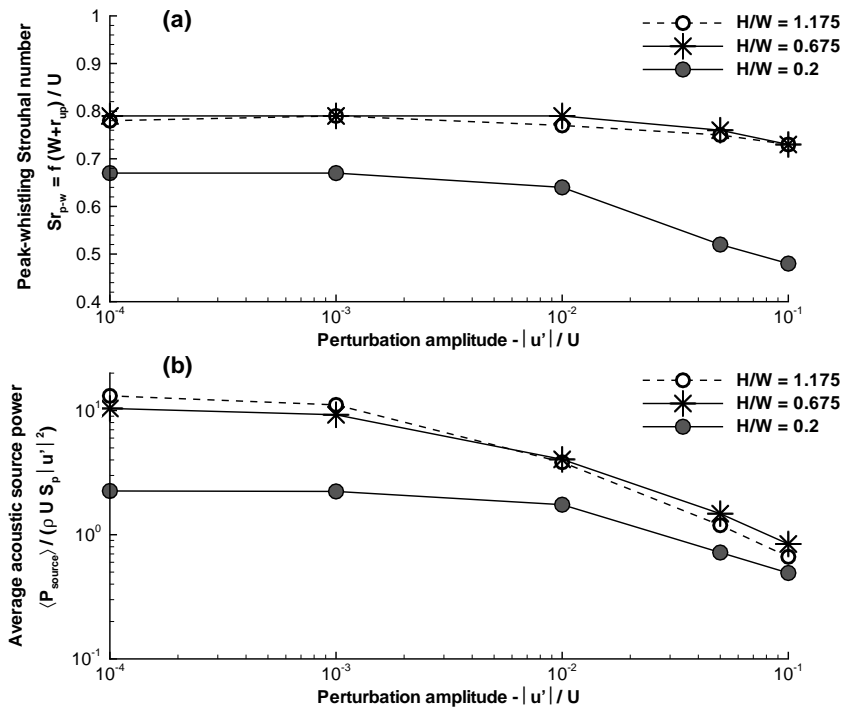
Figure 5.16: Predicted peak-whistling Strouhal number Sr_{p-w} (a) and average acoustic source power $\langle P_{\text{source}} \rangle / (\rho_0 U S_p |u'|^2)$ at the respective peak-whistling Strouhal numbers (b) plotted against the perturbation amplitude $|u'|/U$ for cavity width to depth ratios of $H/W = 1.175$, $H/W = 0.675$ and $H/W = 0.2$ configurations A.

termine the perturbation amplitude. The shallow cavities whistle at lower Strouhal numbers, see figure 5.14, (corresponding to higher Mach numbers), which increases the acoustic losses at the downstream termination predicted by Eq. 5.20-Eq. 5.23. As a consequence, although the cavities with various depths have almost the same dimensionless acoustic source power, the shallow cavities whistle at lower amplitudes as a result of the increased downstream acoustic convective losses.

In accordance with the experimental observations numerically predicted average dimensionless acoustic source powers are independent of the cavity depth for the range $0.4 \leq H/W \leq 1.175$, see figure 5.16. The numerical method, however, overestimates the acoustic source power by a factor of two. The numerical method estimates a decreasing acoustic source power for decreasing cavity depths for very shallow cavity range ($0.2 \leq H/W \leq 0.3$), which is much stronger than the decrease observed in the experiments, see figure 5.17.
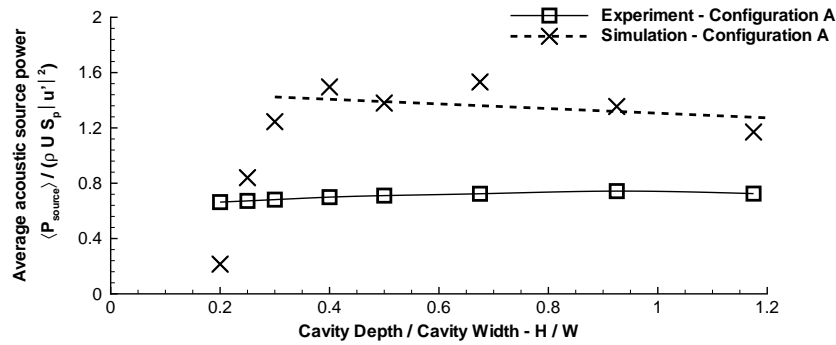
Figure 5.17: Measured and numerically predicted dimensionless average acoustic source power $\langle P_{\mathrm{source}}\rangle/(\rho_0 U S_{\mathrm{p}}|u'|^2)$ for configuration A. Simulations are performed at respective peak fluctuation amplitude observed in the experiments, see figure 5.10.

5.6   Conclusions

Aeroacoustic power generation due to a self-sustained oscillation by an axisymmetric cavity exposed to a grazing flow has been studied both experimentally and numerically. The feedback effect is produced by the velocity fluctuations resulting from a coupling of the vortex shedding at the upstream cavity edge with acoustic standing waves in the pipe.

The peak-whistling Strouhal number $Sr_{\mathrm{p-w}}$, at which the maximum amplitude in pressure fluctuations is registered, is decreasing linearly with cavity width to depth ratio W/H for shallow cavities ($1.5 \leq W/H \leq 4$) at high amplitudes $|u'|/U \geq 10^{-2}$. This is due to the image vortex at the bottom of the cavity. For the deeper cavities a limit value of $Sr_{\mathrm{p-w}}$ is reached which is independent of W/H.

The proposed numerical approach provides excellent predictions of $Sr_{\mathrm{p-w}}$ as a function of H/W both for shallow cavities for which there is a linear relation and for the deeper cavities. The method successfully captures the effect of the incoming flow profile on the peak-whistling Strouhal number. It is found that at high perturbation amplitudes ($|u'|/U \geq 10^{-2}$) for shallow cavities the peak-whistling Strouhal number depends on the perturbation amplitude, while for deep cavities there is not such a dependence.

For both approach velocity profiles that have been considered, the peak-whistling amplitude $|u'|/U$ remains constant in the range $0.5 \leq H/W \leq 1.175$. For shallower cavities, $H/W < 0.5$, the peak-whistling amplitude decreases as a result of the increase in convective acoustical energy losses at the downstream open end of the pipe, associated with the decrease of the peak-whistling Strouhal number.

Dimensionless acoustic source power of the cavity is found to be independent of the depth for deep cavities $H/W \geq 0.675$. For shallower cavities the acoustic source

power depends on the cavity depth. The proposed numerical method overestimates the dimensionless time averaged acoustic source power $\langle P_{\mathrm{source}} \rangle / (\rho_0 U S_{\mathrm{p}} |u'|^2)$ by a factor of 2 and overstates the effect of the cavity depth on the acoustic source power for shallow cavities.

Aeroacoustic power generated by multiple compact axisymmetric cavities: effect of hydrodynamic interference on the sound production

6.1 Abstract

Aeroacoustic sound generation due to self-sustained oscillations by a series of compact axisymmetric cavities exposed to a grazing flow is studied both experimentally and numerically. The driving feedback is produced by the velocity fluctuations resulting from a coupling of vortex sheddings at the upstream cavity edges with acoustic standing waves in the coaxial pipe. When the cavities are separated sufficiently from each other, the whistling behavior of the complete system can be determined from the individual contribution of each cavity. When the cavities are placed close to each other there is a strong hydrodynamic interference between the cavities which affects both the peak-amplitude attained during whistling and the corresponding Strouhal number. This hydrodynamic interference is captured successfully by the proposed numerical method.

6.2 Introduction

Pipe systems with axisymmetric cavities are often used in engineering applications. However, at critical conditions, the flow through such an axisymmetric cavity-pipe

system causes self-sustained oscillations that lead to high-amplitude sound generation and associated mechanical vibration. Grazing flow over axisymmetric cavities in ducted flows have been investigated for a wide range of applications such as control valves [Ziada and Bühlmann, 1989], piping systems [Lafon et al., 2003] and impedance walls [Aurégan and Leroux, 2003; Lange and Ronneberger, 2003].

Despite the geometric simplicity of axisymmetric cavity-pipe configurations, self-sustained cavity oscillations in such systems involve several complex fluid mechanics phenomena. The oscillations can be classified into three categories based on the nature of the feedback: fluid dynamic, fluid-resonant and fluid-elastic oscillations [Rockwell and Naudascher, 1978]. The current work deals with a fluid-resonant mechanism in which the feedback is produced by the velocity fluctuations at the upstream edge of the cavity resulting from a coupling of vortex shedding with a longitudinal acoustic pipe mode. In such a feedback loop, the shear layer instability in the mouth of the cavity and the longitudinal acoustic pipe modes can be considered as the amplifier and the filter of a feedback system, respectively [Blevins, 2001]. This results in stable self-sustained oscillations at discreet frequencies, which is called whistling.

A single cavity in a pipe line with an acoustic feedback due to a longitudinal standing wave has been the focus of a considerable number of experimental studies [Tam and Block, 1978; Schachenmann and Rockwell, 1980; Rockwell and Schachenmann, 1982; Ziada et al., 2003; Geveci et al., 2003; Oshkai et al., 2005; English and Holland, 2010], in which the effect of various geometric parameters such as the depth of the cavity and the width of the cavity are addressed.

On the other hand, there has been only a limited number of studies in the literature in which the sound generation/absorption characteristics of series of axisymmetric cavities adjacent to each other, i.e. there is hydrodynamic interference between them, have been addressed [Derks and Hirschberg, 2004; Aurégan and Leroux, 2008]. Such multiple axisymmetric cavity configurations are mostly considered for mufflers, in which the cavities are acoustically deep i.e. the cavity depth is of the order of the acoustic wave length [Lange and Ronneberger, 2003; Aurégan and Leroux, 2003, 2008].

The authors have recently been interested in the sound generation in corrugated pipes [Tonon et al., 2010; Nakiboğlu et al., 2010, 2011a, 2012]. In corrugated pipes the width and the depth of the cavities are much smaller than the wavelength of the longitudinal acoustic pipe mode i.e. the cavities are acoustically compact sound sources. One approach is to model a corrugated pipe as a system composed of a series of acoustically coupled axisymmetric cavities connected to each other with straight pipe segments. Neglecting a possible hydrodynamic interference between the individual elements of the series of cavities, such a system can be investigated by simulating a single cavity with appropriate boundary conditions. In an earlier work [Nakiboğlu et al., 2011a], the authors had proposed a numerical methodology to in-

vestigate the aeroacoustic response of a single confined compact cavity, exposed to a low Mach number grazing flow, to acoustic excitations. The method combines incompressible simulations with Vortex Sound Theory [Howe, 1975, 1998]. Although this so-called hybrid method is a highly simplified approach compared to the current computational aeroacoustic algorithms [Colonius and Lele, 2004; Brès and Colonius, 2008], it has been quite successful in predicting the Strouhal number ranges of acoustic energy production/absorption and the nonlinear saturation mechanism responsible for the stabilization of the limit cycle oscillation [Nakiboğlu et al., 2011a]. This computationally low cost numerical method also predicts the peak-whistling Strouhal number, at which the maximum amplitude in pressure fluctuations is registered, in close agreement with experiments and explains the dependency of the peak-whistling Strouhal number on the momentum thickness of the velocity profile that the cavity is subjected to [Nakiboğlu et al., 2011a, 2012]. There is, however, an inaccuracy in this approach due to the neglected hydrodynamic interference, particularly when the distance between successive cavities is small.

Hydrodynamic interference considered here has some similarity with the phenomena observed in heat exchanger pipe bundles placed in cross flow. Coupling of vortex shedding with acoustic standing waves is strongly influenced by the hydrodynamic interference between successive cylinders. Flow-excited acoustic behavior of tandem cylinder configuration in a resonating duct is considerably different than that of a single cylinder. A strong effect of spacing ratio has been recorded both on the amplitude of the maximum acoustic pressure and the Strouhal number range of the resonance [Hall et al., 2003; Mohany and Ziada, 2005; Finnegan et al., 2009]. This stresses the need of an assessment for the effect of the hydrodynamic interference, between successive cavities in corrugated pipe, on whistling.

The aim of the present work is to investigate the aeroacoustic sound generation by double and triple axisymmetric cavity configurations exposed to a grazing flow, as a model for the whistling behavior of multiple axisymmetric cavity systems, e.g. corrugated pipes, and to assess the effect of hydrodynamic interference between successive cavities on the whistling. The following section, Sec. 6.3, is dedicated to the experiments. The experimental setup (Sec. 6.3.1), sound generation in hydrodynamically separated cavities (Sec. 6.3.2), hydrodynamic interference among the cavities in close vicinity of each other (Sec. 6.3.3) and effect of plateau length on the hydrodynamic interference (Sec. 6.3.4) is covered in this part. In Sec. 6.4 the numerical methodology is summarized and the predictions of hydrodynamic interference (Sec. 6.4.2) is discussed. In the last section, Sec. 6.5, the conclusions are stated.
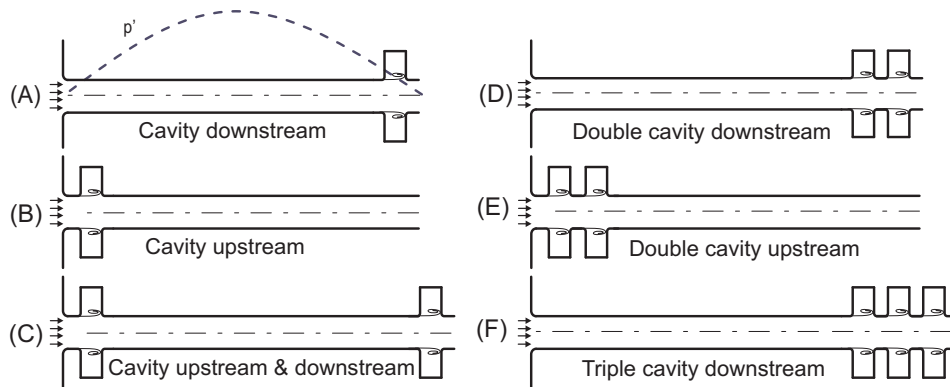
Figure 6.1: The tested cavity configurations. The dotted line in configuration A, indicates the spatial distribution of the pressure amplitude (p') in the standing wave at the first longitudinal acoustic mode.

6.3 Experiments

6.3.1 Experimental setup

An experimental setup has been constructed to investigate self-sustained oscillations due to the coupling of vortex sheddings in a series of axisymmetric cavities exposed to grazing flow with a longitudinal standing wave. The test section is composed of a straight pipe section and a number of axisymmetric cavities, which can be placed at either end of the pipe. The cavity configurations considered in this paper are presented in figure 6.1, each configuration is referred with a letter e.g. double cavity downstream of the pipe is configuration D.

All the experiments have been carried out at the first longitudinal acoustic mode. This is a standing wave of a half-wave length in the pipe ($L \approx \lambda/2$). The system whistles also for the higher acoustic modes (i.e. $L \approx \lambda, 3/2\lambda, \cdots$). Experiments have been performed at the lowest possible whistling mode in order to keep the sound source as compact as possible ($W \ll \lambda$), allowing an incompressible model for the flow in the cavity. Configuration A (single cavity at the downstream termination) is similar to the one used by Schachenmann and Rockwell [1980]; Rockwell and Schachenmann [1982]. In their work the first whistling mode was obtained at the third longitudinal acoustic mode $L \approx 3/2\lambda$. This is due to their configuration combining a cavity with sharp edges with a relatively long pipe. In the current study, cavities have rounded edges which promotes the sound production considerably [Bruggeman et al., 1991; Nakiboğlu et al., 2010]. Furthermore a relatively short pipe segment is used to limit the viscous losses. It should also be noted that in all the configurations the cavities are placed close to a pressure node in order to maximize the sound production [Tonon et al., 2010; Nakiboğlu et al., 2010; Golliard et al., 2010].

The mean flow velocity profile of the flow that is approaching the cavity has a strong influence on the whistling phenomenon [Nakiboğlu et al., 2011a, 2012]. A sand paper strip (ISO/FEPA grid designation - P40) with a width of 5 mm is placed on the inner pipe wall at the inlet of the pipe in order to trip the boundary layer from laminar to turbulent flow. This avoids uncertainties due to the natural transition from laminar to turbulent flow. The cavity in configuration A experiences a developed *turbulent* approach velocity profile with a displacement thickness of $\delta_1 = 1.7 \times 10^{-3}$ m and a momentum thickness of $\delta_2 = 1.2 \times 10^{-3}$ m. The cavity in Configuration B, however, experiences a *top-hat* velocity profile with a thin boundary layer i.e. $\delta_1 = 3.9 \times 10^{-4}$ m and $\delta_2 = 2.0 \times 10^{-4}$ m. These velocity profiles and their effects on the whistling of single cavity configurations A and B have been discussed in an earlier paper [Nakiboğlu et al., 2011b]. In the current work attention is given to the multiple axisymmetric cavities. Yet the same two different velocity profiles, *turbulent* and *top-hat*, are experienced by cavities in other configurations considered here e.g. the upstream and downstream cavities of configuration C experience *top-hat* and *turbulent*, velocity profiles, respectively.

The notation for the relevant geometric parameters are shown in figure 6.2 for configuration D. The same notation is used for all the other configurations as well. There are two straight pipe sections, the long one is $L_1 = 850$ mm and the short one is $L_2 = 15$ mm. Depending on the configuration, see figure 6.1, the positions of these pipes interchange e.g. for configuration E, L_1 is downstream of the cavities and L_2 is upstream. The inner diameter of the pipe sections is $D = 44$ mm. The pipe is made of steel with a roughness height of $\epsilon \leq 4.0 \times 10^{-5}$ m (European Standard EN 10305-1) and has a wall thickness of 6 mm. Such a thick pipe is used to avoid wall vibrations. Measurements of the reflection coefficient for the closed pipe have confirmed that there is no significant effect of pipe wall vibrations on the measurements. The depth of the axisymmetric cavity is $H = 27$ mm and the width of the cavity is $W = 40$ mm, hence height to width ratio is $H/W = 0.675$. For such a deep cavity the whistling characteristics i.e. Strouhal number and the amplitude of the fluctuations are independent of the depth [Nakiboğlu et al., 2010, 2011b]. The setup allows the placement of a second cavity and to vary the plateau (L_p) length, the constant diameter part between the two cavities. It is also possible to mount a third cavity. The radii of curvature of the upstream and downstream cavity edges are denoted by r_{up} and r_{dwn}, respectively. The upstream edge radius of the first cavity and the downstream edge radius of the last cavity is 5 mm, all the other edge radii are 2.5 mm. Experiments have been performed for seven different plateau length to width ratios, namely L_p/W =0, 0.375, 0.625, 0.750, 0.875 and 1.375. It should be noted that the plateau length does not include the edge radii of the cavities, see figure 6.2. Thus, when the plateau length is $L_p = 0$ mm there, still, exists a wall thickness ($r_{dwn} + L_p + r_{up}$) between the cavities, which is 5mm. The total length of the system is denoted by L, which varies in the range $915\,\text{mm} \leq L \leq 1115\,\text{mm}$
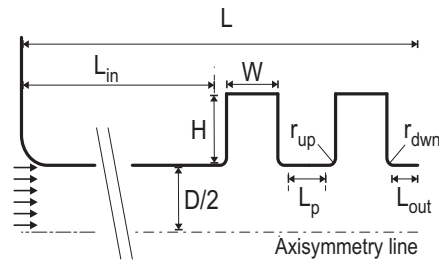
Figure 6.2: The relevant geometric parameters, shown for configuration D.
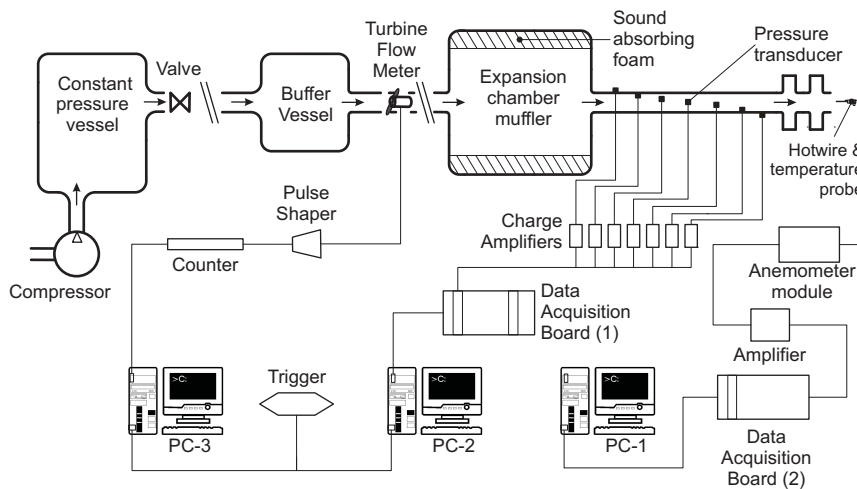
Figure 6.3: Schematic of the experimental setup and instrumentation.

depending on the configuration. All the components of the experimental setup have been manufactured with an accuracy of 0.1 mm.

The set-up used for the experiments is shown in figure 6.3. The upstream termination of the test section is connected to the high-pressure air supply system, which is composed of, from upstream to downstream, a compressor, a constant pressure vessel, a control valve, a buffer vessel, a turbine flow meter and an expansion chamber muffler. The expansion chamber muffler has a length of 1.5 m and a diameter of 0.6 m. It is covered internally with sound absorbing foam with a thickness of 100 mm in order to avoid cavity resonances. The downstream termination is open to the laboratory, a large room of 15 m×4 m×4 m (not an anechoic chamber).

The acoustic pressure in the long straight pipe segment (L_1) is measured using seven acceleration compensated piezo-electric pressure transducers, which are flush mounted. The transducers are calibrated together with their adapter pieces at the end-wall of a closed pipe both for the relative amplitude and relative phase differ-

ence. These microphones have a separation distance of 108.33 mm in axial direction and an angular position difference of $30°$ from each other in azimuthal direction, see figure 6.3. The first and the last transducer are positioned 100 mm from the pipe terminations. The signals from the microphones are amplified by charge amplifiers. These amplifiers are connected to a combined data acquisition-PC system. The frequencies of whistling are in the range of $150-250$ Hz and the sampling rate of the experiments was 5 kHz. Thus the sampling rate satisfies the Nyquist criteria. By sampling for long enough time, a discrete time signal can be obtained whose discrete Fourier transform (DFT) roughly represents the Fourier transform of the continuous time signal [Bracewell, 1986]. For that purpose a sampling duration of 10 s has been used for each data point.

Knowing the pressure fluctuations at seven different spatial positions using the multi-microphone method [Åbom and Bodén, 1988] traveling acoustic plane waves were reconstructed. The term *fluctuation amplitude* is used to specify the maximum dimensionless sound amplitude that is attained in the standing wave. The *fluctuation amplitude* is defined as

$$\frac{|p'_{\max}|}{\rho_0 c_0 U} = \frac{|u'_{\max}|}{U} \tag{6.1}$$

where $|p'_{\max}|$ is the amplitude of the standing pressure wave at a pressure anti-node inside the pipe and $|u'_{\max}|$ is the amplitude of acoustic velocity at a pressure node. Since the term *fluctuation amplitude* always refers to this maximum dimensionless sound amplitude; the subscript *max* will be dropped for convenience. The details of the data processing is provided in an earlier work [Nakiboğlu et al., 2011b].

The temperature of the air is measured at the pipe termination with an accuracy of $0.1°C$ using a digital thermometer. A turbine flow meter is used to measure the average velocity (U) through the volumetric flow rate. The turbine flow meter is connected to a pulse shaper and a counter. The acquisition system of the turbine flow meter and the piezo-electric pressure transducers are synchronized by means of a trigger pulse. The simultaneous measurement of flow velocity and pressure fluctuations allows a waterfall representation of the data, in which the frequency spectra of the whistling at different flow velocities are presented in a single graph. Using this waterfall diagram consecutive modes that appear simultaneously with the dominant hydrodynamic mode can easily be identified [Rockwell et al., 2003; Oshkai et al., 2005]. Such secondary modes were not observed for the flow range studied in the current work and unlike the case of wall cavities, such as the ones studied by Delprat [2006], nonlinear interaction between modes has not been observed. The details of the instrumentation are provided in an earlier paper [Nakiboğlu et al., 2011b].

Figure 6.4:
Dimensionless acoustic velocity fluctuation amplitude $|u'|/U$ plotted against Strouhal number $Sr = f(W + r_{\rm up})/U$ for configurations A, B and C, see figure 6.1.
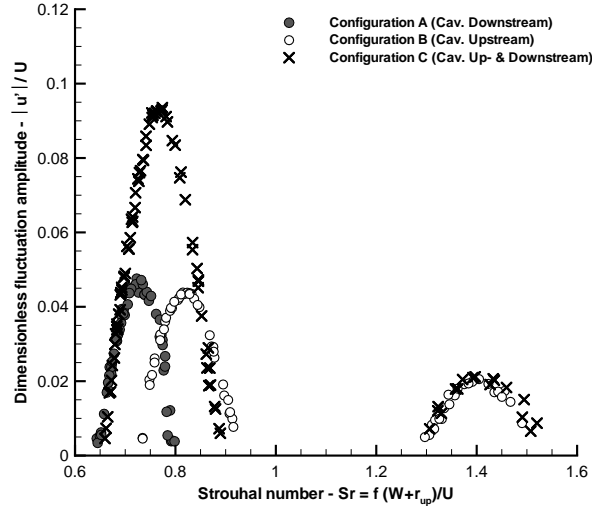
6.3.2 Sound generation in hydrodynamically separated multiple cavities

In figure 6.4 measured dimensionless fluctuation amplitude $|u'|/U$ is plotted against Strouhal number $Sr = f(W + r_{\rm up})/U$ for configurations A, B and C. Considering the acoustics there is only a minor difference between configurations A (single cavity downstream) and B (single cavity upstream). This difference is caused by cavity having a finite width and the upstream and downstream edge of the cavity not being acoustically symmetric in the sense that the vortex is shed from the upstream edge of the cavity. Thus, the spatial position of the vortex core with respect to the standing wave is not identical for these two configurations. The cavity width is, however, much smaller than the wavelength of the standing wave $W \ll \lambda$. Hence this difference between configurations A and B is very small. The variation in the whistling behavior of these two configurations is mainly due to the difference in the velocity profile that the cavities are subjected to, which is discussed in an earlier work of the authors [Nakiboğlu et al., 2011b].

It is seen from figure 6.4 that the peak-whistling Strouhal number $Sr_{\rm p-w}$, the Strouhal number at which the maximum amplitude in pressure fluctuations is registered, is $Sr_{\rm p-w} = 0.73$ and $Sr_{\rm p-w} = 0.82$ for configuration A and configuration B, respectively. For configuration C, where there is a cavity both at the upstream and downstream termination, the system whistles at a peak-whistling Strouhal number of $Sr_{\rm p-w} = 0.77$, which is a compromise between the peak-whistling Strouhal numbers obtained in configurations A and B.

In configuration A there exist only one range of Strouhal numbers, $0.65 \leq Sr \leq 0.80$, for which the whistling is observed, whereas for configuration B there exist

two distinct ranges of Strouhal numbers with whistling, $0.74 \leq Sr \leq 0.92$ and $1.30 \leq Sr \leq 1.50$. The lower and the higher ranges of whistling Strouhal numbers, around $Sr = 0.76$ and $Sr = 1.40$ belong to the second and third hydrodynamic modes, respectively. At the second hydrodynamic mode there exist two vortices at the same moment inside the cavity mouth: one traveling and one forming. Similarly for the third hydrodynamic mode there are three vortices appearing simultaneously at the cavity opening: one forming and two traveling [Bruggeman et al., 1991; Nakiboğlu et al., 2011b]. The disappearance of the whistling for the higher Strouhal number range ($1.30 \leq Sr \leq 1.50$) for configuration A is explained [Nakiboğlu et al., 2011b] by using the linearized theory of an inviscid quasi-parallel free shear layer [Michalke, 1965; Elder, 1980]. Configuration C has also two distinct ranges of Strouhal numbers in which the system whistles. It is evident from figure 6.4 that for the second hydrodynamic mode the range of whistling for configuration C, $0.66 \leq Sr \leq 0.89$, is almost equal to the combined range of whistling for configurations A and B, $0.65 \leq Sr \leq 0.92$. For the third hydrodynamic mode the whistling range of configuration C is identical to the range of whistling of configuration B, $1.30 \leq Sr \leq 1.50$, because configuration A is silent for the third hydrodynamic mode.

Considering the dimensionless fluctuation amplitude $|u'|/U$ a parallel behavior with the Strouhal number is observed for configuration C. The peak-whistling amplitude obtained in configuration C for the second hydrodynamic mode is $|u'|/U = 9.3 \times 10^{-2}$, which is almost equal to the summation of the peak-whistling amplitudes obtained with configuration A, $|u'|/U = 4.7 \times 10^{-2}$ and B, $|u'|/U = 4.3 \times 10^{-2}$. For the third hydrodynamic mode the peak-whistling amplitude of configuration C is identical to that of configuration B, $|u'|/U = 2.1 \times 10^{-2}$. This is expected because configuration A is not whistling at the third hydrodynamic mode.

It is concluded from this set of experiments that when two cavities are placed at different pressure nodes such that there is no hydrodynamic interference, the whistling behavior of the system can be determined from the individual contributions of each cavity.

6.3.3   Hydrodynamic interference

In this section a possible hydrodynamic interference between cavities, which are adjacent to each other, is investigated. In figure 6.5 the dimensionless acoustic velocity fluctuation amplitude $|u'|/U$ is plotted against Strouhal number $Sr = f(W + r_{\mathrm{up}})/U$ for configuration D (double cavity downstream) and for configuration E (double cavity upstream) with a plateau length of $L_{\mathrm{p}} = 0$ (see figure 6.2) together with configuration C, which has already been discussed in the preceding section. It is seen that for the second hydrodynamic mode ($0.65 \leq Sr \leq 0.91$) the difference in the peak-whistling Strouhal number between configuration D, $Sr_{\mathrm{p-w}} = 0.77$, and E, $Sr_{\mathrm{p-w}} = 0.79$, is not as large as between configuration A and B, which are the single

Figure 6.5:
Dimensionless acoustic velocity fluctuation amplitude $|u'|/U$ plotted against Strouhal number $Sr = f(W + r_{\mathrm{up}})/U$ for configurations C, D and E, see figure 6.1.
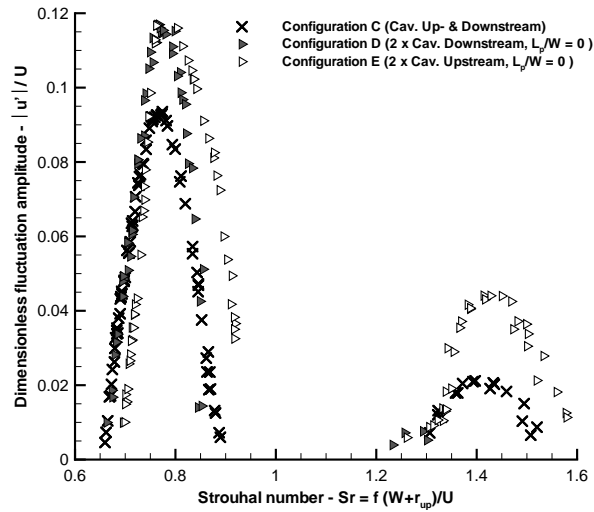
cavity versions of the same configurations. This is expected to be due to the fact that the downstream cavities in configuration D and E are experiencing similar velocity profiles.

Configuration D has the same peak-whistling Strouhal number, $Sr_{\mathrm{p-w}} = 0.77$, as configuration C for the second hydrodynamic mode. This can be explained through the different velocity profiles that the two cavities of configuration D are subjected to. The upstream cavity of configuration D experiences a turbulent velocity profile, as in configuration A (*turbulent*, see Sec. 6.3.1). Assuming that the velocity profile is redeveloping on the plateau between the cavities, the downstream cavity of configuration D experiences a velocity profile with a thin boundary layer as in configuration B (*top-hat*, see Sec. 6.3.1). Thus in configurations C and D each of the two cavities experience similar velocity profiles. As a consequence, it is not surprising that the peak-whistling Strouhal numbers of these two configuration are the same. A weak third hydrodynamic mode is observed for configuration D between $1.23 \leq Sr \leq 1.30$. The appearance of the third hydrodynamic mode also indicates that the downstream cavity in configuration D experiences a boundary layer thinner than that in configuration A.

For configuration E, the third hydrodynamic mode has a dimensionless amplitude of $|u'|/U = 4.4 \times 10^{-2}$, which is two times higher than that of the third hydrodynamic mode observed in configurations B and C $|u'|/U = 2.1 \times 10^{-2}$. As discussed in preceding section, only cavities experiencing a *top-hat* approach velocity profile contribute to the third hydrodynamic mode. This also indicates that both the downstream and the upstream cavities of configuration E experiences a thin boundary layer. This also supports the idea that the velocity profile is redeveloping on

the plateau. The focus in this work is, however, given to the second hydrodynamic mode, at which the peak-whistling is observed. Thus, the rest of the paper will be limited to the second hydrodynamic mode.

It is seen that both configuration C and D whistle in the same Strouhal number range so the convective acoustic losses at the downstream open pipe termination are similar for these two configurations. The acoustic boundary conditions both upstream and downstream are also identical in these configurations. Thus, the total acoustic losses are comparable for configuration C and D. In earlier papers [Nakiboğlu et al., 2011a, 2012] it has been explained that the dimensionless fluctuation amplitude obtained in a system can be determined through an energy balance between the acoustic sources and acoustic losses. Since configuration C and D have comparable acoustic losses and configuration D has a 30% higher dimensionless fluctuation amplitude $|u'|/U = 1.2 \times 10^{-1}$ than configuration C, it can be concluded that the acoustic source power produced in configuration D with cavities in close proximity is higher than the one produced by configuration C.

It has been shown that the spatial position of the cavity with respect to the coupling longitudinal standing wave is important for the sound production. The sound production is maximized when the cavity is placed close to a pressure node [Tonon et al., 2010; Nakiboğlu et al., 2010; Golliard et al., 2010]. It is already known that the difference in acoustic source power produced by a cavity at the downstream pipe termination (configuration A) and at the upstream pipe termination (configuration B), due to a difference in the velocity profile, is rather small, see figure 6.4. Neglecting a possible hydrodynamic interference in configuration D, one would expect configuration C to produce more acoustic source power than configuration D, because in configuration C both cavities at the upstream and downstream termination are very close to pressure nodes. In configuration D, however, both of the cavities are placed at the downstream pipe termination. Thus, in configuration D, the upstream cavity is further away from the pressure node than the downstream cavity. As a consequence the upstream cavity is expected to be less efficient for acoustic power generation than the downstream cavity. It is observed, however, that in the experiments configuration D produces a higher acoustic source power than configuration C. This suggests that in configuration D there exists a constructive hydrodynamic interference between the cavities for the plateau length of $L_{\mathrm{p}} = 0$ mm. This also holds for configuration E, for which the double cavity is placed at upstream termination.

6.3.4   Effect of plateau length

To assess the extent of this hydrodynamic interference and its dependence on the plateau length L_{p} a series of experiments were performed with configuration D with various plateau lengths. In figure 6.6 the dimensionless acoustic velocity fluctuation amplitude $|u'|/U$ is plotted against Strouhal number $Sr = f(W + r_{\mathrm{up}})/U$ for configuration D with plateau length to cavity width ratios of $L_{\mathrm{p}}/W = 0, 0.375, 0.625, 0.750,$

L_{p}/W	$Sr_{\mathrm{p-w}}$		$\lvert u' \rvert/U \times 10^{-2}$	
	Primary	Secondary	Primary	Secondary
0	0.77	N/A	11.5	N/A
0.375	0.74	N/A	12.3	N/A
0.625	0.72	0.82	9.8	2.2
0.750	0.71	0.79	6.4	5.6
0.875	0.67	0.78	3.7	7.4
1.375	N/A	0.77	N/A	10.7

Table 6.1: Peak-whistling Strouhal numbers $Sr_{\mathrm{p-w}}$ and the peak-whistling amplitudes $\lvert u' \rvert/U$ for primary and secondary peaks for configuration D at all the plateau length to cavity width ratios L_{p}/W.

0.875 and 1.375.

As shown already in figure 6.5 when the two cavities are very close to each other, i.e. $L_{\mathrm{p}}/W = 0$, there is a single peak (primary peak). With increasing plateau length this peak shifts to lower Strouhal numbers and decreases in amplitude. At a plateau length of $L_{\mathrm{p}}/W = 0.675$ a secondary peak appears at a higher Strouhal number. As the plateau length is further increased the secondary peak shifts to lower Strouhal numbers with increasing amplitude. At a plateau length of $L_{\mathrm{p}}/W = 1.375$ the secondary peak replaces the primary peak at the same Strouhal number and almost at the same amplitude as found for $L_{\mathrm{p}}/W = 0$. In figure 6.6 the primary and the secondary peaks are indicated with open and solid arrows, respectively. The peak-whistling Strouhal numbers $Sr_{\mathrm{p-w}}$ and the peak-whistling amplitudes $\lvert u' \rvert/U$ for primary and secondary peaks for configuration D for all plateau length to cavity width ratios L_{p}/W are summarized in table 6.1.

Considering the two extremes of the plateau length $L_{\mathrm{p}}/W = 0$ and $L_{\mathrm{p}}/W = 1.375$, the two configurations whistle at the same peak-whistling Strouhal number and almost at the same amplitude. The small decrease in the dimensionless amplitude in the case of $L_{\mathrm{p}}/W = 1.375$ is expected to be due to the fact that the upstream cavity has been moved further away from the pressure node compared to the case of $L_{\mathrm{p}}/W = 0$. In between these two extremes of the plateau length, however, there is a range of plateau lengths around $L_{\mathrm{p}}/W = 0.750$, such that the peak-whistling amplitude of the system is half the peak-whistling amplitude recorded at the extremes ($L_{\mathrm{p}}/W = 0$ and $L_{\mathrm{p}}/W = 1.375$). Thus, the strength of the hydrodynamic interference depends strongly on the plateau length.

As explained in the introduction one of the motivations of the current study is to understand the whistling behavior in corrugated pipes, which can be considered, in first approximation, as a series of axisymmetric cavities placed along a resonating duct. As a consequence it is important to assess whether the hydrodynamic interference observed for double cavities can be scaled up to many cavity configurations. In figure 6.7 dimensionless acoustic velocity fluctuation amplitude $\lvert u' \rvert/U$
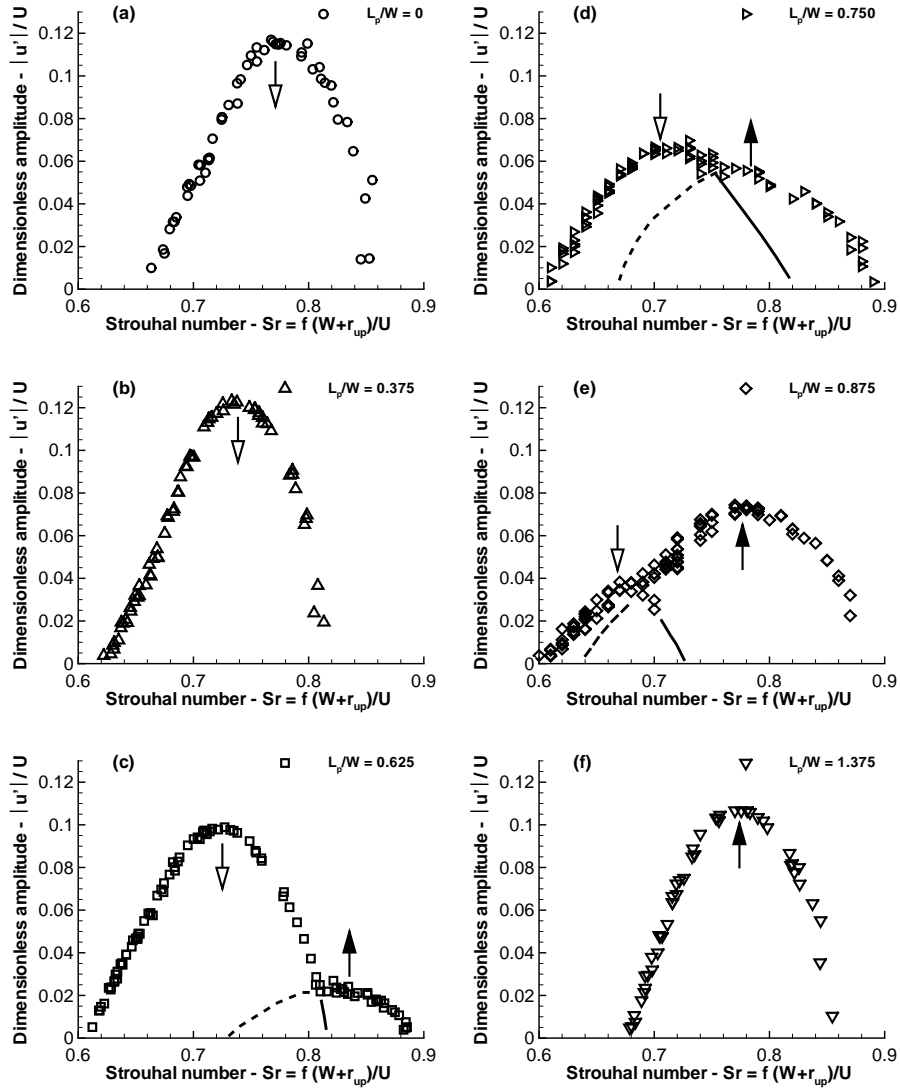
Figure 6.6: Dimensionless acoustic velocity fluctuation amplitude $|u'|/U$ plotted against Strouhal number $Sr = f(W + r_{up})/U$ for plateau length to cavity width ratios of $L_p/W = 0$ (a), 0.375 (b), 0.625 (c), 0.750 (d), 0.875 (e) and 1.375 (f) for configuration D, see figure 6.1.

Figure 6.7:
Dimensionless acoustic velocity fluctuation amplitude $|u'|/U$ plotted against Strouhal number $Sr = f(W + r_{\text{up}})/U$ for plateau length to cavity width ratios of $L_{\text{p}}/W = 0$, 0.875 and 1.375 for configuration F, see figure 6.1.
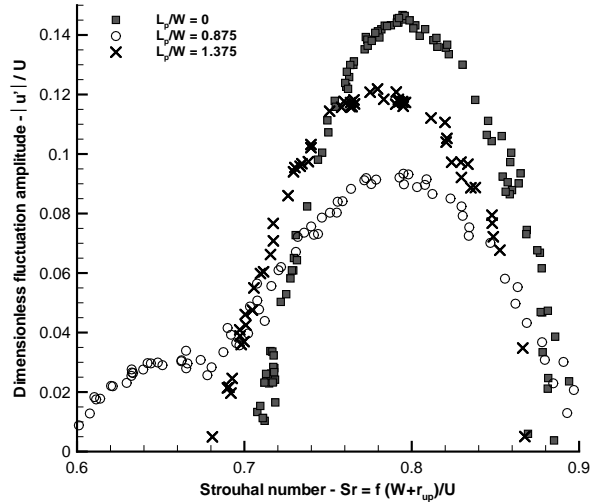
is plotted against Strouhal number $Sr = f(W + r_{\text{up}})/U$ for configuration F, a triple cavity placed close to the downstream termination, see figure 6.1, for plateau length to cavity width ratios of $L_{\text{p}}/W = 0$, 0.875 and 1.375.

In the experiments with a triple cavity, similar to the ones with a double cavity, the plateau length to width ratios of $L_{\text{p}}/W = 0$ and $L_{\text{p}}/W = 1.375$ have a single peak with the same peak-whistling Strouhal number, seen in figure 6.7. The difference in the dimensionless fluctuation amplitude, $|u'|/U$, between the cases $L_{\text{p}}/W = 0$ and $L_{\text{p}}/W = 1.375$ is higher in Configuration F then in configuration D as expected. Because using a longer plateau length ($L_{\text{p}}/W = 1.375$) pushes the cavities further away from the pressure node, thus decreasing the acoustic source power. For the configurations with three cavities this effect is more pronounced than for two cavities. For the case of $L_{\text{p}}/W = 0.875$, again similar to the double cavity configuration, there is a primary peak at a low Strouhal number, $Sr_{\text{p−w}} = 0.65$ with a lower amplitude and a secondary peak at a high Strouhal number, $Sr_{\text{p−w}} = 0.78$ with a higher amplitude. Thus, the hydrodynamic interference observed in double cavity configurations can be scaled up to triple cavity configurations and a similar phenomenon is expected to appear in corrugated pipes.

6.4 Numerical Predictions

6.4.1 Numerical method

In an earlier work Nakiboğlu et al. [2011a] had proposed a numerical methodology to investigate the aeroacoustic response of low Mach number confined flows

to acoustic excitations. The method combines incompressible flow simulations with Vortex Sound Theory to estimate the strength of an acoustic source due to the interference of a single cavity in a pipe flow at high Reynolds number with a low Helmholtz number acoustic field [Martínez-Lera et al., 2009]. This numerical approach is used in the present study to investigate the hydrodynamic interference observed in the experiments with cavities which are in close proximity of each other.

Incompressible simulations

Since the cavity width W (40 mm) is much smaller than the wavelength of the longitudinal standing wave ($\lambda \geq 1750$ mm), one can assume that the wave propagation is locally negligible. Furthermore only low Mach numbers ($Ma \leq 0.05$) are considered. These correspond to the assumption that the flow is locally incompressible [Martínez-Lera et al., 2009]. Therefore incompressible 2D-axisymmetric flow simulations were performed. The simulations were carried out at low Reynolds numbers, $Re = 4 \times 10^3$, without turbulence modeling. The diameter of the pipe (D) and the geometry of the cavity ($W, H, r_{\text{up}}, r_{\text{dwn}}, L_{\text{p}}$) are identical to the ones in the experiments. The inlet is located at $0.175W$ upstream of the first cavity; such a short inlet pipe section is chosen to insure that the imposed inlet mean velocity profile does not evolve significantly before reaching the cavity. The outlet of the numerical domain is placed at a reasonably distant location, $9W$ downstream, from the cavity.

The finite volume commercial code FLUENT 6.3 is used. A pressure-based segregated solution algorithm is employed, the details of the simulation parameters are provided in [Nakiboğlu et al., 2011a]. At the inlet, a fluctuating acoustic axial velocity is imposed, $u'(t)$, uniformly over the time-averaged velocity profile, $u(r)$, at the inlet. The acoustic velocity is a sinusoid with frequency f and amplitude $|u'|$:

$$u'(t) = |u'| \sin(2\pi \, f \, t). \tag{6.2}$$

where $|u'|$ is the amplitude of the acoustic velocity induced by the longitudinal standing wave at the position of the cavity, respectively.

Note acoustic velocity fluctuation, $u'(t)$, changes with time but it is uniform over the profile of the inlet. Time-averaged inlet velocity profile $u(r)$ on the other hand is fixed over time but it changes with the distance from the axis of the pipe. Thus, it has been implicitly assumed that the radial change of velocity and the temporal acoustic fluctuation of the velocity can be decoupled as follows:

$$u(r,t) = u(r) + u'(t) \tag{6.3}$$

In all experiments performed, the cavity is placed close to a pressure node. Thus, through out the paper $|u'|$ stands for the maximum amplitude of the acoustic velocity in the standing wave. The mean velocity profile $u(r)$ is determined experimentally

by means of hotwire measurements, as explained in Sec. 6.3.1. The outlet boundary condition of $\partial u_x / \partial x = 0$ is used. For the majority of simulations 30 periods of the excitation frequency turns out to be enough to dissipate transient repose due to computational methods and initial conditions. For some simulations, however, a steady periodic state is reached only after 70 periods. In each simulation after the steady periodic state is reached, simulations were continued for 10 additional periods. These 10 periods were then used to calculate the time-averaged acoustic source power. The time step is chosen as $\Delta t = 0.01 W/U$.

The computational domains contain around 1.5×10^5 quadrilateral cells. The cells are clustered close to the opening of the cavity and to the walls, where there are high gradients of velocity due to the shear layer and boundary layers, respectively. In the domain between $6W$ and $9W$ downstream of the cavity, cells with high aspect ratio ($\Delta x/\Delta y \gg 1$) are employed. By doing so problems that can arise due to reverse flow at the outlet boundary condition are avoided. A study on mesh dependency has been carried out. In a test case the same computation was performed with two times more densely meshed domains, producing differences in the calculated acoustic source power of less than 5%.

Time-averaged acoustic source power

Following the Vortex Sound Theory of Howe [1975, 1998] and an exact energy corollary of Myers Myers [1986, 1991] for a high Reynolds number flow, the time-averaged acoustic source power produced by a single or series of axisymmetric cavities, $\langle P_{\text{source}} \rangle$, can be determined by a surface integral of the product of fluctuating total enthalpy and the mass flux through the boundary of the control volume, provided that the control volume encloses the compact source region. The details of this procedure is explained in [Nakiboğlu et al., 2011a, 2012].

6.4.2   Prediction of hydrodynamic interference

In this section, the hydrodynamic interference observed in configuration D, double cavity downstream configuration corresponding to measurement data in figure 6.6, is addressed numerically. In figure 6.8 the predicted dimensionless time-averaged acoustic source power $\langle P_{\text{source}} \rangle / (\rho_0 U S_{\text{p}} |u'|^2)$ is plotted against the Strouhal number $Sr = f(W + r_{\text{up}})/U$ for six different plateau length to cavity width ratios, namely, $L_{\text{p}}/W = 0$ (a), 0.375 (b), 0.625 (c), 0.750 (d), 0.875 (e) and 1.375 (f) for configuration D, for a fluctuation amplitude of $|u'|/U = 0.05$.

It should be noted that the numerical method provides an time-averaged acoustic source power. To predict the dimensionless fluctuation amplitude $|u'|/U$, which is measured in the experiments, an energy balance is necessary in which the time-averaged acoustic losses of the system are balanced against the predicted time-averaged

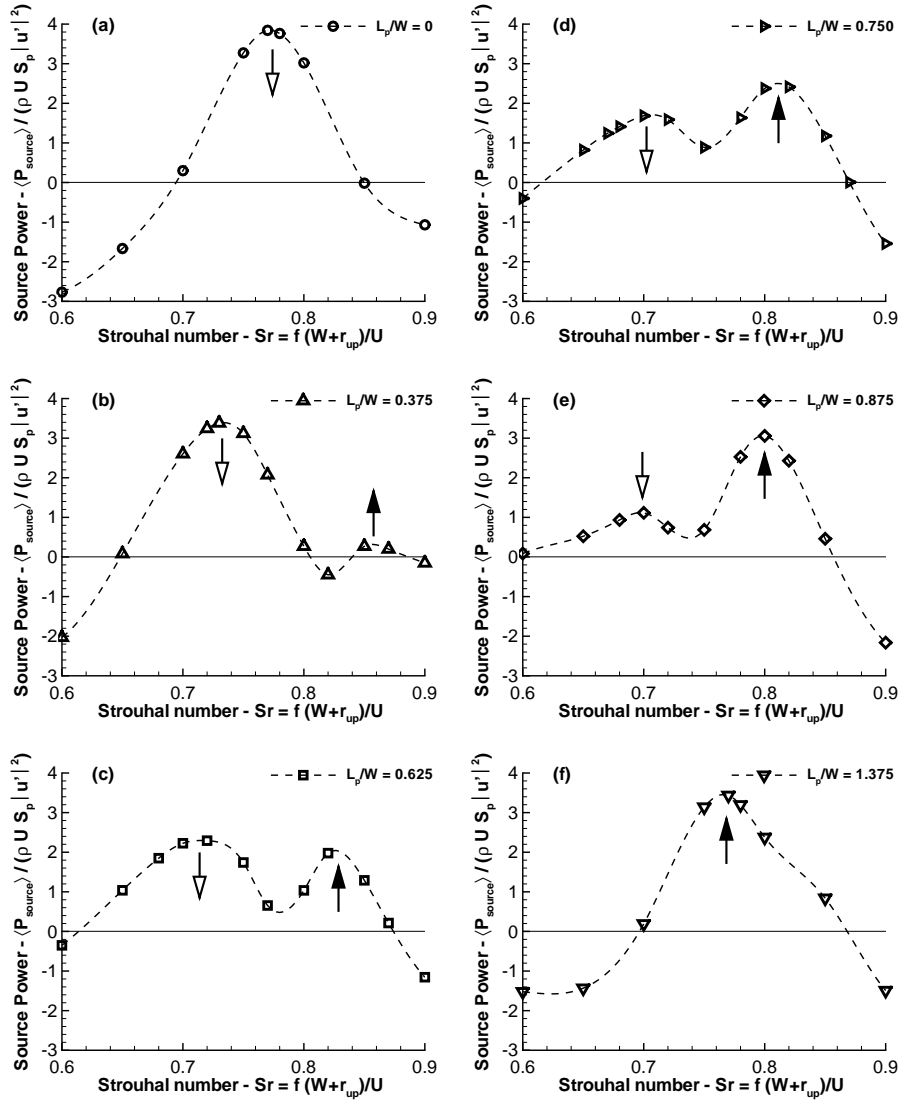**Figure 6.8:** Numerically predicted dimensionless time-averaged acoustic source power $\langle P_{\text{source}}\rangle/(\rho_0 U S_{\text{p}}|u'|^2)$ is plotted against Strouhal number $Sr = f(W + r_{\text{up}})/U$ for plateau length to cavity width ratios of $L_{\text{p}}/W = 0$ (a), 0.375 (b), 0.625 (c), 0.750 (d), 0.875 (e) and 1.375 (f) for configuration D at a fluctuation amplitude of $|u'|/U = 0.05$.

acoustic source power [Nakiboğlu et al., 2011a, 2012]. This approach requires a considerable amount of additional simulations in order to cover the full range of possible dimensionless fluctuation amplitudes. In an earlier work of the authors [Nakiboğlu et al., 2011b] an attempt was made to predict the peak-whistling dimensionless fluctuation amplitude for a single cavity at the downstream termination (configuration of A). The numerical method over estimates the dimensionless fluctuation amplitude by a factor of 2. This approach is not repeated in the current study for the double cavity configurations.

For all the cases considered here for configuration D, the system whistles in the same range of Strouhal numbers $0.6 \leq Sr \leq 0.9$. Thus, given that the system has the same upstream and downstream acoustic boundary conditions, the time-averaged acoustic losses of the system remain more or less the same for all the plateau lengths considered. As a consequence, the predicted time-averaged acoustic source powers can be used on a qualitative basis for comparison with the measured dimensionless fluctuation amplitude $|u'|/U$ in the experiments. The numerical predictions, shown in figure 6.8 capture most of the aspects observed in the corresponding experiments, see figure 6.6. As in the experiments:

- The two extreme values of the plateau lengths, $L_{\mathrm{p}}/W = 0$ and $L_{\mathrm{p}}/W = 1.375$, display a single peak, at the same peak-whistling Strouhal number and at the same time-averaged acoustic source power.

- With increasing plateau length a secondary peak appears at a higher Strouhal number than Strouhal number of the primary peak. As the plateau length further increases both the primary and the secondary peak shift to lower Strouhal numbers. However, the primary peak does this with decreasing acoustic power whereas the secondary peak with increasing acoustic power.

- In between these two extremes of the plateau lengths, $L_{\mathrm{p}}/W = 0$ and $L_{\mathrm{p}}/W = 1.375$, there is a critical plateau length around $L_{\mathrm{p}}/W = 0.625$, for which the time-averaged acoustic source power of the system is about half of the value recorded at the extremes.

The predicted peak-whistling Strouhal numbers $Sr_{\mathrm{p-w}}$ and the peak-whistling time-averaged acoustic source powers $\langle P_{\mathrm{source}}\rangle/(\rho_0 U S_{\mathrm{p}}|u'|^2)$ for the primary and the secondary peaks for configuration D at all the plateau length to cavity width ratios L_{p}/W considered are summarized in table 6.2. It is seen by comparison of tables 6.1 and 6.2 that the numerical method predicts the peak-whistling Strouhal number $Sr_{\mathrm{p-w}}$ for both the primary and the secondary peaks with an accuracy of 3%.

In figure 6.9 normalized vorticity contours given for four different points in time within a single oscillation period in the region around the cavities for configuration D for $L_{\mathrm{p}} = 0$, $Sr_{\mathrm{p-w}} = 0.77$ and $|u'|/U = 0.05$. The moment in time is indicated for each frame in terms of the corresponding acoustic velocity period. The origin of time

L_p/W	$Sr_\mathrm{p-w}$		$\langle P_\mathrm{source}\rangle/(\rho_0 U S_\mathrm{p}|u'|^2)$	
	Primary	Secondary	Primary	Secondary
0	0.77	N/A	3.86	N/A
0.375	0.73	0.86	3.43	0.29
0.625	0.72	0.82	2.25	1.98
0.750	0.71	0.81	1.69	2.51
0.875	0.70	0.80	1.04	3.05
1.375	N/A	0.77	N/A	3.46

Table 6.2: Numerically predicted peak-whistling Strouhal numbers $Sr_\mathrm{p-w}$ and the peak-whistling time-averaged acoustic source powers $\langle P_\mathrm{source}\rangle/(\rho_0 U S_\mathrm{p}|u'|^2)$ for primary and secondary peaks for configuration D at all the plateau length to cavity width ratios L_p/W at a fluctuation amplitude of $|u'|/U = 0.05$.

(the first frame) corresponds to the change in the sign of the acoustic grazing velocity from upstream to downstream. Following the Vortex Sound Theory of Howe [1975], as explained in detail in [Tonon et al., 2010; Nakiboğlu et al., 2010], the spatial position of the vortex core at the cavity mouth and the moment in time with respect to the period of the coupling standing wave determine whether the vortex core produces or absorbs sound. Thus in a system of multiple cavities which are close to each other as in configuration D, a synchronization of the motion of the vortex core at the cavity openings among the consecutive cavities amplifies the respective sound production and absorption process. It is seen from figure 6.9 that the vortex cores for the upstream and the downstream cavity have a perfect synchronization, which results in an amplification of sound production, see figure 6.8-a.

In figure 6.10 and figure 6.11, instantaneous normalized vorticity contours are given for four different moments in time within a single oscillation period in the region around the cavities for configuration D for $L_\mathrm{p}/W = 0.750$, $|u'|/U = 0.05$ at Strouhal numbers of $Sr = 0.75$ and $Sr = 0.82$, respectively. It appears that for the case of $Sr = 0.75$ the hydrodynamic interference suppresses the vortex shedding in the downstream cavity. This strong negative hydrodynamic interference results in a local minimum in the produced time-averaged acoustic source power, see figure 6.8-d.

As seen in figure 6.11 for a Strouhal number of $Sr = 0.82$, although the plateau length is same as in the previous case, there is some synchronization of the vortex motions in the two cavities. This increases the time-averaged acoustic source power, as seen in figure 6.8-d, as a matter of fact this point corresponds to a local maximum. The respective movies for the three cases presented in figure 6.9, 6.10 and 6.11, are provided as supplementary material. It is concluded that the hydrodynamic interference between the adjacent cavities is due to an increased or decreased synchronization of the vortex motion in the two cavities.

Figure 6.9: Instantaneous normalized vorticity contours given for four different moments in time within a single oscillation period in the region around the cavities for configuration D for $L_\mathrm{p} = 0$, $Sr_\mathrm{p-w} = 0.77$ and $|u'|/U = 0.05$.

Figure 6.10: Instantaneous normalized vorticity contours given for four different moments in time within a single oscillation period in the region around the cavities for configuration D for $L_{\mathrm{p}}/W = 0.750$, $Sr_{\mathrm{p-w}} = 0.75$ and $|u'|/U = 0.05$.
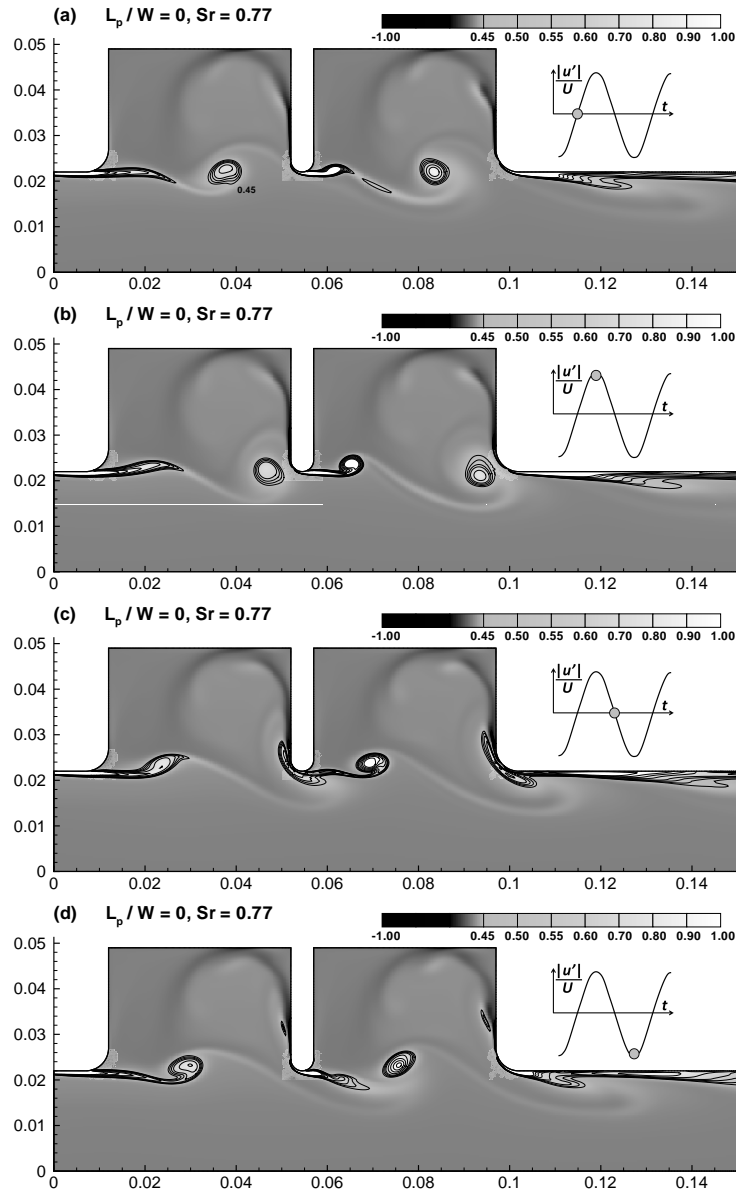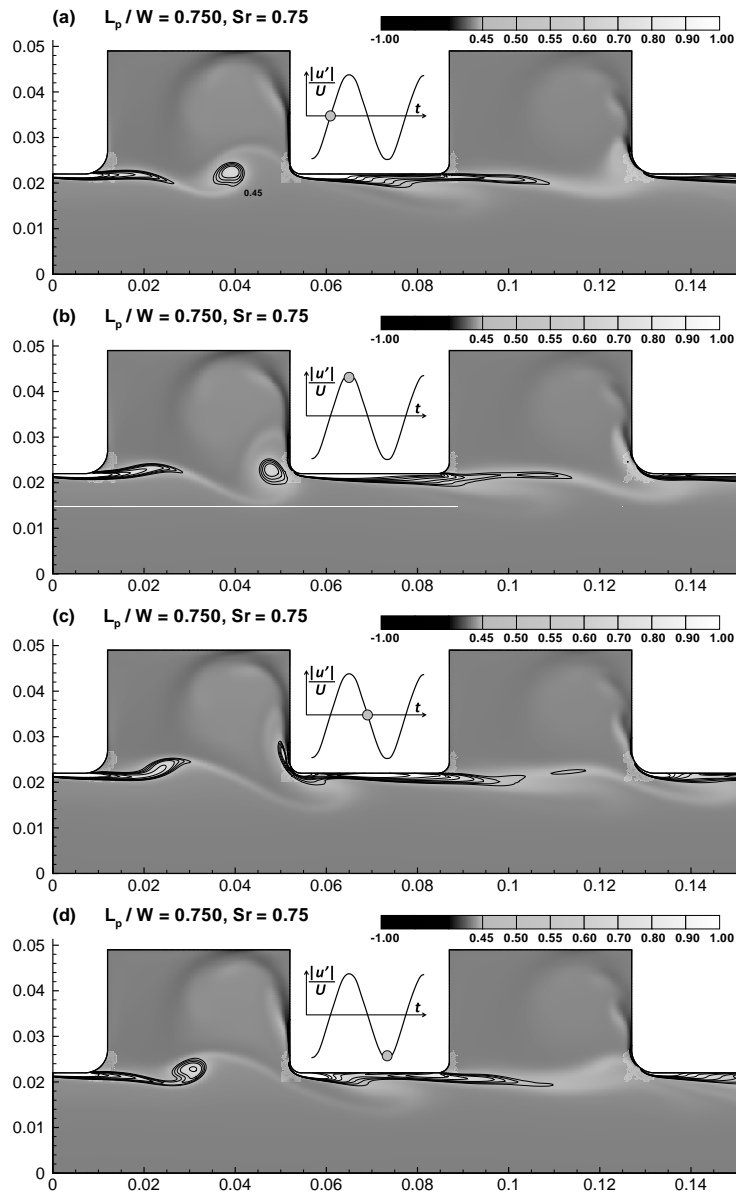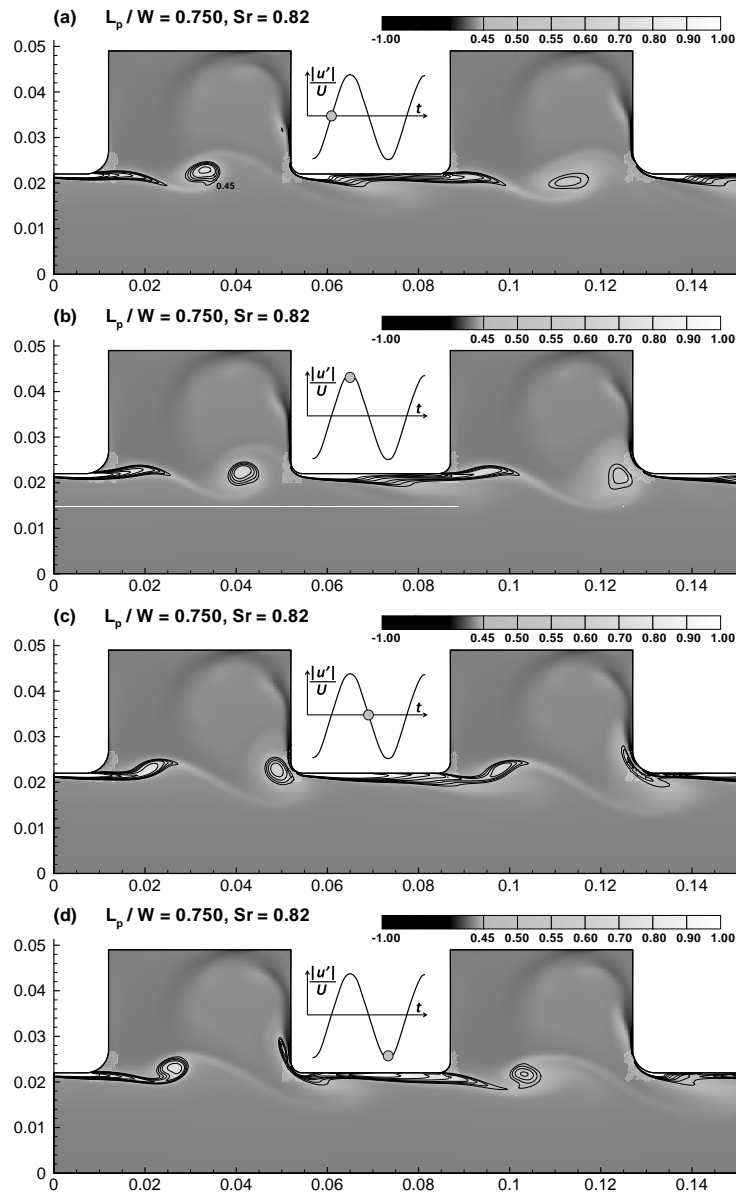
Figure 6.11: Instantaneous normalized vorticity contours given for four different moments in time within a single oscillation period in the region around the cavities for configuration D for $L_{\mathrm{p}}/W = 0.750$, $Sr_{\mathrm{p-w}} = 0.82$ and $|u'|/U = 0.05$.

6.5   Conclusions

Aeroacoustic sound generation due to a self-sustained oscillations, whistling, by a series of axisymmetric cavities exposed to a grazing flow has been studied both experimentally and numerically. The feedback effect is produced by the velocity fluctuations resulting from a coupling of vortex sheddings at the upstream cavity edges with acoustic standing waves in the coaxial pipe.

When the acoustic sources, i.e. the axisymmetric cavities, are placed at different pressure nodes, which are hydrodynamically separated from each other, the total acoustic source power of the system can be determined from the addition of the individual contributions of each cavity.

When the cavities are placed adjacent to each other i.e. around the same pressure node, a strong hydrodynamic interference between the cavities can be observed for $L_{\mathrm{p}}/W = O(1)$. The hydrodynamic interference depends strongly on the distance between the cavities, i.e. L_{p}/W. This affects both the dimensionless peak amplitude, $|u'|/U$, and the Strouhal number, Sr_{p-w}, at which this peak amplitude is observed.

The proposed numerical method successfully captures the observed hydrodynamic interference between adjacent cavities. It provides excellent predictions of the values of $Sr_{\mathrm{p-w}}$ (an accuracy of 3%). The numerical method shows that for adjacent cavities the synchronization of the travelling vortex cores at the cavity openings can increase or decrease due to hydrodynamic interference. The synchronization amplifies the sound production of the multiple cavity system. The numerical method also demonstrates that the hydrodynamic interference can be so strong that it can even suppress the vortex shedding for the downstream cavity, which decreases the sound production/absorption considerably.

Conclusions and Perspectives

In thin walled pipes corrugations provide local stiffness while allowing a global flexibility. This unique characteristic makes corrugated pipes convenient for applications ranging from domestic appliances to natural gas transport. At critical conditions, however, the flow through these pipes drives self-sustained flow oscillations that lead to high-amplitude sound generation, called whistling. The presented work combined experimental, numerical and analytical approaches to provide a solid understanding of the whistling in corrugated pipes. In this chapter the global conclusions emerging from the analysis presented in previous chapters and the perspectives for future research are presented.

7.1   Conclusions

Multiple shallow side branch system as an acoustic analog of a corrugated pipe

Experiments performed with multiple shallow side branch systems and corrugated pipes have shown that these two systems have similar whistling characteristics. In both systems the frequency displays a stepwise increase with increasing Mach number, where the increase on average is approximately linear, which corresponds to a Strouhal number (Sr). The lock-in to longitudinal acoustic pipe modes explains the plateaus in the whistling frequency as a function of the flow velocity. The experiments with multiple side branch systems also show that axisymmetry of the cavities is not a necessary feature for the whistling phenomenon observed in corrugated pipes. (Chapter 2)

The work on multiple side branch systems also confirms that similar to corrugated pipes [Belfroid et al., 2007] a characteristic length, equal to the cavity width

(W) plus the upstream edge radius (r_{up}), minimizes the scatter in the measured Strouhal number (Sr), for different cavity geometries. (Chapter 2)

Hysteresis has been reported in corrugated pipe whistling [Petrie and Huntley, 1980; Nakamura and Fukamachi, 1991; Kristiansen et al., 2011] in which the jump to the next acoustic mode occurs for an increasing flow velocity at a slightly lower flow velocity than for a decreasing flow velocity. A similar hysteresis has been observed also for multiple side branch systems. (Chapter 2)

The peak-whistling Strouhal number

The peak-whistling Strouhal number ($Sr_{\mathrm{p-w}}$), the Strouhal number at which the maximum amplitude in acoustic fluctuations is registered, is independent of the length of the corrugated pipe, however it depends on the ratio of the momentum thickness of the grazing flow boundary layer to the cavity width (δ_2/W). The smaller the momentum thickness the higher the peak-whistling Strouhal number. There is a critical value of Strouhal number based on momentum thickness ($Sr_{\delta 2} = \delta_2 f/U$), above which a hydrodynamic mode does not whistle. This value is accurately predicted by the theory of linear stability of parallel shear flows, proposed by Michalke [1965]. (Chapters 3, 4 and 5)

Influence of geometry of corrugations

The shape of the upstream edge of the corrugation has a strong effect on the amplitude of the acoustic fluctuations. A rounded upstream cavity edge promotes the sound production considerably. (Chapter 2)

The cavity depth to width ratio has a strong effect on the whistling for shallow cavities ($H/W \leq 0.5$) both for the limit cycle amplitude and for the peak-whistling Strouhal number ($Sr_{\mathrm{p-w}}$). For deeper cavities ($H/W \geq 0.5$) both the peak-whistling Strouhal number and the acoustic source power are independent of the cavity depth. For shallow cavities ($H/W \leq 0.5$) it appears that there is a difference in the whistling behavior of side branch systems and axisymmetric cavities, indicating a limitation to the similitude of the acoustics of multiple side branch systems and corrugates pipes. This difference is expected to be due to the difference in pulsation amplitudes between these two systems. Since the amplitude of pulsations recorded in multiple side branch systems are much lower than the one of corrugated pipes, the former system is more sensitive to small variations in damping. (Chapters 2 and 5)

Numerical method

Experiments performed with corrugated pipes and multiple side branch systems showed that sound generation in such systems is a local effect and can be understood in first order approximation by focusing on the flow at a single corrugation.

Judicious choice of both hydrodynamic and acoustic boundary conditions, which will prevail in a corrugated pipe, is crucial for accurate numerical predictions for the sound generation. (Chapters 3, 4, 5 and 6)

If in corrugated pipes the corrugation depth (H) and width (W) are small compared to the wavelength of the longitudinal standing wave (λ), the wave propagation is locally negligible, i.e. each cavity is acoustically compact. This corresponds to the assumption that the flow in the source region is locally incompressible. Thus, it is possible to study the response of the shear layer instability at the corrugation mouth to an imposed acoustic velocity perturbation using an incompressible flow method. (Chapters 3, 4, 5, 6)

Combining the incompressible flow solution with the *Vortex Sound Theory*, the time averaged acoustic source power produced by single or multiple corrugations can be determined by a surface integral of the product of the fluctuating total enthalpy and the mass flux through the boundary of a control volume, enclosing the compact source region. The key idea in this method is to define the source of sound as the difference between the total enthalpy difference calculated across the cavity and the total enthalpy difference in a reference flow without cavity. (Chapters 3, 4, 5, 6)

The proposed numerical method involves 2D-axisymmetric incompressible flow simulations without turbulence modeling, which makes the method a computationally efficient approach. Thus, it was possible to use it extensively to address almost all aspects that have been investigated experimentally.

The proposed numerical method successfully predicts the Strouhal number ranges of acoustic energy production/absorption and the nonlinear saturation mechanism responsible for the stabilization of the limit cycle oscillation. (Chapters 3, 4, 5, 6)

The numerical method predicts peak-whistling Strouhal numbers in close agreement with experimental results and explains the dependency of the peak-whistling Strouhal number on the momentum thickness δ_2. (Chapters 3)

The numerical method predicts accurately the dependency of the peak-whistling Strouhal number on the depth to width ratio H/W of the cavities. For shallow cavities $H/W \leq 0.5$, a linear dependency of the peak-whistling Strouhal number on cavity depth to width ratio is observed. This is explained analytically by using a point-vortex method. (Chapters 5)

The numerical method predicts the average acoustic source power produced by a corrugation within a factor of two. The prediction of the whistling amplitude by means of an energy balance involves calculation of the sound source power as a function of Strouhal number (Sr) within a broad range of acoustical amplitudes ($|u'|/U$). Such a large number of numerical simulations would not be practical for 3-D Direct Numerical Simulations (DNS) or Large Eddy Simulations (LES) when using recently available computational power. (Chapters 4)

Hydrodynamic interference

Extending the single corrugation modeling approach to the neighboring corrugation provides insight into the hydrodynamic interference between successive corrugations. This interference has a significant impact on the whistling behavior, which can be constructive or destructive depending on the separation distance (plateau length, L_p) between the corrugations. (Chapters 6)

The numerical method explains the hydrodynamic interference appearing between successive cavities as a synchronization of the traveling vortex cores at corrugation mouths. The numerical method and experiments on double cavities demonstrates that the hydrodynamic interference can even suppress the vortex shedding at the downstream corrugation. This reduces the sound production considerably. (Chapters 6)

The numerical method accurately predicts the energy production/absorption ranges of Strouhal number (Sr) and peak-whistling Strouhal numbers ($Sr_\mathrm{p-w}$) in energy producing range even in the presence of a strong hydrodynamic interference. Furthermore it successfully explains the dependency of the hydrodynamic interference on the separation distance between the consecutive cavities. (Chapters 6)

Musical aspects

The sound radiation from a short corrugated pipe segment (Hummer) used as a musical instrument has been investigated. An analytical radiation model is proposed which can accurately predict the observed frequency at the listener position as well as the sound pressure level within 3dB. The model predicts qualitatively the amplitude modulation which is essential for the musical quality of the chorus like sound of the Hummer. (Chapters 4)

7.2   Global conclusions

As an overview of the conclusions the work presented in the thesis provides,

- a physical understanding of the aeroacoustic sound generation due to self-sustained oscillations observed in corrugated pipes.

- an extensive accurate set of experimental data for various corrugation geometries and information on the effect of a number of dimensionless geometrical parameters on the whistling namely, pipe length to pipe diameter ratio (L/D), cavity depth to width ratio (H/W), cavity edge radii to width ratio (r_up/W, r_dwn/W), plateau length to cavity width ratio (L_p/W).

- a numerical methodology for the prediction of

- the range of Strouhal number (*Sr*) for which self-sustained oscillations lead to sound generation,

- the maximum dimensionless time averaged acoustic source power produced by a corrugation ($\langle P_{\text{source}} \rangle / (\rho_0 U S_{\text{p}} |u'|^2)$) and the limit cycle acoustic oscillation amplitude ($|u'|/U$) that can be attained in a corrugated pipe during whistling,

- the variation in these two parameters *Sr* and $\langle P_{\text{source}} \rangle / (\rho_0 U S_{\text{p}} |u'|^2)$ due to variation in dimensionless geometrical parameter of corrugations, such as H/W, L_{p}/W, δ_2/W.

7.3   Perspectives

It is possible to design corrugated pipes composed of corrugations with different cavity widths or depths and with various plateau lengths such that the acoustic and hydrodynamic interference between the cavities will counteract and reduce the produced acoustic source power.

It should also be noted that although the main consideration in the present study is the corrugated pipes, some of the conclusions of the study are applicable to various other ducted flows e.g. mufflers, wall perforations, pipe systems with side branches, axisymmetric cavity-pipe configurations and orifices [Lacombe et al., 2011].

In chapter 4 it has been shown that a corrugated segment can remain silent even if the flow is turbulent. Thus, it has been concluded that the absence of whistling is not related to the lack of turbulence as it has been suggested in the early literature [Crawford, 1974; Cadwell, 1994]. Turbulence, however, is expected to be important for a more accurate prediction of the generated acoustic source power by corrugations. The next step might be employing Reynolds-averaged Navier-Stokes (RANS) turbulence modeling, which can improve the predictions of the numerical method while keeping the computational cost of the method relatively low [Lacombe et al., 2011].

This work is limited to cases in which the feedback effect is produced by the velocity fluctuations resulting from a coupling with a longitudinal acoustic standing wave in a corrugated pipe. At very high velocities, however, transverse modes will occur in corrugated pipes. Although the transverse mode is not an effective sound radiating source, it leads to very high fluctuation amplitudes inside the cavity. Also as a result of nonlinear wave propagation a strongly radiating second harmonic of the oscillation frequency can occur [Kriesels et al., 1995].

Bending a corrugated pipe can have a significant effect on the whistling behavior. In chapter 4, it has been demonstrated that bending can suppress the whistling at some specific conditions. A systematic study, however, has not been performed.

Experiments on Hummer indicated a non-constant rotation velocity during the performance, which leads to accelerations and decelerations in the flow. Thus hys-

teresis are expected to appear (see, chapter 2) in the whistling behaviour, which can have an important effect on the musical quality of the Hummer. This phenomenon has not been investigated in this thesis.

Bibliography

Allam, S. and M. Åbom, 2006: Investigation of damping and radiation using full plane wave decomposition in ducts. *J. Sound Vib.*, **292**, 519–534.

Angus, M. T. and M. T. Lyon, 2008: Quiet gas connector. *United States Patent Application Publication*, **US20080012331A1**.

Aurégan, Y. and M. Leroux, 2003: Failures in the displacement models for flow duct with perforations: an experimental investigation. *J. Sound Vib.*, **265**, 109–121.

Aurégan, Y. and M. Leroux, 2008: Experimental evidence of an instability over an impedance wall in a duct with flow. *J. Sound Vib.*, **317**, 432–439.

Banks-Lee, P. and H. Peng, 1989: Length error analysis for impedance tube measurements. *J. Acoust. Soc. Am.*, **85**, 1769–1772.

Bastiaansen, J., 2005: Characterisation of flow-induced pulsations in corrugated pipes. M.S. thesis, TNO, Delft, the Netherlands.

Belfroid, S. P. C., D. P. Shatto, and R. M. C. A. M. Peters, 2007: Flow induced pulsations caused by corrugated tubes, San Antonio, Texas. ASME-PVP, PVP2007-26503.

Binnie, A. M., 1960: Self-induced waves in a conduit with corrugated walls i. experiments with water in an open horizontal channel with vertically corrugated sides. *Proc. R. Soc. London Ser. A*, **259**, 18–27.

Binnie, A. M., 1961: Self-induced waves in a conduit with corrugated walls ii. experiments with air in corrugated and finned tubes. *Proc. R. Soc. London Ser. A*, **262**, 179–191.

Blake, W. K., 1986: *Mechanics of flow induced sound and vibration: Vol 1 & Vol 2*. Academic Press, New York, USA.

Blevins, R. D., 1984: *Applied Fluid Dynamics Handbook*, 55–56. Krieger Pub., Malabar, FL.

Blevins, R. D., 2001: *Flow induced vibration*, 2nd *Edition*. Krieger Publishing Company, Malabar, Florida.

Bracewell, R. N., 1986: *The Fourier transform and its applications*. McGraw Hill, Boston, MA.

Brès, G. and T. Colonius, 2008: Three-dimensional instabilities in compressible flow over open cavities. *J. Fluid Mech.*, **599**, 309–339.

Bruggeman, J. C., 1987a: Flow induced pulsations in pipe systems. Ph.D. thesis, Eindhoven University of Technology, Eindhoven, the Netherlands.

Bruggeman, J. C., 1987b: The propagation of low-frequency sound in a two-dimensional duct system with t-joints and right angle bends: theory and experiment. *J. Acoust.Soc.Am.*, **82**, 1045–1051.

Bruggeman, J. C., A. Hirschberg, M. E. H. vanDongen, A. P. J. Wijnands, and J. Gorter, 1991: Self-sustained aero-acoustic pulsations in gas transport systems: experimental study of the influence of closed side branches. *J. Sound Vib.*, **150**, 371–393.

Bruggeman, J. C., P. J. Wijnands, and J. Gorter, 1986: Self-sustained low frequency resonance in low Mach number gas flow through pipelines with side branch cavities, Seattle, Washington. AIAA, No. 86-1924.

Burstyn, W., 1922: Eine neue pfeife (a new pipe). *Z. Tech. Phys.*, **3**, 179–180.

Cadwell, L. H., 1994: Singing corrugated pipes revisited. *Am. J.Phys.*, **62**, 224–227.

Cargill, A. M., 1971: Low frequency acoustic radiation from a jet pipe - a second order theory. *J. Sound Vib.*, **83(3)**, 339–354.

Cargill, A. M., 1982: Low-frequency sound radiation and generation due to the interaction of unsteady flow with a jet pipe. *J. Fluid Mech.*, **121**, 59–105.

Cermak, P., 1922: Über die tonbildung bei metallschläuchen mit eingedrücktem spiralgang (on the sound generation in flexible metal hoses with spiraling grooves). *Phys. Z.*, **23**, 394–397.

Charwat, A. F., 1961: An investigation of separated flows: part 1, the pressure field. *J. Aerospace Sciences*, **28**, 457–470.

Colonius, T. and S. K. Lele, 2004: Computational aeroacoustics: progress on nonlinear problems of sound generation. *Progress in Aerospace Sciences*, **40**, 345–416.

Crawford, F. S., 1974: Singing corrugated pipes. *Am. J. Phys.*, **62**, 278–288.

Curle, N., 1955: The influence of solid boundaries upon aerodynamic sound. *Proc. R. Soc. Lond. A*, **231**, 505–514.

da Silva, A. R., G. P. Scavone, and A. Lefebvre, 2009: Sound reflection at the open end of axisymmetric ducts issuing a subsonic meanflow: A numerical study. *J. Sound Vib.*, **327**, 507–528.

Davies, P. O. A. L., 1981: Flow-acoustic coupling in ducts. *J. Sound Vib.*, **77(2)**, 191–209.

Davies, P. O. A. L., 1988: Practical flow duct acoustics. *J. Sound Vib.*, **124(1)**, 91–115.

Debut, V., J. Antunes, and M. Moreira, 2007: Experimental study of the flow-excited acoustical lock-in in a corrugated pipe., Cairns, Australia. 14th International Conference on Sound and Vibration.

Debut, V., J. Antunes, and M. Moreira, 2008: Flow-acoustic interaction in corrugated pipes: time domain simulation of experimental phenomena. *Flow Induced Vibration*, I. Zolotarev and J. Horácek, Eds., Institute of Thermomechanics, Prague, Czech Republic, 9th International Conference on Flow-Induced Vibration, 6 p.

Delprat, N., 2006: Rossiter's formula: A simple spectral model for a complex amplitude modulation process ? *Phys. Fluids*, **18(7)**, 071 703.

Dequand, S., S. J. Hulshoff, and A. Hirschberg, 2003a: Self-sustained oscillations in a closed side branch system. *J. Sound Vib.*, **265**, 359–386.

Dequand, S., X. Luo, J. F. H. Willems, and A. Hirschberg, 2003b: Helmholtz-like resonator self-sustained oscillations, part 1. *AIAA Journal*, **41(3)**, 408–415.

Derks, M. M. G. and A. Hirschberg, 2004: Self-sustained oscillations of the flow along helmholtz resonators in a tandem configuration, Ecole Polytechnique, Paris. Proceedings of 8th Int. Conf. on Fluid-Induced Vibrations, 435–440.

Dowling, A. P. and J. F. Williams, 1983: *Sound and sources of sound*, 187–190. Ellis Horwood Ltd, West Sussex, England.

Eggels, J. G. M., F. Unger, M. H. Weiss, J. Westerwell, R. J. Adrian, R. Friedrich, and F. T. M. Nieuwstadt, 1994: Fully developed turbulent pipe flow: a comparison between direct numerical simulation and experiment. *J. Fluid Mech.*, **268**, 175–209.

Elder, S. A., 1980: Forced oscillations of a separated shear layer with application to cavity flow-tone effects. *J. Acoust. Soc. Am.*, **67(3)**, 774–781.

Elder, S. A., T. M. Farabee, and F. C. DeMetz, 1982: Mechanisms of flow-excited cavity tones at low Mach number. *J. Acoust. Soc. Am.*, **72(2)**, 532–549.

Elliott, J. W., 2004: Corrugated pipe flow. *Lecture Notes on the Mathematics of Acoustics*, M. C. M. Wrigth, Ed., Imperial College Press, 207–222.

English, E. J. and K. R. Holland, 2010: Aeroacoustic sound generation in simple expansion chambers. *J. Acoust. Soc. Am.*, **128(5)**, 2589–2595.

Ethembabaoglu, S., 1973: *On the fluctuating flow characteristics in the vicinity of gate slots*. Division of Hydraulic Engineering, Norwegian Institute of Technology, University of Trondheim, Trondheim, Norway, quoted by Rockwell and Naudascher, 1978.

Finnegan, S. L., C. Meskell, and S. Ziada, 2009: Experimental investigation of the aeroacoustic sources in a tandem cylinder configuration. ASME-PVP, PVP2009-77757.

Fletcher, J. C., 1979: Air flow and sound generation in musical wind instruments. *Ann. Rev. Fluid Mech.*, **11**, 95–121.

Fletcher, N. H. and T. D. Rossing, 1991: *The physics of Musical Instruments*, 436–447. Springer-Verlag, New York.

Freymunt, P., 1966: On transition in a separated laminar boundary layer. *J. Fluid Mech.*, **25**, 683–704.

Geveci, M., P. Oshkai, D. Rockwell, J. C. Lin, and M. Pollack, 2003: Imaging of the self-excited oscillation of flow past a cavity during generation of a flowtone. *J. Fluid. Struct.*, **18**, 79–92.

Gloerfelt, X., 2009: *Cavity noise*, von Karman Lecture Notes on aerodynamic noise from wall-bounded flows, Brussels.

Golliard, J., 2002: Noise of Helmholtz-resonator like cavities excited by low Mach-number turbulent flows. Ph.D. thesis, École Supérieure d'Ingénieurs de Poitiers, Poitiers, France.

Golliard, J., D. Tonon, and S. P. C. Belfroid, 2010: Experimental investigation of the source locations for whistling short corrugated pipes, Montreal, Canada. Proceedings of ASME 2010 3rd Joint US-European Fluids Engineering Summer Meeting and 8th International Conference on Nanochannels, Microchannels and Minichannels.

Goyder, H., 2009: On the modelling of noise generation in corrugated pipes, Prague, Czech Republic. ASME-PVP, PVP2009-77321.

Goyder, H., 2010: On the modelling of noise generation in corrugated pipes. *J. Pressure Vessel Technol.*, **132:4**.

Gutin, L., 1948: *On the sound field of a rotating propeller*, NACA TM No.1195, Original in Russian:Zhurnal Tekhnicheskoi Fiziki 1936; 12:76–83.

Hall, J. W., S. Ziada, and D. S. Weaver, 2003: Vortex-shedding from single and tandem cylinders in the presence of applied sound. *J. Fluids Struct*, **18**, 741–758.

Heller, S. S. and D. B. Bliss, 1975: The physical mechanism of flow induced pressure fluctuations in cavities and concepts for their suppression, Washington, DC. AIAA, 75-491.

Hirschberg, A., 2001: *Lecture notes: Advances in aeroacoustics*, von Karman Institute for Fluid Dynamics, Sint-Genesius-Rode, Belgium.

Hirschberg, A., J. C. Bruggeman, A. P. J. Wijnands, and N. Smits, 1989: The whistler nozzle and horn as aero-acoustic sound sources in pipe systems. *Acustica*, **68**, 157–160.

Hofmans, G. C., 1998: Vortex sound in confined flows. Ph.D. thesis, Eindhoven University of Technology, Eindhoven, the Netherlands.

Hourigan, K., M. C. Welsh, M. C. Thompson, and A. N. Stokes, 1990: Aerodynamic sources of acoustic resonance in a duct with baffles. *J. Fluids and Structures*, **4(4)**, 345–370.

Howe, M. S., 1975: Contributions to the theory of aerodynamic sound, with application to excess jet noise and the theory of the flute. *J. Fluid Mech.*, **71**, 625–673.

Howe, M. S., 1980: The dissipation of sound at an edge. *J. Sound Vib.*, **70**, 407–411.

Howe, M. S., 1984: On the absorption of sound by turbulence and other hydrodynamic flows. *IMA J. Appl. Math.*, **32**, 187–209.

Howe, M. S., 1997: Edge, cavity and aperture tones at very low mach numbers. *J. Fluid Mech.*, **330**, 61–84.

Howe, M. S., 1998: *Acoustics of Fluid-Structure Interactions*. Cambridge Univesity Press, Cambridge, UK.

Huang, X. Y. and S. Weaver, 1991: On the active control of shear layer oscillations across a cavity in the presence of pipeline acoustic resonance. *J. Fluid. Struct.*, **5**, 207–219.

Ingard, U. and V. K. Singhal, 1975: Effect of flow on the acoustic resonances of an open-ended duct. *J. Acoust. Soc. Am.*, **58(4)**, 788–793.

Keller, J. J., 1984: Non-linear self-excited acoustic oscillations in cavities. *J. Sound Vib.*, **94**, 397–409.

Kergomard, J., 1985: Comments on "wall effects on sound propagation in tubes". *J. Sound Vib.*, **98**, 149–153.

Kirchhoff, G., 1868: Ueber den einfluss der wärmeleitung in einem gase auf die schallbewegung. *Annalen der Physik*, **210(6)**, 177–193.

Kooijman, G., A. Hirschberg, and J. Golliard, 2008: Acoustical response of orifices under grazing flow: Effect of boundary layer profile and edge geometry. *J. Sound Vib.*, **315**, 849–874.

Kop'ev, V. F., M. A. Mironov, and V. S. Solntseva, 2008: Aeroacoustic interaction in a corrugated duct. *Acoustical Phys.*, **54**, 197–203.

Kriesels, P. C., M. C. A. M. Peters, A. Hirschberg, A. P. J. Wijnands, A.Iafrati, G. Riccardi, R. Piva, and J. C. Bruggeman, 1995: High amplitude vortex-induced pulsations in a gas transport system. *J. Sound Vib.*, **184**, 343–368.

Krishnamurty, K., 1955: *Acoustic radiation from two-dimensional rectangular cutouts in aerodynamic surfaces*, NACA Technical Note No:3487, NACA, USA.

Kristiansen, U. R., P. O. Mattei, C. Pinhede, and M. Amielh, 2011: Experimental study of the influence of low frequency flow modulation on the whistling behavior of a corrugated pipe. *J. Acoust. Soc. Am.*, **130**, 1851–1855.

Kristiansen, U. R. and G. A. Wiik, 2007: Experiments on sound generation in corrugated pipes with flow. *J. Acoust. Soc. Am.*, **121**, 1337–1344.

Kronland-Martinet, R. and T. Voinier, 2008: Real-time perceptual simulation of moving sources: application to the leslie cabinet and 3d sound immersion. *EURASIP Journal on Audio, Speech, and Music Processing*, **849696**.

Lacombe, R., P. Moussou, and Y. Auregan, 2011: Identification of whistling ability of a single hole orifice from an incompressible flow simulation, Baltimore, Maryland. ASME-PVP, PVP2011-57355.

Lafon, P., S. Caillaud, J. P. Devos, and C. Lambert, 2003: Aeroacoustical coupling in a ducted shallow cavity and fluid/structure effects on a steam line. *J. Fluids Struct.*, **18**, 695–713.

Lange, B. and D. Ronneberger, 2003: Active noise control by use of an aeroacoustic instability. *Acta Acustica united with Acustica*, **89**, 658–665.

Martínez-Lera, P., C. Schram, S. Föller, R. Kaess, and W. Polifke, 2009: Identification of the aeroacoustic response of a low Mach number flow through a T-joint. *J. Acoust. Soc. Am.*, **126(2)**, 582–586.

Meile, T., J.-L. Boillat, and A. Schleiss, 2010: Unsteady flow in a channel with large scale bank roughness, Braunschweig, Germany. River Flow, EPFL-CONF-151686.

Michalke, A., 1965: On spatially growing disturbances in an inviscid shear layer. *J. Fluid Mech.*, **23(3)**, 521–544.

Milne-Thomson, L. M., 1968: *Theoretical Hydrodynamics*. Macmillan, London, UK.

Mohany, A. and S. Ziada, 2005: Flow-excited acoustic resonance of two tandem cylinders in cross-flow. *J. Fluids Struct*, **21**, 103–119.

Morfey, C. L., 1971: Sound transmission and generation in ducts with flow. *J. Sound Vib.*, **14**, 37–55.

Munt, R. M., 1977: The interaction of sound with a subsonic jet issuing from a semi-infinite cylindrical pipe. *J. Fluid Mech.*, **83**, 609–640.

Munt, R. M., 1990: Acoustic transmission properties of a jet pipe with subsonic jet flow: I. the cold jet reflection coefficient. *J. Sound Vib.*, **142**, 413–436.

Myers, M. K., 1986: An exact energy corollary for homentropic flow. *J. Sound Vib.*, **109(2)**, 277–284.

Myers, M. K., 1991: Transport of energy by disturbances in arbitrary steady flows. *J. Fluid Mech.*, **226**, 383–400.

Nakamura, Y. and N. Fukamachi, 1984: Sound generation in a magic pipe. *J. Japan Sot. Fluid Mech. Nagare*, **3**, 199–203.

Nakamura, Y. and N. Fukamachi, 1991: Sound generation in corrugated tubes. *Fluid Dynamics Research*, **7**, 255–261.

Nakiboğlu, G., S. Belfroid, J. Golliard, and A. Hirschberg, 2011a: On the whistling corrugated pipes: effect of pipe length and flow profile. *J. Fluid Mech.*, **672**, 78–108.

Nakiboğlu, G., S. P. C. Belfroid, D. Tonon, J. Willems, and A. Hirschberg, 2009: A parametric study on the whistling of multiple side branch system as a model for corrugated pipes, Prague, Czech Republic. ASME-PVP, PVP2009-77754.

Nakiboğlu, G., S. P. C. Belfroid, J. F. H. Willems, and A. Hirschberg, 2010: Whistling behavior of periodic systems: corrugated pipes and multiple side branch system. *Int. J. Mech. Sci.*, **52(11)**, 1458–1470.

Nakiboğlu, G., H. B. M. Manders, and A. Hirschberg, 2011b: Aeroacoustic power generated by a compact axisymmetric cavity: prediction of self-sustained oscillation and influence of the depth. *J. Fluid Mech.*, **Submitted**.

Nakiboğlu, G., O. Rudenko, and A. Hirschberg, 2012: Aeroacoustics of the swinging corrugated tube: voice of the dragon. *J. Acoust. Soc. Am.*, **131(1)**, 749–765.

Nederveen, C. J., 1998: *Acoustical aspects of woodwind instruments*, 160. Northern Illinois University Press, DeKalb,IL.

Nelson, P. A., N. A. Halliwell, and P. E. Doak, 1983: Fluid dynamics of a flow excited resonance, part ii: Flow acoustic interaction. *J. Sound Vib.*, **91**, 375–402.

Oshkai, P., D. Rockwell, and M. Pollack, 2005: Shallow cavity flow tones: transformation from large- to small-scale modes. *J. Sound Vib.*, **280**, 777–813.

Patankar, S. V. and D. B. Spalding, 1972: A calculation procedure for heat mass and momentum transfer in three dimensional parabolic flows. *Int J. Heat Mass Transfer*, **15**, 1787–1806.

Peters, M. C. A. M., 1993: Aeroacoustic sources in internal flows. Ph.D. thesis, Technische Universiteit Eindhoven, Eindhoven, the Netherlands.

Peters, M. C. A. M., A. Hirschberg, A. J. Reijnen, and A. P. J. Wijnands, 1993: Damping and reflection coefficient measurements for an open pipe at low Mach and low Helmholtz numbers. *J. Fluid Mech.*, **256**, 499–534.

Petrie, A. M. and I. D. Huntley, 1980: The acoustic output produced by a steady airflow through a corrugated duct. *J. Sound Vib.*, **70(1)**, 1–9.

Pierce, A. D., 1989: *Acoustics: An Introduction to Its Physical Principles and Applications*. 2d ed., Acoustical Society of America, Woodbury, New York.

Popescu, M. and S. T. Johansen, 2008: Acoustic wave propagation in low Mach flow pipe, Rono, Nevada. AIAA, No. 09-2407.

Popescu, M. and S. T. Johansen, 2009: Modelling of aero-acoustic wave propagation in low mach number corrugated pipe flow. *Progress in Computational Fluid Dynamics*, **9**, 417–425.

Powell, A., 1964: Theory of vortex sound. *J. Acoust. Soc. Am.*, **36**, 177–195.

Åbom, M. and H. Bodén, 1988: Error analysis of two-microphone measurements in ducts with flow. *J. Acoust. Soc. Am.*, **83**, 2429–2438.

Rayleigh, J. W. S., 1896: *The Theory of Sound - Volume I & II*. Macmillan, London, UK.

Rienstra, S. W., 1983: A small strouhal number analysis for acoustic wave-jet flow-pipe interaction. *J. Sound Vib.*, **86**, 539–556.

Rienstra, S. W. and A. Hirschberg, 2004: *Lecture notes: an introduction to acoustics*, 278–292. Eindhoven University of Technology, Eindhoven, Netherlands.

Rockwell, D., 1983: Oscillation of impinging shear layer. *AIAA Journal*, **21**, 645–664.

Rockwell, D., C. J. Lin, P. Oshkai, M. Reiss, and M. Pollack, 2003: Shallow cavity flow tone experiments: onset of locked-on states. *J. Fluid. Struct.*, **17**, 381–414.

Rockwell, D. and E. Naudascher, 1978: Review:self-sustaining oscillations of flow past cavities. *ASME J. Fluid Eng.*, **100**, 152–165.

Rockwell, D. and A. Schachenmann, 1982: Self-generation of organized waves in an impinging turbulent jet at low mach numbers. *J. Fluid Mech.*, **117**, 425–441.

Ronneberger, D. and C. D. Ahrens, 1977: Wall shear stress caused by small amplitude perturbations of turbulent boundary-layer flow: an experimental investigation. *J. Fluid Mech.*, **83(3)**, 433–464.

Roshko, A., 1955: *Some measurements of flow in a rectangular cutout*, NACA Technical Note No:3488, NACA, USA.

Rowley, C. W., D. R. Williams, T. Colonius, R. M. Murray, and D. G. Macmynowski, 2006: Linear models for control of cavity flow oscillations. *J. Fluid Mech.*, **547**, 317–330.

Rowley, C. W. and E. D. R. Williams, 2006: Dynamics and control of high-reynolds-number flow over open cavities. *Ann. Rev. Fluid Mech.*, **38**, 251–276.

Sarohia, V., 1977: Experimental investigation of oscillations in flow over shallow cavities. *AIAA Journal*, **15(7)**, 984–991.

Schachenmann, A. and D. Rockwell, 1980: Self-sustained oscillations of turbulent pipe flow terminated by an axisymmetric cavity. *J. Sound Vib.*, **73**, 61–72.

Schickele, P., 1976: *The Definitive Biography of P.D.Q. Bach*, 172–195. Random House, New York.

Schlichting, H., 1979: *Boundary layer theory*. McGraw Hill, New York.

Serafin, S. and J. Kojs, 2005: Computer models and compositional applications of plastic corrugated tubes. *Organised Sound*, **10:1**, 67–73.

Shapiro, A. H., 1953: *The Dynamics and Thermodynamics of Compressible Fluid Flow*, 92–93. Ronald, New York.

Silverman, M. P. and G. M. Cushman, 1989: Voice of the dragon: the rotating corrugated resonator. *Eur. J. Phys.*, **10**, 298–304.

Smith, J., S. Serafin, J. Abel, and D. Berners, 2002: Doppler simulation and the leslie, Hamburg, Germany. Proc. of the 5th Int. Conference on Digital Audio Effects (DAFx-02), 8 p.

Strouhal, V., 1878: Ueber eine besondere art der tonerregung. *Annu. Phys. Chem. (Wied. Annu. Phys.)*, **5**, 216–251.

Tam, C. K. W. and P. J. W. Block, 1978: On the tones and pressure oscillations induced by flow over rectangular cavities. *J. Fluid Mech.*, **89**, 373–399.

Tijdeman, H., 1975: On the propagation of sound waves in cylindrical tubes. *J. Sound Vib.*, **39(1)**, 1–33.

Tonon, D., B. J. T. Landry, S. P. C. Belfroid, J. F. H. Willems, G. C. J. Hofmans, and A. Hirschberg, 2010: Whistling of a pipe system with multiple side branches: comparison with corrugated pipes. *J. Sound Vib.*, **329**, 1007–1024.

Tummers, R. M. J., 2006: The aero-acoustics of corrugated pipes: wave damping and whistling behaviour. M.S. thesis, TNO, Delft, the Netherlands.

Welsh, M. C., A. N. Stokes, and R. Parker, 1984: Flow-resonant sound interaction in a duct containing a plate, part i: semi-circular leading edge. *J. Sound Vib.*, **95(3)**, 305–323.

Ziada, S. and E. T. Bühlmann, 1989: Flow impingement as an excitation source in control valves. *J. Fluids Struct*, **6**, 583–601.

Ziada, S. and E. T. Bühlmann, 1991: Flow-induced vibration in long corrugated pipes, IMechE, England. International Conference on Flow-Induced Vib.

Ziada, S., H. Ng, and C. E. Blake, 2003: Flow excited resonance of a confined shallow cavity in low Mach number flow and its control. *J. Fluid. Struct.*, **18**, 79–92.

Ziada, S. and S. Shine, 1999: Strouhal numbers of flow-excited acoustic resonance of closed side branches. *J. Fluid. Struct.*, **13**, 127–142.

List of publications

List of publications related to the work presented in this thesis.

Journal Articles

- **Nakiboğlu, G.** and Hirschberg, A. Aeroacoustic power generated by multiple compact axisymmetric cavities: effect of hydrodynamic interference on the sound production, *Physics of Fluids*, Submitted, 2011.

- **Nakiboğlu, G.**, Manders, H. B. M. and Hirschberg, A. Aeroacoustic power generated by a compact axisymmetric cavity: Prediction of self-sustained oscillation and influence of the depth, *Journal of Fluid Mechanics*, Submitted, 2011.

- **Nakiboğlu, G.**, Rudenko, O. and Hirschberg, A. Aeroacoustics of swinging corrugated tube: Voice of the Dragon, *Journal of Acoustic Society of America*, Vol 131(1), 749-765, 2012.

- **Nakiboğlu, G.**, Belfroid, S. P. C., Golliard, J. and Hirschberg, A. On the whistling of corrugated pipes: pipe length and flow profile, *Journal of Fluid Mechanics*, Vol 672: 78-108, 2011.

- **Nakiboğlu, G.**, Belfroid, S. P. C., Willems, J. F. H. and Hirschberg, A. Whistling behavior of periodic systems: Corrugated pipes and multiple side branch system, *International Journal of Mechanical Sciences*, Vol 52: 1458-1470, 2010.

Conference proceedings

- **Nakiboğlu, G.**, Rudenko, O., Golliard, J. and Hirschberg, A., Hydrodynamic interaction between whistling axisymmetric cavities in the presence of a coupling longitudinal standing wave, *Proceedings of ASME Pressure Vessels and Piping Division Conference*, PVP2011-57487, Baltimore, Maryland, USA, 2011.

- Golliard, J., Diez, N. G., **Nakiboğlu, G.**, Hirschberg, A. and Belfroid, S. Aeroacoustic source identification in gas transport pipe system, *Proceedings of ASME Pressure Vessels and Piping Division Conference*, PVP2011-57309, Baltimore, Maryland, USA, 2011.

- **Nakiboğlu, G.**, Rudenko, O. and Hirschberg, A. Effect of flow profile and cavity depth on the whistling of an axisymmetric cavity in the presence of a coupling longitudinal standing wave, *Proceedings of* 18th *International Congress on Sound and Vibration (ICSV)*, Rio de Janeiro, Brazil, 2011.

- Rudenko, O., **Nakiboğlu, G.**, and Hirschberg, A. Voice of the Dragon: experiment and theory. A serious study of a child's toy, *Proceedings of* 18th *International Congress on Sound and Vibration (ICSV)*, Rio de Janeiro, Brazil, 2011.

- **Nakiboğlu, G.**, Hirschberg, A. A numerical study of the aeroacoustic interaction of a cavity with a confined flow: effect of edge geometry in corrugated pipes, *Proceedings of ASME* 3rd *Joint US-European Fluids Engineering Summer Meeting and* 8th *International Conference on Nanochannels, Microchannels, and Minichannels*, FEDSM-ICNMM2010-30300, Montreal, Canada, 2010.

- Tonon, D., **Nakiboğlu, G.**, Golliard, J. and Hirschberg, A. Voice of the dragon: the mystery of the missing fundamental mode. *Proceedings of* 20th *International Symposium on Music Acoustics*, Sydney, Australia, 2010.

- **Nakiboğlu, G.**, Hirschberg, A. A numerical study on the effect of confinement ratio in whistling corrugated pipes. *Proceedings of* 17th *International Congress on Sound and Vibration (ICSV)*, Cairo, Egypt, 2010.

- Tonon, D., **Nakiboğlu, G.**, Willems, J.F.H., Hirschberg, A., Leandro, R. E., Polifke, W. and Riezebos, H. J. Self-sustained aeroacoustic oscillations in multiple side branch pipe systems. *Proceedings of* 15th *AIAA/CEAS Aeroacoustics Conference (30th AIAA Aeroacoustics Conference)*, Miami, Florida, 2009.

- **Nakiboğlu, G.**, Belfroid, P. C. S., Tonon, D., Willems, F. H. J. and Hirschberg, A. A Parametric study on the whistling of multiple Side branch system as a model for corrugated pipes. *Proceedings of ASME Pressure Vessels and Piping Division Conference*, PVP2009-77754, Prague, Czech Republic, 2009.

———————————————————————————————————————

Previous publications of the author.

Journal Articles

- **Nakiboğlu, G.**, Gorlé, C., Horváth, I., van Beeck, J. and Blocken, B. Stack gas dispersion measurements with Large Scale-PIV, Aspiration Probes and Light Scattering Techniques and comparison with CFD. *Atmospheric Environment*, Vol 43(21):3396-3406, 2009.

- Özlugedik S., **Nakiboğlu, G.**, Sert, C., Elhan, A., Tonuk, E., Akyar, S. and Tekdemir, I. Numerical study of the aerodynamic effects of septoplasty and partial lateral turbinectomy. *Laryngoscope*, Vol 118(2):330-334, 2008.

Conference proceedings

- **Nakiboğlu, G.**, van Beeck, J., Horváth I. Determination of concentration by means of light scattering and digital image postprocessing. *Proceedings of 12th International Conference on Harmonisation within Atmospheric Dispersion Modelling for Regulatory Purposes*, Cavtat, Croatia, 2008.

- Sert C., **Nakiboğlu, G.** Use of Computational Fluid Dynamics (CFD) in Teaching Fluid Mechanics. *Proceedings of ASEE Annual Conference and Exposition*, Honolulu, Hawaii, 2007.

- Özlugedik S., **Nakiboğlu, G.**, Sert, C., Elhan, A., Tonuk, E., Akyar, S., Tekdemir, I. Aerodynamic effect of septoplasty and partial resection of the concha bullosa (in Turkish). *Proceedings of 29th Turkish National Congress of Otorhinolaryngology and Head & Neck Surgery*, Antalya, Turkey, 2007. (3rd Best-Paper Award)

Summary

Aeroacoustics of corrugated pipes

In thin walled pipes corrugations provide local stiffness while allowing global flexibility. This unique characteristic makes corrugated pipes convenient for applications ranging from domestic appliances to natural gas transportation. At critical conditions, however, the flow through these pipes drives self-sustained flow oscillations that lead to high-amplitude sound generation, called whistling.

While the literature provides crucial information on the whistling of corrugated pipes, there has been no attempt until now to develop a quantitative prediction method for the whistling of corrugated tubes. The main objective of the thesis is to develop a physical understanding of aeroacoustic sound generation due to self sustained flow oscillations in ducted cavities and to provide a quantitative prediction method for the whistling in corrugated pipes. The presented work combines experimental, numerical and analytical approaches to achieve this goal.

Experiments have been performed not only for corrugated pipes but also for multiple side branch systems and axisymmetric cavities in a pipe. These different setups are designed to address different aspects of the whistling in corrugated pipes. During experiments the emphasis has been on an accurate determination of the acoustic and hydrodynamic boundary conditions, which is essential for the numerical method. The extensive set of experimental data provides information on the effect of a number of geometrical parameters on the whistling namely, the length of the pipe, the cavity depth, the cavity width, the cavity edge radius and the separation distance between the cavities. Experiments also provide an understanding of the nature of the acoustic sources and the effect of velocity profile on the whistling.

In corrugated pipes the cavities are small compared to the wave length of the acoustic waves, which allows the use of a simplified approach. A numerical method that combines 2D-axisymmetric incompressible flow simulations with *Vortex-Sound Theory* is proposed to determine the time averaged acoustic source power produced by single or multiple axisymmetric cavities. The proposed numerical method is a computationally efficient approach. Thus, it was possible to use it extensively to address most of the aspects that have been investigated experimentally. Once

equipped with realistic acoustic and hydrodynamic boundary conditions, the numerical method appears to be very successful in predicting many aspects of the whistling including: Strouhal number ranges of acoustic energy production and absorption, the Strouhal number of maximum acoustic energy production (peak-whistling Strouhal number), the nonlinear saturation mechanism responsible for the stabilization of the limit cycle oscillation, the effect of the velocity profile on the whistling, the hydrodynamic interference observed between successive cavities. Using an energy balance whistling amplitude can be predicted within a factor two for moderate-high pulsation amplitude range.

The sound radiation from a short corrugated pipe segment (Hummer), used as a musical instrument, has been investigated. An analytical radiation model is proposed for the prediction of the observed frequency and the sound pressure level at the listener position. The radiation model also qualitatively explains the amplitude modulation, which provides the chorus like sound quality of this instrument.

Acknowledgments

It would not have been possible to write this doctoral thesis without the help and support of the kind people around me, to only some of whom it is possible to give particular mention here.

It is difficult to overstate my gratitude to Avraham Hirschberg (Mico). I am grateful for his continued encouragement and invaluable suggestions during this work. Without him this research work would not have been at this level of quality and certainly I would not have had as much fun as I did. It has been an honor to be his last Ph.D. student. I think we will all miss "So.... how is life ?" I should also mentioned that I have learned the real meaning of the *back-of-the-envelope calculation* from him.

I would also like to thank Harry Hoeijmakers for all the valuable comments that he provided.

I appreciate the valuable discussions that I had with Joachim Golliard, Stefan Belfroid, Paula Martínez-Lera, Christophe Schram and Han-Kwang Nienhuys.

I wish to thank my colleges: Oleksii Rudenko, Devis Tonon, Elise Moers, Raoul Liew, Jorge Vieyra Salas, Ergün Cekli and Sebastian Schmieschek for their contribution to my thesis through our fruitful discussions.

I would like to thank technical staff in particular Jan Willems, Henny Manders, Freek van Uittert, Ad Holten, Eric de Cocq, Leo van Hout, Gerald Oerlemans, Jorgen van der Veen; without their support experiments would not have been possible.

I would like to express my gratitude to our group secretary Brigitte A. M. van de Wijdeven for all her help in various aspects of life ranging from traveling forms to details of the Dutch childcare system.

Theo, Gerald, Brigitte, Jos, Berend en Mico wil ik bedanken voor hun lessen in het Nederlands. Ik heb het gevoel dat ik binnenkort alles wat ik heb geleerd zal vergeten, maar ik zal onze *kletsen* me herinneren.

Of course, the picture would be incomplete without the people in the Cascade who create a nice working environment. Thank you Alejandro, Altuğ, Anita, Aniruddha, Anton, Ariel, Bas, Badr, Berend, Brigitte, Calin, Christian, David, Evelyn, Federico, Florian (Günther and Janoschek), Folkert, Hao, Herman, Humberto, Jos, Jens, Jemil, Luca, Marly, Marjan, Margit, Mira, Naveed, Nelly, Özge, Paul (Aben and

Bleomen), Prasad, Rudie, Rafal, Richard, Rini, Stefan, Sudhir, Theo, Timm, Valetina, Vincent, Vitor, Willem, Yan.

Sizi biraz sona yazdım kusura bakmazsınız umarim :) Siz olmasaydınız ben buralara gelemezdim (çok da bir yer değil gerçi ama). Anneciğim ve babacığım hep yanımda olduğunuz için ikinize de çok teşekkür ederim.

Abi seni daha da sona yazdım sen de kusura bakma. Öncelikle orta okuldan başlayarak doktorayı bitirene kadar sıkılmadan (!), usanmadan (!) bana sürekli olarak matematik ve fizik anlatığın için teşekkür ederim. Benim yazdığım makalelerin çoğunu okuyup düzelttiğin için ayrıca teşekkür ederim. Gerçi soracaklarım daha bitmedi !

Enfin, ma reconnaissance infinie va à ma Judith(im). C'est un bonheur journalier d'avoir ton soutien moral, ta tendresse et ton amour. Je ne sais pas comment te remercier assez pour notre petite köfte, Nathalie. C'est pour nous la fin d'une époque et le début d'une grande aventure, notre histoire....

Curriculum Vitae

Born on October 1, 1981 in Kahramanmaraş, Turkije.

EDUCATION

Doctor of Philosophy   10/2008 - 03/2012
Department of Applied Physics   Eindhoven
Eindhoven University of Technology   The Netherlands
Topic: *Aeroacoustics of corrugated pipes.*

Post-Master in Fluid Dynamics   10/2007 - 06/2008
Environmental and Applied Fluid Dynamics Department   Rhode-St-Genése
von Karman Institute for Fluid Dynamics   Belgium
Topic: *Velocity and concentration measurements of a stack gas dispersion in an atmospheric boundary layer.*

Master of Science   09/2004 - 06/2007
Department of Mechanical Engineering   Ankara
Middle East Technical University   Turkey
Topic: *Development of an Educational CFD Software for Two Dimensional Incompressible Flows.*

Bachelor of Science   09/2000 - 06/2004
Department of Mechanical Engineering   Ankara
Middle East Technical University   Turkey

EXPERIENCE

Research and Development Engineer   06/2006 - 08/2007
Propulsion System Design Department   Ankara
ROKETSAN Missiles Industries Inc.   Turkey

Volunteer Researcher in Biofluidics   02/2006 - 08/2007
Mechanical Engineering Department   Ankara
Middle East Technical University   Turkey
Faculty of Medicine, Ankara University
Topic: CFD simulations of nasal airflow: on the effect of septal deviation and concha bullosa.

CFD Application Engineer   11/2004 - 01/2006
PUNTO Engineering   Ankara
METUTECH Technopark   Turkey